

Higher moments of net-charge multiplicity distributions in $Au + Au$ collisions in PHENIX experiment at RHIC



THESIS SUBMITTED FOR THE DEGREE OF

Doctor of Philosophy

in

Physics

by

Prakhar Garg

Supervisor

Prof. B. K. Singh

Co-supervisor

Prof. C. P. Singh

DEPARTMENT OF PHYSICS
BANARAS HINDU UNIVERSITY
VARANASI - 221005, INDIA

Enrollment No.: 275291

September 2014

**Copyright © Faculty of Science
Banaras Hindu University, Varanasi, India, 2014
All Rights Reserved**

Acknowledgements

I would like to dedicate a few lines in order to express my gratitude to all those people who have contributed in some way to complete this dissertation.

First of all, I am greatly indebted to my supervisor Prof. B. K. Singh, who has profoundly and continuously influenced my information throughout Ph. D. period. I acquired the ability to learn, to think, and to question by myself, to talk and to communicate with people in a professional and concise way, to be strict and cautious in research but respectful to people's work at the same time, and last but not least, the attitude that "one should either not do something or give it his best". His sense of humour, strictness to his students and constant support at the same time, all make an invaluable mix from which I, as his student, benefited a lot. I am very much thankful for his patience which he dealt with me during my hard time, his critical remarks and valuable suggestions.

I would also like to acknowledge my co-supervisor Prof. C. P. Singh for his magnanimous support during my Ph. D. period. I still remember his morning class during my masters which I used to wait eagerly and never missed it intentionally. He introduced me first with the heavy ion collision physics and fascinated me about it. I am very much thankful to him for his care and encouragement during various stages of my Ph. D.

I take this opportunity to express my sincere thanks to Prof. R. S. Tiwari, Head of the Department, for providing me all the necessary facilities available in the department during my research work. I would also like to thank Prof. R. P. Malik and Dr. V. Singh

for their friendly and supportive behavior.

I would like to express my sincere thanks to Prof. Itzhak Tserruya, Prof. Sasha Milov, Dr. Ilia Ravinovich, Dr. Deepali Sharma, Dr. Maxim Naglis, Dr. Yousuke Watanabe and Dr. Mihael Makek for very fruitful discussions related to Hadron Blind Detector, guidance, support and being friendly and helpful during my stay at Weizmann Institute of Science, Israel. I am very much thankful to Prof. Tserruya and Dr. Ilia who were patient enough to teach me in the early stage of my Ph. D.

I am also thankful to Prof. Craig Woody and Bob Azmoun for many useful discussions and their help related to detectors during my stay at BNL.

I had the pleasure to work with Prof. A. K. Mohanty, Dr. Dipak Mishra and Dr. Pawan Kumar Netrakanti from BARC, Mumbai who devoted their valuable time and effort in making me understand the higher moment analysis and its related phenomenology. I am thankful to your mentorship which made my journey of Ph. D. comfortable. Also I wish to thank Prof. Bedangadas Mohanty of NISER, Bhuvneshwar for fruitful discussions, help and guidance.

I am grateful to my co-research fellows Sourav Tarafdar, Arun Soma, Saurabh Gupta, Raj Singh, Prashant Srivastava, Ashwini Kumar, Arun Prakash, Lakhwinder Singh, Triloki and Swatantra Tiwari for their active participation at various stages of my research work and for the pleasant time we spent together. I would like to thank Prof. Alka Nigam and her family for care, love and generous support. She never let me feel away from my home. I also want to thank all my colleagues, comrades and friends in the Physics Department with whom I shared a lot of working days but also many hours of amusement and entertainment.

My feelings of gratitude extend to Mr. A. K. Mishra, Mr. R. S. Mishra, and Mr. R. K. Singh for their efficient efforts to manage all the official work. The financial support from Department of Science and Technology (DST), University Grant Commission (UGC) and Council of Scientific and Industrial Research (CSIR), New Delhi at various

stages of my research period is gratefully acknowledged.

I am also thankful to the organizers of different schools/ conferences/ symposium/ workshops, that I have attended during my research period, for providing me an opportunity to interact with experts of my field and present my research ideas in front of national and international physics community.

Finally, I wish to end these lines by heartily acknowledge all my family members, specially my mother and father for their unconditional love, care and patience. Their consideration for my situation and their unceasing support is what made my work possible.

(Prakhar Garg)

Preface

The phenomenology of Quantum Chromodynamics (QCD) at finite temperature (T) and baryon number density is one of the least explored regimes of the theory. QCD predicts a phase transition from hadron gas (HG) phase to quark gluon plasma (QGP) phase at high temperature and/or baryon density. The exact nature of the phase transition is still not established. However, various QCD based models indicate that at large net-baryon chemical potential (μ_B) and lower T the transition from hadronic phase to the Quark Gluon-Plasma (QGP) phase is of first order. On the other hand, lattice QCD calculation with physical quark masses suggests that the phase transition at high T and lower μ_B could be a simple cross over from hadron phase to QGP phase. It further suggests that the first order phase transition line should end somewhere at finite μ_B and that point will be a critical point.

Experimentally such a system of strong interactions can be created by colliding two nuclei at high energy. The variation of T and μ_B can be made available by varying the center of mass energy ($\sqrt{s_{NN}}$). Hence through relativistic heavy-ion collisions we can explore a two dimensional phase diagram, T versus μ_B , of strong interactions.

Recently, it has been proposed that the higher order fluctuation variables i.e. higher moments (mean (μ) = $\langle x \rangle$, variance (σ^2) = $\langle (x - \mu)^2 \rangle$, skewness (S) = $\frac{\langle (x - \mu)^3 \rangle}{\sigma^3}$ and kurtosis (κ) = $\frac{\langle (x - \mu)^4 \rangle}{\sigma^4} - 3$) of conserved quantities, such as net-baryon, net-charge and net-strangeness distributions are related to their corresponding thermodynamic susceptibility. As an example the third order charge susceptibility is $\chi_{(Q)}^3 = \langle (\delta N_Q)^3 \rangle / VT^3 \sim S$. Further, model calculations demonstrate that these susceptibilities and hence the higher moments are sensitive to the correlation length (ζ), as $\langle (\delta N_Q)^3 \rangle \propto \zeta^{4.5}$ and for the forth order cumulant as: $\langle (\delta N_Q)^3 \rangle - 3\langle (\delta N_Q)^2 \rangle^2 \propto \zeta^7$, which is expected to diverge at the QCD critical point. Therefore, any non-monotonic behavior of the experimentally measured higher moments with $\sqrt{s_{NN}}$ may lead to the location of QCD critical point, if it exists. Since the volume of the system is hard to

determine experimentally and to avoid the volume fluctuations, the ratios of susceptibility, such as $\frac{\chi_Q^4}{\chi_Q^2}$ and $\frac{\chi_Q^3}{\chi_Q^2}$ are used to compare with the experimental data as $\kappa\sigma^2 = \frac{\chi_Q^4}{\chi_Q^2}$ and $S\sigma = \frac{\chi_Q^3}{\chi_Q^2}$.

Our main motivation of performing higher moments analysis in heavy ion collision experiment is to locate the critical point at which the first-order transition between hadron matter and quark-gluon plasma (QGP) ends. Currently there is no systematic way of locating this point from the first principles as model and lattice calculations face many challenges at finite μ_B . Therefore, several experimental programs besides RHIC have been planned to perform heavy ion collision experiments to locate the QCD critical point, such as SPS/LHC at CERN (Switzerland), FAIR at GSI (Germany) and NICA at JINR (Russia).

In year 2010 (Run-10), RHIC started Beam Energy Scan (BES) program to tune the center of mass energy from $\sqrt{s_{NN}} = 200$ GeV down to $\sqrt{s_{NN}} = 7.7$ GeV. The data collected by PHENIX with Au+Au collisions at 200 GeV in year 2007 (Run-7), other lower energies 7.7 GeV, 62.4 GeV and 39 GeV during year 2010 (Run-10) and data for $\sqrt{s_{NN}} = 19.6$ GeV and 27 GeV is taken in year 2011 (Run-11). The large uniform acceptance of PHENIX detectors provides us an excellent opportunity to search for the QCD critical point at RHIC, if it exists in the experimentally accessible area of phase diagram.

This thesis attempts a systematic study of higher moments of net-charge multiplicity distributions in Au+Au collisions measured by PHENIX detector at 7.7 GeV, 19.6 GeV, 27 GeV, 39 GeV, 62.4 GeV and 200 GeV center of mass energies per nucleon pair. Besides, the statistical thermal model based conserved number fluctuation and the importance of reconstruction efficiency correction is discussed. The thesis is organized in the following chapters:

Chapter 1 gives an introduction of QCD phase diagram and QCD critical point. Also, an overview of present and future experimental facilities to explore the QCD phase

diagram are discussed. Particular emphasis is given to the experimental approach to probe the QCD critical point as the present work is centered around it.

In **Chapter 2**, we briefly describe the Relativistic Heavy Ion Collider (RHIC), the experimental facility, dedicated to study the heavy ion collisions at Brookhaven National Laboratory (BNL), USA. Further, the PHENIX experiment and it's detector subsystems are introduced. PHENIX detector is an agglomeration of several sophisticated detectors, meant for different purposes. Therefore, more emphasis is given to the set of detectors used in the present analysis.

Electron pairs or di-leptons in general are unique probe to study the hot and dense matter formed in relativistic heavy ion collisions at RHIC. But the experimental challenge is the huge combinatorial background created by e^+e^- pairs from copiously produced π^0 Dalitz decay and γ conversions. In order to reduce this background, a Hadron Blind Detector (HBD) was proposed in PHENIX for electron identification in high-density hadron environment. The operation principle and performance studies of HBD carried out with p+p collisions at RHIC are also discussed.

In **Chapter 3**, the moments and cumulants of the multiplicity distributions and their relations are discussed. Also, the method of calculating correlated errors and the efficiency corrections to the cumulants are briefly described. Further, it presents the details how the real data sets collected by PHENIX are being used for the analysis. The ion beam in RHIC don't remain well focussed all the time. Whenever the quality of beam becomes bad, it is stopped (or dumped) and PHENIX stops taking data. After the beam quality is recovered, PHENIX detector is restarted to collect data. The period from the start of beam when PHENIX starts taking data until the beam is dumped or PHENIX stops taking data is called a *Run*. Therefore the first step is to insure the Run quality. Once we identify good runs then we move forward to identify good collision events. To check the quality of the selected events, the information from different subsystems is used and the pile-up events are removed. After selecting good

events out of good runs the track (profile of the produced particles in an event) cuts are applied so that tracks used for the analysis are of good quality and lower the probability of secondary background tracks. Afterwards, centrality bin width effect, transverse momentum (p_T) dependence, acceptance (η and ϕ) dependence, track matching effects, effect of tracking efficiency, effect of collision vertex selection on various moments are studied. Also, the effect of resonance decay on various moments with the help of **PHENIX Integrated Simulation Analysis** (PISA) is analyzed. Mostly the Events are generated with HIJING (Heavy Ion Jet Interaction Generator) and UrQMD (Ultra-relativistic Quantum Molecular Dynamics) event generators for simulation studies.

Further, in this chapter the recent results of higher moments of net-charge multiplicity distributions for Au+Au collisions at $\sqrt{s_{NN}}$ varying from 7.7 GeV to 200 GeV measured by PHENIX detector at RHIC are shown. The energy and centrality dependence of the higher moments and their products are also shown for the net-charge multiplicity distributions. The results are compared with the values obtained from different heavy-ion collisions models. Although, to confirm the existence of critical point, additional energies with larger statistics are required, which are planned in the BES II program of RHIC.

In **Chapter 4**, net-baryon, net-charge and net-strangeness number fluctuations in high energy heavy-ion collisions are discussed within the framework of a Hadron Resonance Gas (HRG) model. HRG is a statistical-thermal model in which hadrons and resonances are treated as non-interacting and point-like particles in the present study. Resonances are included in the model to incorporate the attractive interactions among hadrons.

Ratios of the conserved number susceptibilities calculated in HRG model are being compared to the corresponding experimental measurements to extract information about the freeze-out condition and the phase structure of strongly interacting systems. The importance of considering the actual experimental acceptances in terms of kine-

matics (η and p_T), the detected charge state, effect of collective motion of particles in the system and the resonance decay contributions before comparisons are made to the theoretical calculations, is emphasized.

In **Chapter 5**, a Bayes method is used to obtain the event-by-event true distributions of net-charge from the corresponding measured distributions which are subjected to detector effects like finite particle counting efficiencies. For this study, HIJING and THERMINATOR event generators are used to simulate the charged particle distributions produced in Au+Au collisions at $\sqrt{s_{NN}} = 19.6$ to 200 GeV respectively. It is shown that the unfolded distribution has similar mean, variance, skewness and kurtosis as the true distributions for all the collision centralities studied. The product of the moments σ^2/M , $S\sigma$ and $\kappa\sigma^2$ which show an opposite trends versus N_{part} for the measured distributions compared to the true distributions are faithfully unfolded back to agree with the true distributions.

Chapter 6 provides the summary and conclusions drawn from this thesis work and some future insights are also provided in this area of research.

Contents

Acknowledgements	ix
1 Introduction	1
1.1 Quark Gluon Plasma and Heavy ion collisions	4
1.2 QCD Phase Diagram and QCD Critical Point	6
1.2.1 Conjectured QCD Phase Diagram	6
1.2.2 QCD Critical End Point	9
1.3 QCD Critical point: brief experimental overview	11
1.4 Fluctuations and Correlations to probe QCD Critical Point	14
2 Experimental Overview	18
2.1 The Relativistic Heavy Ion Collider	18
2.2 The PHENIX Detector	21
2.2.1 PHENIX coordinate system and acceptance	24
2.3 Global Event Characterization	25
2.3.1 Global Detectors	25
2.3.2 Collision Centrality Determination	26
2.3.3 Collision Vertex Determination	28
2.4 Charged particles tracking	28

2.4.1	Central arm tracking detectors	29
2.4.2	Track reconstruction	33
2.4.3	Momentum determination	36
2.5	Electron Identification	37
2.5.1	Ring Imaging Cherenkov Detector	38
2.5.2	Electromagnetic Calorimeter	38
2.6	Hadron Blind Detector	39
2.6.1	Detector concept and performance	41
2.6.2	Electrons Background in RUN-9	42
2.6.3	Detector Alignment Corrections	43
2.6.4	Position Resolution of HBD	44
2.6.5	Hadron Rejection Factor	44
2.6.6	Event Accumulator to study HBD pattern recognition	47
2.7	PHENIX data acquisition system	50
3	Data Analysis and Results of Higher moments	53
3.1	Analysis Overview	53
3.2	Data sets, Event selection and Track selection	54
3.2.1	Event Selection	54
3.2.2	Track selection	58
3.3	Moments Methodology in Heavy Ion Collisions	61
3.4	Relation between central moments and cumulants of Event-by-Event Fluctuations	61
3.4.1	Moments and Cumulants of Poisson Distribution	63
3.4.2	Cumulants of Negative Binomial Distribution (NBD)	65

3.5	Error Estimation of Cumulants	65
3.6	Formulation for Efficiency correction	66
3.7	Event-by-event net-charge distributions	69
3.8	HIJING and UrQMD Event Generators	72
3.9	Systematic effects	75
3.9.1	Centrality Resolution Effect and Bin Width Correction	75
3.9.2	Effect of kinematics on higher moments	77
3.9.3	Effect of events Z_{vertex} selection on various moments	81
3.9.4	Resonance decay effect on the various moments	81
3.9.5	Effect of PC3 and EMC track matching	82
3.10	Reconstruction Efficiency Correction for Cumulants	84
3.11	Analysis Results	87
3.11.1	Centrality dependence of moments and their products as a function of N_{part}	88
3.11.2	Energy dependence for Product of Moments	90
4	Conserved Number Fluctuations in Ideal Hadron Resonance Gas Model	93
4.1	Hadron Resonance Gas Model	95
4.2	Results	98
4.2.1	Effect of Kinematic acceptance in η and p_T	98
4.2.2	Effect of Conserved charge states	99
4.2.3	Effect of flow	101
4.2.4	Effect of Resonance decay	103
4.3	Summary	106

5 Unfolding of event-by-event net-charge distributions in heavy-ion collision	108
5.1 Event generators	112
5.2 Bayes method for unfolding of distributions	113
5.3 Results and Discussions	116
5.4 Summary	123
6 Summary	125
Bibliography	128

Figures

1.1	The running coupling α_s as a function of energy scale Q , measured in different experiments and from theoretical calculations [5].	3
1.2	Time-evolution of a heavy ion collision. Nuclei approach each other at the speed of light and collide, creating new matter in the process. The new matter expands and cools as a fluid, eventually freezing into particles.	5
1.3	Schematic phase diagram of water in pressure-temperature ($P - T$) plane [35].	7
1.4	Conjectured QCD Phase Diagram in $T - \mu_B$ plane [10]	8
1.5	Comparison of predictions for the location of the QCD critical point on the phase diagram [40]	10
2.1	RHICs 2.4 mile ring has six intersection points where its two rings of accelerating magnets cross, allowing the particle beams to collide.	19
2.2	The PHENIX detector layout in the 2007 run. The upper panel shows the beam view where the two central arms and central magnet can be seen. The lower panel shows the side view where the two muon arms and the two muon magnets are shown.	21
2.3	The PHENIX detector layout in Run-10 (left column) and in Run-11 (right column)	22
2.4	Magnetic field lines in the PHENIX detector, for the two central magnet coils in +- (left) and ++ (right) modes.	23

2.5 (a) PHENIX global coordinate system (left) (b) PHENIX acceptance for identified electrons, muons, photons and hadrons (right).	25
2.6 PHENIX Centrality measurement and ZDC BBC Correlation [73]	26
2.7 Schematic view of one arm of the PHENIX DC subsystem.	30
2.8 (a) Wire structure of a DC keystone. (b) The relative arrangement of the U, V and X wire layers.	30
2.9 Schematic view of the PHENIX PC subsystem. Several sectors of PC3 and PC2 in the West arm are removed for clarity.	32
2.10 The pad and pixel geometry (left). A cell defined by three pixels from tree neighboring pads is shown in the center (right).	32
2.11 Left: Schematic view of a track in the DC in cartesian and polar co-ordinates. The X1 and X2 hits in the DC are shown as small circles. Right: Schematic view of a track in the DC r-z plane.	35
2.12 Background (B) and Signal (S) with statistical (bar) and systematic (boxes) uncertainties. The inset shows S/B ratio [85].	40
2.13 Schematic of HBD working principle in forward bias mode (left) and in reverse bias mode (right)	41
2.14 Electrons background in Run-9 minimum bias data	43
2.15 Matching distribution for the electron tracks in Z (cm)	44
2.16 Matching distribution for the electron tracks in Φ (rad)	45
2.17 The variation of matching resolution of the electron tracks in Z and Φ with respect to momentum.	45
2.18 (left) Hadron charge spectra in reverse (red) and forward bias (blue) (right) Hadron Rejection Factor as a function of charge threshold.	46
2.19 Three electrons in an event (red squares) from Run-10 minimum bias data are represented by red squares (Charge Threshold= 31.6 ADC).	47

2.20	Detector occupancy with centrality	48
2.21	Fraction of electron loose with centrality for integrated momentum and different momentum bins.	49
2.22	Cluster charge per electron track with different number of accumulated events .	49
2.23	HBD signal/Background vs central arm tracks.	50
2.24	Block diagram of PHENIX DAQ.	51
3.1	The correlation plot for Au+Au collisions at 19.6 GeV: BBC charge vs DCH tracks, PC1 hits and PC3 hits before applying the cuts are shown in top row. Bottom row shows the correlations after applying the cuts.	55
3.2	The DCH track, PC1 hit and PC3 hit distributions before selecting the good events for 200 GeV Au+Au collisions in Run-7.	56
3.3	The correlation plots for BBC charge vs DCH tracks, PC1 hits, PC3 hits and ZDC energy before applying the cuts for 200 GeV data.	57
3.4	The correlation plots for BBC charge vs DCH tracks, PC1 hits and PC3 hits after applying the cuts for 200 GeV data.	58
3.5	The DCH track, PC1 hit and PC3 hit distributions after selecting the good events for 200 GeV Au+Au collisions in Run-7.	59
3.6	Uniform η vs p_T acceptance for all charged hadrons used for the analysis. . . .	60
3.7	A pictorial view of negative and positive skewed distributions are shown with black curve (left two panels) as compared to normal distribution (red). Further, right most panel shows distributions with positive (green) and negative (blue) kurtosis with respect to the normal distribution (red).	62
3.8	Event-by-event net-charge (ΔN) distributions for Au+Au collisions at different energies for 0-5% (left panel) and 55-60% (right panel) centrality bins.	69

3.9 Event-by-event positive charge (N_+) distributions for different centralities at $\sqrt{s_{NN}} = 27$ GeV. The distributions are fitted with Negative Binomial distribution (NBD).	70
3.10 Event-by-event positive charge (N_-) distribution for different centralities at $\sqrt{s_{NN}} = 27$ GeV. The distributions are fitted with Negative Binomial distribution (NBD).	71
3.11 The mean, standard deviation, skewness and kurtosis for Au+Au collisions at various energies as a function of centrality (in terms of number of participating nucleons) for net-charge distributions are obtained from HIJING events.	72
3.12 Products of moments ($\frac{\sigma^2}{M}$, $S\sigma$ and $\kappa\sigma^2$) are plotted with respect to the average number of participating nucleons, obtained from HIJING events for net-charge distributions.	73
3.13 The mean, standard deviation, skewness and kurtosis for Au+Au collisions at various energies as a function of centrality (in terms of number of participating nucleons) are shown using UrQMD events.	74
3.14 Products of moments, $\frac{\sigma^2}{M}$, $S\sigma$ and $\kappa\sigma^2$, plotted with respect to the average number of participating nucleons, obtained from UrQMD events for net-charge distributions.	74
3.15 Various moments and their product of net-charge distributions as a function of centrality bin for 3% bin width (left two columns) and 5% bin width (right two columns) for Au+Au collisions at $\sqrt{s_{NN}} = 200$ GeV: open symbols are before bin width correction and the star symbols are after correction. Left side of the x-axis implies peripheral collisions and right side corresponds to central collisions. .	76
3.16 Various moments of net-charge distributions as a function of centrality bins (10% bin width) at $\sqrt{s_{NN}}=200$ GeV.	76
3.17 Moments and their product for net-charge distributions reconstructed in different p_T bins as a function of N_{part}	78

3.18 Acceptance dependence of various moments of net-charge for the most central bins (0-5%) for Au+Au 200 GeV HIJING events. The solid triangles (blue) are for tracks within $\Delta\eta < 1.0$ and the open triangles (red) are for tracks within PHENIX acceptance in η	79
3.19 Various moments of net-charge distributions for the most central bins (0-5%) for Au+Au collisions at $\sqrt{s_{NN}} = 200$ GeV HIJING events in different η selection windows. The solid triangles (blue) are tracks within $\Delta\phi < 2\pi$ and the open triangles (red) are tracks within PHENIX acceptance in ϕ	80
3.20 Centrality dependence of various moments of net-charge for Au+Au collisions at $\sqrt{s_{NN}} = 27$ GeV for different Z_{vertex} cuts.	81
3.21 Centrality dependence of product of moments ($S\sigma$ and $\kappa\sigma^2$) of net-charge for Au+Au collisions at different collision energies for different Z_{vertex} cuts.	82
3.22 Centrality dependence of various moments of net-charge for Au+Au collisions at $\sqrt{s_{NN}} = 200$ GeV using HIJING event generator. Solid symbols are for with resonance decay option “ON” and open symbols are for “NO” decay option.	83
3.23 The centrality dependence of various moments of the net-charge distributions at various $\sqrt{s_{NN}}$ are shown with EMC-PC3 matching and without matching of selected tracks.	84
3.24 Centrality dependence of various moments of net-charge for Au+Au collisions at $\sqrt{s_{NN}} = 27$ GeV using HIJING event generator. Solid symbols are for generated tracks and open symbols are for reconstructed tracks after passing through PHENIX detector setup.	85
3.25 Centrality dependence on ratio and products of moments of net-charge for Au+Au collisions at $\sqrt{s_{NN}} = 27$ GeV using HIJING event generator. Solid symbols are for generated tracks and open symbols are for reconstructed tracks after passing through GEANT detector simulation.	86

3.26 Mean of an event-by-event distribution for positive and negative hadrons obtained from HIJING at $\sqrt{s_{NN}} = 27\text{GeV}$ for different N_{part} is compared with reconstructed distributions from PISA setup (left two panels). The ratio of reconstructed to generated number of tracks i.e. efficiency (ϵ) is shown for both positive and negative hadrons (rightmost panel).	86
3.27 The p_T dependance of efficiency for different magnetic field settings in PHENIX for π^+ (Pos) and π^- (Neg) using EXODUS	87
3.28 The efficiency corrected centrality dependency of various moments, such as M , σ , S and κ are plotted for different energies from $\sqrt{s_{NN}} = 7.7$ to 200 GeV.	89
3.29 The efficiency corrected centrality dependence of $\frac{\sigma^2}{M}$, $S\sigma$ and $\kappa\sigma^2$ is plotted for different energies from $\sqrt{s_{NN}} = 7.7$ to 200 GeV.	90
3.30 The beam energy dependency of $\frac{\sigma^2}{M}$, $S\sigma$ and $\kappa\sigma^2$ are plotted for 0 – 5% central collisions. The blue line represents HRG model predictions. The vertical lines represent the statistical error bar and box represent systematic error.	91
4.1 The η acceptance dependence of $\chi_x^{(3)}/\chi_x^{(2)}$ and $\chi_x^{(4)}/\chi_x^{(2)}$ for two different beam energies. In panel (a) and (b) x = net-baryon B , (c) and (d) x = net-charge Q , and in (e) and (f) x = net-strangeness S . The results with (labeled “dep.”) and without (labeled “fixed”) the η dependence of chemical freeze-out parameters μ_B and T are shown.	98
4.2 The p_T acceptance dependence of $\chi_x^{(3)}/\chi_x^{(2)}$ and $\chi_x^{(4)}/\chi_x^{(2)}$ for different $\sqrt{s_{NN}}$. Where x stands for either net-baryon (B) (panels (a) and (b)), net-charge (Q) (panels (c) and (d)), and net-strangeness (S) (panels (e) and (f)).	100
4.3 Variation of $\chi_x^{(3)}/\chi_x^{(2)}$ and $\chi_x^{(4)}/\chi_x^{(2)}$ for net-baryon (B), net-charge (Q), and net-strangeness (S) as a function of collision energy ($\sqrt{s_{NN}}$). The results are shown for different baryons (panels (a) and (b)), electric charge states (panels (c) and (d)) and strangeness number (panels (e) and (f)) considered in the calculation.	101

4.4	The variation of $\chi_x^{(3)}/\chi_x^{(2)}$ and $\chi_x^{(4)}/\chi_x^{(2)}$ for net-baryon (B), net-charge (Q), and net-strangeness (S) with different beam energies ($\sqrt{s_{\text{NN}}}$) with and without resonance decay daughter particle acceptance effects.	103
5.1	Top panel: Event-by-event distribution of positive, negative and net-charge (denoted as “True”, solid line) in Au+Au collisions for impact parameter $b = 1.7$ fm at $\sqrt{s_{\text{NN}}} = 19.6$ GeV from HIJING event generator. Also shown are the corresponding distributions after applying acceptance and efficiency effects as discussed in the text (denoted as “Measured”, open circles). The unfolded distributions are shown as red stars and denoted as “Bayes”. Bottom panel: Shows the ratio of the unfolded to the True distributions.	115
5.2	Mean, standard deviation, skewness and kurtosis of net-charge distribution in Au+Au collisions at $\sqrt{s_{\text{NN}}} = 19.6$ GeV from HIJING event generator. Results are shown for the True, measured and Bayes unfolded distributions as a function of N_{part}	117
5.3	Ratio of the unfolded to the True net-charge distribution moments of Fig. 5.2 as a function of N_{part}	118
5.4	Ratio (panel a) and product of moments (panel (b) and (c)) of net-charge distributions in Au+Au collisions at $\sqrt{s_{\text{NN}}} = 19.6$ GeV from HIJING event generator. The results are for the True, measured and Bayes unfolded distributions as a function of N_{part}	119
5.5	Mean, standard deviation, skewness and kurtosis of net-charge distribution in Au+Au collisions at $\sqrt{s_{\text{NN}}} = 200$ GeV from THERMINATOR event generator. Results are shown for the True, measured and Bayes unfolded distributions as a function of N_{part}	120
5.6	Product of moments of net-charge distributions in Au+Au collisions at $\sqrt{s_{\text{NN}}} = 200$ GeV from THERMINATOR event generator. The results are for the True, measured and Bayes unfolded distributions as a function of N_{part}	120

5.7	Product of moments of net-charge distributions in Au+Au collisions at $\sqrt{s_{\text{NN}}} = 19.6$ GeV from HIJING event generator with constant efficiency of 65%. The results are for the True, measured and Bayes unfolded distributions as a function of N_{part}	121
5.8	Product of moments of net-charge distributions in Au+Au collisions at $\sqrt{s_{\text{NN}}} = 200$ GeV from THERMINATOR event generator with constant efficiency of 65%. The results are for the True, measured and Bayes unfolded distributions as a function of N_{part}	121
5.9	Mean, standard deviation, skewness and kurtosis of net-charge distribution in 0-5% Au+Au collisions as a function of $\sqrt{s_{\text{NN}}}$ from HJING event generator. Results are shown for the True, measured and Bayes unfolded distributions . .	122
5.10	Product of moments of net-charge distribution in 0-5% Au+Au collisions as a function of $\sqrt{s_{\text{NN}}}$ from HIJING event generator. The results are for the True, measured and Bayes unfolded distributions.	123

Tables

1.1	Past, current and future accelerator experiments for heavy-ion collisions:	12
2.1	The RHIC runs and the integrated luminosity delivered to the PHENIX experiment:	20
2.2	Summary of the PHENIX central arm subsystems.	24
2.3	The centrality classes and the corresponding average number of nucleon- nucleon collisions, participants and impact parameter for Au+Au collisions at $\sqrt{s_{NN}} = 200$ GeV from Glauber Calculation:	27
2.4	Summary of the DC track quality.	35
3.1	Number of good events selected for the analysis at different $\sqrt{s_{NN}}$:	57
4.1	Ratios of the moments for net-charge within $ \eta < 0.5$, and $0.2 < p_T < 2.0$ GeV/ c .104	
4.2	Ratios of the moments for net-charge within $ \eta < 0.35$, and $0.3 < p_T < 1.0$ GeV/ c :	105
4.3	Ratios of the moments for net-kaon within $ \eta < 0.5$, and $0.2 < p_T < 2.0$ GeV/ c .106	
4.4	Ratios of the moments for net-proton within $ \eta < 0.5$, and $0.4 < p_T < 0.8$ GeV/ c .107	

Chapter 1

Introduction

Human beings have been always questing about the ultimate building blocks of the matter as well as their interaction mechanisms. The visible matter of the Universe mainly consists of two types of fundamental particles - quarks and leptons along with their anti-particles. The interactions among these fundamental particles are mediated by gauge-bosons e.g., photons (γ), gluons (g), W^\pm , Z^0 , and gravitons (G). Quarks (anti-quarks) exist in six different flavours and similarly there are six different types of leptons (anti-leptons) also : electron (positron), muon (anti-muon), tau (anti-tau) lepton, and the corresponding three neutrinos (anti-neutrinos). Each quark (anti-quark) can exist in three possible colours e.g. red (anti-red), blue (anti-blue) and green (anti-green). These colour charges generate the strong interactions among the quarks (anti-quarks). Quarks and antiquarks form two different type of colour neutral bound states named as baryons (three quark states) and mesons (quark-antiquark states). Gluons which mediate the strong interactions between quarks, are bi-coloured vector particles and exist in eight possible kinds. Further, gluons have zero rest mass and spin 1. The quantum field theory (QFT) which describes the interactions between point-like constituents quarks and gluons is known as Quantum Chromodynamics (QCD) just as the interactions between two electrically charged particles (i.e. electromagnetic interaction) is governed by quantum electrodynamics (QED). However, QCD is a non-abelian gauge theory in contrast to QED which is an abelian gauge theory. The non-abelian nature of the QCD arises since the gluons carry colour charges and hence are self-interacting while photons are electrically neutral particles and hence they do not possess self-interactions. Two

basic properties of the QCD theory are:

- Asymptotic freedom and
- Confinement.

The strong interaction between quarks and gluons at large distances (gives confinement) and asymptotic freedom at short distance are the two remarkable features of QCD, discovered by Gross, Politzer and Wilczek in 1973 [1]. According to the behavior of short distance and large distance, the static QCD potential can suitably be described as:

$$V_s = -\frac{4}{3} \times \frac{\alpha_s}{r} + k \times r, \quad (1.1)$$

where the first term dominates at small distance, arises from single-gluon exchange, similar to the Coulomb potential between two charges in QED, while the second term is presumably linked to the confinement of quarks and gluons inside hadrons.

The renormalized effective QCD coupling $\alpha_s(\mu) = g_s^2/4\pi$ depends on the renormalization scale (running coupling), similar to that in QED. However, the QED running coupling increases with energy scale, while the gluon self-interactions lead to a completely different behavior in QCD.

The running coupling constant α_s in QCD can be expressed in terms of a squared four momentum transfer Q^2 , the number of quark flavours N_f and the typical QCD scale $\Lambda_{QCD} \approx 0.2$ GeV [2] [3]:

$$\alpha_s(Q^2) = \frac{g_s^2}{4\pi} = \frac{12\pi}{(33 - 2N_f) \ln(\frac{Q^2}{\Lambda_{QCD}^2})}. \quad (1.2)$$

The running of α_s is confirmed precisely by experimental results as shown in Fig. 1.1 [4]. From Eq. 1.2, it is clear that $\alpha_s \rightarrow \infty$ when $Q^2 = \Lambda_{QCD}^2$, and $\alpha_s \rightarrow 0$ when $Q^2 \rightarrow \infty$. Thus the QCD scale parameter determines the strength of the coupling constant.

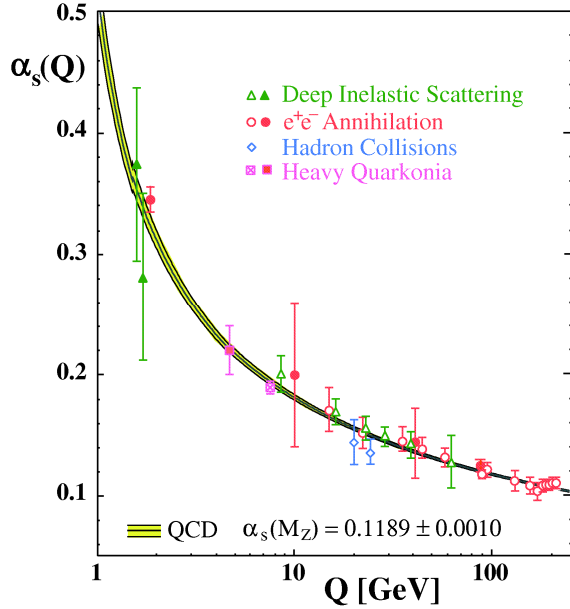


Figure 1.1. The running coupling α_s as a function of energy scale Q , measured in different experiments and from theoretical calculations [5].

The infinite value of the running coupling constant when $Q^2 = \Lambda_{QCD}^2$ (i.e, the large distance limit) gives the “quark confinement” property of the QCD whereas zero value of the running coupling constant when $Q^2 \rightarrow \infty$ (i.e, the short distance limit) is referred as the “asymptotic freedom”. Consequently, at very large temperatures and/or densities, the interactions which confine quarks and gluons inside hadrons should become sufficiently weak to release them as free particles. The phase in which quarks and gluons are deconfined is termed as Quark Gluon Plasma (QGP) [6] [7] [8]. In QGP , a long range colour force is Debye screened due to collective effects similar to the case of electromagnetic plasma [9]. Thus the quarks can only interact via a short range, weak potential and consequently they tend to behave as almost free and deconfined particles after a critical value of temperature and /or density is achieved. The transition from colour insulating hadronic matter to colour conducting QGP is a new kind of phase transition since these two states of matter are very much different in nature.

On the other hand, when $Q^2 \rightarrow \infty$, QCD can be calculated perturbatively in high momentum transfer or short distance approach (pQCD) while for $Q^2 = \Lambda_{QCD}^2$, QCD is non-perturbative. In the strong coupling case, pQCD is irrelevant and some other methods may become essential like Lattice QCD and AdS/CFT.

1.1 Quark Gluon Plasma and Heavy ion collisions

QCD predicts that the quarks and gluons are confined in the hadrons in the normal conditions while a new form of matter, the quark-gluon plasma (QGP), dominated by quark and gluon degrees of freedom can be formed by heating and/or compressing normal nuclear matter. The QGP exist in early Universe, when the universe was only a few tens of microseconds old. On the other hand, a compact star, such as neutron star, is much cooler than the QGP, but it is compressed by its own weight to such high densities that it is reasonable to imagine that quark matter can again exist in the core. Experimentally, QGP can be created by “heating”, i.e. by depositing energy into the colliding system. A unique experimental tool to reproduce the similar environment is to collide two heavy ions at very high energy. One expects to create matter under conditions that are sufficient for deconfinement. The heavy ions are accelerated and collided in the relativistic heavy ion colliders, which is designed to search for the new form of matter i.e. QGP. By colliding two nuclei at different energies, we can produce hot dense nuclear matter at various temperature (T) and baryon chemical potential (μ_B). Hence, it allows us to access the different regions of the QCD phase diagram in order to search for the QCD critical point and map the first order phase transition boundary. Initially in 70s and early 80s some accelerators used for particle physics were converted to accelerate heavy ions such as Bevatron at the Berkeley Lab. At the same time the energies of the accelerators used for nuclear research increased, such as in NSCL/MSU and GSI in Darmstadt. By the mid 80s the heavy ions were injected into some of the highest energy proton accelerators also, i.e. Alternating Gradient

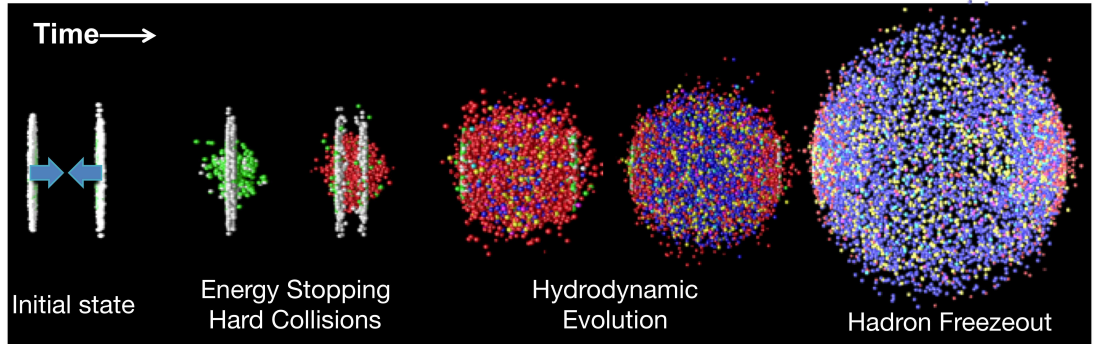


Figure 1.2. Time-evolution of a heavy ion collision. Nuclei approach each other at the speed of light and collide, creating new matter in the process. The new matter expands and cools as a fluid, eventually freezing into particles.

Synchrotron (AGS) at Brookhaven National Laboratory (BNL) and the Super Proton Synchrotron (SPS) at the European Center for Nuclear Research (CERN). By the early 90s the injection of the heavy ions was at the planning phase of new accelerators, like Relativistic Heavy Ion Collider (RHIC) at BNL and Large Hadron Collider (LHC) at CERN. RHIC has successfully performed Au+Au and Cu+Cu collisions at $\sqrt{s_{NN}} = 200$ GeV, which is the designed top energy for heavy ion collisions. In 2010, Pb+Pb head on collisions at $\sqrt{s_{NN}} = 2.76$ TeV were performed by LHC at CERN.

Fig. 1.2 shows a space-time evolution of the matter formed in a relativistic heavy ion collision. Because of the Lorentz contraction effect in the moving direction, two nuclei can be seen as two thin disks approaching each other at high velocity. The energy density estimated with Bjorken approximation [11] for Au+Au central collision at RHIC top energy ($\sim 5\text{GeV}/\text{fm}^3$) is much higher than the energy density expected for the formation of QGP from the Lattice QCD calculation ($\sim 1\text{GeV}/\text{fm}^3$). The physics processes at the initial stage ($\sim 1\text{fm}/c$) are dominated by hard scatterings, such as quark pair production, jet production and fragmentation. During the initial stage of the collisions, heavy ions deposit their energy into the collision region and hadrons "melt" into quarks and gluons to form QGP. The subsequent processes are the expansion and

hadronization of QGP, when the fireball cools down and partons are hadronized into hadrons ($1 \sim 10 \text{ fm}/c$) also. Then, the system reaches a stage called chemical freeze-out, where the abundance of the hadrons are fixed and the inelastic interaction between hadrons ceases. Finally, the system is dilute enough and comes to the kinetic freeze-out as an end, when hadrons cease their elastic interactions ($10 \sim 15 \text{ fm}/c$). Plenty of exciting physics results reveal that the matter created at RHIC top energy is quite different from what we observed before and it can not be described by hadronic degrees of freedom. Those measurements provide strong hints that the strongly interacting QGP has been formed at top energy of Au+Au collisions at RHIC.

1.2 QCD Phase Diagram and QCD Critical Point

A lot of progress has been made recently to understand the QCD phase transition but most of the things are still not clear and there are many unanswered questions in this field, e.g., the relation between deconfining and chiral symmetry restoring phase transition, position of critical point (CP) on the phase diagram and its properties and the signals for detection of QGP formation. Recently many papers have addressed these questions in order to understand the phase diagram of QCD [12–34]. However, it is still a burning topic and needs further investigations. The studies about QGP help us in our understanding regarding the early stages of the Universe after the Big-Bang. Similarly the properties of dense matter are needed to understand the properties of the inner core of neutron stars.

1.2.1 Conjectured QCD Phase Diagram

A phase diagram mainly gives the information about the location of the phase boundaries (phase transitions) as well as the physics of the phases that these transitions delineate. The phase transitions involve the thermodynamic singularities of the system.

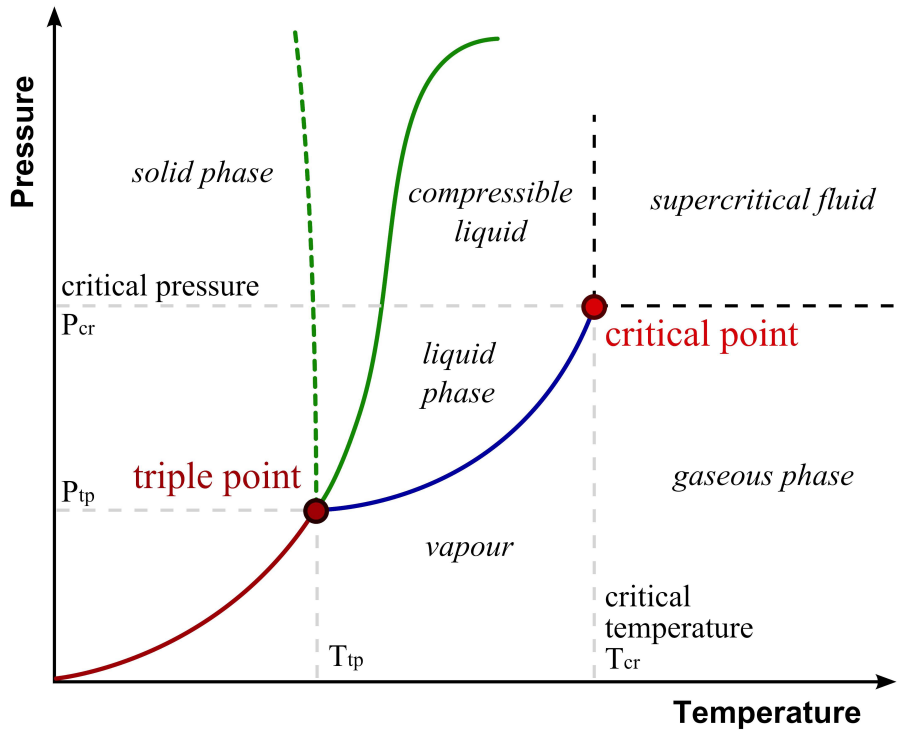


Figure 1.3. Schematic phase diagram of water in pressure-temperature ($P - T$) plane [35].

According to the Ehrenfest classification, a phase transition is of first-order, if at least one of the first derivatives of the grand canonical potential is discontinuous, and of second order if the first are continuous but the second derivatives are not. Thus in a first order phase transition the discontinuous first derivative can usually serve as an order parameter. According to Landau, a first order phase transition is defined by the appearance of different phases in phase coexistence, which can be distinguished and are characterized by order parameters.

Fig. 1.3 presents the schematic phase diagram of water. The control parameters in this case are temperature (T) and pressure (P). Three regions correspond to ice, water and the steam phases. The solid lines mark the various co-existent curves where two phases are in equilibrium. Two special points in the phase diagram are *triple point* ($T_{tr} = 273.16$ K, $P_{tr} = 600$ Nm $^{-2}$), where all three phases co-exist and the critical point

or more clearly called as *critical end point* ($T_c = 647$ K, $P_c = 2.21 \times 10^7$ Nm $^{-2}$) where the meniscus separating liquid and vapour disappears and the two fluid phases become indistinguishable. For $T < T_c$, the transition between liquid and vapour is *first-order*, implying discontinuities in entropy and volume, respectively [36].

At the critical end point (CEP), the transition becomes *second order*, which means that the singularity instead occurs in specific heat (C_P) and isothermal compressibility (κ_T) of the fluid which are related to the second derivative of the free energy :

$$\begin{aligned} C_P &= -T \left(\frac{\partial^2 G}{\partial T^2} \right)_P \\ \kappa_T &= -\frac{1}{V} \left(\frac{\partial^2 G}{\partial P^2} \right)_T \end{aligned} \quad (1.3)$$

Therefore, C_P and κ_T diverges at CEP. Just beyond the CEP, thermodynamic observables still vary very rapidly. This is known as the *crossover region*.

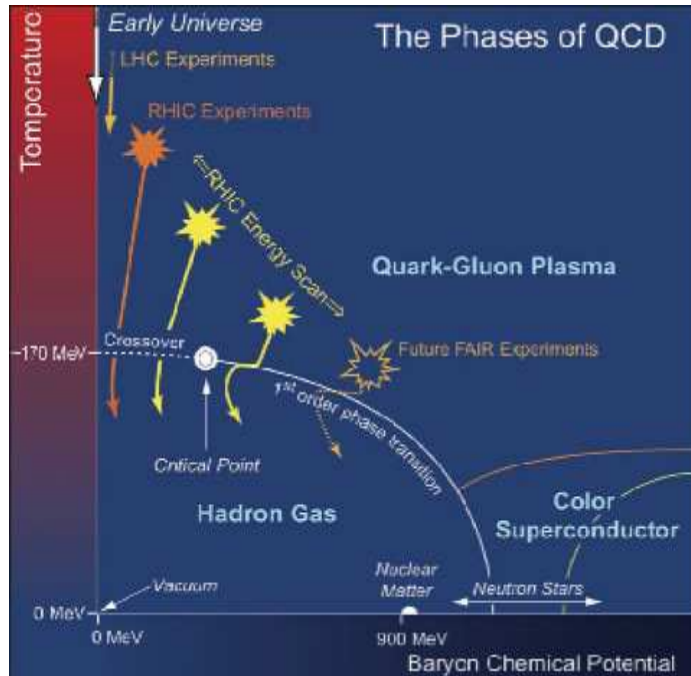


Figure 1.4. Conjectured QCD Phase Diagram in $T - \mu_B$ plane [10]

Fig. 1.4 shows the conjectured (or proposed) QCD phase diagram in $T - \mu_B$ plane. There should be at least three fundamental states of matter in QCD [37] : In low density and temperature region, we have the hadronic phase with broken chiral symmetry, in which quarks and gluons are confined in hadrons. On the other hand, in high density and temperature region, the confinement breaks down and deconfined quarks and gluons become relevant degrees of freedom. This phase is known as QGP. The third conjectured phase is a colour superconducting phase at low temperature and high μ_B .

1.2.2 QCD Critical End Point

The temperature driven transition at zero μ_B has been studied extensively by lattice QCD techniques. Recent lattice calculations on the basis of the staggered fermion and Wilson fermion indicate a rapid crossover from the hadronic phase to the QGP phase for realistic u , d and s quark masses [38] [39]. The pseudo-critical temperature T_c , which characterizes the crossover location lies in the range $150 - 200$ MeV as shown in Fig. 1.4. The μ_B driven transition at zero T is a first order phase transition. This conclusion is less robust, since the first principle lattice calculations are not controllable in this regime due to notorious sign problem at finite μ_B . Nevertheless, a number of different model approaches indicate that the transition in this region is strongly first order. However, most of these models are essentially extensions of the linear sigma model, such as the Nambu model with or without Polyakov loop dynamics, and small modifications may alter the conclusions.

Since the first order line originating at zero T cannot end at the vertical axis $\mu_B = 0$, the line must end somewhere in the midst of the phase diagram. This end point of a first order phase transition line is a critical end point (CEP) of the second order. This is the most common critical phenomena in condensed matter physics. CEP in the proposed QCD phase diagram has much importance to understand the critical (or

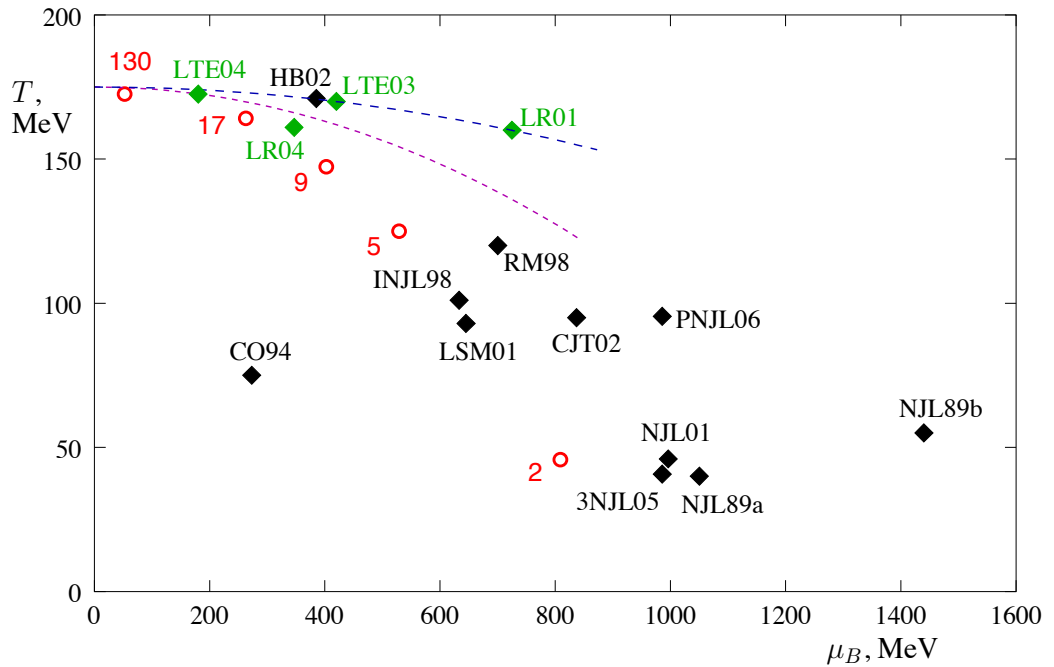


Figure 1.5. Comparison of predictions for the location of the QCD critical point on the phase diagram [40]

non-perturbative) nature of the strongly interacting matter and its governing theory, QCD. If the critical end point exists, the correlation length of an order parameter, ξ , diverges and thermodynamic quantities have singular behaviour at the point, like the specific heat at the liquid-gas critical end point. Due to such singularity, the critical end point is expected to be useful for the experimental probe of the QCD phase structure in the relativistic heavy ion colliders.

Theoretically, finding the coordinates (T, μ_B) of the CEP is a well-defined task. We need to construct the partition function of QCD and find out the singularity corresponding to the end of the first order phase transition line. But this procedure is severely impaired by the notorious sign problem in lattice calculations. Thus nature guards its secrets better at finite μ_B and, therefore, to find the exact location of CEP which involves finite value of μ_B is a tedious task for the theoreticians. Certain methods were proposed to circumvent this problem [41]. However, the results obtained from

different methods are quite different from each other as is shown in Fig. 1.5. Thus lack of an unanimous method to circumvent the sign problem still poses a tough challenge in the search of exact location of CEP.

1.3 QCD Critical point: brief experimental overview

Relativistic heavy-ion collision provides a tool to realize a high energy density environment in order to study the signatures for different phases of strongly interacting matter and location of CEP as suggested by the conjectured QCD phase diagram [42] [43] [44] [45] [46]. In nuclear collisions, we expect the occurrence of high energy density in two different ways: in the “stopping regime” at a laboratory beam energy ≤ 10 GeV/A, where A is the number of nucleons in the colliding nucleus; and in the “central rapidity regime” at a beam energy ≥ 100 GeV/A. The medium formed in the stopping regime is a baryon-rich plasma, because when the nuclei are stopped together, the baryon density is found to be very large. However, at higher energies, the nuclear transparency increases and nuclei almost pass through each other, leaving an excited vacuum behind them. The energy thus trapped may become liberated in the form of multiple pion production. This region is called the central region and has very small baryon content. In this region, hadrons are formed mainly because of the quark-antiquark pairs and gluons, and thus the medium formed is almost baryon-free. For the intermediate colliding energies, the medium formed lies somewhat in between the stopping and the transparent regimes. Thus we can say that by using different kind of heavy ion collisions in the laboratory, we can form different types of medium which thus probes the various aspects of phases of QCD matter. Table 1.1 gives the summary of the accelerators, collision energy in center-of-mass frame and the colliding nuclei used for heavy-ion collisions. The HIC at LHC and higher RHIC energies at-

Table 1.1. Past, current and future accelerator experiments for heavy-ion collisions:

Accelerator	Collision Energy in CM Frame	Colliding Nuclei	Starting year
AGS (BNL, 1986)	~ 5 A GeV	p+A, O+A, Si+A, Au+Au	1986
SPS (CERN, 1986)	17.3 A GeV, 19.4 A GeV	Pb+Pb	1986
RHIC (BNL, 2000)	200 A GeV, 130 A GeV, 62.4 A GeV	p+A, S+U	2000
LHC (CERN, 2008)	5.5 A TeV	p+p, d+Au, Au+Au, Cu+Cu	2009
CBM (GSI)	3.97, 8.1 A GeV	p+p, p+Pb, Pb+Pb	2018
		p+p, p+Au, Au+AU	

tempts to create a high temperature and quite dense medium which is more suitable to probe the formation of quark-gluon plasma phase and the crossover region between HG phase to QGP phase (as predicted by lattice QCD calculations). Complementary to these HIC experiments, CBM at GSI will shed light on the high baryon-dense medium in the stopping regime. The created medium can thus provide a way to study the various phase structures (e.g., colour super-conductor phase, QCD critical end point, quarkyonic phase etc.) at high-baryon density of the conjectured phase diagram.

Experimentally, search for the QCD critical point and its signatures have been undertaken from SPS to RHIC experiments. In NA49 experiment, transverse momentum fluctuation, Φ_{p_T} , [47] [48] and the particle multiplicity fluctuation (the scaled variance) [49], ω , are used. In this experiment, central Pb+Pb collisions are studied at 20A, 30A, 40A, 80A, and 158A GeV collision energy. Both Φ_{p_T} and ω , measure of transverse and particle multiplicity fluctuation, show no increase or non-monotonic behavior [48], [49] as a function of colliding energies. The system size dependance of the above fluctuations are also studied for intermediate system C+C and Si+Si interaction at 158A GeV. The higher moments of p_T fluctuation, $\Phi_{p_T}^{(n)}$ have also been studied to amplify the signal of the critical point in the above colliding system. No critical point

signature has been found in these results. Besides, it was suggested that particle ratio fluctuation might also provide the signature of critical point because hadron production at freeze-out carry the nature of the deconfinement phase transition. The NA49 [50] and STAR [51] experiments have also analyzed the data for dynamical fluctuation, σ_{dyn} , for the particle ratio like K/π , p/π , and K/p . In this case, the difference of the width of the particle ratio fluctuation for data and that of the mixed events are considered the dynamical fluctuation of particle ratio. These results show no non-monotonic behavior as a function of the beam energies. The NA49 intermittency result shows some clue for the presence of QCD critical point. In this analysis, second factorial moments, F_2 , of low-mass $\pi^+\pi^-$ pair in central Si+Si interaction at 158A GeV (which is $\sqrt{s_{NN}} = 17.8$ GeV) are studied. The magnitude of the net-proton and σ field are characterized by the order parameter for the second order phase transition associated with QCD critical point. In this case, difference of F_2 between data and mixed events, $\Delta F_2(M)$, as a function of transverse momentum space of bin, shows intermittency signal in the data. The intermittency results for the Si+Si system approaches the QCD critical point prediction [52]. These results provides strong evidence for existence of the critical point in the proximity of the Si+Si and Pb+Pb freeze-out state. Future experiments like NA61/SHINE at the CERN SPS, which is the successor of the NA49 experiment, is dedicated experiment for the search of the critical point. Whereas RHIC beam energy scan program aims to probe the QCD critical point in wide range of the temperature and baryon chemical point. Future collider JINR NICA ($3GeV < \sqrt{s_{NN}} < 9GeV$) and GSI FAIR ($2.3GeV < \sqrt{s_{NN}} < 8.5GeV$) have also planned of the search for QCD critical point.

1.4 Fluctuations and Correlations to probe QCD Critical Point

One of the actively pursued signatures of the possible critical end point and a first-order co-existence region in the QCD phase diagram is intimately connected with the study and measurement of fluctuations and correlations [53]. A system in thermal equilibrium (for a grand-canonical ensemble) is characterized by its partition function :

$$Z = \text{Tr} \left[\exp \left(-\frac{H - \sum_i \mu_i Q_i}{T} \right) \right], \quad (1.4)$$

where H is the Hamiltonian of the system, Q_i and μ_i denote the conserved charges and the corresponding chemical potential, respectively. The mean and the (co)-variance are then expressed in terms of derivatives of the partition function with respect to the appropriate chemical potential,

$$\langle Q_i \rangle = T \frac{\partial}{\partial \mu_i} \ln(Z), \quad (1.5)$$

and

$$\langle \delta Q_i \delta Q_j \rangle = T^2 \frac{\partial^2}{\partial \mu_i \partial \mu_j} \ln(Z) = V T \chi_{i,j} \quad (1.6)$$

where $\delta Q_i = Q_i - \langle Q_i \rangle$ and the generalized susceptibility,

$$\chi_{i,j} = \frac{T}{V} \frac{\partial^2}{\partial \mu_i \partial \mu_j} \ln(Z). \quad (1.7)$$

The diagonal susceptibilities, $\chi_{i,i}$ are a measure for the fluctuations of the system whereas $\chi_{i,j}$ ($i \neq j$) characterize the correlations between the conserved charges Q_i and Q_j . The susceptibilities can be given by the integral over the density-density correlation function which is characterized by typical correlation lengths ξ_{ij} . In the ideal gas case, all the correlations vanish and thus the fluctuations are proportional to the num-

ber of particles in the system and thus grow linearly with system size V . At the CEP, ξ diverges at the critical temperature as $\xi \approx |T - T_c|^{-\nu}$, where exponent $\nu > 0$. The volume dependence of the susceptibilities is governed by the integral of the correlation function, $\chi_{i,j} \approx \xi^2 \approx V^{2/3}$, so that fluctuation grows like,

$$\langle (\delta Q_i)^2 \rangle \approx V^{5/3}, \quad \text{for a second order phase transition} \quad (1.8)$$

In case of a first order transition, we have co-existence of phases with different densities, and the correlation function is a constant, $C(r) = \text{const} \neq 0$. Consequently, the fluctuations scale like $\langle (\delta Q_i)^2 \rangle \approx V^2$, for such transitions.

It is proposed that a combination of event-by-event observables, including suppressed fluctuations in T and μ and, simultaneously, enhanced fluctuations in the multiplicity of soft pions can act like a signal for the existence of CEP on QCD phase diagram in Ref. [54]. This proposal is based on the fact that QCD CEP is a genuine thermodynamic singularity at which susceptibility diverges and the order parameter fluctuates for long wavelengths. The resulting signatures share one common property, they are non-monotonic as a function of experimentally varied parameters such as the collision energy, centrality, rapidity or ion size. Once the control parameter is varied by experiments which causes the freezeout point in the $T - \mu$ plane to move towards, through, and then past the vicinity of the CEP. These fluctuations first increase, reach a maximum and then decrease, as a non-monotonic function of the control parameter. The obvious choice is center-of-mass energy $\sqrt{s_{NN}}$ since it is known experimentally that the variation in collision energy causes variation in T and μ . This way one can scan the QCD phase diagram to find out these non-monotonic fluctuations which provides the location of CEP.

Proton number fluctuation has also been proposed as the signal of CEP [55]. The long range fluctuation of the order parameter in this case induces a characteristic correlation between protons which can be measured in heavy-ion collisions. Thus the

experimental signature for phase transition and CEP is the non-monotonous dependence on \sqrt{s} , centrality etc. of the event-by-event fluctuations. However, fluctuations in particle multiplicities, net charge, net baryon, particle ratios or mean transverse momentum are related to the quadratic variances. Typically, the singular contribution to quadratic variances induced by the proximity of CEP is proportional to ξ^2 , where ξ is the correlation length. The magnitude of ξ is severely limited by the finite time effects due to critical slowing down which is the property of system near CEP. However, if one takes the higher non-Gaussian moments (e.g., skewness S , kurtosis κ etc.) of fluctuations which are much more sensitive in the proximity of CEP, then they can provide a better measure to locate the CEP on QCD phase diagram. The non-monotonous behaviour of skewness (S) and kurtosis (κ) of net quantum number with respect to $\sqrt{s_{NN}}$ and/or with centrality is also proposed as the possible signatures of CEP [56].

The skewness is defined as follows:

$$S = \frac{<(x - \mu)^3>}{\sigma^3}, \quad (1.9)$$

where σ^2 is variance of the distribution and can be calculated using $\sigma^2 = <(x - \mu)^2>$.

Similarly κ can be calculated as follows:

$$\kappa = \frac{<(x - \mu)^4>}{\sigma^4} - 3 \quad (1.10)$$

Further, ratio of different higher moments e.g, $S\sigma$ and $\kappa\sigma^2$ etc. has been calculated to cancel out volume dependence. Recently, Stephanov proposed that the quartic cumulant (and kurtosis) of the order parameter fluctuations is universally negative when the critical point is approached on the crossover side of the phase separation line. As a consequence, the kurtosis of a fluctuating observable e.g., proton multiplicity, may become smaller than the value given by independent Poisson statistics.

The first experimental study about a non-statistical fluctuation in higher moments of multiplicity distributions was done by STAR collaboration. They have calculated the

kurtosis (κ), skewness (S), variance (σ^2) and their products of the net-proton multiplicity ($N_p - N_{\bar{p}}$) distribution at mid-rapidity for Au-Au collisions at different $\sqrt{s_{NN}}$ from 7.7 GeV to 200 GeV [57]. They have compared these results with the corresponding results of baseline models (where there is no critical fluctuation) and studied the $\sqrt{s_{NN}}$ dependence of $\kappa\sigma^2$. They find interesting behaviour around $\sqrt{s_{NN}} = 19.6$ GeV [57]. However, in order to draw a firm conclusion, more data are needed especially below 19.6 GeV e.g., at $\sqrt{s_{NN}} = 15$ GeV with large statistics.

In Ref. [58] the results of the statistical moments of net-kaon multiplicity over wide range of collision energy points i.e. at $\sqrt{s_{NN}} = 7.7, 11.5, 19.6, 27, 39, 62.4$ and 200 GeV. They studied the variations of $\kappa\sigma^2$ and $S\sigma$ with respect to centrality as well as $\sqrt{s_{NN}}$. The results are compared with the corresponding results from HG expectation (baseline). The conclusion from this analysis is that there is no beam-energy and centrality localized large enhancements in the net-kaon moments. Although net-charge results of STAR experiments suffer a large statistical uncertainty and make the conclusion difficult [59].

PHENIX collaboration have also calculated the statistical moments of net-charge distribution at four different $\sqrt{s_{NN}}$ i.e., 200, 62.4, 39 and 7.7 GeV (Refs. [60] and [61]). These data are compared with the UrQMD (**U**ltra-**r**elativistic **Q**uantum **M**olecular **D**ynamics) [62] and HIJING (**H**eavy **I**on **J**et **I**Nteraction **G**enerator) [63] simulation results processed through the PHENIX acceptance and detector response. No excess in the experimental data from the baseline UrQMD and HIJING simulations was reported. This thesis presents the recent results of higher moments for net-charge multiplicity distributions measured at various $\sqrt{s_{NN}}$ by PHENIX detector.

Chapter 2

Experimental Overview

This chapter briefly describes the Relativistic Heavy Ion Collider (RHIC), the experimental facility dedicated to the study of heavy ion collisions at Brookhaven National Laboratory (BNL), USA. Also, a detailed description is given for the PHENIX detector which is used to collect the data analyzed in this thesis.

2.1 The Relativistic Heavy Ion Collider

RHIC is able to realize A+A collisions for a wide variety of nuclei up to 100 GeV per nucleon, p+p collisions with spin-polarized proton beams up to 250 GeV, and also asymmetric collisions like $d + Au$, $p + Au$ and $^3He + Au$. A schematic layout of the RHIC accelerator complex is shown in Fig. 2.1. The RHIC complex consists of Tandem Van de Graaff, Linear Accelerator (LINAC), Heavy Ion Transfer Line (HILT), AGS-to-RHIC Transfer Line (ATR), Booster synchrotron, Alternating Gradient Synchrotron (AGS) and RHIC main rings. Three accelerators in the injector chain boost the energy of ions, and strip electrons from the atoms. The first acceleration stage for ions is in the Tandem Van de Graaff accelerator, while for protons, the 200 MeV linear accelerator (Linac) is used. As an example, gold nuclei leaving the Tandem Van de Graaff have an energy of about 1 MeV per nucleon and have an electric charge $Q = +31$ (31 of 79 electrons stripped from the gold atom). The particles are then accelerated by the Booster Synchrotron to 95 MeV per nucleon, which injects the projectile now with $Q = +77$ into the Alternating Gradient Synchrotron (AGS), before they finally reach

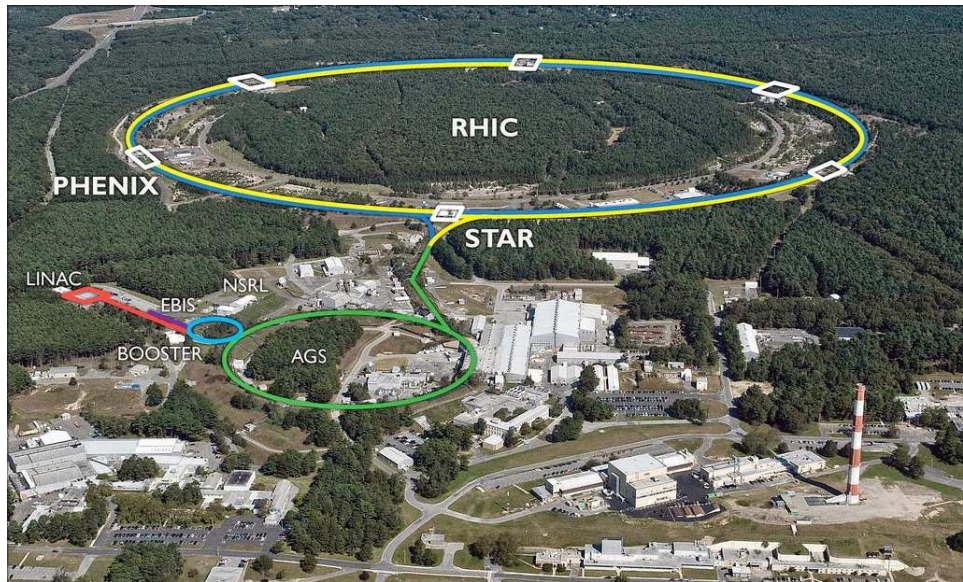


Figure 2.1. RHIC's 2.4 mile ring has six intersection points where its two rings of accelerating magnets cross, allowing the particle beams to collide.

8.86 GeV per nucleon and are injected in a $Q = +79$ state (no electrons left) into the RHIC storage ring over the AGS-to-RHIC Transfer Line (ATR) [64]. RHIC has two independent hexagonally shaped rings with a circumference of $\sim 3.8 \text{ km}$, one for a clockwise and the other for counter-clockwise traveling beam. The rings are designed to cross at the middle of the six relatively straight sections allowing the ions to collide. Out of the six interaction points, four have been occupied by experiments, designed to study heavy ion collisions: STAR [65], PHOBOS [66], BRAHMS [67] and PHENIX [68]. STAR and PHENIX are still active, while PHOBOS and BRAHMS have completed their operation after 2005 and 2006, respectively. Since the pilot run in 1999 and up to 2014 RHIC had performed Au+Au, d+Au, Cu+Cu, $^3\text{He}+\text{Au}$, U+U and polarized protons runs. The collision species, energy, and integrated luminosity of various runs are listed in Table 2.1. The analysis presented in this thesis is based on the Au+Au data from Run-7 ($\sqrt{s_{NN}} = 200 \text{ GeV}$), Run-10 ($\sqrt{s_{NN}} = 7.7 \text{ GeV}$, 39 GeV and 62.4 GeV) and Run-11 ($\sqrt{s_{NN}} = 19.6 \text{ GeV}$ and 27 GeV).

Table 2.1. The RHIC runs and the integrated luminosity delivered to the PHENIX experiment:

RHIC Run	Year	Species	Energy	$\int L dt$
Run-01	2000	Au+Au	130 GeV	$1 \mu b^{-1}$
Run-02	2001-2	Au+Au	200 GeV	$24 \mu b^{-1}$
		Au+Au	19 GeV	$0.4 \mu b^{-1}$
		p+p	200 GeV	$150 nb^{-1}$
Run-03	2002/3	d+Au	200 GeV	$2.74 nb^{-1}$
		p+p	200 GeV	$0.35 nb^{-1}$
Run-04	2003/4	Au+Au	200 GeV	$241 \mu b^{-1}$
		Au+Au	62.4 GeV	$9 \mu b^{-1}$
Run-05	2005	Cu+Cu	200 GeV	$3 nb^{-1}$
		Cu+Cu	62.4 GeV	$0.19 nb^{-1}$
		Cu+Cu	22.4 GeV	$2.7 \mu b^{-1}$
Run-06	2006	p+p	200 GeV	$10.7 pb^{-1}$
		p+p	62.4 GeV	$100 nb^{-1}$
Run-07	2007	Au+Au	200 GeV	$813 \mu b^{-1}$
Run-08	2007/2008	d+Au	200 GeV	$80 nb^{-1}$
		p+p	200 GeV	$5.2 pb^{-1}$
		Au+Au	9.2 GeV	—
Run-09	2009	p+p	200 GeV	$16 pb^{-1}$
		p+p	500 GeV	$14 pb^{-1}$
Run-10	2010	Au+Au	200 GeV	$1.3 nb^{-1}$
		Au+Au	62.4 GeV	$100 \mu b^{-1}$
		Au+Au	39 GeV	$40 \mu b^{-1}$
		Au+Au	7.7 GeV	$260 mb^{-1}$
Run-11	2011	p+p	500 GeV	$27 pb^{-1}$
		Au+Au	200 GeV	$915 \mu b^{-1}$
		Au+Au	27 GeV	$5.2 \mu b^{-1}$
		Au+Au	19.6 GeV	—
Run-12	2012	p+p	200 GeV	$9.2 pb^{-1}$
		p+p	510 GeV	$30 pb^{-1}$
		U+U	193 GeV	$171 \mu b^{-1}$
		Cu+Au	200 GeV	$4.96 nb^{-1}$
Run-13	2013	p+p	510 GeV	$156 pb^{-1}$
Run-14	2014	Au+Au	15 GeV	$44.2 \mu b^{-1}$
		Au+Au	200 GeV	$> 1.5 nb^{-1}$
		^3He+Au	200 GeV	—

2.2 The PHENIX Detector

The layout of the PHENIX detector as used in Run-7, Run-10, and Run-11 is shown in Figs. 2.2 and 2.3. The PHENIX detector comprises of four spectrometer arms. The two central arms (East and West) are instrumented to detect electrons, photons and charged hadrons. They cover $|\eta| < 0.35$ in pseudo-rapidity and 90° in azimuthal angle. The two forward (muon) arms (North and South) are instrumented to detect muons. They have full azimuthal coverage for $1.2 < |\eta| < 2.4$. There are three magnets in PHENIX: the Central Magnet provides an axial magnetic field for the central arms while the Muon Magnets produce a radial field for the muon arms. A set of inner coils in the central magnet, installed for Run-4, allows to perform measurements with different magnetic field configurations in the central arms. Prior to the installation of inner coils in the first three runs (Run-1, Run-2 and Run-3), all data were taken with only the outer coils of the Central Magnet powered (0+ mode).

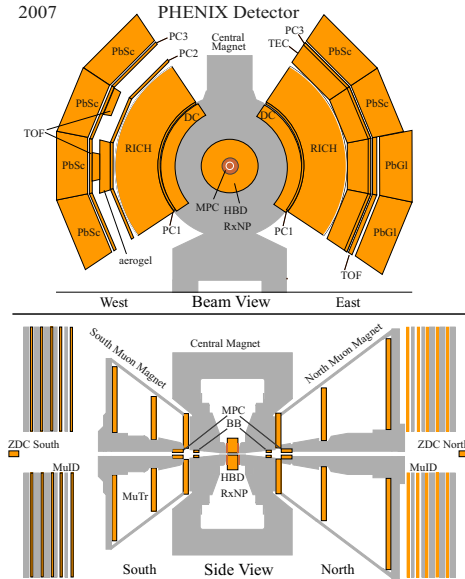


Figure 2.2. The PHENIX detector layout in the 2007 run. The upper panel shows the beam view where the two central arms and central magnet can be seen. The lower panel shows the side view where the two muon arms and the two muon magnets are shown.

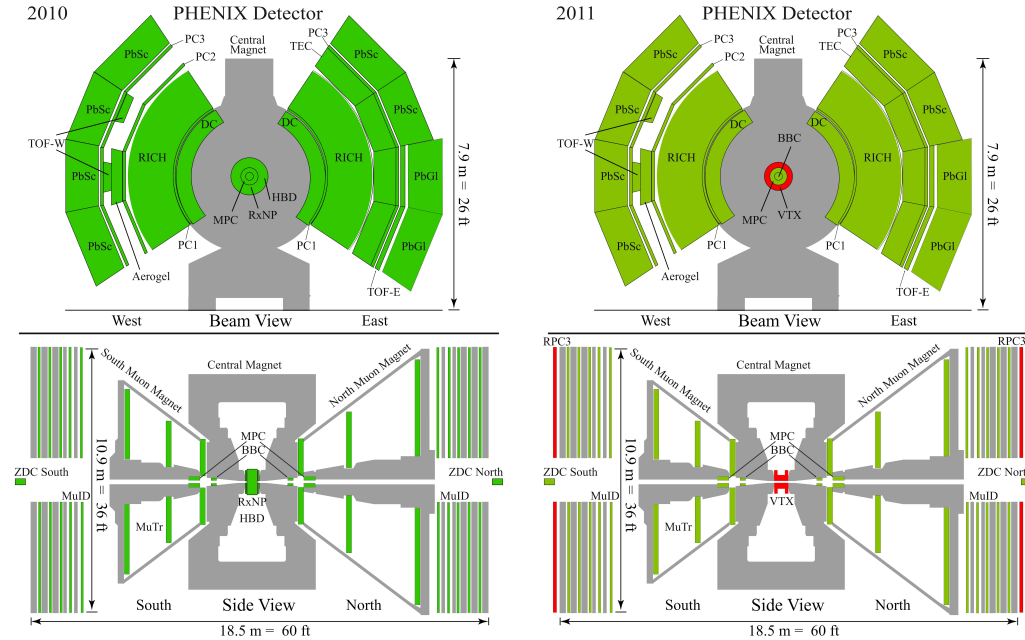


Figure 2.3. The PHENIX detector layout in Run-10 (left column) and in Run-11 (right column)

Charged particles are bent in the plane perpendicular to the beam axis. The bending angles are accurately measured by the drift chambers and are used to determine the particle momentum. The effective magnetic field integral in this configuration is equal to $\int B dl = 0.78 \text{ Tm}$. Taking data in the mode where both the outer and inner coils are energized to have adding fields (+ + or - - mode) gives a better momentum resolution due to the larger effective magnetic field integral of $\int B dl = 1.15 \text{ Tm}$. In the mode with opposite coil polarity (+ - or - + mode), which provides an effective magnetic field integral of $\int B dl = 0.43 \text{ Tm}$, the magnetic field in the vertex region is cancelled up to a radial distance of $\sim 60 \text{ cm}$, which is essential for the operation of the Hadron Blind Detector (HBD). The left panel of Fig. 2.4 shows the magnetic field lines for the +- Central Magnet coils operation mode and the right panel shows the same for the ++ mode.

The central arms contain a tracking system consisting of Drift Chambers (DC)

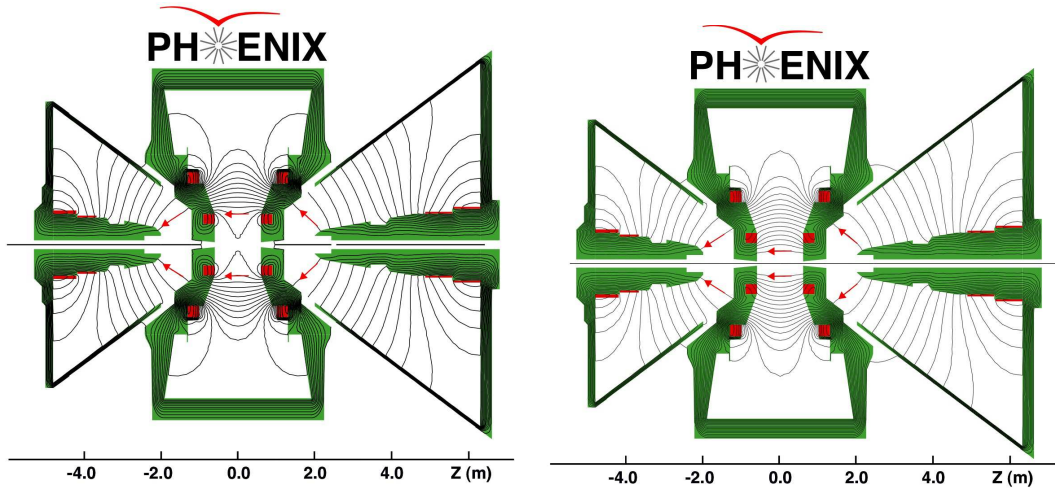


Figure 2.4. Magnetic field lines in the PHENIX detector, for the two central magnet coils in +- (left) and ++ (right) modes.

and Pad Chambers (PC) [69]. There are two types of Electro-Magnetic Calorimeters (EMCal), one is made of lead-glass (PbGl) and the other is made of lead and scintillator material (PbSc), both measure the energy of electrons and photons. There is also a Ring-Imaging Cherenkov Counter (RICH) for electron identification and a set of Time-Of-Flight detectors (TOF) and Aerogel Cherenkov Counters (ACC) for charged hadron identification. These subsystems, together with the initial time information measured in the Beam-Beam Counters (BBC), are capable to identify hadrons, electrons and photons over a large momentum range. The Hadron Blind Detector (HBD) was used in Run-9 and Run-10 to improve the electron identification for the measurement of low mass di-leptons. The Zero Degree Calorimeters (ZDC) and the BBC are dedicated subsystems that determine the collision vertex and event centrality and also provide the minimum bias interaction trigger. The analysis described in this work mainly utilizes the BBC, ZDC, DC, PC and EMCal subsystems of the PHENIX detector.

Table 2.2. Summary of the PHENIX central arm subsystems.

Subsystem	$\Delta\eta$	$\Delta\Phi$	Specifications
Magnet: central	± 0.35	360^0	Upto $1.15\text{T}\times\text{m}$
Beam-beam counters (BBC)	$\pm 3.1\text{to}3.9$	360^0	Start timing, fast vertex
Zero-degree Calorimeter (ZDC)	$\pm 2\text{mrad}$	360^0	Minimum-bias trigger
Drift Chambers (DC)	± 0.35	2×90^0	Good momentum and mass resolution $\Delta m/m = 0.4\%$ at $m = 1\text{GeV}$
Pad Chambers (PC)	± 0.35	2×90^0	Pattern recognition tracking in non- bend direction
TEC	± 0.35	90^0	Pattern recognition, dE/dx
Ring-Imaging Cherenkov Detector (RICH)	± 0.35	2×90^0	Electron identification
Time-of-flight (TOF)	± 0.35	45^0	hadron ID, $\sigma < 100\text{ps}$
PbSc EMCal	± 0.35	$900 + 45^0$	Electron/Photon ID
PbGl EMCal	± 0.35	45^0	Good e^\pm/π^\pm separation at $p > 1\text{ GeV}/c$ by EM shower and $p < 0.35\text{ GeV}/c$ by TOF. K^\pm/π^\pm separation up to $2.4\text{GeV}/c$ by TOF

2.2.1 PHENIX coordinate system and acceptance

The global coordinate system used in PHENIX is shown in Fig. 2.5. Coordinates are defined relative to the beam axis with the origin located at the center of the interaction region (IR). For both cartesian and cylindrical coordinate systems, the beam line defines the Z axis with the positive direction pointing to the North. The Y axis points upwards and the X axis points horizontally to the west arm, so that we have a right handed coordinate system.

Cylindrical coordinates (θ, ϕ, z) are often used where the polar angle θ is defined relative to the beam axis Z, such that $\theta = 90^0$ is perpendicular to it and the azimuthal angle ϕ is 0^0 at the x axis (west). Fig. 2.5 shows the PHENIX acceptance in terms of pseudo-rapidity (η) and Phi (ϕ). Each one of the two central arms covers the pseudo-rapidity range, $|\eta| < 0.35$ ($70^0 < \theta < 110^0$), with 90^0 in ϕ and are offset from each

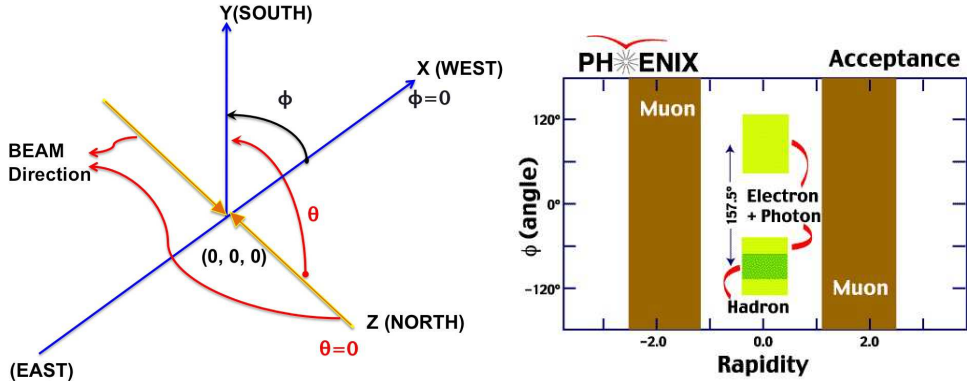


Figure 2.5. (a) PHENIX global coordinate system (left) (b) PHENIX acceptance for identified electrons, muons, photons and hadrons (right).

other by 67.5^0 . Table 2.2 describes the acceptance of central arm detectors with their specifications.

2.3 Global Event Characterization

2.3.1 Global Detectors

The global detectors are placed in the North and South arms at forward and backward rapidity. Mainly two systems are used to determine the global event information such as the time and location along the beam axis of the collision, and the collision centrality: two identical arrays of Cherenkov counters (BBC) [70] [71] and a pair of zero degree calorimeter (ZDC) [72]. The BBC and ZDC are located around the beam direction at ± 1.44 m and ± 18.25 m respectively (see Fig. 2.3). Each BBC is made of 64 meshed dynodes photomultiplier tubes (Hamamatsu R6178) equipped with quartz Cherenkov radiators. The ZDC are small transverse area hadron calorimeters that measure the total energy of the spectator neutrons emitted from nuclear fragments after a collision. Charged particles like protons are bended away from the ZDC by the beam dipole magnets. The ZDC detectors consist each of alternating layers of tungsten and quartz

Cherenkov fibers arranged in ribbons and placed at zero degree.

2.3.2 Collision Centrality Determination

The centrality of a collision is defined in terms of a percent of the total inelastic cross-section. The percentage is defined in such a way that it approximately corresponds to the impact parameter of the collision. As an example, 0% centrality collision is a direct, head on collision with an impact parameter of 0 fm . A larger centrality relates to a larger impact parameter. The number of participating nucleons (N_{part}) depends on the impact parameter (and the radius of the colliding nuclei). A very peripheral event will have the gold nuclei barely touching and so there are only a few participating nucleons. The total multiplicity of particles measured also depends on N_{part} . This can be used to characterize the centrality of an event. In previous years the centrality was measured via the correlation of energy deposition in the BBCs and ZDCs as is shown in the right panel of Fig. 2.6.

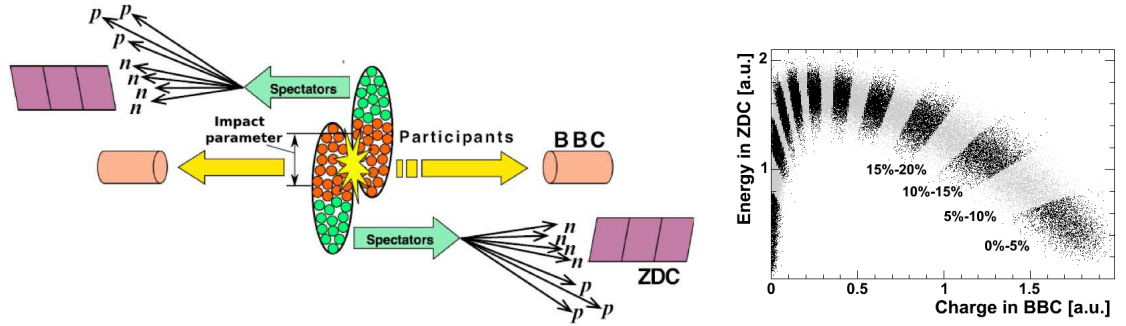


Figure 2.6. PHENIX Centrality measurement and ZDC BBC Correlation [73]

Another method using only the BBC charge was developed for the 2007 data set and beyond. This method realizes the assumption that the total charge deposited in each BBC is linearly proportional to the number of participants, N_{part} . It has been demonstrated that under this linearity condition, the charge sum follows a negative

Table 2.3. The centrality classes and the corresponding average number of nucleon- nucleon collisions, participants and impact parameter for Au+Au collisions at $\sqrt{s_{NN}} = 200$ GeV from Glauber Calculation:

Class	$\langle N_{part} \rangle$	N_{coll}	$\langle b \rangle (fm)$
0-5%	351.4	1065.4	2.3
5-10%	299.0	845.4	4.1
10-15%	253.9	672.4	5.2
15-20%	215.3	532.7	6.2
20-25%	181.6	421.8	7.0
25-30%	151.5	325.6	7.8
30-35%	125.7	251.0	8.4
35-40%	102.7	188.6	9.1
40-45%	82.9	139.4	9.7
45-50%	65.9	101.3	10.2
50-55%	51.6	72.1	10.7
55-60%	39.4	49.9	11.2

binomial distribution, as does the measured particle multiplicity. The boundaries of $n\%$ centrality (x_n) are determined by Eqn. 2.1. In Eqn. 2.1, Q^{BBC} is the total charge sum in the BBC and A^{BBC} is the efficiency of the BBC.

$$x_n = \sum_{i=0}^n i \cdot \left(\frac{Q_{all}^{BBC}}{A_{eff}^{BBC}} \right) \quad (2.1)$$

The centrality values at lower energies are used from the standard PHENIX recalibrators, which are determined in Au+Au collisions using E_T information from Electromagnetic Calorimeters. At low energies, the BBC total charge cannot be used for centrality determination. Therefore, 19.6 GeV and 27 GeV datasets of Run-11 use the default centrality determination which is based on the number of PC1 clusters. Further, it can introduce auto-correlations for our central arm analyses. For this reason the EMCAL total transverse energy (E_T) is used for centrality determination to reduce these effects. The centrality determination at 7 GeV is carried with Reaction Plane

Detectors. The Glauber simulation results on N_{coll} and N_{part} for different centrality bins at $\sqrt{s_{NN}} = 200$ GeV are shown in Table 2.3.

2.3.3 Collision Vertex Determination

The event vertex of a collision in the Z-direction (along the beam axis) is determined by using the BBCs. The timing difference between particles hitting the BBC^{NORTH} and BBC^{SOUTH} detector determines the Z-vertex as is shown in equation 2.2. Here, c is the speed of light and t_S and t_N is the time at which the south (north) BBC fired.

$$z_{vertex} = \frac{c}{2} * (t_S - t_N) \quad (2.2)$$

With the excellent timing resolution (52 ± 4 ps) of the BBCs, a z-vertex resolution of 1.2 cm in p+p and 0.3 cm in central Au+Au collisions is achieved. The z-vertex of a collision is an important piece of information. The spread of collisions delivered to us by RHIC is not narrow in z. Ideally, one would want the collision to occur in the very center of the PHENIX detector. For most analyses a cut of ± 30 cm is placed on the events.

2.4 Charged particles tracking

There are two primary charged particle tracking subsystems in PHENIX, namely Drift Chambers and Pad Chambers. The DC along with PC1 are part of inner tracking system, while PC2 and PC3 form the outer tracker. The details of PC and DC are given in the next section.

2.4.1 Central arm tracking detectors

Drift Chamber

The drift chamber [74] is the main tracking detector for PHENIX which is at a radial distance of 2.02 m to 2.46 m from the interaction point. It is 1.8 m long in the Z direction and each arm covers 90^0 in azimuthal angle (ϕ). The drift chamber assists in determining the quality of tracks, as well as determining the azimuthal angle, charge sign, transverse momentum and allows for pointing of a charged track to various sub-systems. A schematic of the frame of one arm of the drift chamber is shown in Fig. 2.7. Each drift chamber is composed of 20 identical keystones (Fig. 2.7). Each keystone has six radial layers of wire nets, labeled as X1, X2, U1, U2, V1, V2. The drift chamber is a multi-wire chamber filled with a 50%/50% mixture of Argon and Ethane gas, specifically chosen for stability of the drift velocity over small variations of the electric field strength, where the detector is operated (approximately 1 kV/cm, resulting in a drift velocity on the order of $50\mu\text{m}/\text{ns}$). The drift chamber tracks charged particles by measuring the ionization from the track passing through the gas inside the detector. A static electric field is applied in the detector. Thus there will be two clouds of ionization charges drifting in opposite directions from the field. The drift chamber uses the ionization electrons as the signal since they have a larger drift velocity. A gain on the order of 10^4 is obtained for above mentioned gas mixture and field set inside the chambers. The time it takes for ionizing particles to produce a signal is measured.

Fig. 2.8 shows the wire layout of a keystone. The X1, X2, U1, U2, V1, V2 planes are indicated in the side view of the keystone on the left. The dashed lines represent the anode plane and the dotted lines represent the cathode plane. A zoom in of single anode plane wire net is shown in the center of the figure. The right side of the figure shows the orientation of the wire layers from the top view.

The X1 and X2 wires are aligned parallel to the beam pipe to perform precise track measurements in the $r - \phi$ plane. The U and V stereo wires are oriented at

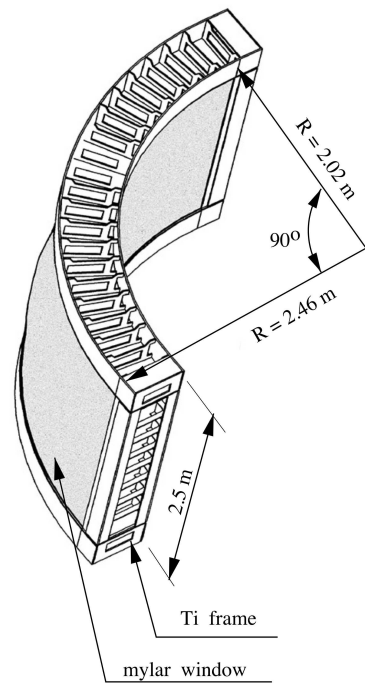


Figure 2.7. Schematic view of one arm of the PHENIX DC subsystem.

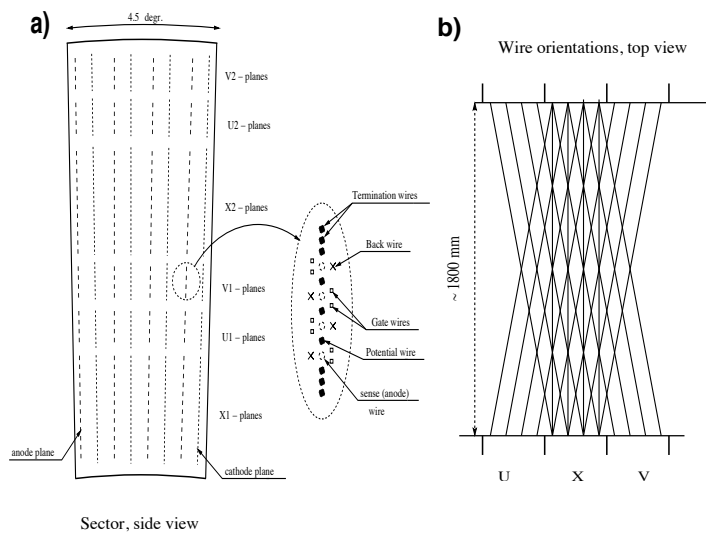


Figure 2.8. (a) Wire structure of a DC keystone. (b) The relative arrangement of the U, V and X wire layers.

$\sim \pm 6^0$ angle relative to the X wires and measure the z coordinate of the track. The magnitude of the stereo angle is such that the z resolution would be comparable to that of the pad chambers. Each wire module contains, alternating in azimuth direction, four anode and four cathode planes. In addition to anode and cathode wires, each plane contains gate wires and back wires as shown in the left panel of Fig. 2.8. The latter shape the electrical field lines such that every sense wire is alternatively sensitive to drift charges from only one side, therefore limiting the left-right ambiguity to a region of ± 2 mm. In order to allow for pattern recognition with up to 500 tracks, each sense wire is electrically insulated in the middle by a $100 \mu\text{m}$ thick kapton strip, effectively doubling the number of readout channels. In total the drift chamber contains 6500 wires and therefore 13000 readout channels.

Pad Chamber

The Pad Chambers (PCs) are essential to accurate particle tracking in PHENIX [75] [76] [77]. The PCs allow for additional track quality constraints and determine the z-position of a track. They also allow for charged hadron rejection in various analysis with the EMCAL and the RICH. There are three layers of PCs. PC1 resides right after the drift chamber. PC2 is located immediately after the RICH detector (in the west arm only). PC3 is directly in front of the EMCAL (See Fig. 2.3). There are three layers of Pad Chambers in the West arm (PC1, PC2 and PC3) and two layers in the East arm (PC1 and PC3). PC1, PC2 and PC3 layers are located at radii of 249 cm, 419 cm and 499 cm from the interaction point respectively.

Each PC layer consists of eight sectors. Each PC1 sector covers 11.25^0 in azimuth and $|\eta| < 0.35$ in pseudo-rapidity. PC2 and PC3 sectors have a square shape for better mechanical rigidity and cover each 22.5^0 in azimuth and 1/2 of the central arm acceptance in pseudo-rapidity ($-0.35 < \eta < 0$ or $0 < \eta < 0.35$). A schematic 3D view of the PC subsystem is shown in Fig. 2.9. The pad chambers consist of a single

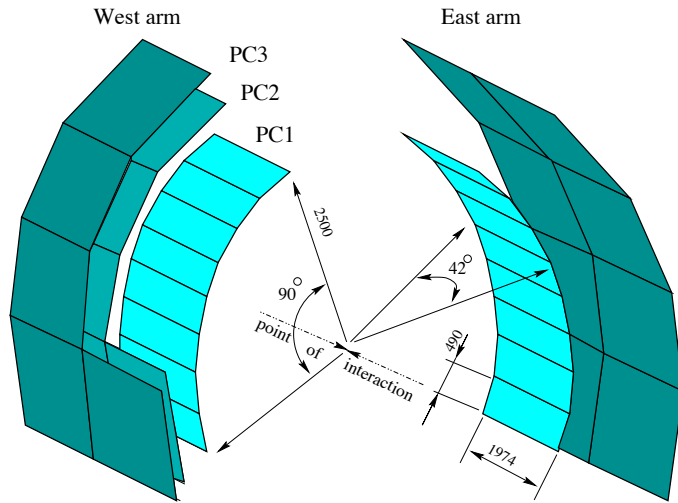


Figure 2.9. Schematic view of the PHENIX PC subsystem. Several sectors of PC3 and PC2 in the West arm are removed for clarity.

plane of anode and field wires in a gas volume, surrounded from above and below by cathode planes located at ± 6 mm. The bottom cathode is made of solid copper. The top cathode plane is segmented into a fine array of pixels as shown in Fig. 2.10.

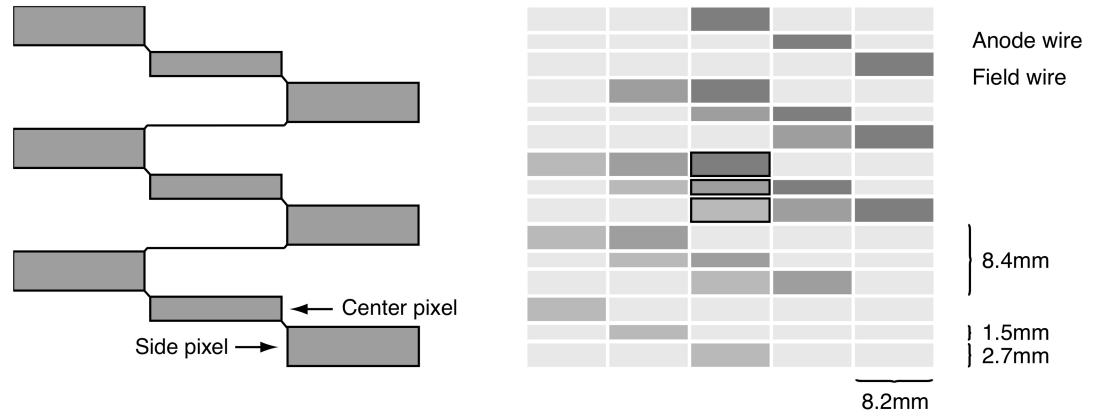


Figure 2.10. The pad and pixel geometry (left). A cell defined by three pixels from three neighboring pads is shown in the center (right).

The basic unit is a pad formed by nine non-neighboring pixels connected together which are read out by one common channel. One cell contains three adjacent pixels

in the ϕ direction and an avalanche must be sensed by all three pixels to form a valid hit. The three pixels in a cell always belong to different but neighboring channels and each cell corresponds to a unique channel triplet. This interlinked design scheme saves a factor of nine in readout channels while allowing a fine position resolution of 1.7 mm in the z direction in PC1. The signals from the pixels are transmitted, amplified and discriminated outside of the gas volume by the Read Out Cards (ROCs).

2.4.2 Track reconstruction

In Fig. 2.11 a charged particle is shown to bend in $r - \phi$ and r-z planes. The co-ordinates shown in the figure are as follows:

- ϕ : azimuthal angle of the intersection point of the track candidate with a reference circle located at a radius of 2.2 m, at the middle of the drift chamber
- ϕ_0 : tracks azimuthal angle at the vertex
- α : angle of the track candidate with respect to an infinite momentum (i.e. straight) track having the same intersection point with the reference circle in the $r - \phi$ plane. α is proportional to the inverse of the transverse momentum and its sign depends on the charge of the particle
- z_{ed} : z coordinate of the track at the intersection point with the reference circle of the DC
- β : inclination angle of the track with respect to the z-axis at the intersection point in the r-z plane
- δ : inclination of the track as compared to an infinite momentum track at the DC reference radius of 2.2 m in the r-z plane
- θ : polar angle of the infinite momentum track

- θ_0 : track's polar angle at the vertex.

Hits from the X1 and X2 wires of the DC projected to the x-y plane are used to define the ϕ and α angles for all track candidates. This is done using a combinatorial Hough transform technique [78] in which it is assumed that the tracks are straight in the DC and come from the vertex. The next step is background tracks subtraction. A real track is required to have at least 8 hits in X1 and X2 wires associated to it, otherwise it is discarded. A track association is done by an iterative fitting approach, weighting hits according to their deviation from the straight line guess of the trajectory. If the hit is farther from the straight line guess, it gets the smaller weight and therefore the fit is not disturbed by hits from noise or other tracks. Each hit is allowed to correspond only to a single track and normally the closest track candidate is chosen. Then, information about z_{vtx} measured by BBC, reconstructed clusters in the PC1 and hits in the UV wires of the DC are utilized to reconstruct the track in the r-z plane. If there is an unambiguous associated cluster in the PC1 within 2 cm from the projection of the track candidate to the PC1 plane, the zed of the track is defined by the z-coordinate of this cluster and z_{vtx} . If no cluster is found or if there is ambiguity in the cluster association, then the hits from the UV wires of the DC are used to determine zed. Details about the track reconstruction technique in the PHENIX central arm are given in Ref. [79].

Track Quality

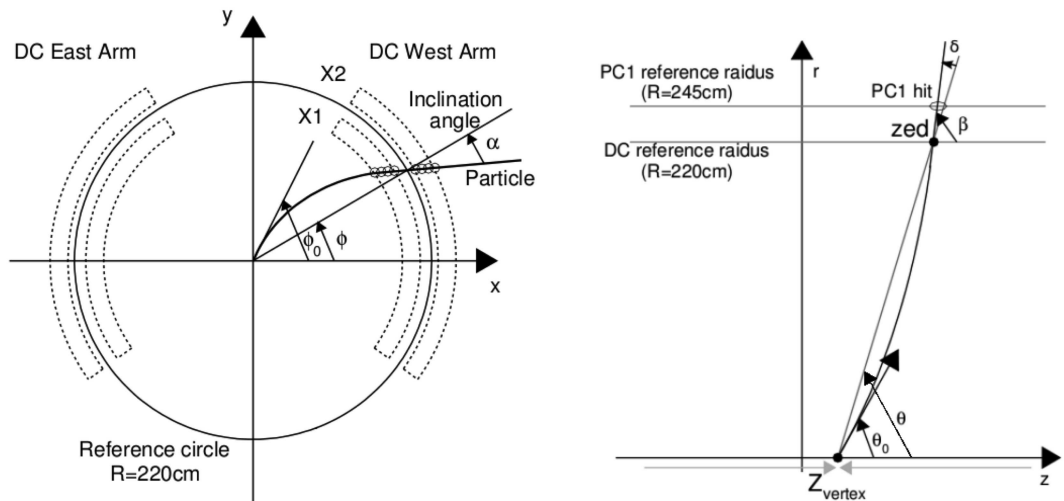
All the reconstructed tracks are assigned a track quality value based on the hits in DC and PC1. This information is implemented in the data as a 6-bit variable called track quality (Q_{track}), for each track and defined using the binary system as follows:

$$Q_{track} = A \times 2^0 + B \times 2^1 + C \times 2^2 + D \times 2^3 + E \times 2^4 + F \times 2^5 \quad (2.3)$$

- A=1, if the X1 plane is used.

Table 2.4. Summary of the DC track quality.

Comment	A	B	C	D	E	F	Q_{track}
$PC1_{\text{found}}^{\text{unique}} \& UV_{\text{found}}^{\text{unique}}$	1	0	1	1	1	1	61
	0	1	1	1	1	1	62
	1	1	1	1	1	1	63
$PC1_{\text{found}}^{\text{unique}} \& \text{no UV}$	1	0	0	0	1	1	49
	0	1	0	0	1	1	50
	1	1	0	0	1	1	51
$PC1_{\text{found}}^{\text{ambiguous}} \& UV_{\text{found}}^{\text{unique}}$	1	0	1	1	1	0	29
	0	1	1	1	1	0	30
	1	1	1	1	1	0	31
$PC1_{\text{found}}^{\text{ambiguous}} \& UV_{\text{found}}$	1	0	1	0	1	0	21
	0	1	1	0	1	0	22
	1	1	1	0	1	0	23
$PC1_{\text{found}}^{\text{ambiguous}} \& \text{no UV}$	1	0	0	0	1	0	17
	0	1	0	0	1	0	18
	1	1	0	0	1	0	19

**Figure 2.11.** Left: Schematic view of a track in the DC in cartesian and polar co-ordinates. The X1 and X2 hits in the DC are shown as small circles. Right: Schematic view of a track in the DC r-z plane.

- B=1, if the X2 plane is used.
- C=1, if there are hits in the UV plane.
- D=1, if there are unique hits in the UV plane.
- E =1, if there are hits in PC1.
- F =1, if there are unique hits in PC1.

Otherwise A, B, C, D, E, F are assigned 0. Both A and B can never be "0" simultaneously, since every track is required to have at least 8 X1 and X2 hits. More details of Quality conventions are shown in Table 2.4. In this analysis, tracks of quality 63 and 31 are analyzed. 63 is the highest quality and means that the track is reconstructed with hits in the X1 and X2 planes and also has a unique hit in both PC1 and the UV planes. A quality of 31 requires that the track has a unique UV hit and an unambiguous hit in PC1 along with the required X1 and X2 hits.

2.4.3 Momentum determination

The transverse momentum (p_T) of a charged track can be related with the deflection angle α in the magnetic field as follows:

$$\alpha \simeq \frac{K}{p_T} \quad (2.4)$$

Here K is related to field integral along the track trajectory. However, due to complex magnetic field configuration of PHENIX, it is hard to know the exact value of K , therefore simulation derived look-up tables are used to estimate p_T . For an accurate momentum measurement, one must use the full tracking model. Therefore we use a non-linear grid interpolation technique, where the momentum of a charged particle is determined through the knowledge of the magnetic field and the intersection of its

trajectory with few planes of the tracking detectors. This grid provides the field integral $f(p, r, \theta_0, z)$ as a function of the total track momentum (p), the radius (r) from the beam axis, the theta angle (θ_0) of the track and the position z of the collision vertex. The grid is generated by propagating particles through the measured magnetic field map and numerically integrating f for each grid point. The field integral $f(p, r, \theta_0, z)$ varies linearly with the ϕ for a given radius r . ϕ is given by the original angle of emission, ϕ_0 , plus the kick due to the magnetic field.

$$\phi = \phi_0 + q \frac{f(p, r, \theta_0, z)}{p} \quad (2.5)$$

An iterative procedure is used to find the true momentum, starting with an initial estimate of the momentum obtained from the reconstructed angle α , and the measured polar angle θ from the PC1/DC match. For each hit associated with the track, the field integral $f(p, r, \theta_0, z)$ value is extracted from the grid. A fit in ϕ vs f is performed to extract the quantities ϕ_0 and q/p for every track and the extracted values are then fed back into the Eq. 2.5. A similar procedure is used in the r - z plane to find the value of the θ_0 angle. The momentum resolution for reconstructed charged particles with momentum above 200 MeV/c is

$$\frac{\sigma_p}{p} = 0.7\% \oplus 1\% (GeV/c) \quad (2.6)$$

where multiple scattering ($\sigma_{m.s.}$) contributes the first term and the second is due to the intrinsic DC resolution.

2.5 Electron Identification

There are two primary detectors for electron identification in PHENIX: a ring imaging Cherenkov detector and an electromagnetic calorimeter.

2.5.1 Ring Imaging Cherenkov Detector

The Ring Imaging Cherenkov detector (RICH) is situated in both central arms [80] [81], that serves as the primary device for electron identification in PHENIX. It is a gaseous Cherenkov detector that provides an e/π rejection better than one part in 10^3 at momenta below 4.87 GeV/c. In addition to that, RICH is part of the PHENIX Level-1 electron trigger that enables to collect the rare electron and di-electron events in p + p and d + Au collisions. Each RICH detector has a gas volume of $40\ m^3$, an entrance window with an area of $8.9\ m^2$, and an exit window with an area of $21.6\ m^2$. The radiator gas is CO_2 , which has a refractive index $n=1.00410$ at 20^0C and 1 atm pressure [82]. Electrons or pions that pass through the gas emit Cherenkov radiation which is detected by PMTs. Pions start to radiate inside the gas at 4.65 GeV/c. On average, electrons moving at the speed of light will radiate about 12 photons per ring for a 1.2 m path length. The ring diameter is about 11.8 cm (as Cherenkov angle, θ , is given by $\cos\theta = \frac{1}{n\beta}$ with n the index of refraction of the gas and β the fraction of the velocity of light the particle carries). The number of hits found is quantified by the n_0 variable which is defined as the number of hit PMTs within a ring around the track projection with an inner radius of 3.4 cm and an outer radius of 8.4 cm. This search ring is chosen based on the known ring diameter and the position resolution of the PMTs, defined by the PMT size (about 2.5 cm).

2.5.2 Electromagnetic Calorimeter

The Electromagnetic Calorimeter (EMCal) is made up of eight sectors with four sectors in each arm. The east arm has two different types of calorimeters, lead glass (PbGl) and lead scintillator (PbSc). Both types have slightly different efficiencies and tower segmentation. This allows for a comparison of EMCal measurements with two distinct types of calorimeters. Both types of sectors have good energy and position resolution, the PbSc sectors have good timing and linearity of response to charged particles, while

the PbGl sectors have a good energy resolution and a finer granularity. PbSc tower has a cross-section of $5.25 \times 5.25 \text{ cm}^2$ and a length of 37.0 cm ($18 X_0$) and contains 66 sampling cells made of alternating tiles of Pb and scintillator. These cells are connected with optical fibers to wavelength shifters for light collection. The light is read out by phototubes at the back of the towers. Four optically isolated towers are mechanically grouped together into a single structural identity called a module. The modules are grouped together as an array of 12×12 towers called a super-module (SM). Then 18 of these super-modules (in a 3×6 grid) are joined together to form a sector. PbSc sectors are fully in West arm but only 2 sectors are there in East arm shared with 2 sectors of PbGl as is shown in Fig. 2.3.

The PbGl is a Cherenkov calorimeter, consists of an array of thick optical glass towers embedded with 51% Pb-Oxide. Each PbGl tower has a cross-section of $4.0 \times 4.0 \text{ cm}^2$ and is 40 cm long ($14.3 X_0$). The towers are grouped in 6×4 to form modules, which in turn are grouped into 192 super-modules as an array of 16×12 towers. At the back of the towers PMTs are used for readout.

2.6 Hadron Blind Detector

Hadron Blind Detector (HBD) was developed and installed as an upgrade of the PHENIX experiment at Relativistic Heavy Ion Collider (RHIC) for the measurement of electron pairs particularly in the low mass region ($m \leq 1 \text{ GeV}/c^2$ including the light vector mesons ρ , ω and ϕ) [83]. Dileptons are valuable probes for the hot and dense matter formed in ultra-relativistic heavy-ion collisions. They play a crucial role in the quest for the QCD phase transition from hadron gas (HG) to the quark gluon plasma (QGP) expected to be formed in these collisions. They can provide evidence of chiral symmetry restoration and deconfinement phase transition [84]. Dileptons also offer the possibility to identify the thermal radiation emitted from the QGP via $q\bar{q}$ annihilation. Such a radiation is regarded as a very strong signal of deconfinement. There is no

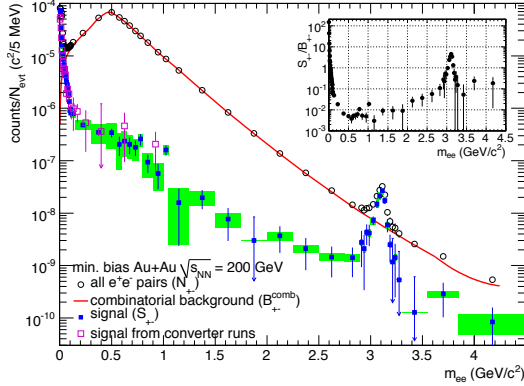


Figure 2.12. Background (B) and Signal (S) with statistical (bar) and systematic (boxes) uncertainties. The inset shows S/B ratio [85].

convincing evidence for thermal radiation from the QGP at lower energies either in the dilepton or in the real photon channels. Theoretical calculations have singled out the dilepton intermediate mass range ($m = 1-3$ GeV/c^2) as the most appropriate window for the observation of QGP thermal radiation [86].

The measurement of di-leptons in heavy ion collisions is a challenging task because of the huge combinatorial background in the low mass region. Electron pairs measured in PHENIX from Run-4 showed very low signal-to-background ratio $S/B \sim 1/200$ in the low mass region with large statistical and systematic uncertainties (Fig. 2.12). Moreover, the limited azimuthal angular acceptance in the central arms and the strong magnetic field beginning radially at $R=0$, makes the identification and rejection of electron-positron pairs from Dalitz decays and photon conversions very difficult. Therefore, the improved S/B is needed for further studies of low mass dilepton spectra. The main sources of combinatorial background are coming from $\pi^0 \rightarrow \gamma e^+e^-$ and $\pi^0 \rightarrow \gamma\gamma \rightarrow \gamma e^+e^-$, and the fact is exploited that these channels have small opening angle, so by using the opening angle one must be able to distinguish single hits from double hits in HBD.

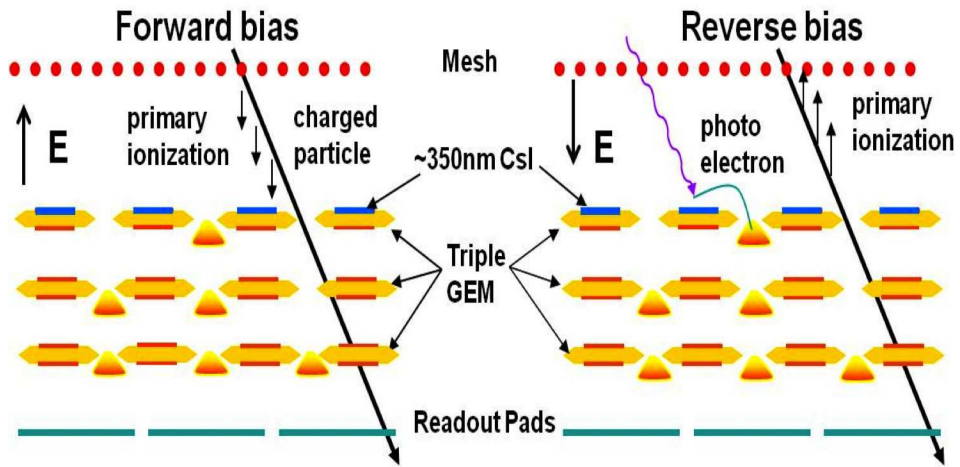


Figure 2.13. Schematic of HBD working principle in forward bias mode (left) and in reverse bias mode (right)

2.6.1 Detector concept and performance

The main task of HBD is to recognize and reject γ -conversions and π^0 Dalitz decay pairs using the fact of their small opening angle. In order to conserve the opening angle of the decay pairs, HBD is placed in the magnetic field free region. HBD consists of a Cherenkov radiator operated with pure CF_4 in a proximity focus configuration directly coupled to a triple-GEM detector element with a CsI photocathode on the top GEM [87] and a pad readout. The choice of CF_4 , both as radiator and detector gas in a windowless geometry, results in a very large bandwidth (from ~ 6 eV given by the threshold of the CsI to ~ 11.5 eV given by the CF_4 cut-off) and consequently in a large figure of merit N_0 and a large number of photo electrons N_{pe} . One of the important advantages of using GEMs is that it allows the use of a reflective photocathode which is totally screened from photons produced in the avalanche process. HBD contains two arms in east and west side of PHENIX co-ordinate system and its acceptance in pseudorapidity is $|\eta| \leq 0.45$ and in azimuthal angle ($\Delta\Phi$) is 135^0 .

The entire detector was rebuilt after Run-7 with extreme care to maintain a clean

environment during the GEM assembly. A considerable fraction of the damaged GEMs was successfully recuperated by washing them with de-ionized water, and the rest were replaced with spare ones. The HBD was re-integrated into PHENIX in the summer of 2008 and successfully took physics data during Run-9 and in Run-10. The HBD performance and calibration based on p+p collisions at $\sqrt{s_{NN}} = 200$ GeV data set is described in the following sections.

2.6.2 Electrons Background in RUN-9

PHENIX detector did not allow a good measurement of low-mass electron pairs before RUN-9, this is because of two reasons: first, tracks with momentum $p < 200$ MeV/c cannot escape from the magnetic field region, and second the angular acceptance in the central arms is limited. So, it often happens that only one electron track originating from Dalitz decay or conversion pair gets detected, this result in a huge combinatorial background.

The Electrons from RUN-9 are shown in Fig. 2.14, the tracking of the electrons in the central arms is reconstructed with the standard cuts used in all PHENIX experiment electron analyses, namely the good track quality in the drift chamber (DC), number of fired phototubes in the PHENIX Ring Imaging Cherenkov detector (RICH) and E/p cut where E is the electron energy derived from EMCal and p is its momentum derived from DC. It is seen that in both, minimum bias (mb) and EMCal-RICH Triggered Data we have many electrons with background contamination. If the Z position for an event is more than ± 20 cm we get many more electrons due to the multiple scattering from detector materials. This is why Z position between ± 20 cm is used to remove this possibility in the following studies.

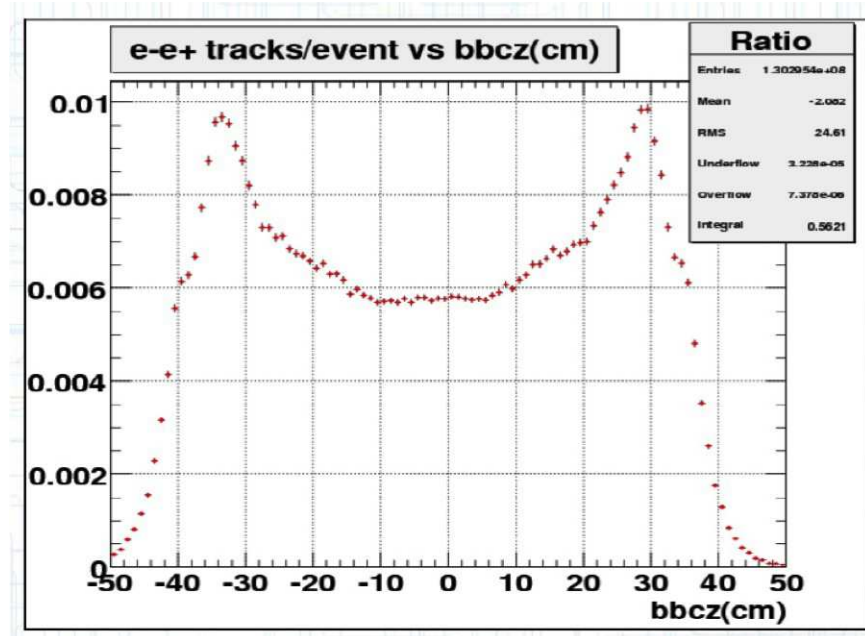


Figure 2.14. Electrons background in Run-9 minimum bias data

2.6.3 Detector Alignment Corrections

After each access in PHENIX, all the detector subsystems need to be aligned because of the movement of the detector during maintenance. Similarly for HBD, position corrections during RUN-9 in both Z and Φ directions are performed.

For this study Hadrons in zero magnetic field configuration of PHENIX are selected from RUN-9 for p+p collisions at $\sqrt{s_{NN}}=200$ GeV to ignore the bending of the track due to the magnetic field. These corrections are done on module by module basic and for each module they are derived and one need to implement them before starting HBD based analysis. Also these corrections for RUN-10 have been derived and they are comparable to RUN-10 corrections. Figs. 2.152.16 show the distribution of difference between hit position and projection from central arm in Z and Φ directions after implementing the matching corrections. It is evident from these distributions that they are centered at zero, showing the detector is well aligned.

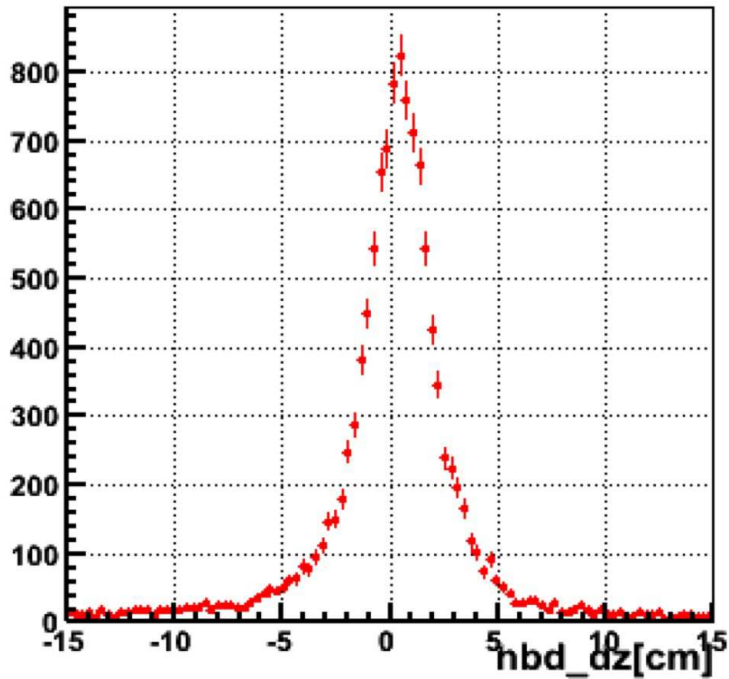


Figure 2.15. Matching distribution for the electron tracks in Z (cm)

2.6.4 Position Resolution of HBD

The tracking to the HBD is done using the electrons in the central arms reconstructed to the HBD in order to find out the closest cluster. It is done by the matching of Central Arm tracks to the HBD. The matching distributions (difference between projection point and the closest cluster in HBD) of electron tracks in Φ and Z are determined for different track momentum bins. In Fig. 2.17, the momentum dependence of the sigma of ΔZ and $\Delta\Phi$ is shown and the asymptotic resolution in Z and Φ are obtained as ~ 1.05 cm and 8 mrad respectively [88].

2.6.5 Hadron Rejection Factor

The hadron blindness property of the HBD is achieved by operating the detector in the reversed bias mode. In this mode, the mesh is set at a higher voltage with respect to

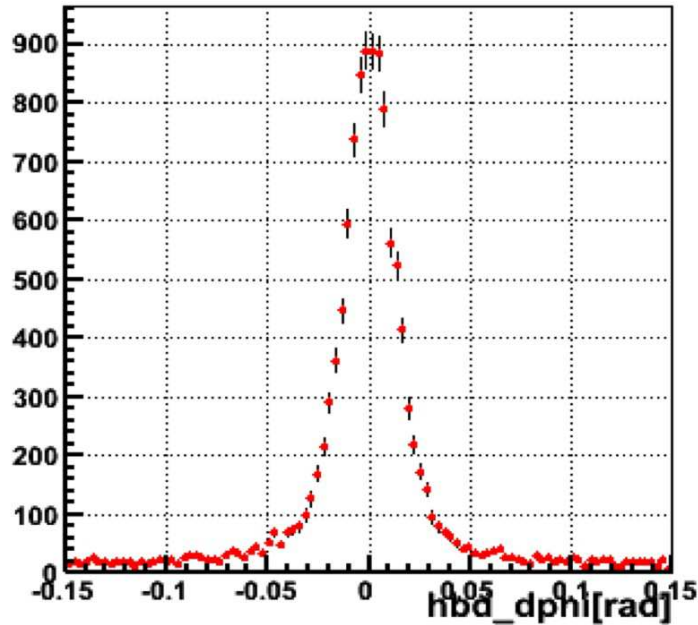


Figure 2.16. Matching distribution for the electron tracks in Φ (rad)

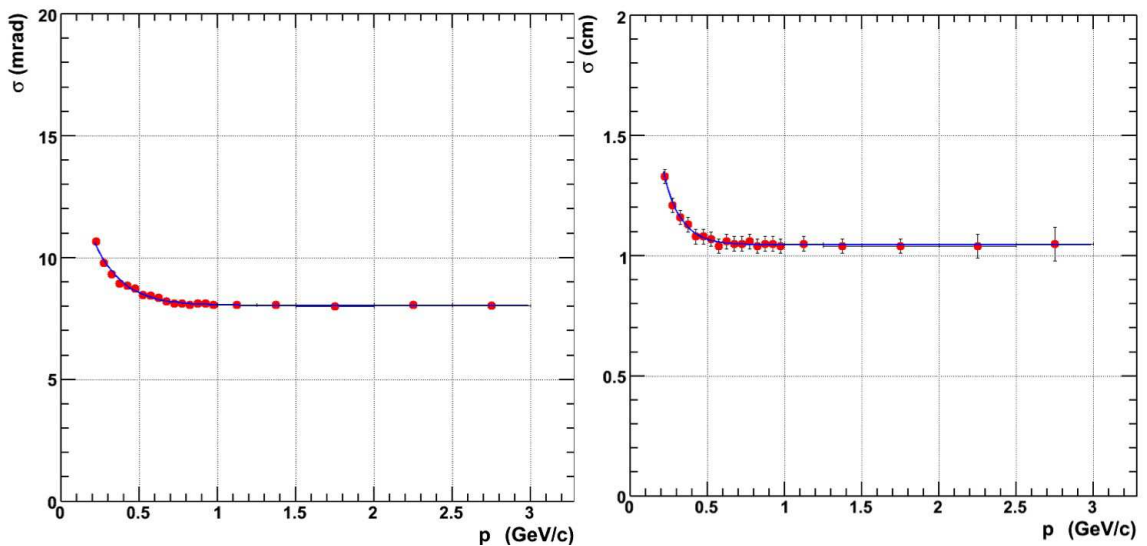


Figure 2.17. The variation of matching resolution of the electron tracks in Z and Φ with respect to momentum.

the GEM and consequently the ionization charge deposited by a charged particle in the drift region between the entrance mesh and the top GEM is mostly repelled towards the

mesh. The hadron response in HBD, operational in reverse bias mode is very important for the HBD rejection power. All good quality tracks which are reconstructed in the Central Arms and don't pass the electron identification criteria are considered as the hadrons. They are projected to the HBD and the closest (within 3σ matching cuts) cluster is reconstructed. Hadron rejection factor (HRF) derived from Run-9 reverse bias data is shown below for one module. Also HRF calculation on module by module basis has been done and the HRF gain dependence is also checked to be reasonably constant for Run-9.

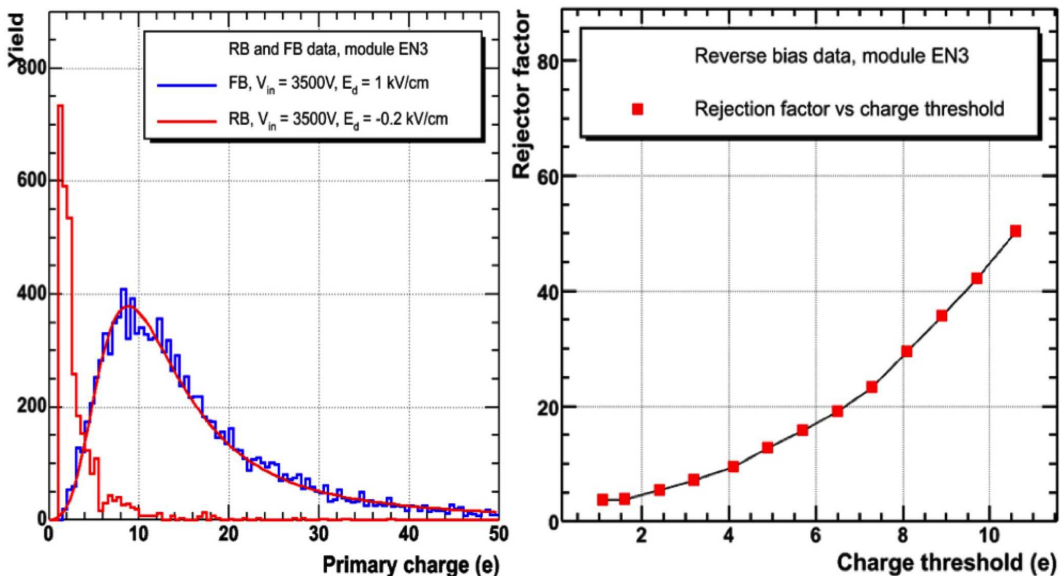


Figure 2.18. (left) Hadron charge spectra in reverse (red) and forward bias (blue) (right) Hadron Rejection Factor as a function of charge threshold.

In Fig. 2.18, a drop in pulse height of hadrons in RB mode of HBD is demonstrated. Hadron rejection factor (ratio of the number of hadron tracks identified in central arm detectors to the number of corresponding matched hits in the HBD) as a function of threshold charge in reverse bias mode of HBD for a single module is shown in Fig. 2.18. Also a very good separation between single electrons and hadrons in RB has been observed as single electron response peaked at ~ 20 photoelectrons whereas electrons from hadrons are peaked at ~ 40 due to single and double hits in HBD respectively.

Single electron efficiency for the full HBD extracted from di-electrons in the J/Ψ mass region is obtained approximately as 90%.

2.6.6 Event Accumulator to study HBD pattern recognition

Besides the analysis of the peripheral events as we move to more central events, the detector has to cope with a high multiplicity events. The detector occupancy is huge due to the large number of the scintillation hits. It is studied with the help of a software tool in PHENIX called Event Accumulator. Fig. 2.19 shows the typical HBD event display for visualization of track hits.

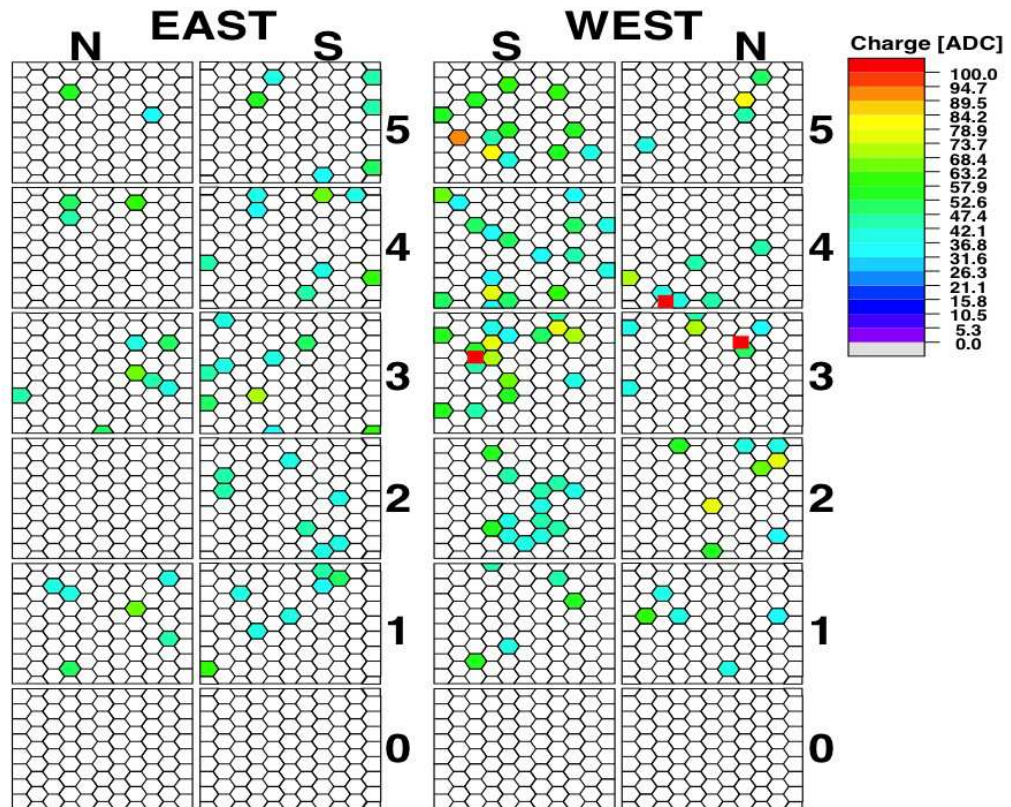


Figure 2.19. Three electrons in an event (red squares) from Run-10 minimum bias data are represented by red squares (Charge Threshold= 31.6 ADC).

HBD is very efficient at determining tracks from p+p events. HBD reconstruction

is less efficient in determining Au+Au tracks due to overlapping of tracks so the idea is to obtain electron identification in Au+Au collisions by comparing “Accumulated” p+p events to known reconstructions in Au+Au. For this study, Instead of using Monte Carlo, we use real data by accumulating many p+p events to emulate one Au+Au event.

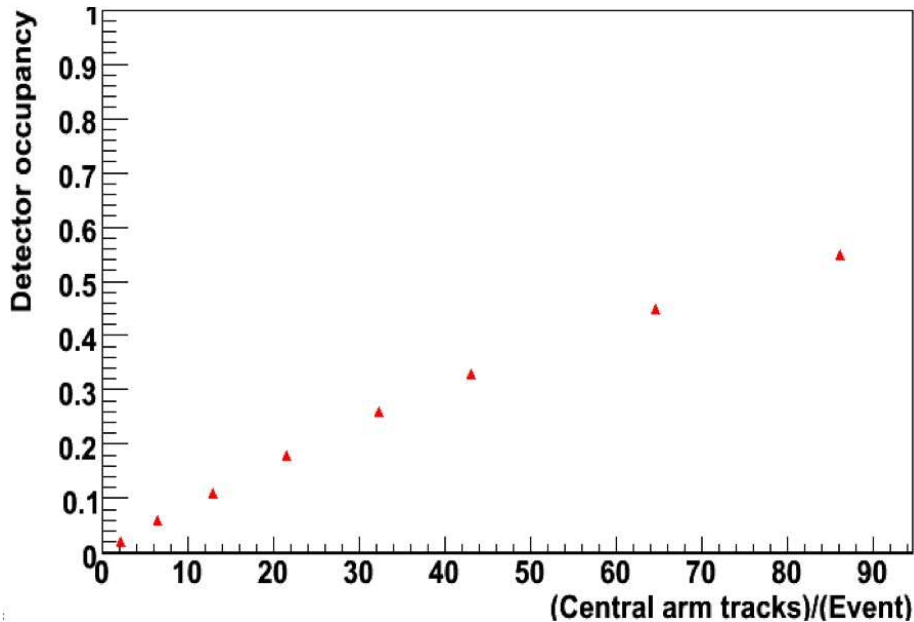


Figure 2.20. Detector occupancy with centrality

In the original version of Event Accumulator code significant changes are done and few of the results are shown below.

As we go towards high multiplicity the HBD clustering algorithm for Run-9 do not work effectively because of the high detector occupancy as is shown in Fig. 2.20. How many electrons HBD effectively start loosing with increasing the central arm tracks per event is shown in Fig. 2.21 for different momentum selection criterion. It also indicates that the electron identification gets poor in high multiplicity environment.

The main reason for this de-efficiency is that, as the centrality increases we pick more and more background because the cluster size for electrons track grows (Fig. 2.22) and effective signal goes down for HBD as is clear from Fig. 2.23.

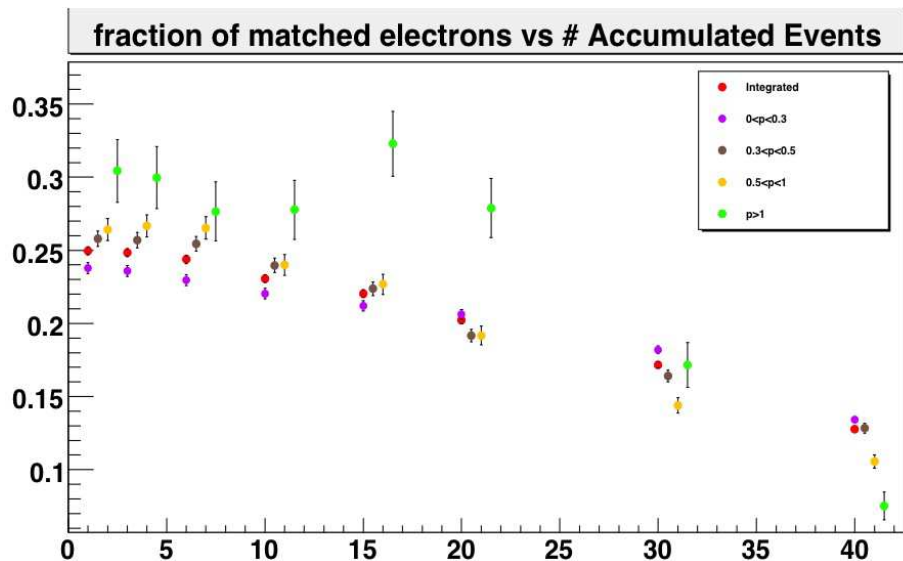


Figure 2.21. Fraction of electron loose with centrality for integrated momentum and different momentum bins.

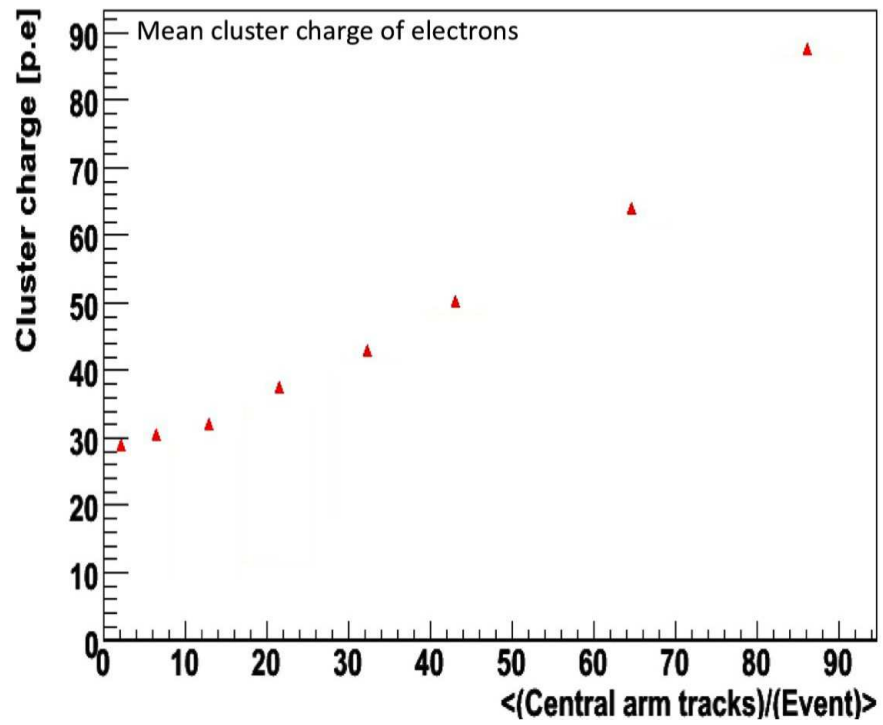


Figure 2.22. Cluster charge per electron track with different number of accumulated events

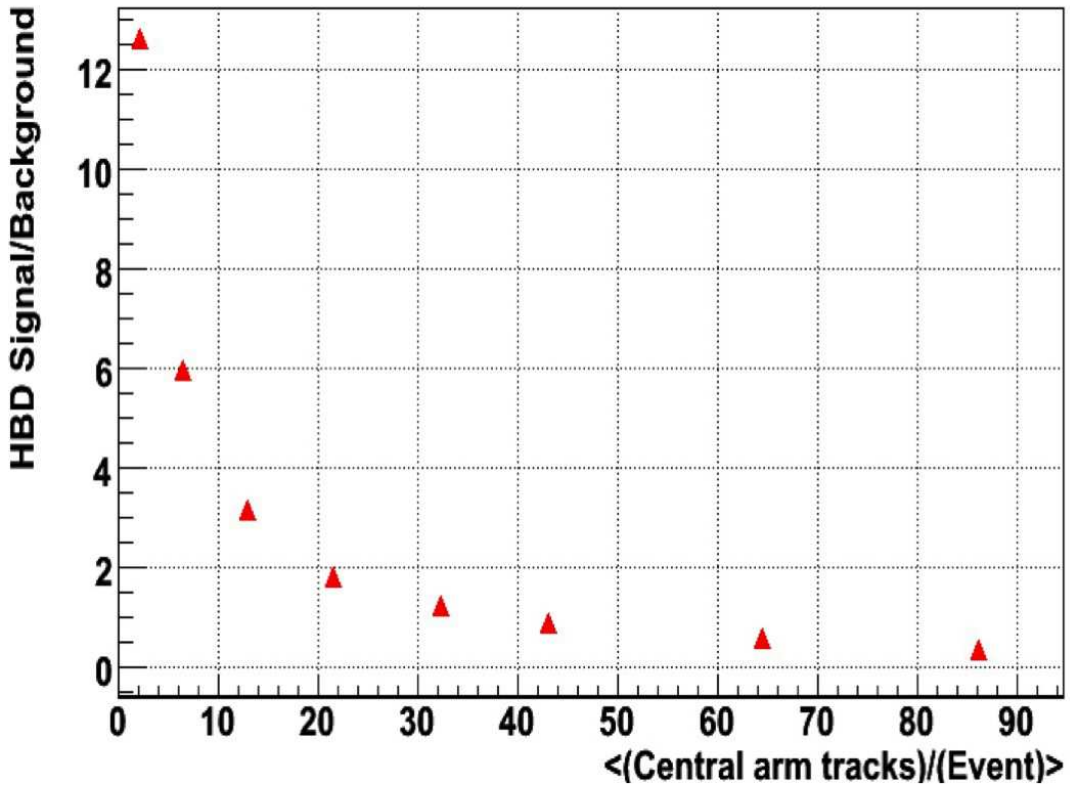


Figure 2.23. HBD signal/Background vs central arm tracks.

In Summary, Hadron Blind Detector performed well in PHENIX during RHIC Runs in 2009 (p+p) and 2010 (Au+Au). The performance studies carried with p+p data show good hadron rejection power of HBD and good separation between electrons coming from resonances or heavy quarks and neutral hadrons. There will be consequent improvements in di-electron S/B. Thus the final results using HBD will be exciting to see in near future.

2.7 PHENIX data acquisition system

The PHENIX On-Line system takes signals from the Front End Modules (FEM) on each detector subsystem for the purpose of generating events for physics analysis. The

PHENIX data acquisition (DAQ) system processes the signals from each detector subsystem, produces the trigger decision, and stores the triggered data [89] [90]. The interaction rate at design luminosity of RHIC varies from a few kHz (~ 200 kbytes event size) for Au+Au central collisions to approximately 500 kHz (~ 60 kbytes event size) for minimum bias p+p collisions. The PHENIX DAQ was designed to handle these high interaction rates and event sizes with the provision to accommodate future improvements in the luminosity. The schematic of the PHENIX DAQ system is shown in Fig. 2.24. The DAQ contains several electronics modules like Master Timing Module (MTM), Granule Timing Module (GTM), Global Level-1 Trigger (GL1), Local Level-1 Trigger (LL1), Front End Module (FEM), Data Collection Modules (DCM). All of them are pipelined and synchronized with the RHIC beam clock. The PHENIX DAQ is nearly free of dead-time until the input rate is higher than the maximum data-taking rate.

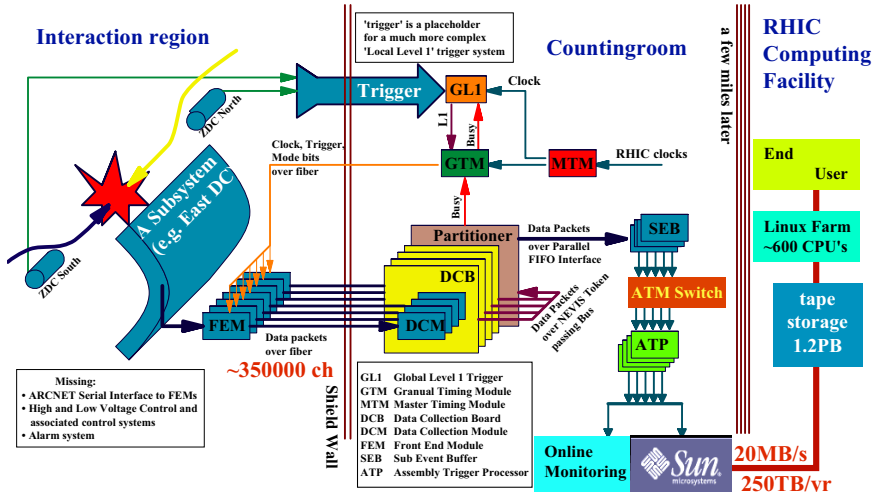


Figure 2.24. Block diagram of PHENIX DAQ.

The PHENIX subsystems are sampled on each beam crossing with 9.4 MHz. Data cannot be digitized at such a high rate, so the analog response from each subsystem is transferred by cables to the FEMs which are located near the detectors in the beam

intersecting region. The transferred data are processed by Front End Electronics (FEE) that buffers the data of 40 beam bunch crossings to wait for the decision of GL1. The MTM receives the 9.4 MHz RHIC clock and delivers it to the GTM and GL1. The LL1 system communicates directly with a few fast detectors such as BBC, EMCAL and RICH. Subsystem specific LL1 modules process the input data from the corresponding detector and produce a set of reduced-bit input for each RHIC beam crossing and sends it to the GL1. The GL1 then makes a trigger decision based on the assembled bits from the various LL1 subsystems, the DAQ busy signal and the trigger scale-down counter. Whenever a beam crossing satisfies the trigger criteria, the GTM delivers the clock, the control commands and an event accept signal to the FEMs of each detector. After receiving the accept signal, each FEM starts to digitize the data. The triggered data fragments from the FEMs are transferred to the DCMs via optical fibers. The DCMs perform zero suppression, error checking and data reformatting. The formatted data are compressed and sent to the PHENIX Event Builder (EvB). The EvB consists of 39 Sub Event Buffers (SEBs), Asynchronous Transfer Mode (ATM) switch and 52 Assembly Trigger Processors (ATPs). The EvB receives many parallel data streams from the DCMs, assembles the data fragments from each stream into complete events and provides an environment for the higher level triggers to operate. Finally accepted events are transmitted to the PHENIX Online Control System (ONCS) for temporary storage in the buffer boxes. The data in the buffer boxes are used for online quality monitoring and calibration processes. Later on the data are transferred to the RHIC Computing Facility (RCF) for permanent storage on tapes.

Chapter 3

Data Analysis and Results of Higher moments

This chapter presents the details of analysis performed for the measurement of higher moments of net-charge multiplicity distributions of charged hadrons. Higher moments of net-charge distributions at various beam energies have been analyzed for Au+Au collisions from Run-7 (200 GeV), Run-10 (7.7 GeV, 39 GeV and 62.4 GeV) and Run-11 (19.6 GeV and 27 GeV). It is necessary in the event-by-event fluctuation analysis to suppress background fluctuation originating from bad and outlier runs. For this, a detailed study has been performed. Besides, finite bin width effect, detector effect, effect of residual magnetic field, efficiency correction for cumulants, and systematic as well as statistical error estimation have been discussed in the following sections.

3.1 Analysis Overview

The analysis is based on the data sets that correspond to three RHIC running periods Run-07, Run-10 and Run-11. The magnetic field configuration of PHENIX detector for different energies is ”-+” for $\sqrt{s_{NN}}= 7.7$ GeV, 39 GeV, 62.4 GeV and 200 GeV, ”++” for $\sqrt{s_{NN}}= 19.6$ GeV and ”- -” for $\sqrt{s_{NN}}= 27$ GeV.

Since, the analysis follow mostly a similar procedure for all the energies, so they are discussed in parallel, highlighting the differences where ever they exist. Mainly, the

steps for higher moment analysis can be summarized as follows:

- Event Selection, Track selection and Quality assurance (QA) studies
- Moments and Higher moments calculations with Statistical and Systematic Error estimation
- The reconstruction efficiency correction to the measured moments
- Monte Carlo simulations to account for the acceptance and reconstruction effects
- Comparison with the baseline Models

Next sections describe in detail the steps highlighted above.

3.2 Data sets, Event selection and Track selection

This section presents an overview of various data sets used in the analysis and the global event selection criteria for minimum-bias events.

3.2.1 Event Selection

In all the datasets, minimum bias triggered events with $|Z_{vertex}^{bbc}| < 30$ cm are selected for the analysis. There are other cuts applied to the events to remove the pile-up and many other junk events. The selected event must have 2 or more hits in both north and south BBCs. Also the selection of BBC timing in both north and south should be between 2 ns to 8 ns. The centrality values are used from the standard PHENIX re-calibrators, which are determined in Au+Au collisions using transverse energy (E_T) information from EmCal for 19.6 GeV and 27 GeV while for other energies it is extracted from BBC charge as is discussed in Chapter 2. The Centrality determination for 7.7 GeV is done

with PHENIX Reaction Plane Detector. The reason for choosing different centrality methods is to avoid the auto-correlations for our central arm analyses which may effect our results and the availability of the global detectors in a particular run.

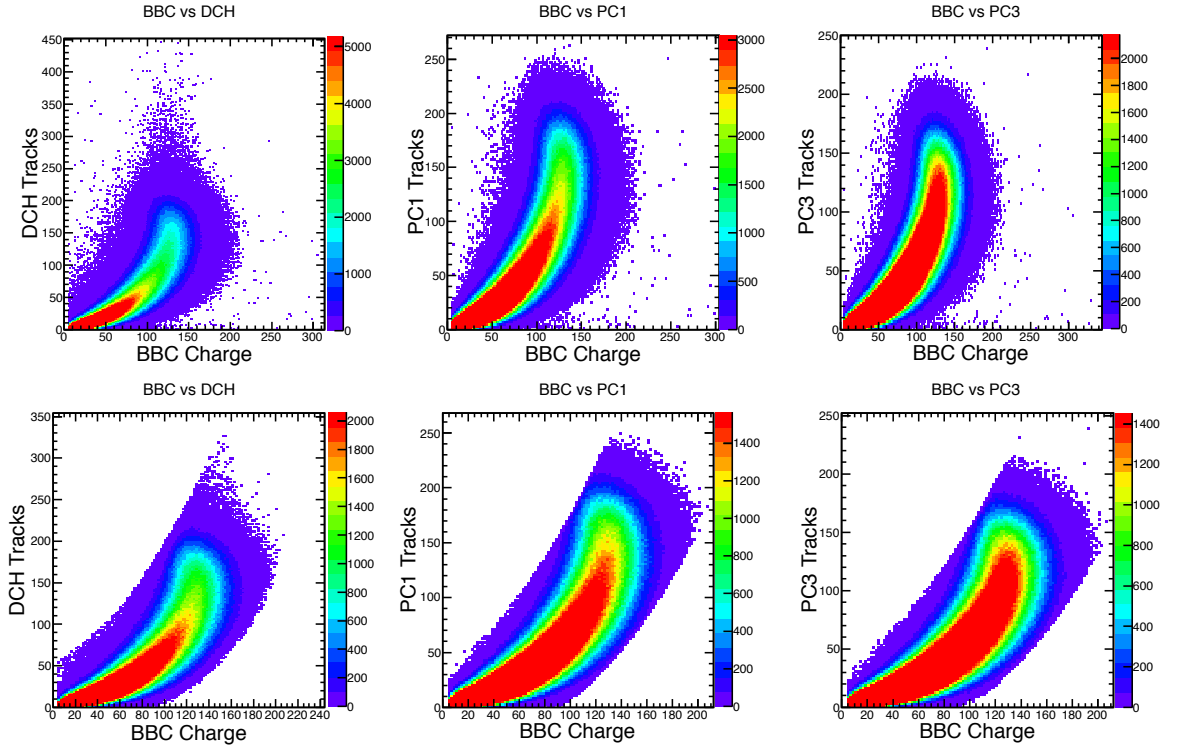


Figure 3.1. The correlation plot for Au+Au collisions at 19.6 GeV: BBC charge vs DCH tracks, PC1 hits and PC3 hits before applying the cuts are shown in top row. Bottom row shows the correlations after applying the cuts.

To check the quality of the selected events, the information from the BBC, ZDC, DCH, PC1 and PC3 is used. Different scattered plots: BBC charge vs DCH charge, BBC charge vs PC1 hits and BBC charge PC3 hits are shown in Fig. 3.1. The pile-up events are shown up in all the detectors.

For 200 GeV data set of Run-7, these effects are more prominent than at other energies. The pile-up events are removed by excluding the events above the geometrical cut line (Fig. 3.3) in the BBC vs ZDC correlation plot. The cut line is selected to maximize the background removal. This cut effectively removes the pile-up events

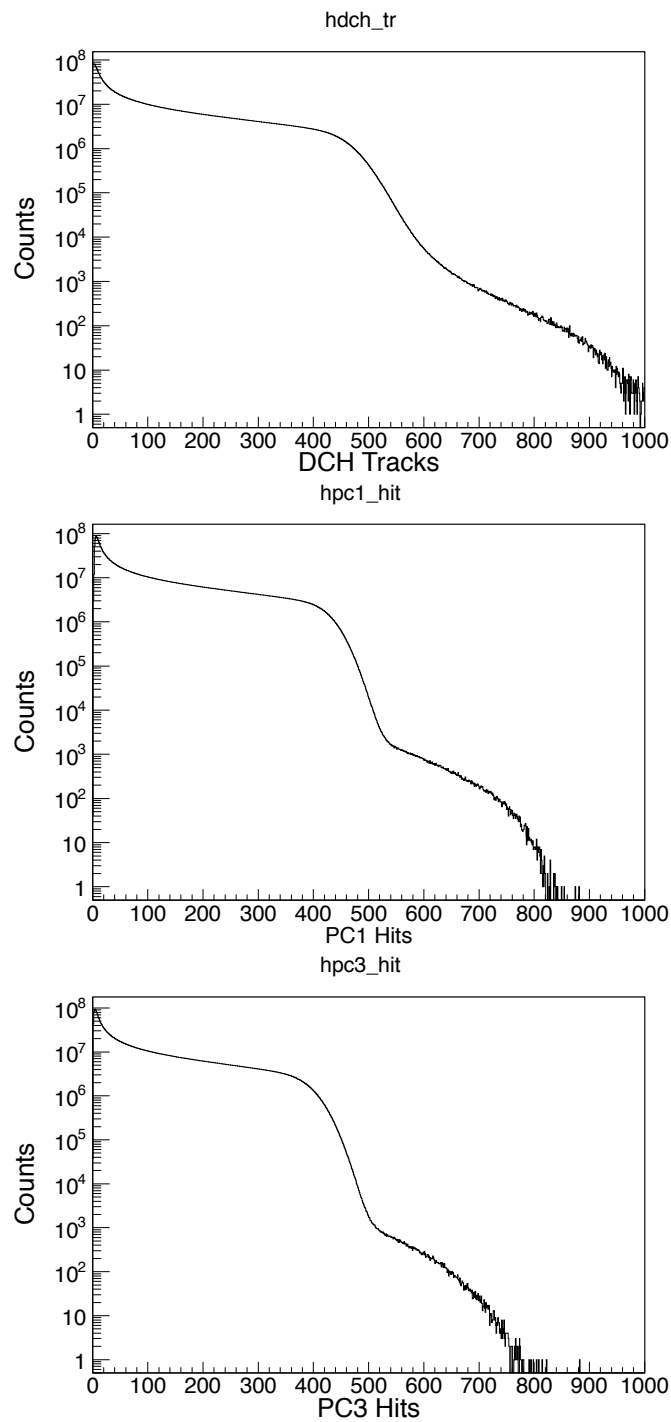


Figure 3.2. The DCH track, PC1 hit and PC3 hit distributions before selecting the good events for 200 GeV Au+Au collisions in Run-7.

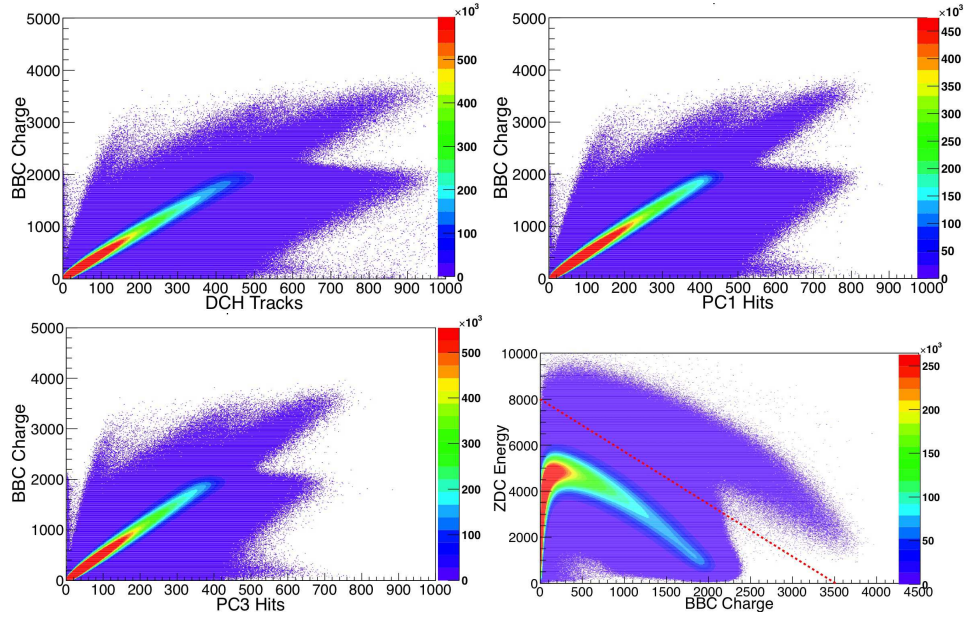


Figure 3.3. The correlation plots for BBC charge vs DCH tracks, PC1 hits, PC3 hits and ZDC energy before applying the cuts for 200 GeV data.

mostly in the mid-central and the central collisions. As shown in Fig. 3.3, the correlation of BBC charge vs DCH, PC1 and PC3 are linear. The events are rejected which lie outside the 5σ (6σ) in the lower (higher) side from the mean value of the correlation plot in this analysis. For systematics, the event selection cuts are tightened to study the moments of the net-charge distributions. With the tighter cuts, there is no difference in various moments of net-charge distributions. Same cuts are applied for other energies also. The DCH track, PC1 hit and PC3 hit distributions after removing the pile-up

Table 3.1. Number of good events selected for the analysis at different $\sqrt{s_{NN}}$:

Energy (Run No.)	No. of Events
7.7 GeV (Run-10)	~ 1 M
19.6 GeV (Run-11)	~ 6 M
27 GeV (Run-11)	~ 20 M
39 GeV (Run-10)	~ 155 M
62.4 GeV (Run-10)	~ 476 M
200 GeV (Run-10)	~ 3260 M

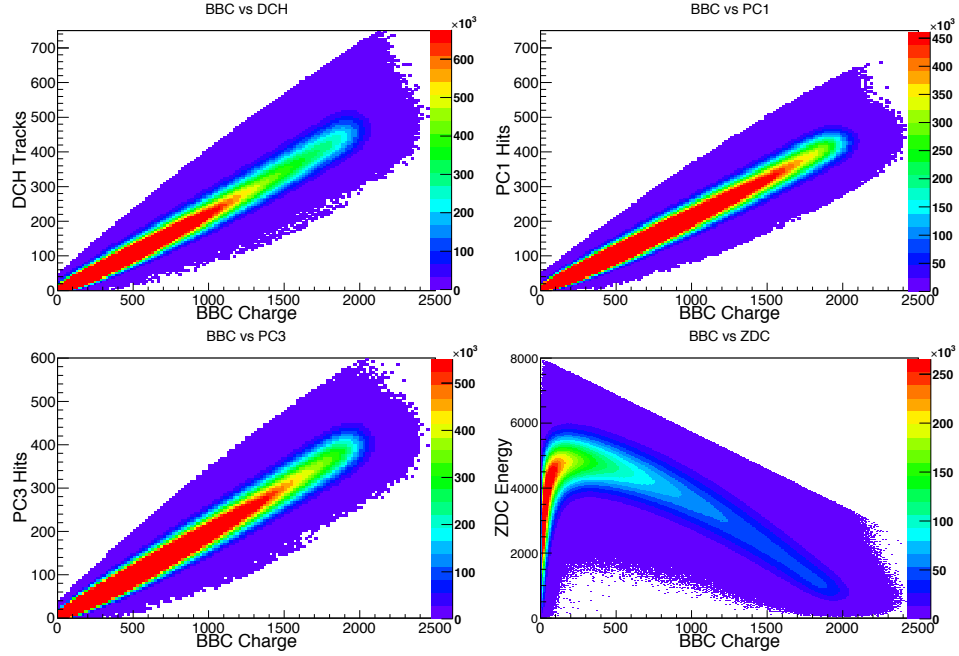


Figure 3.4. The correlation plots for BBC charge vs DCH tracks, PC1 hits and PC3 hits after applying the cuts for 200 GeV data.

and other fake events are shown in Fig 3.5. After applying the above cuts, the total number of events used in the analysis are listed in Table 3.1.

3.2.2 Track selection

After selecting the good events, several track selection cuts are applied to the globally reconstructed tracks within PHENIX acceptance, covering a pseudo-rapidity range of $|\eta| < 0.35$. The applied cuts are as follows:

- The selected tracks have transverse momentum ($0.3 \text{ GeV}/c < p_T < 2.0 \text{ GeV}/c$)
- The drift chamber track quality (dchQuality) is of 31 and 63 only
- A maximum of 1 associated RICH ring fired PMT is used to help the electron background rejection

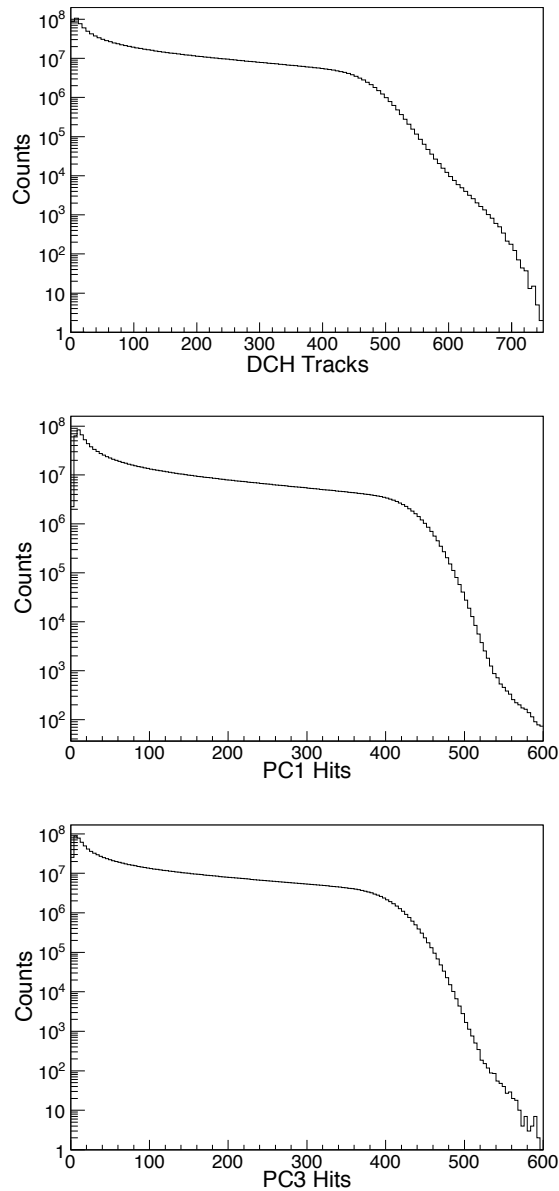


Figure 3.5. The DCH track, PC1 hit and PC3 hit distributions after selecting the good events for 200 GeV Au+Au collisions in Run-7.

- A drift chamber zed co-ordinate requirement of $|zed| < 75.0 \text{ cm}$ to reduce the background coming from the magnet
- Track matching to PC3 cluster within 2.0σ
- Track matching to EMC cluster within 2.5σ

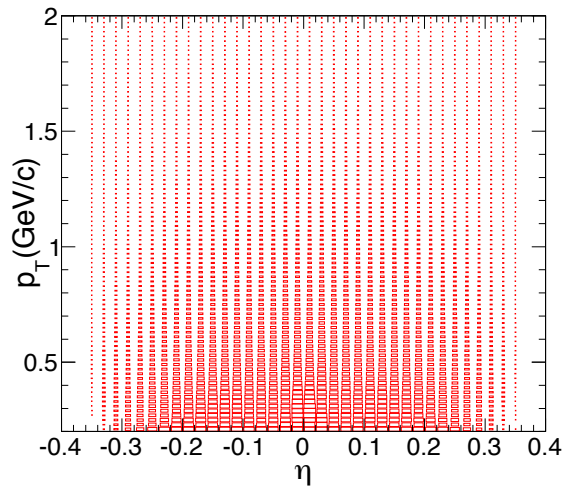


Figure 3.6. Uniform η vs p_T acceptance for all charged hadrons used for the analysis.

Above track cuts are applied so that the tracks used for this analysis are of good quality and the probability of secondary background tracks is less. Fig. 3.6 shows the uniform PHENIX acceptance in η and ϕ for the selected tracks.

Apart from the above track cuts, additional **proximity cuts** are applied to all possible track combinations within each event to help in removing the ghost tracks which artificially increase the particle multiplicity. The pair of tracks is considered to be in the proximity if:

- the associated PC1 clusters of the two tracks are within 3.5 cm and
- the drift chamber phi co-ordinates are within 0.018 radians and the drift chamber *zed* co-ordinates are within 0.28 cm.

If two tracks are in close proximity as per the above criteria, then those tracks are removed from the analysis.

3.3 Moments Methodology in Heavy Ion Collisions

Moments are popularly used to characterize the shape of a probability distribution in statistics. For example, the second central moment (moment about the mean) i.e. variance (σ^2) describes the width of a probability distribution. The skewness (S) and kurtosis (κ) are used to describe how the distributions are skewed and peaked from its mean value respectively as is discussed in Fig. 3.7. Another alternative method to moments of a distribution is called cumulant. The cumulants determine the moments in the sense that any two probability distributions whose cumulants are identical will have identical moments as well, and similarly the moments determine the cumulants. In heavy ion collisions, the higher moments of a distribution of conserved quantities, like net-baryon, net-charge and net-strangeness are predicted to be sensitive to the correlation length and are directly connected to the thermodynamic susceptibilities as computed in Lattice QCD and in Hadron Resonance Gas (HRG) model. In this section, the definitions and properties of moments and cumulants are described. The efficiency correction to moments and their statistical error estimation is also discussed briefly.

3.4 Relation between central moments and cumulants of Event-by-Event Fluctuations

In statistics probability distribution functions can be characterized by various moments, such as mean (M), variance (σ^2), skewness (S) and kurtosis (κ). Before introducing the above moments used in our analysis, we will define central moments and cumulants, which are alternative methods to describe a distribution.

Experimentally one measures event-by-event conserved numbers, for example, net-proton numbers, $N_{p-\bar{p}} = N_p - N_{\bar{p}}$, which is proton number minus antiproton number. The average value over whole event ensemble is denoted by $\mu = \langle N \rangle$, where the single

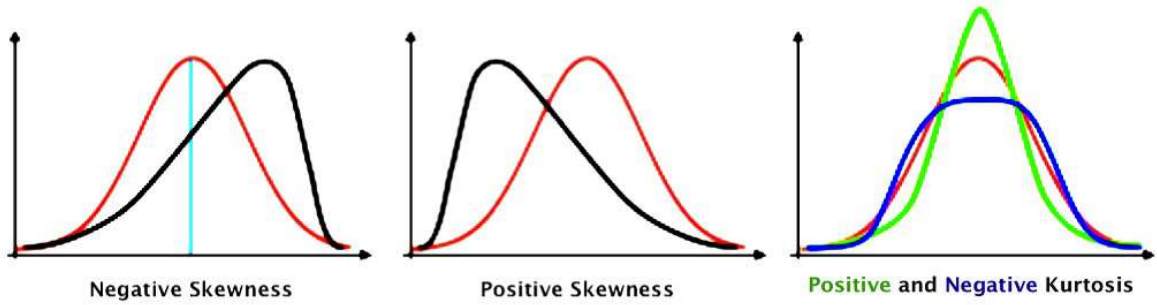


Figure 3.7. A pictorial view of negative and positive skewed distributions are shown with black curve (left two panels) as compared to normal distribution (red). Further, right most panel shows distributions with positive (green) and negative (blue) kurtosis with respect to the normal distribution (red).

angle bracket is used to indicate ensemble average of an event-by-event distribution. The deviation of N from its mean value is defined as:

$$\delta N = N - \langle N \rangle = N - \mu. \quad (3.1)$$

and the r^{th} order sample estimates for central moments are defined as:

$$\mu_r = \langle (\delta N)^r \rangle \quad (3.2)$$

$$\mu_1 = 0 \quad (3.3)$$

Then we can define the sample estimates for various order cumulants of event-by-event distributions as:

$$C_1 = \mu \text{ (mean)} \quad (3.4)$$

$$C_2 = \mu_2 \quad (3.5)$$

$$C_3 = \mu_3 \quad (3.6)$$

$$C_n (n > 3) = \mu_n - \sum_{m=2}^{n-2} \binom{n-1}{m-1} C_m \mu_{n-m} \quad (3.7)$$

An important property of the cumulants is their additivity for independent variables. If X and Y are two independent random variables, then we have $C_{i,X+Y} = C_{i,X} + C_{i,Y}$ for i^{th} order cumulant. This particular property of cumulants is shown in Ref [57].

Once we have the definition of cumulants, sample estimators for skewness and kurtosis can be given as:

$$M = C_{1,N}, \sigma^2 = C_{2,N}, S = \frac{C_{3,N}}{(C_{2,N})^{3/2}} \text{ and } \kappa = \frac{C_{4,N}}{(C_{2,N})^2} \quad (3.8)$$

Then, the moments product $\kappa\sigma^2$ and $S\sigma$ can be expressed in terms of cumulant ratios in following manner:

$$\frac{\sigma^2}{M} = \frac{C_{2,N}}{C_{1,N}}, \kappa\sigma^2 = \frac{C_{4,N}}{C_{2,N}} \text{ and } S\sigma = \frac{C_{3,N}}{C_{2,N}}. \quad (3.9)$$

With the above definition of various moments, we can calculate various moments and moment products with the measured event-by-event conserved number distributions.

3.4.1 Moments and Cumulants of Poisson Distribution

Various background effects result in statistical fluctuations which obey the Poisson statistics. If we assume that our true signals are not correlated with those statistical backgrounds, then the Poisson value of our observables can serve as a baseline.

Poisson distribution is a limiting case of the Binomial Distribution for large number of independent trials n , with small probability of success p such that the expectation value of the number of successes $\mu = \langle m \rangle = np$ remains constant, i.e. the probability of m counts when one expects μ is given by:

$$P(\mu = m) = \frac{\mu^m e^{-\mu}}{m!} \quad (3.10)$$

Therefore various moments (M , σ , S , κ) as well as moment products ($\kappa\sigma^2$, $S\sigma$) of single Poisson distribution are given as:

$$\begin{aligned} M &= \mu \\ \sigma &= \sqrt{\mu} \\ S &= \frac{1}{\sqrt{\mu}} \\ \kappa &= \frac{1}{\mu} \end{aligned} \quad (3.11)$$

and hence $S\sigma = \kappa\sigma^2 = 1$, for Poisson distributions. The difference of two independent Poisson distributions will be distributed as “Skellam” distribution. The moments of Skellam distribution build with two Poisson distributions with mean μ_1 and μ_2 are deduced as follows:

$$\begin{aligned} M &= \mu_1 + \mu_2 \\ \sigma &= \sqrt{(\mu_1 + \mu_2)} \\ S &= \frac{(\mu_1 - \mu_2)}{(\mu_1 + \mu_2)^{3/2}} \\ \kappa &= \frac{1}{(\mu_1 + \mu_2)} \\ S\sigma &= \frac{(\mu_1 - \mu_2)}{(\mu_1 + \mu_2)} \\ \kappa\sigma^2 &= 1. \end{aligned} \quad (3.12)$$

In our case we are dealing with the difference of two distributions, for example, net-charge distribution.

3.4.2 Cumulants of Negative Binomial Distribution (NBD)

The negative binomial process can be thought of as a compound Poisson process Ref. [113]. It can be expressed as:

$$NB(k; r, p) = \frac{1}{r!} \frac{\Gamma(r+k)}{\Gamma(k)} (1-p)^k p^r. \quad (3.13)$$

Where p is the probability of success and k is the failure before the r^{th} success. Here r is also known as stopping parameter. The limiting cases of NBD or Binomial distribution are the Poisson and Gaussian distribution. For Gaussian distribution, the skewness and kurtosis are zero as it is a symmetric distribution. The NBD is valid when mean (μ) of the distribution is less than that of the variance (σ^2) i.e. $\mu < \sigma^2$. The probability of success is defined as $p = \mu$. The cumulants of the NBD can be expressed in terms of p and r as follows,

$$\begin{aligned} c_1 &= \frac{r(1-p)}{p} \sim \mu \\ c_2 &= \frac{r(1-p)}{p^2} \sim \sigma^2 \\ c_3 &= \frac{r(p-1)(p-2)}{p^3} \\ c_4 &= \frac{-r(p-1)(6-6p+p^2)}{p^4} \end{aligned} \quad (3.14)$$

Now moments of NBD can be derived from these cumulants as is given in Eq. 3.8.

3.5 Error Estimation of Cumulants

To perform precise higher moments measurement, the error analysis is crucial for extracting physics message due to the statistic hungry properties of the moments analysis.

Here we show the errors for various moments that are used in data analysis based on the Delta theorem in statistics and probability theory. This method has been extensively described in Ref. [121]. The variance of moments are calculated as follows:

$$Var(\sigma) = (m_4 - 1)\sigma^2/(4n) \quad (3.15)$$

$$Var(S) = [9 - 6m_4 + m_3^2(35 + 9m_4)/4 - 3m_3m_5 + m_6]/n \quad (3.16)$$

$$Var(\hat{\kappa}) = [-m_4^2 + 4m_4^3 + 16m_3^2(1 + m_4) - 8m_3m_5 - 4m_4m_6 + m_8]/n \quad (3.17)$$

$$Var(\hat{S}\hat{\sigma}) = [9 - 6m_4 + m_3^2(6 + m_4) - 2m_3m_5 + m_6]\sigma^2/n \quad (3.18)$$

$$Var(\hat{\kappa}\hat{\sigma}^2) = [-9 + 6m_4^2 + m_4^3 + 8m_3^2(5 + m_4) - 8m_3m_5 + m_4(9 - 2m_6) - 6m_6 + m_8]\sigma^4/n. \quad (3.19)$$

Here m_r are the normalized central moments ($m_r = \frac{\mu_r}{\sigma^r}$) over a sample of n events.

3.6 Formulation for Efficiency correction

The acceptance corrections to various moments of particle distributions have already been discussed in the literature. For example, corrections to the variance or second order cumulants of the net-charge and net-baryon number distributions have been investigated in Refs. [110–112], while acceptance effects on factorial moments have been addressed in Ref. [114, 115]. In this section the corrections to higher order cumulants which are central to the discussion of the QCD critical point are discussed. More details on acceptance corrections and their importance have been discussed in Ref. [91].

Suppose we have an underlying probability distribution $P(N_1, N_2)$ which captures the full dynamics of the system and the probability distribution $p(n_1, n_2)$ of the actually observed multiplicities. Here N_1 and N_2 represent the multiplicity of produced positive (baryon or strange) and negative charge particles (antibaryon or antistrange) while n_1 and n_2 correspond the same but for experimentally measured multiplicities.

Therefore, the assumption that all acceptance corrections can be modeled by a binomial probability distribution, leads to the following relation

$$p(n_1, n_2) = \sum_{N_1=n_1}^{\infty} \sum_{N_2=n_2}^{\infty} P(N_1, N_2) \frac{N_1!}{n_1!(N_1 - n_1)!} p_1^{n_1} (1 - p_1)^{N_1 - n_1} \times \frac{N_2!}{n_2!(N_2 - n_2)!} p_2^{n_2} (1 - p_2)^{N_2 - n_2}. \quad (3.20)$$

The parameters p_1 and p_2 describe all possible acceptance effects in our system for particles and their counterparts. For example, the detector acceptance is modeled by the binomial distribution and it can be different for different particle species.

Further, the factorial moments are related to their probability distributions as:

$$F_{ik} \equiv \left\langle \frac{N_1!}{(N_1 - i)!} \frac{N_2!}{(N_2 - k)!} \right\rangle = \sum_{N_1=i}^{\infty} \sum_{N_2=k}^{\infty} P(N_1, N_2) \frac{N_1!}{(N_1 - i)!} \frac{N_2!}{(N_2 - k)!}, \quad (3.21)$$

$$f_{ik} \equiv \left\langle \frac{n_1!}{(n_1 - i)!} \frac{n_2!}{(n_2 - k)!} \right\rangle = \sum_{n_1=i}^{\infty} \sum_{n_2=k}^{\infty} p(n_1, n_2) \frac{n_1!}{(n_1 - i)!} \frac{n_2!}{(n_2 - k)!}. \quad (3.22)$$

Therefore, using Eq 3.20, the factorial moments are connected as:

$$F_{ik} = \frac{1}{p_1^i p_2^k} f_{ik}, \quad (3.23)$$

Here F_{ik} and f_{ik} correspond to the factorial moments of truly produced and experimentally measured multiplicities.

Finally f_{ik} can be expressed by the cumulants c_n , which will allow us to relate the cumulants of actually produced distribution (K_n) to the experimentally observed cumulants (c_m). However, the factorial moments f_{ik} and F_{ik} in general cannot be solely expressed in terms of the cumulants of the net-distributions, c_n and K_m , respectively but additional terms, not related to cumulants arises.

Here we present the general relations between cumulants K_n characterized by

the “required acceptance”, and the measurable factorial moments at a given acceptance parameters p_1 and p_2 . As seen in Eqs. (3.25-3.27) it is not possible to express cumulants K_n solely by cumulants c_m but also factorial moments F_{ik} appear. Therefore, K_n are solely represented by the factorial moments F_{ik} as follows:

$$K_1 = \langle N_1 \rangle - \langle N_2 \rangle, \quad (3.24)$$

$$K_2 = N - K_1^2 + F_{02} - 2F_{11} + F_{20}, \quad (3.25)$$

$$\begin{aligned} K_3 = & K_1 + 2K_1^3 - F_{03} - 3F_{02} + 3F_{12} + 3F_{20} - 3F_{21} + F_{30} \\ & - 3K_1(N + F_{02} - 2F_{11} + F_{20}), \end{aligned} \quad (3.26)$$

$$\begin{aligned} K_4 = & N - 6K_1^4 + F_{04} + 6F_{03} + 7F_{02} - 2F_{11} - 6F_{12} - 4F_{13} \\ & + 7F_{20} - 6F_{21} + 6F_{22} + 6F_{30} - 4F_{31} + F_{40} \\ & + 12K_1^2(N + F_{02} - 2F_{11} + F_{20}) - 3(N + F_{02} - 2F_{11} + F_{20})^2 \\ & - 4K_1(K_1 - F_{03} - 3F_{02} + 3F_{12} + 3F_{20} - 3F_{21} + F_{30}), \end{aligned} \quad (3.27)$$

If we assume that the efficiency to detect positive (baryon or strange) and negative (anti-baryon and anti-strange) hadrons is same then the relation between cumulants of truly produced net-charge distributions (K_i) and experimentally derived net-charge distributions (C_i) have the following relations.

$$K_2^{X-Y} = (C_2^{x-y} + (\varepsilon - 1)(\langle x \rangle + \langle y \rangle)) / \varepsilon^2 \quad (3.28)$$

$$K_3^{X-Y} = (C_3^{x-y} + 3(\varepsilon - 1)(C_2^x - C_2^y) + (\varepsilon - 1)(\varepsilon - 2)(\langle x \rangle - \langle y \rangle)) / \varepsilon^3 \quad (3.29)$$

$$\begin{aligned} K_4^{(X-Y)} = & (C_4(x - y) - 2(\varepsilon - 1)C_3(x + y) + 8(\varepsilon - 1)(C_3(x) + C_3(y)) \\ & + (5 - \varepsilon)(\varepsilon - 1)C_2(x + y) + 8(\varepsilon - 2)(\varepsilon - 1)(C_2(x) \\ & + C_2(y)) + (\varepsilon^2 - 6\varepsilon + 6)(\varepsilon - 1)(\langle x \rangle + \langle y \rangle)) / \varepsilon^4. \end{aligned} \quad (3.30)$$

Where (X, Y) and (x, y) are the numbers of positively & negatively charged particles

produced and measured respectively. ε is the reconstruction efficiency of charged particles. The same expressions are also used in Ref. [57].

3.7 Event-by-event net-charge distributions

After selecting good tracks out of good events according to previous section, event-by-event net-charge distributions are obtained from PHENIX data. In order to construct the net-charge multiplicity distributions positively charged and negatively charged hadrons are counted on an event-by-event basis. Figs. [3.9-3.10] show the multiplicity distributions for positive and negative hadrons for $\sqrt{s_{NN}} = 27$ GeV as an example. To get the net-charge multiplicity distributions, number of negatively charged hadrons are subtracted from the number of positively charged hadrons on an event-by-event basis.

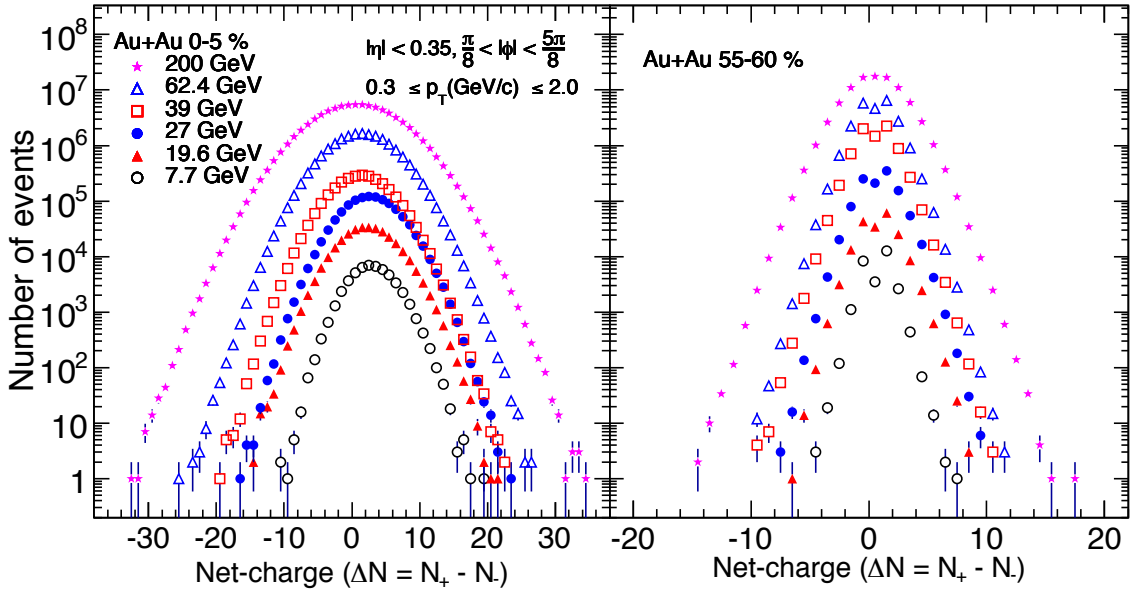


Figure 3.8. Event-by-event net-charge (ΔN) distributions for Au+Au collisions at different energies for 0-5% (left panel) and 55-60% (right panel) centrality bins.

Event-by-event, net-charge multiplicity distributions for Au+Au collisions at different $\sqrt{s_{NN}}$ for two different centralities (0-5)% and (55-60)% are shown in Fig.3.8. The distributions are symmetric around the mean value but get wider as we go from peripheral to central collisions i.e. variance (σ) increases.

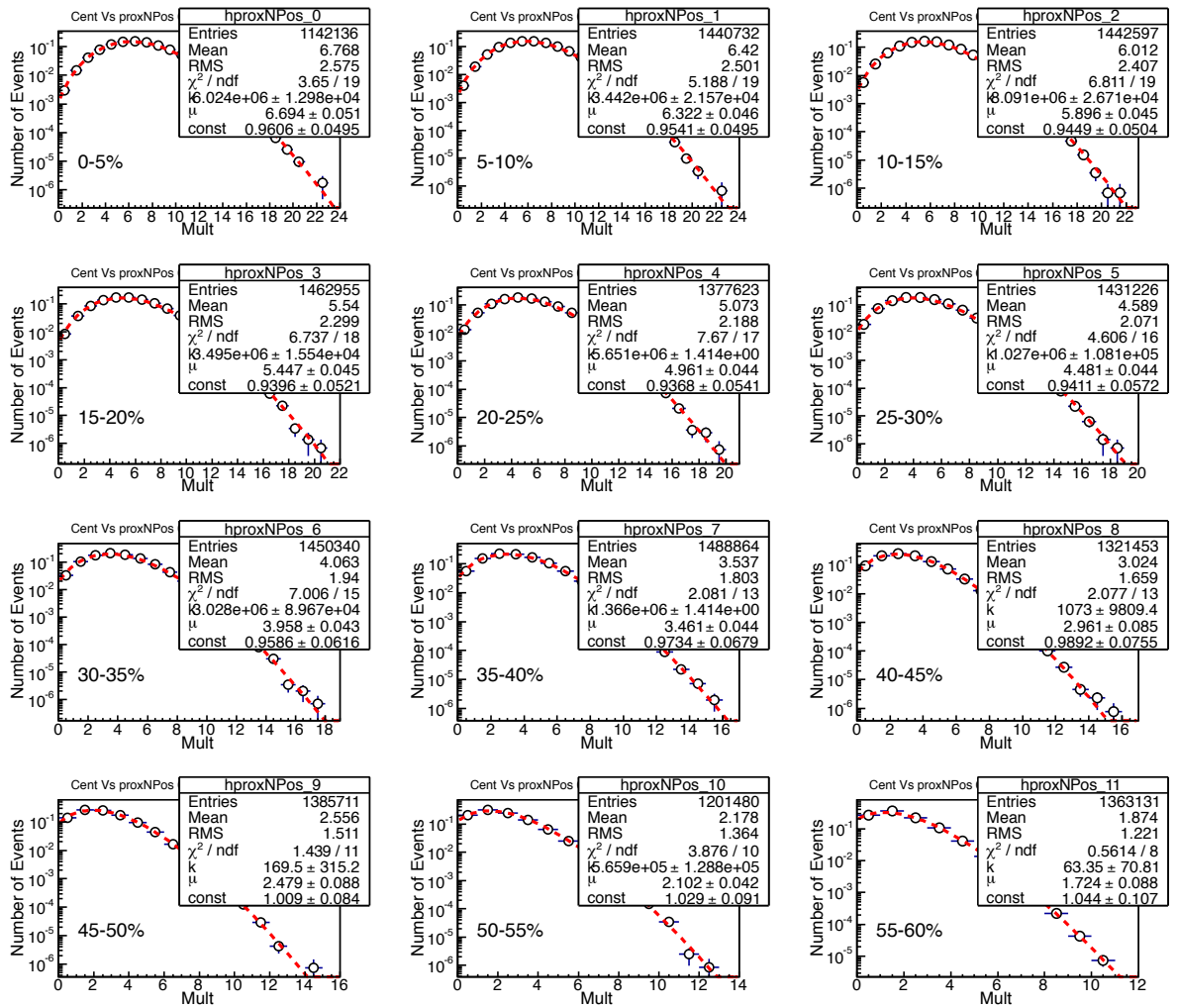


Figure 3.9. Event-by-event positive charge (N_+) distributions for different centralities at $\sqrt{s_{NN}} = 27$ GeV. The distributions are fitted with Negative Binomial distribution (NBD).

Similar trend of net-charge distributions have been observed for different energies of a particular centrality. These effects will be shown up in higher moments (S and κ) of net-charge distributions also.

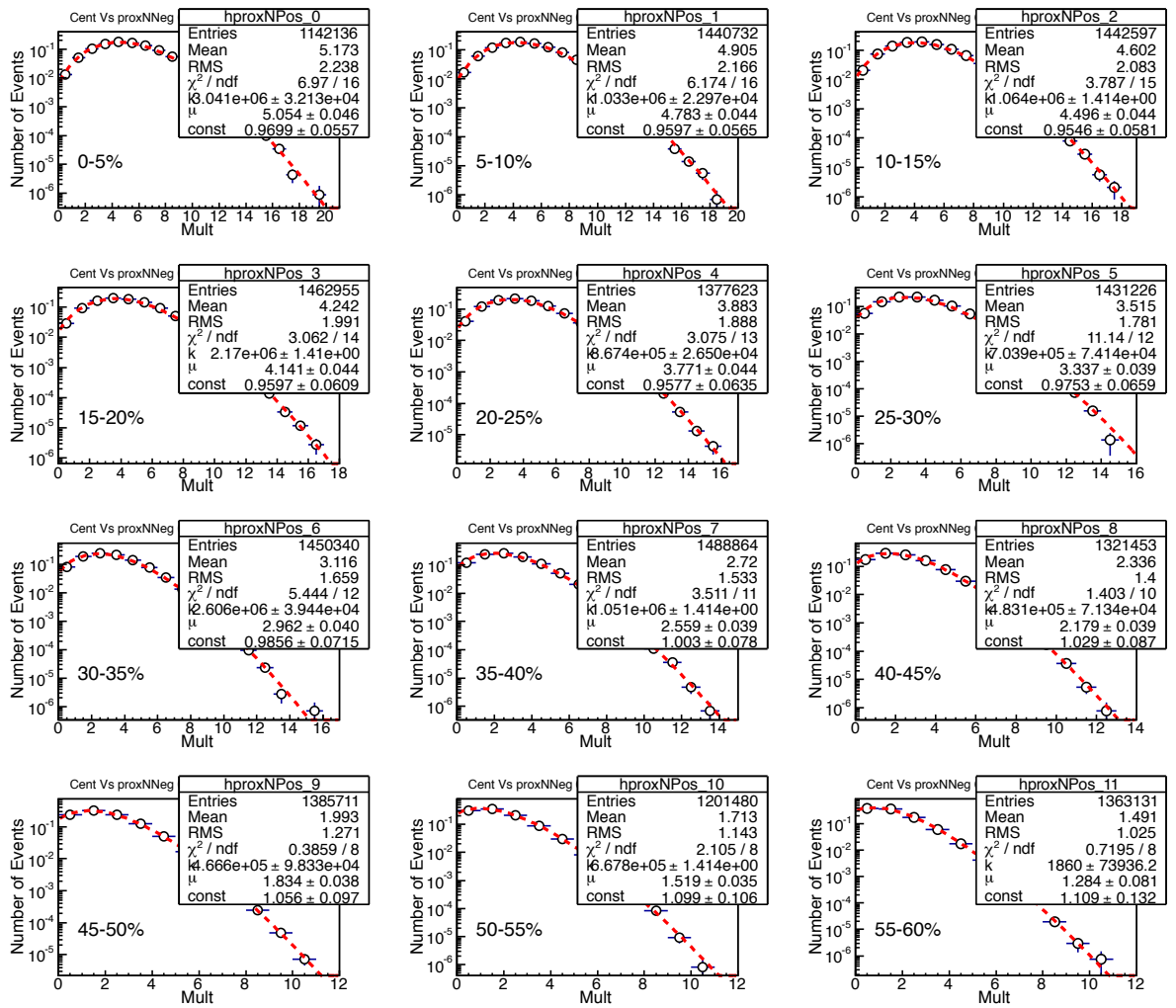


Figure 3.10. Event-by-event positive charge (N_-) distribution for different centralities at $\sqrt{s_{NN}} = 27$ GeV. The distributions are fitted with Negative Binomial distribution (NBD).

3.8 HIJING and UrQMD Event Generators

Charged particles multiplicity distributions as well as the net-charge distributions are sensitive to particle production mechanisms [116]. Various models use different underlying physics for particle production. For the data analysis part of this thesis, only HIJING and UrQMD models are used for simulation studies.

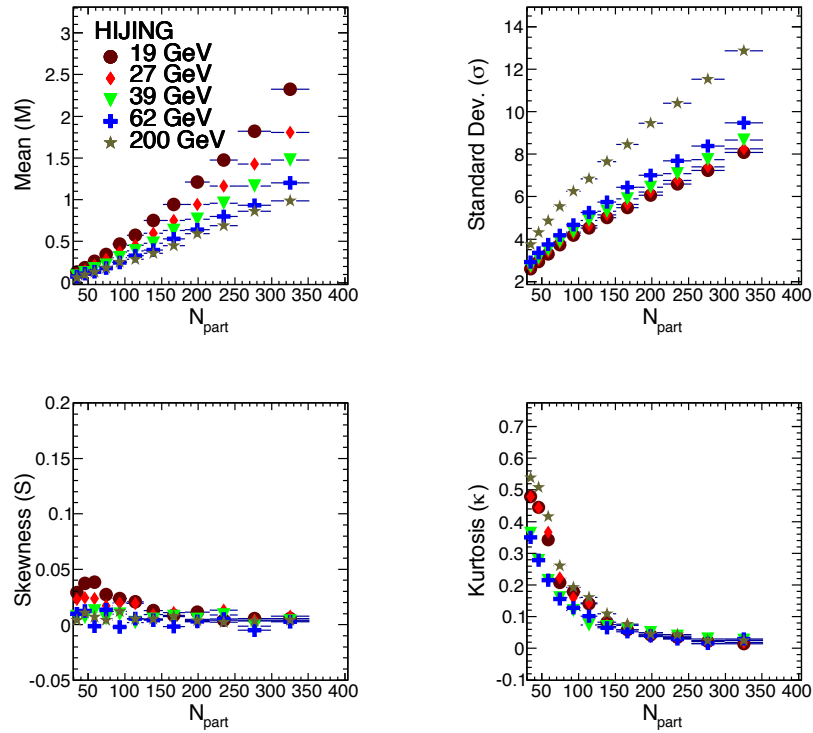


Figure 3.11. The mean, standard deviation, skewness and kurtosis for Au+Au collisions at various energies as a function of centrality (in terms of number of participating nucleons) for net-charge distributions are obtained from HIJING events.

The HIJING [63] model treats the heavy-ion collisions as a superposition of nucleon-nucleon collisions. It can be used to study the effect of jets and mini-jets on the produced particles. UrQMD [62], is a hadronic transport model including strings. It has been used successful to describe stopping power and hadronic re-scattering processes. These models do not contain any physics which is sensitive to the critical point.

Thus these models can provide a baseline study for the physics analysis specific to QCD critical point.

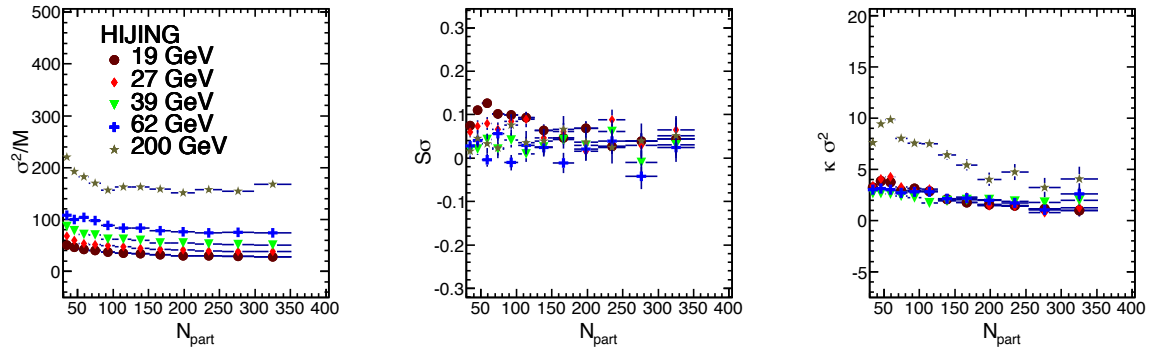


Figure 3.12. Products of moments ($\frac{\sigma^2}{M}$, $S\sigma$ and $\kappa\sigma^2$) are plotted with respect to the average number of participating nucleons, obtained from HIJING events for net-charge distributions.

Fig. 3.11 and Fig. 3.13 show the M , σ , S and κ as a function of centrality for Au+Au collisions at different $\sqrt{s_{NN}}$ deduced from HIJING and UrQMD models, respectively. The M and σ values increase while going from peripheral to central collisions for both the models, whereas S and κ values decrease with increase in collision centrality.

It has been observed that the mean of the distributions is close to zero for high energy collisions and shifts towards positive values for lower energies. The distributions are seen to be wider for higher energy collisions compared to those of the lower energies. We have studied the centrality dependence of $S\sigma$ and $\kappa\sigma^2$ in Figs. 3.12 and 3.14 as a function of centrality for Au+Au collisions at various $\sqrt{s_{NN}}$ also.

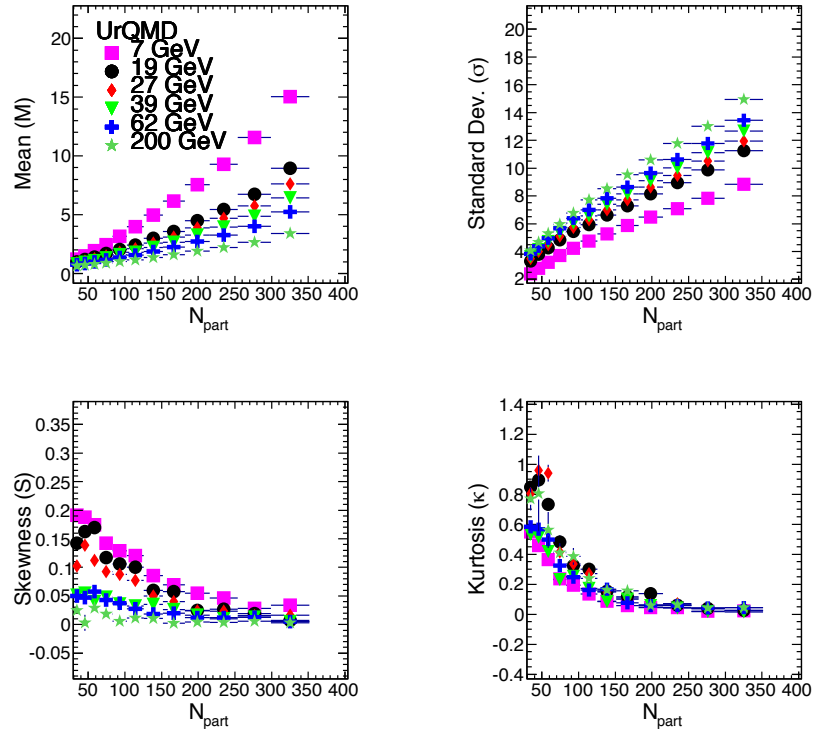


Figure 3.13. The mean, standard deviation, skewness and kurtosis for Au+Au collisions at various energies as a function of centrality (in terms of number of participating nucleons) are shown using UrQMD events.

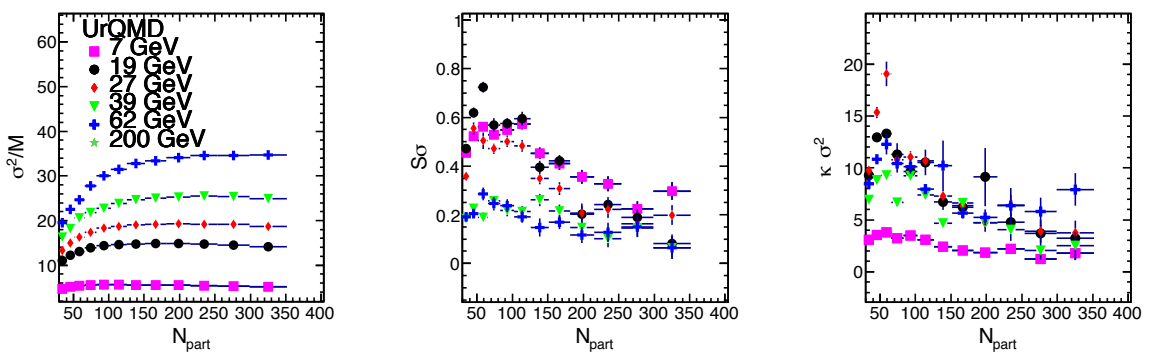


Figure 3.14. Products of moments, $\frac{\sigma^2}{M}$, $S\sigma$ and $\kappa\sigma^2$, plotted with respect to the average number of participating nucleons, obtained from UrQMD events for net-charge distributions.

3.9 Systematic effects

3.9.1 Centrality Resolution Effect and Bin Width Correction

One of the major non-dynamic contribution to the multiplicity fluctuation comes from the geometric variations in the collision system due to variations in the impact parameter arising from the finite width of the centrality bins. The wider the centrality bin, the larger are these geometrical fluctuations. Hence, before calculating various moments of the net-charge distributions for a particular centrality (like 0-5%, 5-10%, ...), we have to consider the centrality bin width effect.

A given centrality class is a collection of events having a range of impact parameters or $\langle N_{part} \rangle$, thus comprising of events with different charged particle multiplicities. This results in additional fluctuations in the number of produced particles within each centrality class. Centrality classes are chosen using three different centrality bin widths, viz., 3%, 5% and 10% of the cross section. From Figs. [3.15-3.16], it is observed that M and σ of net-charge distributions are close to each other for all three centrality classes, whereas deviations are observed in S , κ , and their products ($S\sigma$, $\kappa\sigma^2$). This deviation is the result of choosing centrality class with a large bin.

The effect due to the finite centrality bin can be reduced by choosing smaller bins. In some cases, because of practical reasons such as resolution of centrality determination, statistics of available events, it is not possible to choose fine bins. In this case, a centrality bin width weighting method can be used to minimize the effect. For this, net-charge distributions are constructed for finer bins in centrality within a centrality class. Moments of the distributions are obtained for each finer bin and weighted to get the final moments, according to:

$$X = \frac{\sum_i n_i X_i}{\sum_i n_i}. \quad (3.31)$$

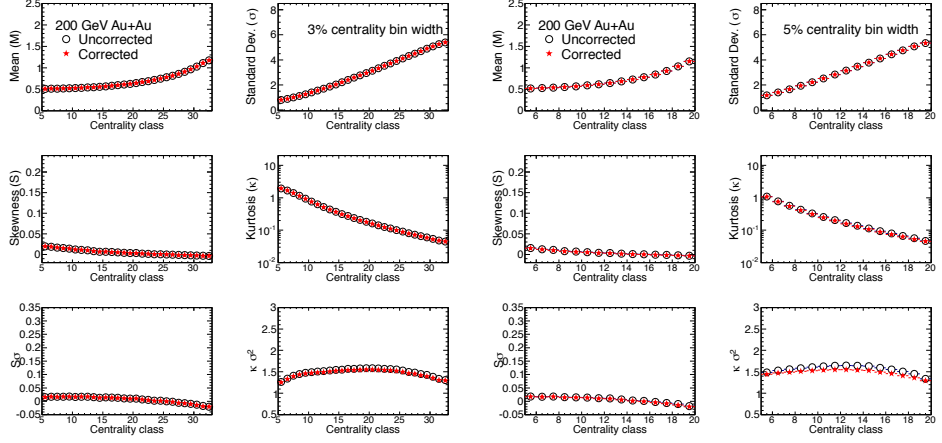


Figure 3.15. Various moments and their product of net-charge distributions as a function of centrality bin for 3% bin width (left two columns) and 5% bin width (right two columns) for Au+Au collisions at $\sqrt{s_{NN}} = 200$ GeV: open symbols are before bin width correction and the star symbols are after correction. Left side of the x-axis implies peripheral collisions and right side corresponds to central collisions.

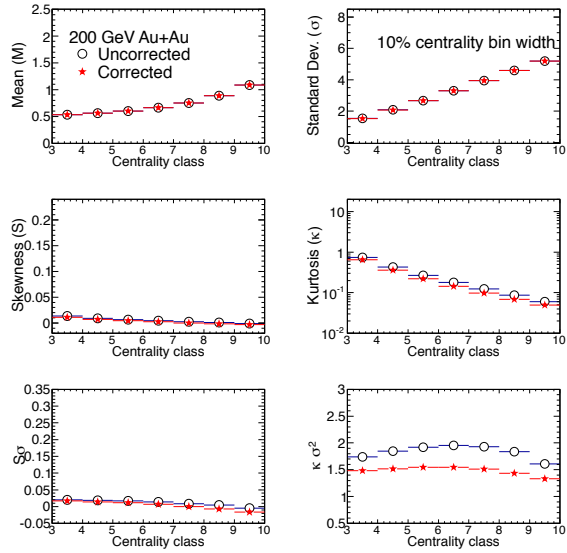


Figure 3.16. Various moments of net-charge distributions as a function of centrality bins (10% bin width) at $\sqrt{s_{NN}}=200$ GeV.

Here X represents a given moment, the index i runs over each fine centrality bin, n_i is the number of events in the i^{th} bin, and $\sum_i n_i$ is the total number of events in a given centrality class. The bin width corrected moments of net-charge distributions in

each centrality class with appropriate weighting are shown in Figs. 3.15 and 3.16. After this correction, no centrality bin width dependence is observed in these three centrality classes. Hence the correction method does an appropriate job in correcting the finite centrality bin width effect.

PHENIX measures the centrality bin width with 1% accuracy. In our analysis usually we report results from wider centrality bins such as 0-5%, 5-10% or even wider bins such as 0-10%, 10-20%. To eliminate the centrality bin width effect, various moments for 1% centrality bin width are calculated and then weighted average value for the wider bins is estimated.

3.9.2 Effect of kinematics on higher moments

p_T dependence

In this subsection the effect of p_T selection on various moments has been studied as a function of N_{part} over different p_T -range over which the charged particles are measured by PHENIX detector. As mentioned before, the base values are obtained by taking $p_T=0.3\text{-}2.0$ GeV/c. We have selected the lower $p_T = 0.3$ GeV/c, because the track efficiencies are almost constant from 0.3 GeV to 2.0 GeV as is discussed later in this chapter. As we go down from 0.3 GeV/c the π^+ and π^- efficiencies reduce about 20% for the central collisions (up to 0 – 15% centrality). The net-charge distributions have significant contribution from pions and they are mainly produced in low p_T . Therefore, it is important to study the lower bound of p_T selection.

In addition to that, experimentally it is difficult to correct the higher moment variables for the track reconstruction efficiency on an event-by-event basis. Therefore, it is better to select the p_T region where the reconstruction efficiencies are maximum. As an example, Fig. 3.17 shows various moments as a function of centrality $\langle N_{part} \rangle$ for different lower p_T cuts applied to the measured particles for 7.7 GeV. Similarly, p_T

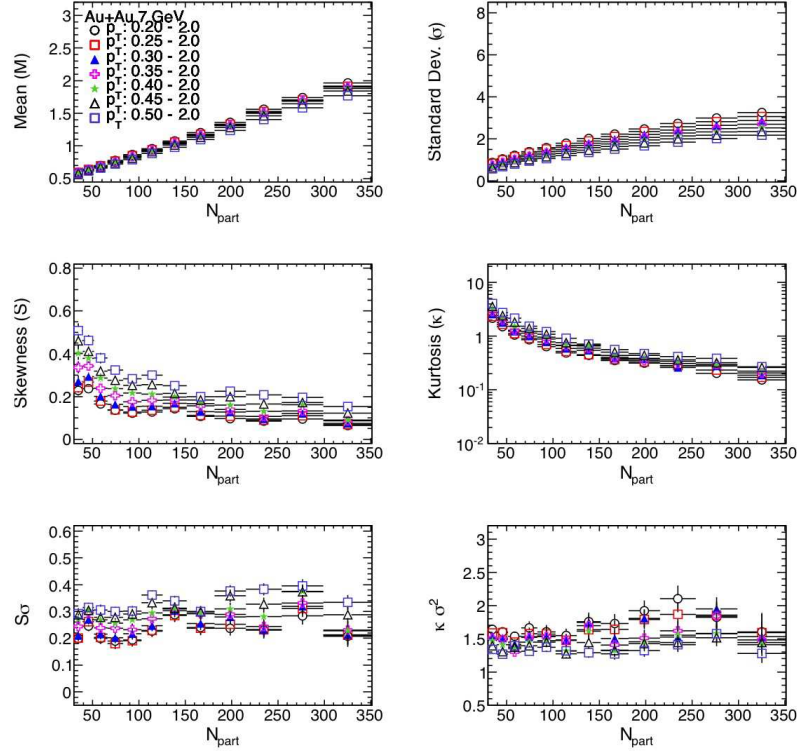


Figure 3.17. Moments and their product for net-charge distributions reconstructed in different p_T bins as a function of N_{part} .

selection study is carried for all other energies as well and it is found that the effect is significant particularly for product of moments.

η and ϕ dependence

In this subsection the effect of choosing different ϕ and η window on net-charge higher moments is demonstrated at $\sqrt{s_{NN}} = 200$ GeV. For this study HIJING event generator with decay option 'ON' is used to generate the events.

Fig. 3.18 shows the various moments of most central bin (0-5%) as a function of different ϕ acceptance selection. For this study, two cases have been studied:

- tracks within $\Delta\eta < 1.0$

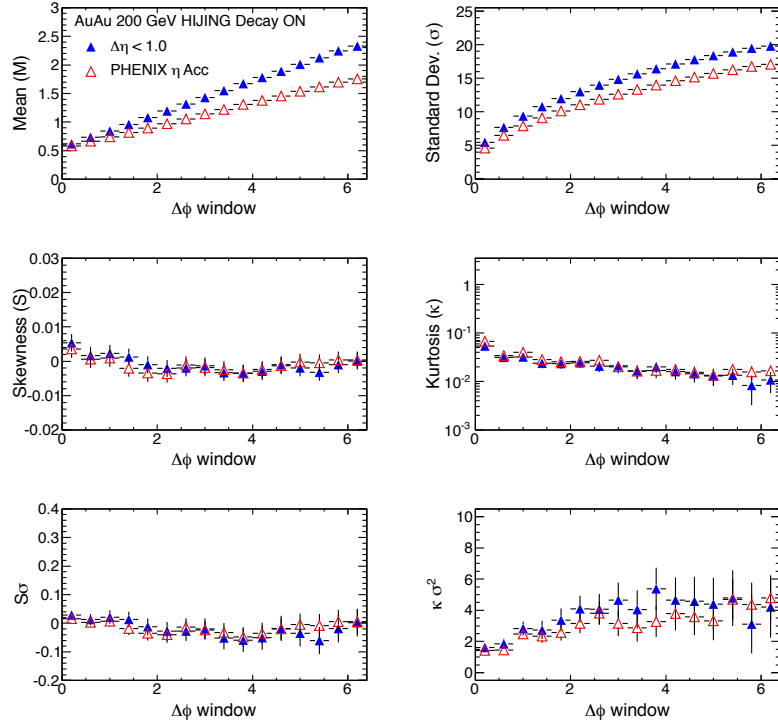


Figure 3.18. Acceptance dependence of various moments of net-charge for the most central bins (0-5%) for Au+Au 200 GeV HIJING events. The solid triangles (blue) are for tracks within $\Delta\eta < 1.0$ and the open triangles (red) are for tracks within PHENIX acceptance in η .

- tracks within PHENIX η acceptance ($\Delta\eta < 0.7$)

The ϕ -window of 0.2 radian has been used for this study. The first $\Delta\phi$ is 0.2 radian and then the window width have been increased by 0.2 and studied up to $\Delta\phi = 2\pi$. As shown in Fig. 3.18, mean and σ are dependent on $\Delta\phi$, but S and κ have weak dependence. The $\kappa\sigma^2$ depends on $\Delta\phi$ up to certain $\Delta\phi$ value but afterwards it does not change. Similar trends have been observed for tracks within PHENIX acceptance at other energies also.

Fig. 3.19 shows various moments for most central bin (0-5%) as a function of different η -acceptance. For this purpose also two cases have been studied:

- tracks within full ϕ acceptance ($\Delta\phi < 2\pi$)

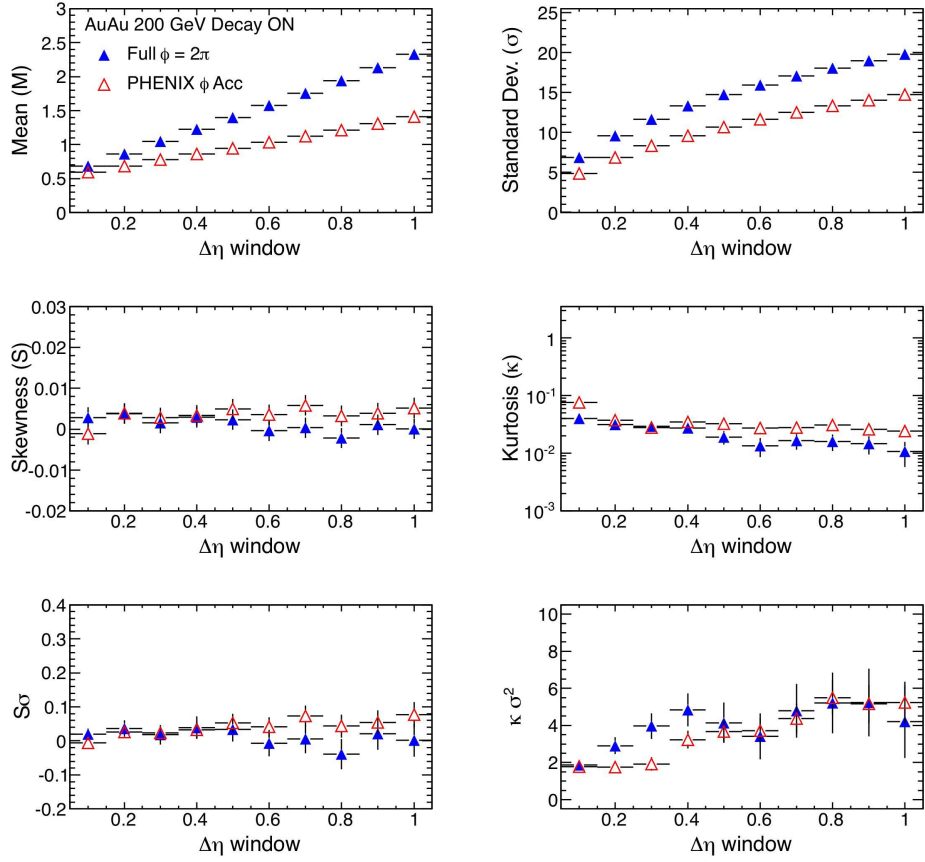


Figure 3.19. Various moments of net-charge distributions for the most central bins (0-5%) for Au+Au collisions at $\sqrt{s_{NN}} = 200$ GeV HIJING events in different η selection windows. The solid triangles (blue) are tracks within $\Delta\phi < 2\pi$ and the open triangles (red) are tracks within PHENIX acceptance in ϕ .

- tracks within PHENIX ϕ acceptance ($\pi/2 + \pi/2$).

The η -window of 0.1 has been used for this study. The M and σ have η -dependence but the S and κ have small effect. Similar behaviour has been reflected in $S\sigma$ and $\kappa\sigma^2$ values. There is η -dependence up to certain η -acceptance after lets say $\Delta\eta > 0.6$, the values do not change much. Similar behaviour has been observed, if we accept the tracks which are within PHENIX ϕ -acceptance only.

3.9.3 Effect of events Z_{vertex} selection on various moments

The effect of Z_{vertex} selection on various moments have been studied. For this study we have used Z_{vertex} cut $< \pm 10$ and ± 30 cm to check if the various moments get affected by taking tighter vertex cut on PHENIX data. Figs. [3.20-3.21] show the centrality dependence of various moments for both the mentioned Z_{vertex} cut for 27 GeV as an example. It is observed that the Z_{vertex} don't have much effect on moments and their products. Therefore, $Z_{vertex} < \pm 30$ is used in our analysis for all energies to increase the event statistics.

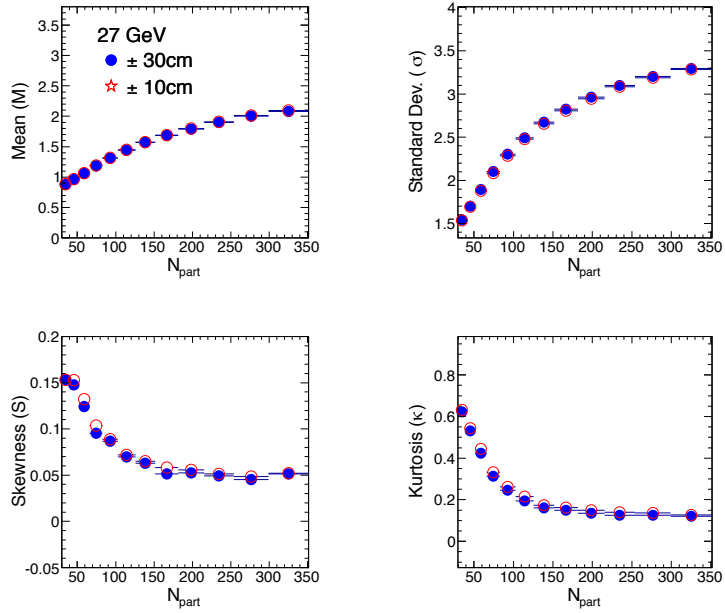


Figure 3.20. Centrality dependence of various moments of net-charge for Au+Au collisions at $\sqrt{s_{NN}} = 27$ GeV for different Z_{vertex} cuts.

3.9.4 Resonance decay effect on the various moments

In order to study the resonance decay effects on the various moments, we have used HIJING event generator, version 1.37. For this study, HIJING is used with default

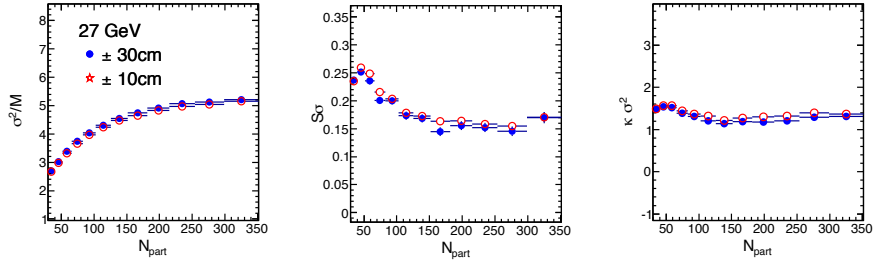


Figure 3.21. Centrality dependence of product of moments ($S\sigma$ and $\kappa\sigma^2$) of net-charge for Au+Au collisions at different collision energies for different Z_{vertex} cuts.

settings with jet suppression “ON” and resonance decay “ON (OFF)” for decayed (no-decay) case. The accepted tracks within PHENIX η and ϕ acceptance with same p_T ($0.3 < p_T < 2.0$ GeV/c) as used in real data analysis. To remove the auto correlation of tracks, the centrality from the HIJING events are calculated using the particles which are within BBC acceptance ($-3.9 < \eta < 3.0$ and $3.0 < \eta < 3.9$) with full azimuthal acceptance.

For each centrality bin (0-5%, 5-10%,...) 0.5 M events are generated for 200 GeV. The difference of the total “+ve” and “-ve” particles are calculated in event-by-event basis to get the net-charge distributions.

Figs. 3.22 show the centrality dependence of various moments of net-charge distributions for both with and without resonance decay options for 200 GeV HIJING events. From the Fig. 3.22, all moments (M , S and κ) except the σ values are similar for both resonance decay and no-decay cases. In case of $S\sigma$ the difference is small although $\kappa\sigma^2$ values get affected by the resonance decay contributions within PHENIX acceptance.

3.9.5 Effect of PC3 and EMC track matching

In order to study the effect of selected tracks which are both in PC3 and EMC, all the tracks which have $PC3sd\phi$ and $PC3sdz$ are within 2.5σ are accepted for our analysis. Apart from that, we have used another track selection cut by matching the same PC3

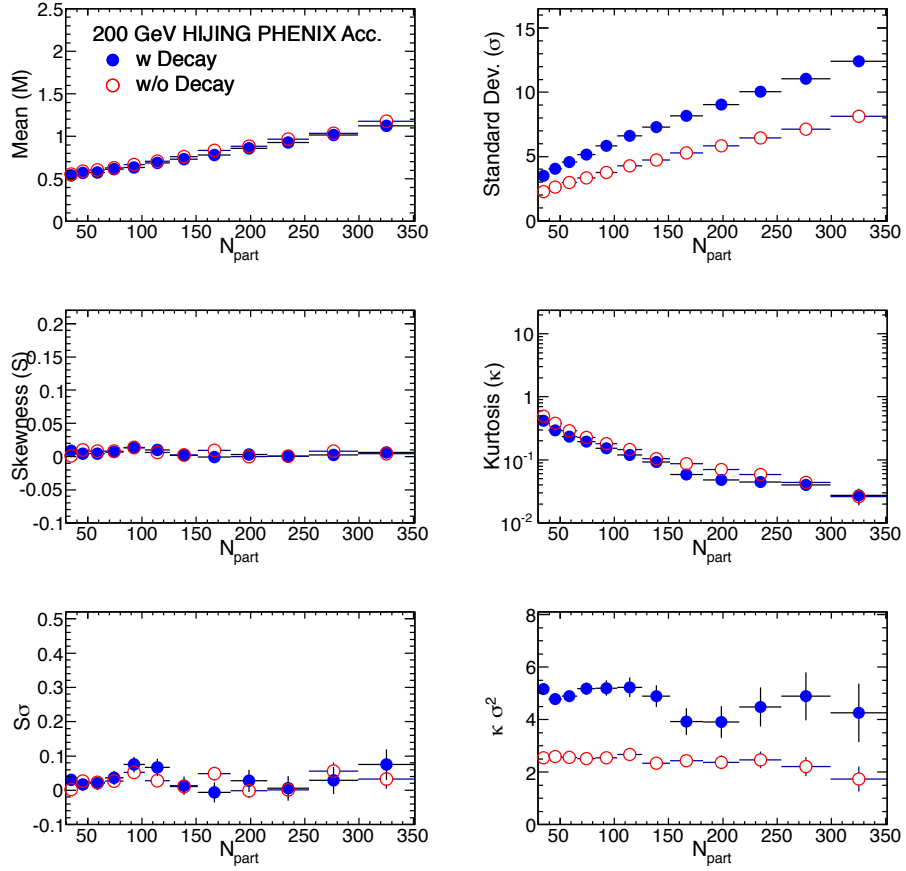


Figure 3.22. Centrality dependence of various moments of net-charge for Au+Au collisions at $\sqrt{s_{NN}} = 200$ GeV using HIJING event generator. Solid symbols are for with resonance decay option “ON” and open symbols are for “NO” decay option.

track with EMC. The PC3 matched tracks should have $EMCs d\phi$ and $EMCs dz$ within 3.0σ .

Fig. 3.23 shows $S\sigma$ and $\kappa\sigma^2$ for different energies (7, 39, 62.4 and 200 GeV) with and without PC3-EMC matching as an example. This study shows a weak dependence of PC3-EMC matching for our observables.

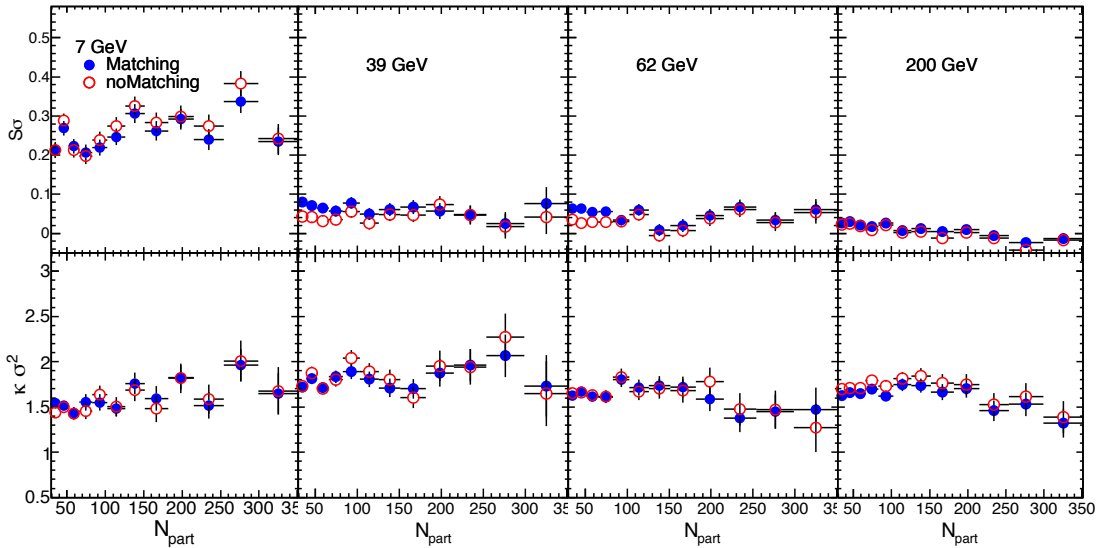


Figure 3.23. The centrality dependence of various moments of the net-charge distributions at various $\sqrt{s_{NN}}$ are shown with EMC-PC3 matching and without matching of selected tracks.

3.10 Reconstruction Efficiency Correction for Cumulants

Experimentally it is difficult to correct the various moments for the track reconstruction efficiencies on an event-by-event basis. Although, an alternative method of efficiency correction to conserved number fluctuations has been proposed in Ref. [91] which is also discussed previously. We have investigated the effects of detector effects and track reconstruction efficiencies on various moments. For this study, we have used the HIJING event generator.

The HIJING is used with default settings with jet suppression “ON” and resonance decay option “ON”. The moments of the generated tracks are obtained by accepting tracks which are within η and ϕ acceptance of PHENIX with p_T ($0.3 < p_T < 2.0$) GeV/c. The moments of the reconstructed tracks are obtained by passing the HIJING generated particles through PISA with the detector set-up for the corresponding Run

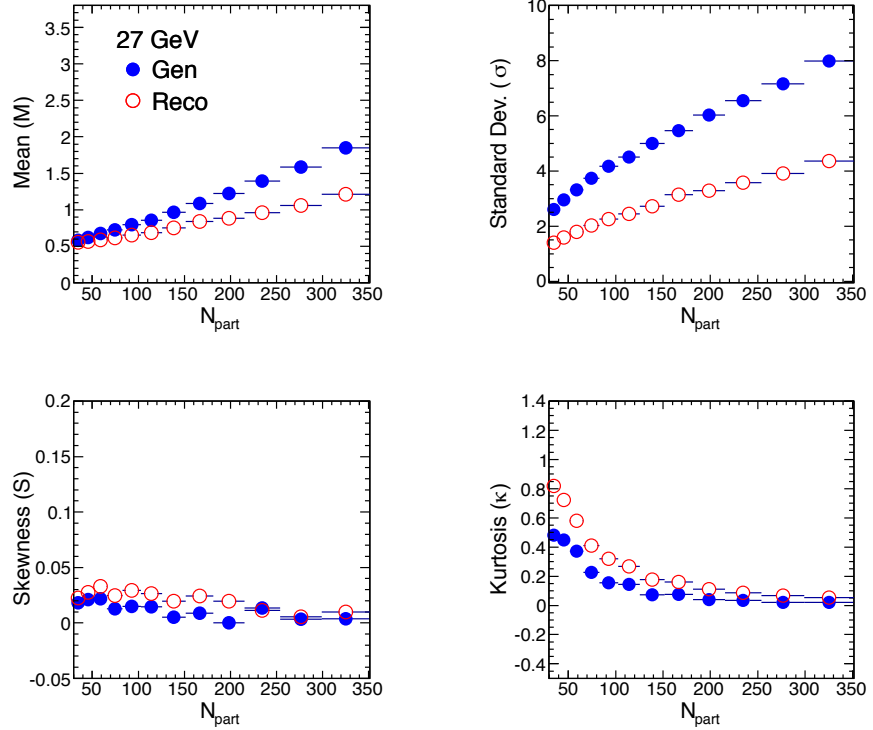


Figure 3.24. Centrality dependence of various moments of net-charge for Au+Au collisions at $\sqrt{s_{NN}} = 27$ GeV using HIJING event generator. Solid symbols are for generated tracks and open symbols are for reconstructed tracks after passing through PHENIX detector setup.

configuration. The simulated data are analyzed using the same event and track selection cuts as used for the real data. Same analysis procedure is followed for reconstructed, simulated and the real data.

Figs. 3.24 and 3.25 show the centrality dependence of various moments of net-charge distributions for generated (solid) and reconstructed (open) tracks for 27 GeV HIJING data for an example. From Fig. 3.24, it is evident that M , σ , S and κ have different values but have similar behavior for generated and reconstructed tracks as a function of N_{part} . Although, $\frac{\sigma^2}{M}$, $S\sigma$ and $\kappa\sigma^2$ have different behavior.

These effects mainly come into picture because of the detector efficiency for different data sets depending upon their energy, detectors setup and residual magnetic field inside the central arm tracking detectors. It emphasize the fact that experimentally

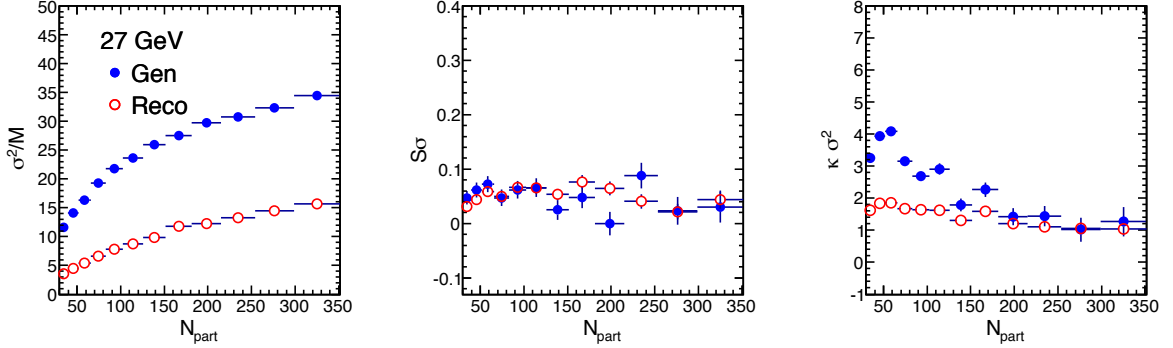


Figure 3.25. Centrality dependence on ratio and products of moments of net-charge for Au+Au collisions at $\sqrt{s_{NN}} = 27$ GeV using HIJING event generator. Solid symbols are for generated tracks and open symbols are for reconstructed tracks after passing through GEANT detector simulation.

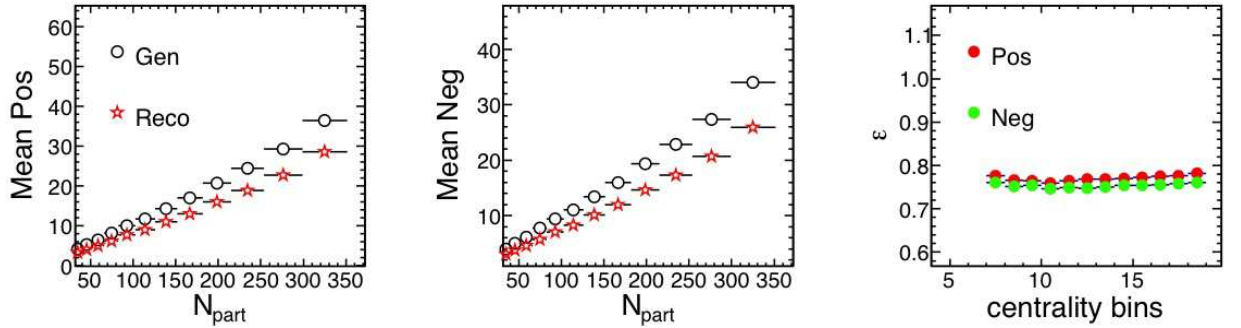


Figure 3.26. Mean of an event-by-event distribution for positive and negative hadrons obtained from HIJING at $\sqrt{s_{NN}} = 27$ GeV for different N_{part} is compared with reconstructed distributions from PISA setup (left two panels). The ratio of reconstructed to generated number of tracks i.e. efficiency (ϵ) is shown for both positive and negative hadrons (right-most panel).

obtained moments and their products should be corrected for finite counting efficiency before any physics conclusion is drawn.

Fig. 3.26 shows the number of positively and negatively charged hadrons (left two panel) for generated tracks in HIJING and reconstructed from PHENIX detector setup (PISA) and the rightmost panel shows the reconstruction efficiency in different centrality bin. It is observed that the efficiencies are almost same over the centrality and for different charged species.

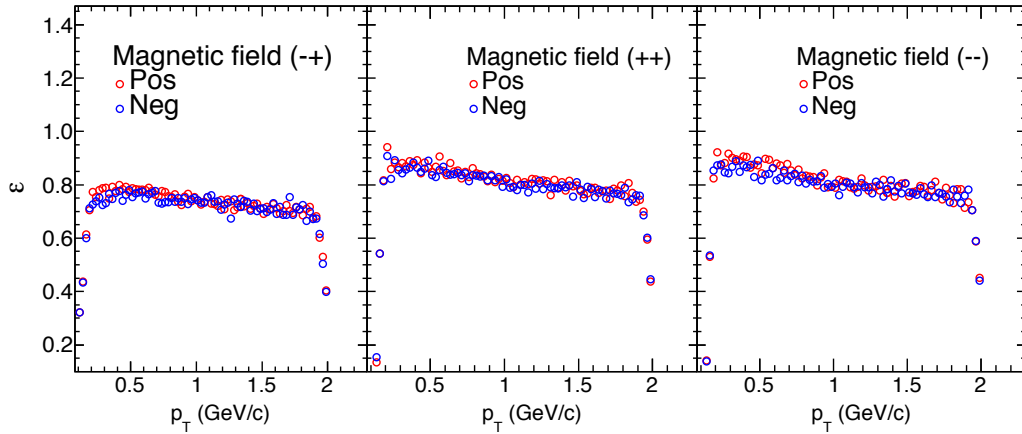


Figure 3.27. The p_T dependance of efficiency for different magnetic field settings in PHENIX for π^+ (Pos) and π^- (Neg) using EXODUS

In Fig. 3.27 the reconstruction efficiency is shown as a function of p_T for different PHENIX magnetic field settings. For this study we have used a single particle generator (EXODUS) to generate π^+ and π^- . These pions are reconstructed through PHENIX magnetic field (no detector medium) in order to study the effect of residual magnetic field only. It is found that the reconstruction efficiency depends on magnetic field configuration but it is almost same for π^+ and π^- within the p_T range used in our analysis. The reconstruction efficiencies are calculated using HIJING in the same magnetic field and detector configurations as is there in real data of PHENIX. The moments and their products are corrected for reconstruction efficiency as is discussed previously.

3.11 Analysis Results

The recent results for higher moments and their product measured by PHENIX detector at RHIC are shown in this section. The results shown here are corrected for reconstruction efficiencies derived for each data set. The statistical errors are calculated using Delta theorem as is discussed before. Also the systematics is included for

various effects as is shown in the previous section.

3.11.1 Centrality dependence of moments and their products as a function of N_{part}

Centrality dependence of M , σ , S and κ for the net-charge distributions are extracted for Au+Au collisions at all six colliding energies. In Fig. 3.28, the first four efficiency corrected moments of the net-charge distributions are plotted in terms of N_{part} for all colliding energies. The statistical errors dominate in most cases since the systematic errors are within symbol size. For all the colliding energies, we observe that the M and σ values increase from peripheral to central collisions, whereas S and κ values decrease with increasing N_{part} . The Mean of 19.6 GeV and 27 GeV shows non-monotonic behavior with centrality and energy. It may be corrected if efficiency corrections are applied for each PHENIX arm individually for positive and negative charge particles, which is not considered in the present work. Although it will have a small effect on the results for product of moments.

The centrality dependence of the moments can be understood by the central limit theorem (CLT), which assumes that each of the collisions is a collection of a finite number of identical, independent emission sources. According to CLT the dependence of the moments on the number of participating nucleons is given as follows:

$$\begin{aligned} M &\propto \langle N_{part} \rangle, \\ \sigma &\propto \sqrt{\langle N_{part} \rangle}, \\ S &\propto \frac{1}{\sqrt{\langle N_{part} \rangle}}, \\ \kappa &\propto \frac{1}{\langle N_{part} \rangle}. \end{aligned} \tag{3.32}$$

Under this assumption, N_{part} can be considered a proxy for the volume of the

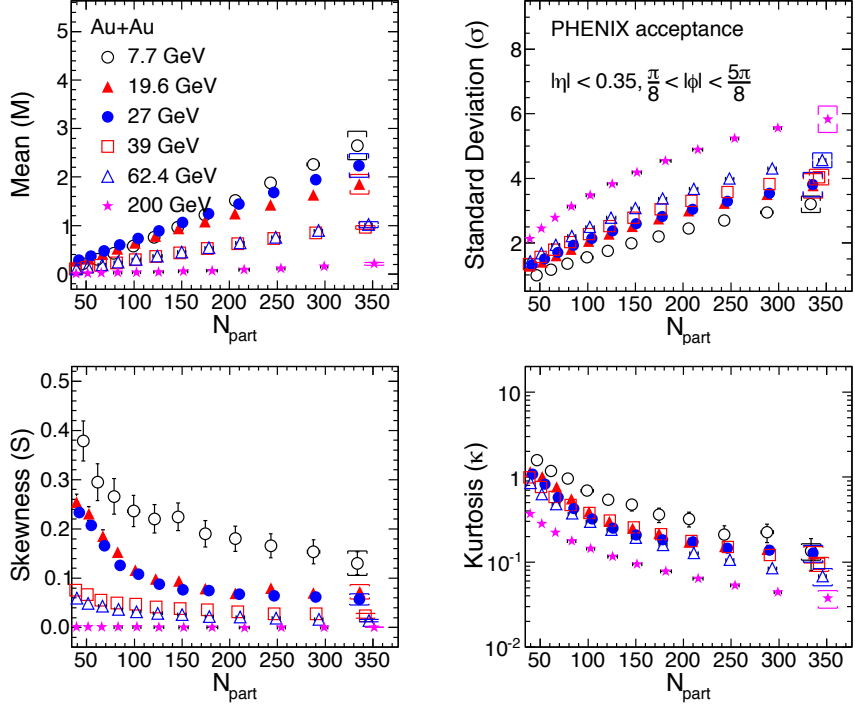


Figure 3.28. The efficiency corrected centrality dependency of various moments, such as M , σ , S and κ are plotted for different energies from $\sqrt{s_{NN}}=7.7$ to 200 GeV.

colliding system at a given centrality. Thus, the centrality dependence of the moments at a given energy follows the general expectations from of CLT, indicating that the moments depend on the system volume. This is one of the reasons to construct different combinations of moments, which removes the volume dependences.

Fig. 3.29 shows the efficiency corrected $\frac{\sigma^2}{M}$, $S\sigma$ and $\kappa\sigma^2$ as a function of centrality for different $\sqrt{s_{NN}}$. All three are observed to be almost independent of N_{part} or system size. It is in agreement with the fact that product of moments are independent of volume of the system as the volume term is shown to cancel while constructing $\frac{\sigma^2}{M}$, $S\sigma$ and $\kappa\sigma^2$ according to theoretical calculations [122].

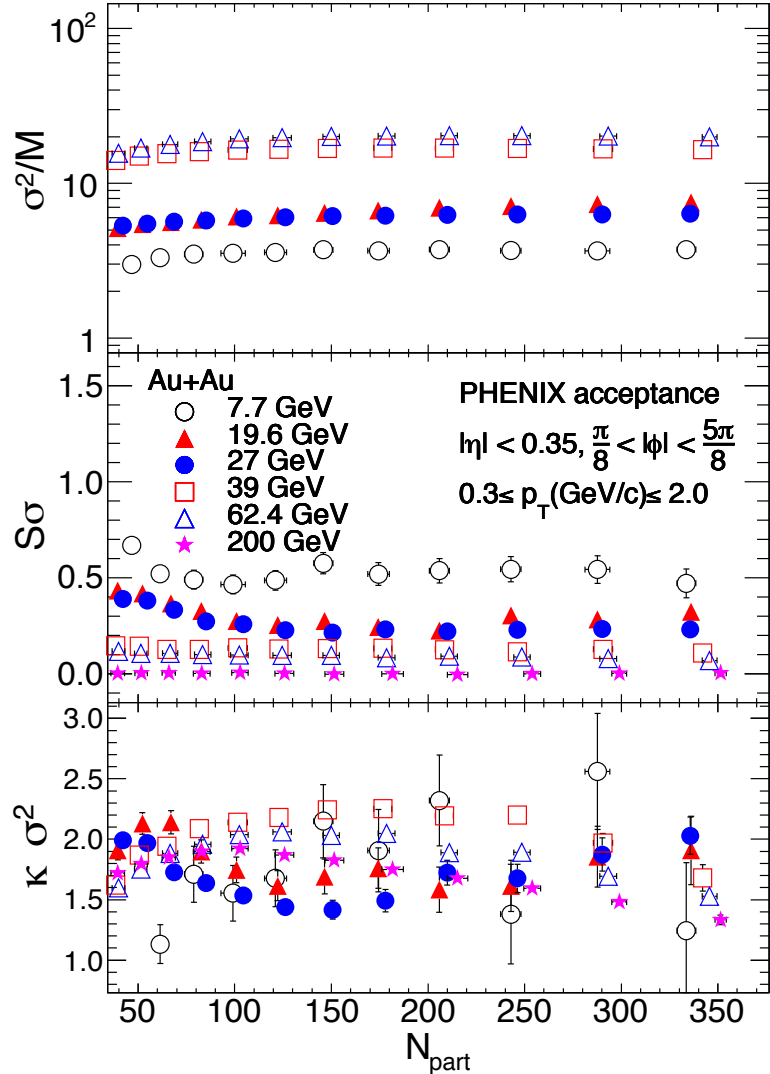


Figure 3.29. The efficiency corrected centrality dependence of $\frac{\sigma^2}{M}$, $S\sigma$ and $\kappa\sigma^2$ is plotted for different energies from $\sqrt{s_{NN}}=7.7$ to 200 GeV.

3.11.2 Energy dependence for Product of Moments

Fig. 3.30 shows the beam-energy dependence of efficiency corrected $\frac{\sigma^2}{M}$, $S\sigma$ and $\kappa\sigma^2$ for 0 – 5% centrality bin. Both the statistical and systematic errors are plotted. Also, results are compared with more realistic Hadron Resonance Gas (HRG) Model with in the PHENIX acceptance [117]. HRG is compared with the experimental data as a

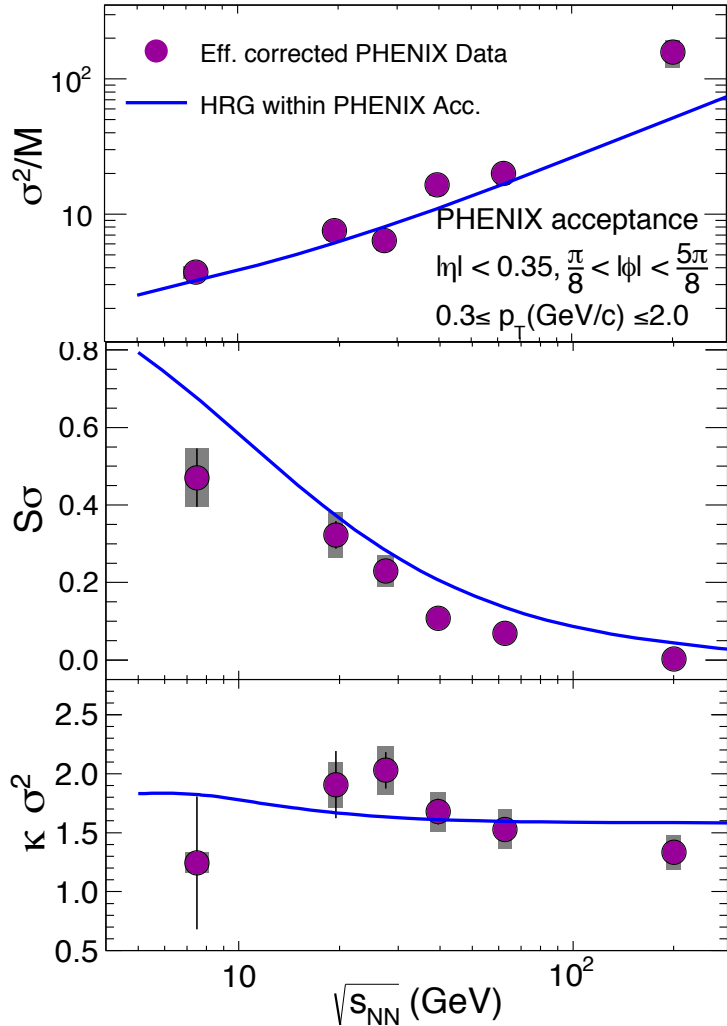


Figure 3.30. The beam energy dependency of $\frac{\sigma^2}{M}$, $S\sigma$ and $\kappa\sigma^2$ are plotted for 0–5% central collisions. The blue line represents HRG model predictions. The vertical lines represent the statistical error bar and box represent systematic error.

baseline for the fluctuations of critical origin. The values of $\frac{\sigma^2}{M}$ are observed to increase with increasing beam energy. The middle panel of Fig. 3.30 show the values of $S\sigma$, which are close to zero for $\sqrt{s_{NN}}=200$ GeV and increase with decreasing beam energy. The bottom panel of the Fig. 3.30 shows $\kappa\sigma^2$ as a function of beam energy. The values of $\kappa\sigma^2$ as a function of beam energy show almost no energy dependence for central collision within the statistical errors, excluding at $\sqrt{s_{NN}}=19.6$ GeV and 27 GeV. The

non-monotonic behavior with energy and higher values of $\kappa\sigma^2$ as compared to HRG predictions are found. Also $\kappa\sigma^2$ at these two energies is above the expectations from HIJING and UrQMD within PHENIX acceptance (as is discussed earlier in this chapter) which makes these energies interesting to explore. The non-monotonic behavior of $\kappa\sigma^2$ has been observed by net-proton fluctuation results by STAR experiment near the same energies [57] but their net-charge fluctuation results [59] suffer with large uncertainties to conclude about the location of critical point.

These two energies need to be explored with higher statistics of events at other energies around 19.6 GeV and 27 GeV for the confirmation of non-monotonic behaviour. In PHENIX, proper implementation of efficiency corrections need to be done, for example, arm-wise efficiency corrections for negative and positive hadrons, to conclude about the position of QCD critical point.

Chapter 4

Conserved Number Fluctuations in Ideal Hadron Resonance Gas Model

Measurement of the moments of distribution for conserved quantities like net-baryon, net-charge and net-strangeness number for systems undergoing strong interactions as in high energy heavy-ion collisions, have provided rich physics insights [122–131]. The most crucial realization is that the product of moments of the conserved number distributions are measurable experimentally and can be linked to susceptibilities (χ) computed in Quantum Chromodynamic (QCD) based calculations [123, 126]. For example, $S\sigma = \chi^{(3)}/\chi^{(2)}$ and $\kappa\sigma^2 = \chi^{(4)}/\chi^{(2)}$, where σ is the standard deviation, S is the skewness, κ is the kurtosis of the measured conserved number distribution, $\chi^{(n)}$ are the n^{th} order theoretically calculated susceptibilities associated with these conserved numbers. Such a connection between theory and high energy heavy-ion collision experiment has led to furthering our understanding about the freeze-out conditions [124, 125]. Thus, providing us the details of quark-hadron transition [123, 129] and plays a crucial role for the search of possible QCD critical point in the QCD phase diagram [126]. In all such physics cases there is a need to establish a reference point for the measurements. Computing these quantities within the framework of a hadron resonance gas (HRG) model [132] provides us a reference for both experimental data and QCD based calculations [133].

The experimental measurements have their own limitations. They are usually available for a fraction of the total kinematic phase space, due to the finite detector ge-

ometries and can detect only certain species out of the produced particles. For example, measurements related to net-baryon number distribution is restricted by the kinematic range in p_T where their identification is possible. In addition, baryons like neutron are not commonly measured in most of the high energy heavy-ion collision experiments. While for the net-charge number distribution, the limitation is usually in kinematic range available in η and the details of how contribution from different charge states and resonances are dealt with in the measurements. The kinematic acceptance in a typical high energy heavy-ion collision experiment like STAR [58] and PHENIX [60] at the Relativistic Heavy-Ion Collider facility (RHIC) for net-charge multiplicity distributions are: $|\eta| < 0.5$, $0.2 < p_T < 2.0$ GeV/ c and $|\eta| < 0.35$, $0.3 < p_T < 1.0$ GeV/ c , respectively. While for net-baryon number and net-strangeness related studies carried out in the STAR experiment within $|\eta| < 0.5$, is through the measurement of net-protons and net-kaons in the range of $0.4 < p_T < 0.8$ GeV/ c and $0.2 < p_T < 2.0$ GeV/ c , respectively [58, 126].

The main goal of the present work is to demonstrate the use of HRG model (discussed in next section), the effect of the above experimental limitations on the physics observables $\chi^{(3)}/\chi^{(2)}$ and $\chi^{(4)}/\chi^{(2)}$. Our model based study clearly indicates that the value of the observables related to net-charge and net-strangeness strongly depends on the experimental kinematic and charge state acceptances. Where charge state could be electric charge (Q) = 1 or higher for net-charge measurements and strangeness number (S) = 1 or higher for net-strangeness measurements. In contrast, the net-baryon number studies are found to be minimally affected by these experimental limitations. In the present work, we have not considered the initial baryon distribution due to the participant number fluctuations in the heavy-ion collisions on the results for net-baryon fluctuations [134]. Another important effect that could influence the values of the higher moments of the net-charge, net-strangeness and net-baryon number distributions in limited acceptance, are the conservation laws related to charge, strangeness and baryon number.

This chapter is organized as follows. In Section 4.1, we will discuss the HRG model used in this study. In Section 4.2, the results for the observable $\chi^{(3)}/\chi^{(2)}$ and $\chi^{(4)}/\chi^{(2)}$ are presented for different kinematic acceptances, charge states, effect of collective flow of particle in the system and the resonance decay contributions. We also provide a table listing the values of these observable for typical experimental conditions as encountered in STAR & PHENIX experiments at RHIC facility and ALICE experiment at the Large Hadron Collider (LHC) Facility. Finally in Section 4.3, we summarize our findings and mention the implications of this work to the current experimental measurements in high energy heavy-ion collisions.

4.1 Hadron Resonance Gas Model

In the HRG model, we include all the relevant degrees of freedom of the confined, strongly interacting matter and also implicitly take into account the interactions that result in resonance formation [122]. It is well known that the fireball created in heavy ion collision does not remain static, rather expands both in longitudinal and transverse directions until freeze out occurs. However, to keep the model simple, we first consider a static homogeneous fireball and flow effects are included subsequently.

In heavy ion collision, no conserved number fluctuation would be seen in measurements with full phase space coverage as B , Q and S are strictly conserved. However, since most of the experiments cover only limited phase space, the part of the fireball accessible to the measurements may resemble with the Grand Canonical Ensemble (GCE) where energy (momentum), charge and number are not conserved locally. In general, the magnitude of multiplicity fluctuations and correlations in limited phase space crucially depends on the choice of the statistical ensemble that imposes different conservation laws [135, 136]. Since no extensive quantities like energy, momentum and charge are needed to be locally conserved in GCE, the particles following Maxwell-Boltzmann distribution are assumed to be uncorrelated and fluctuations are expected to follow Poisson

statistics even in the limited phase space when quantum effects are ignored. In case of particles following Bose-Einstein or Fermi-Dirac distributions, within finite phase space, Poisson statistics is not expected to be obeyed and hence the deviations from Poisson limit can be studied.

In the ambit of GCE framework, the logarithm of the partition function (Z) in the HRG model is given as:

$$\ln Z(T, V, \mu) = \sum_B \ln Z_i(T, V, \mu_i) + \sum_M \ln Z_i(T, V, \mu_i) , \quad (4.1)$$

where,

$$\ln Z_i(T, V, \mu_i) = \pm \frac{V g_i}{2\pi^2} \int d^3 p \ln \{1 \pm \exp[(\mu_i - E)/T]\}, \quad (4.2)$$

here T is the temperature, V is the volume of the system, μ_i is the chemical potential, E is the energy and g_i is the degeneracy factor of the i^{th} particle. The total chemical potential is given by $\mu_i = B_i \mu_B + Q_i \mu_Q + S_i \mu_S$, where B_i , Q_i and S_i are the baryon, electric charge and strangeness number of the i^{th} particle, with corresponding chemical potentials μ_B , μ_Q and μ_S , respectively. The '+' and '-' signs are for baryons and mesons respectively. The thermodynamic pressure (P) can then be deduced for the limit of large volume as

$$\frac{P}{T^4} = \frac{1}{V T^3} \ln Z_i = \pm \frac{g_i}{2\pi^2 T^3} \int d^3 p \ln \{1 \pm \exp[(\mu_i - E)/T]\}. \quad (4.3)$$

The n^{th} order generalized susceptibility for baryons can be expressed as [122]:

$$\chi_{x, baryon}^{(n)} = \frac{X^n}{V T^3} \int d^3 p \sum_{k=0}^{\infty} (-1)^k (k+1)^{n-1} \exp \left\{ \frac{-(k+1)E}{T} \right\} \exp \left\{ \frac{(k+1)\mu}{T} \right\}, \quad (4.4)$$

and for mesons,

$$\chi_{x,meson}^{(n)} = \frac{X^n}{VT^3} \int d^3p \sum_{k=0}^{\infty} (k+1)^{n-1} \exp\left\{\frac{-(k+1)E}{T}\right\} \exp\left\{\frac{(k+1)\mu}{T}\right\}. \quad (4.5)$$

The factor X represents either B , Q or S of the i^{th} particle depending on whether the computed χ_x represents baryon or electric charge or strangeness susceptibility.

For a particle of mass m in static fireball with p_T , η and ϕ (azimuthal angle), the volume element (d^3p) and energy (E) can be written as $d^3p = p_T m_T \cosh \eta dp_T d\eta d\phi$ and $E = m_T \cosh \eta$, where $m_T = \sqrt{p_T^2 + m^2}$, respectively. The experimental acceptances can be incorporated by considering the appropriate integration ranges in η , p_T , ϕ and charge states by considering the values of $|X|$. The total generalized susceptibilities will then be the sum of the contribution from baryons and mesons as, $\chi_x^{(n)} = \sum \chi_{x,baryon}^{(n)} + \sum \chi_{x,meson}^{(n)}$.

In order to make the connection with the experiments, the beam energy dependence of μ and T parameters of the HRG model needs to be provided. These are extracted from a statistical thermal model description of measured particle yields in the experiment at various $\sqrt{s_{NN}}$ [137–139]. This is followed by the parameterization of μ_B and T as a function of $\sqrt{s_{NN}}$ [137]. The μ_B dependence of the temperature is given as $T(\mu_B) = a - b\mu_B^2 - c\mu_B^4$ with $a = 0.166 \pm 0.002$ GeV, $b = 0.139 \pm 0.016$ GeV $^{-1}$, and $c = 0.053 \pm 0.021$ GeV $^{-3}$. The $\sqrt{s_{NN}}$ dependence of μ_B is given as $\mu_B(\sqrt{s_{NN}}) = \frac{d}{1+e^{\sqrt{s_{NN}}}}$ with $d = (1.308 \pm 0.028)$ GeV and $e = (0.273 \pm 0.008)$ GeV $^{-1}$. Further the ratio of baryon to strangeness chemical potential is parameterized as $\frac{\mu_S}{\mu_B} \simeq 0.164 + 0.018\sqrt{s_{NN}}$. We have seen that the value of T and μ_B obtained using the yields extrapolated to 4π or from mid-rapidity measurements, have little impact on our study. However in order to study the rapidity (η) dependence, the μ_B parameterizations $\mu_B = 0.024 + 0.011\eta^2$ and $\mu_B = 0.237 + 0.011\eta^2$ at $\sqrt{s_{NN}} = 200$ [140] and $\sqrt{s_{NN}} = 17.3$ [141], respectively are used in the present work.

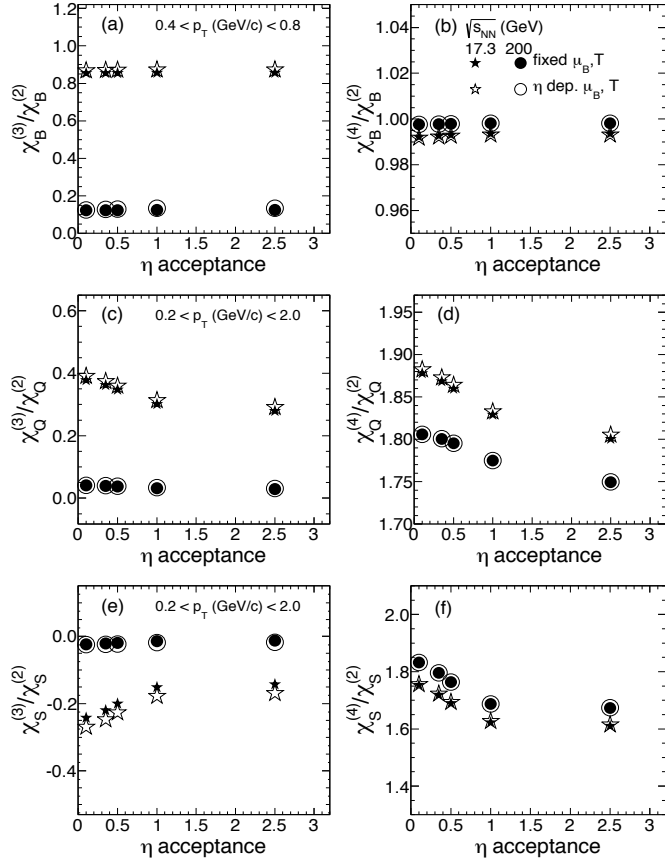


Figure 4.1. The η acceptance dependence of $\chi_x^{(3)}/\chi_x^{(2)}$ and $\chi_x^{(4)}/\chi_x^{(2)}$ for two different beam energies. In panel (a) and (b) x = net-baryon B , (c) and (d) x = net-charge Q , and in (e) and (f) x = net-strangeness S . The results with (labeled “dep.”) and without (labeled “fixed”) the η dependence of chemical freeze-out parameters μ_B and T are shown.

4.2 Results

4.2.1 Effect of Kinematic acceptance in η and p_T

Fig. 4.1 shows the variation of $\chi_x^{(3)}/\chi_x^{(2)}$ and $\chi_x^{(4)}/\chi_x^{(2)}$ as a function of η acceptance for $\sqrt{s_{NN}} = 200$ GeV and $\sqrt{s_{NN}} = 17.3$ GeV. Where x stands for either net-baryon (B) (Fig. 4.1 (a) and (b)), net-charge (Q) (Fig. 4.1 (c) and (d)), or net-strangeness (S) (Fig. 4.1 (e) and (f)). For each beam energy we show the effect of considering HRG parameters (μ, T) fixed to parameterization based on mid-rapidity data and also

a parameterization based on the η dependent value of (μ, T) . The difference between the two cases are small. For the subsequent studies we only present results for different $\sqrt{s_{\text{NN}}}$ using the parameterization of the chemical freeze-out parameters based on the measurement of particle yields at mid-rapidity. A clear dependence of $\chi_x^{(3)}/\chi_x^{(2)}$ and $\chi_x^{(4)}/\chi_x^{(2)}$ on η acceptance is observed for net-charge (Fig. 4.1 (c) and (d)) and net-strangeness (Fig. 4.1 (e) and (f)). The $\chi_B^{(3)}/\chi_B^{(2)}$ and $\chi_B^{(4)}/\chi_B^{(2)}$ values (Fig. 4.1 (a) and (b)) are found to be independent of η acceptance for the two beam energies studied. This underscores the need to carefully consider η acceptance effects when comparing HRG model results to experimental data, especially for net-charge and net-strangeness fluctuation measurements.

Fig. 4.2 shows the variation of $\chi_x^{(3)}/\chi_x^{(2)}$ and $\chi_x^{(4)}/\chi_x^{(2)}$ as a function of $\sqrt{s_{\text{NN}}}$ for various p_T acceptances. The choice of these particular values of p_T acceptance ranges are motivated by the existence of corresponding experimental measurements [58, 60, 126]. It is observed that $\chi_x^{(3)}/\chi_x^{(2)}$ and $\chi_x^{(4)}/\chi_x^{(2)}$ have a clear p_T acceptance dependence at all beam energies for net-charge (Fig. 4.2 (c) and (d)) and net-strangeness (Fig. 4.2 (e) and (f)). However the p_T acceptance dependence for net-baryon (Fig. 4.2 (a) and (b)) is substantially weaker. Hence the p_T acceptance study also emphasizes the need to consider the actual experimental acceptance for model comparisons for fluctuation measurement. At the same time both the kinematic acceptance studies in η and p_T show that net-baryon fluctuation measures are least affected.

4.2.2 Effect of Conserved charge states

Fig. 4.3 shows the variation of $\chi_x^{(3)}/\chi_x^{(2)}$ and $\chi_x^{(4)}/\chi_x^{(2)}$ as a function of $\sqrt{s_{\text{NN}}}$ for various types of baryons (Fig. 4.3 (a) and (b)), values of electric charge states, $|Q| = 1$ and $|Q| > 1$ (Fig. 4.3 (c) and (d)), and values of strangeness number, $|S| = 1$ and $|S| > 1$ (Fig. 4.3 (e) and (f)). In each of the cases the observables are compared to the respective values with inclusion of all conserved charge states and baryons. We find a

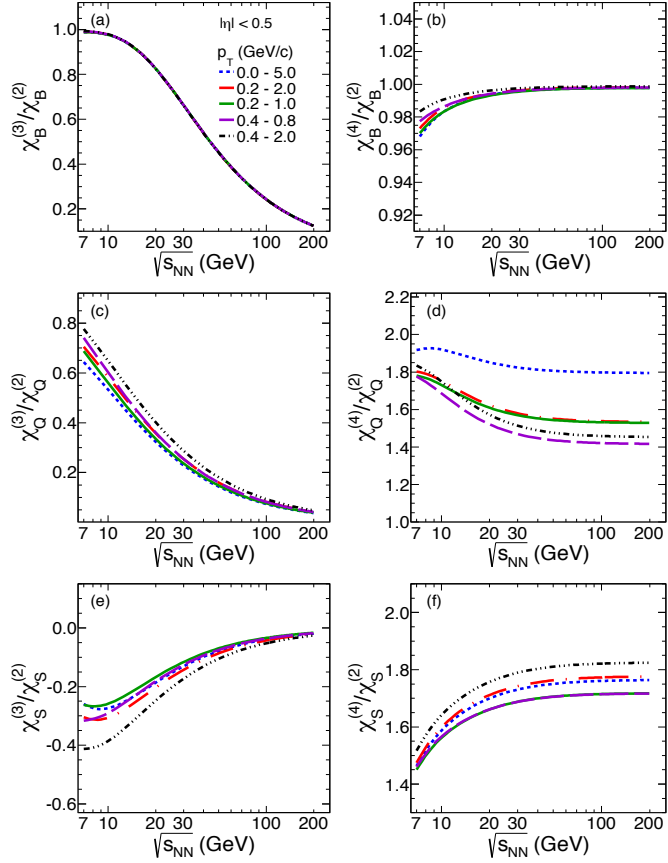


Figure 4.2. The p_T acceptance dependence of $\chi_x^{(3)}/\chi_x^{(2)}$ and $\chi_x^{(4)}/\chi_x^{(2)}$ for different $\sqrt{s_{NN}}$. Where x stands for either net-baryon (B) (panels (a) and (b)), net-charge (Q) (panels (c) and (d)), and net-strangeness (S) (panels (e) and (f)).

strong dependence of the $\chi_Q^{(3)}/\chi_Q^{(2)}$ and $\chi_Q^{(4)}/\chi_Q^{(2)}$ on whether we consider $|Q| = 1$ or $|Q| > 1$, both differing from the case of inclusion of all charge states. Same is the situation for net-strangeness. On the other hand, successive inclusion of different baryons, starting with protons seems to have some small effect on the $\chi_B^{(3)}/\chi_B^{(2)}$ and $\chi_B^{(4)}/\chi_B^{(2)}$ values only at the lower beam energies. The absence of baryons with $|B| > 1$ makes the net-baryon number fluctuations more advantageous and are less prone to kinematic acceptances as compared to the net-charge or net-strangeness fluctuation measurements.

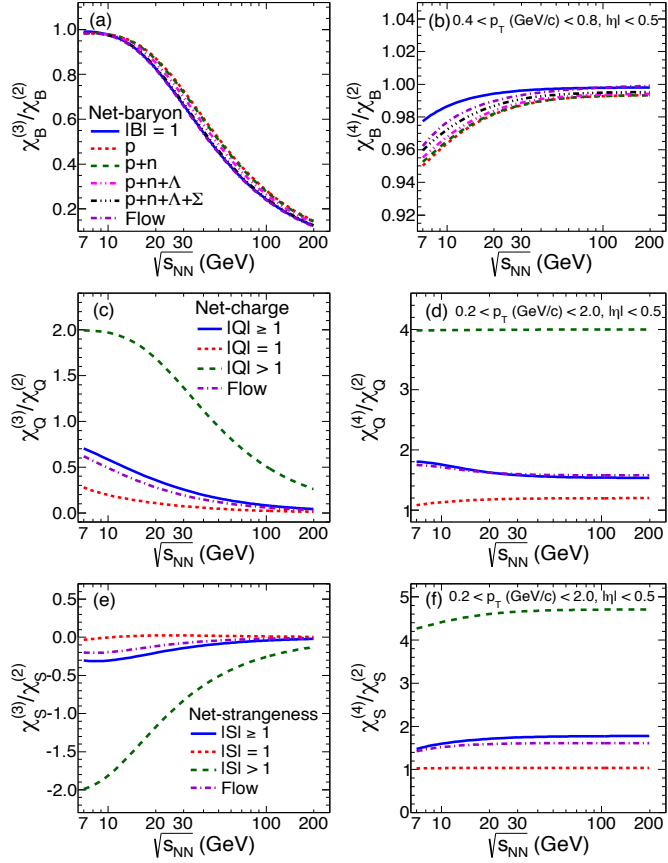


Figure 4.3. Variation of $\chi_x^{(3)}/\chi_x^{(2)}$ and $\chi_x^{(4)}/\chi_x^{(2)}$ for net-baryon (B), net-charge (Q), and net-strangeness (S) as a function of collision energy ($\sqrt{s_{NN}}$). The results are shown for different baryons (panels (a) and (b)), electric charge states (panels (c) and (d)) and strangeness number (panels (e) and (f)) considered in the calculation.

4.2.3 Effect of flow

To study the effect of flow on the ratios of susceptibilities in the HRG model, we now consider an expanding fireball with four velocity,

$$u^\mu = \cosh y_T (\cosh y_0, \tanh y_T, 0, \sinh y_0), \quad (4.6)$$

where y_0 is the longitudinal and $y_T = \tanh^{-1}(\beta_r)$ is the transverse rapidity of the fireball flowing with radial flow velocity β_r . The four-momentum of the particle can be

expressed as:

$$p^\mu = (m_T \cosh \eta, p_T \cos \phi, p_T \sin \phi, m_T \sinh \eta). \quad (4.7)$$

In the presence of flow, the logarithm of the partition function for i^{th} particle having four momentum p^μ can be expressed as:

$$\ln Z_i(T, V, \mu_i) = \pm \frac{g_i}{(2\pi)^3} \int_{\sigma} d^3 p \frac{p^\mu d\sigma_\mu}{p^0} \ln \{1 \pm \exp[(\mu_i - p^\mu u_\mu)/T]\}, \quad (4.8)$$

where σ represents the space-time surface whose surface elements can be represented by four vector denoted by $d\sigma_\mu$ and p^0 is the energy of the particle. Assuming instantaneous freeze out (at time τ_f) in the radial direction r , $p^\mu d\sigma_\mu$ simplifies as [142]:

$$p^\mu d\sigma_\mu = \tau_f r dr d\phi dy_0 m_T \cosh(\eta - y_0). \quad (4.9)$$

The limit of integration for r varies from 0 to R_f (freeze out radius), ϕ from 0 to 2π , y_0 from $-y_0^{min}$ to y_0^{max} ($= \ln(\sqrt{s_{NN}}/m_p)$, where m_p is mass of proton). The other variables p_T and η vary within the experimental acceptances. Note that we recover eq. 4.2 for the case of static fireball ($y_T = y_0 = 0$) where $p^\mu u_\mu = E$ and the integral over $(p^\mu d\sigma_\mu)/p^0$ becomes proportional to $4\pi V$. Therefore, for a constant β_r , the flow effect on the susceptibilities can be incorporated by replacing $d^3 p$ integral in Eq. 4.4 and Eq. 4.5 with $p_T dp_T d\eta d\phi dy_0 m_T \cosh(\eta - y_0)$ and the energy E in the exponentials by the invariant $p^\mu u_\mu$ as defined above. Further, under the assumption that the flow velocity β_r is independent of radial position, the r integration turns out to be a constant which is proportional to the volume at freeze-out. To simplicity of the calculations, we have used a constant β_r (same as β_s of ref [143]). Fig. 4.3 also shows the effect of flow (longitudinal + transverse) on the ratios of susceptibilities as a function of collision energy. It is noticed that the ratios of the susceptibilities like $\chi_x^{(4)}/\chi_x^{(2)}$ for net-baryon, net-charge and net-strangeness are affected by less than (2 - 4)% as compared to the corresponding static values represented by solid blue line.

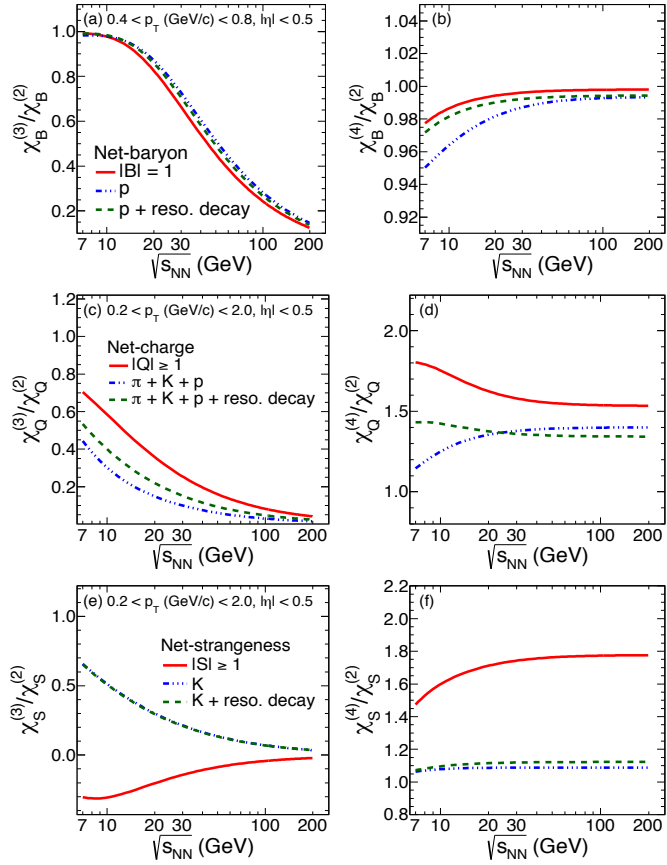


Figure 4.4. The variation of $\chi_x^{(3)}/\chi_x^{(2)}$ and $\chi_x^{(4)}/\chi_x^{(2)}$ for net-baryon (B), net-charge (Q), and net-strangeness (S) with different beam energies ($\sqrt{s_{NN}}$) with and without resonance decay daughter particle acceptance effects.

4.2.4 Effect of Resonance decay

The generalized susceptibility of n^{th} order can be written as,

$$\chi^n = \sum_p \chi_p^n + \sum_R \epsilon_R^n \chi_R^n, \quad (4.10)$$

where χ_p^n and χ_R^n are the contributions to the n^{th} order susceptibility due to primordial and resonance yields respectively. The factor ϵ_R^n is an event averaged efficiency at which resonance R contributes to the generalized susceptibility. Note that $\epsilon_R^n = 1$ when all the decay particles are fully accepted and $\epsilon_R^n < 1$ due to finite detector and kinematic

acceptances. Consider the example of the resonance Δ^{++} which decays into p and π^+ with branching ratio b . Using a toy Monte Carlo simulation, we generate Δ^{++} distribution with Poisson statistics and build the charge distributions both for Δ^{++} and the decay particles (proton and pion together) within the experimental acceptances. The Poisson distribution for Δ^{++} is a reasonable assumption as momentum distributions of resonance particles can be approximated by the classical Maxwell-Boltzmann function due to their large masses, although it is not true for their decay products. Therefore, we estimate the efficiency ϵ^n by taking the ratios of the n^{th} order cumulant of the charge distributions after and before decays. Similar procedures are adopted for other resonances to estimate the average efficiencies ϵ_R^n depending on the charge, strangeness and baryon number as appropriate.

Table 4.1. Ratios of the moments for net-charge within $|\eta| < 0.5$, and $0.2 < p_T < 2.0$ GeV/c .

$\sqrt{s_{NN}}$ (GeV)	$\chi_Q^{(3)}/\chi_Q^{(2)}$	$\chi_Q^{(4)}/\chi_Q^{(2)}$
5	0.526	1.413
7.7	0.414	1.430
11.5	0.321	1.407
15	0.265	1.390
19.6	0.215	1.375
27	0.165	1.361
39	0.119	1.352
62.4	0.077	1.346
130	0.038	1.343
200	0.025	1.342
2760	0.002	1.341

The results of $\chi_x^{(3)}/\chi_x^{(2)}$ and $\chi_x^{(4)}/\chi_x^{(2)}$ with and without considering the effect of resonance daughter particle acceptances are shown in Fig. 4.4. In Fig. 4.4(a) and (b), three cases for $\chi_B^{(3)}/\chi_B^{(2)}$ and $\chi_B^{(4)}/\chi_B^{(2)}$ are shown within a realistic acceptance of $|\eta| < 0.5$ and $0.4 < p_T < 0.8$ GeV/c . The results for all baryons without any resonance decay (solid red curve), results for protons without any resonance decay contribution (dotted blue curve) and results for protons with resonance decay (dashed green curve).

Similarly Fig. 4.4(c) and (d) shows $\chi_Q^{(3)}/\chi_Q^{(2)}$ and $\chi_Q^{(4)}/\chi_Q^{(2)}$ respectively, for all charges without resonance decay (solid red curve), pions, kaons and protons without resonance decay (dotted blue curve) and pions, kaons and protons with resonance decay (dashed green curve). Fig. 4.4(e) and (f), shows the results for all strangeness without resonance decay (solid red curve), kaons without resonance decay (dotted blue curve) and kaons with resonance decay (dashed green curve).

Table 4.2. Ratios of the moments for net-charge within $|\eta| < 0.35$, and $0.3 < p_T < 1.0$ GeV/c :

$\sqrt{s_{NN}}$ (GeV)	$\chi_Q^{(3)}/\chi_Q^{(2)}$	$\chi_Q^{(4)}/\chi_Q^{(2)}$
5	0.432	1.231
7.7	0.332	1.245
11.5	0.256	1.233
15	0.212	1.222
19.6	0.172	1.213
27	0.132	1.205
39	0.095	1.199
62.4	0.062	1.196
130	0.031	1.194
200	0.020	1.193
2760	0.001	1.193

It may be mentioned here that the efficiency ϵ_R^n is an event averaged quantity and will have fluctuations on an event by event basis. Although ϵ_R^n has inherent fluctuation, a rough estimate shows that it's effect on the ratio of $\chi_Q^{(4)}/\chi_Q^{(2)}$ is $\sim 2\%$ which we have ignored in the present study. Therefore, the present estimate of the effect of resonance decays on the ratio of susceptibilities are approximate. Nevertheless, it brings out the importance of resonance decays which certainly affect all the ratios. With these assumption, the effects of resonance decay due to finite experimental acceptances are large for net-charge and net-strangeness as compared to net-baryons. The acceptance used in this study are modest and are close to the present experimental acceptances. Through our work we have emphasized the need for considering experimental acceptances of various kinds in model, such as HRG, before they are considered to provide

Table 4.3. Ratios of the moments for net-kaon within $|\eta| < 0.5$, and $0.2 < p_T < 2.0$ GeV/c .

$\sqrt{s_{NN}}$ (GeV)	$\chi_K^{(3)}/\chi_K^{(2)}$	$\chi_K^{(4)}/\chi_K^{(2)}$
5	0.726	1.058
7.7	0.560	1.090
11.5	0.428	1.108
15	0.353	1.115
19.6	0.288	1.120
27	0.222	1.123
39	0.162	1.125
62.4	0.107	1.127
130	0.054	1.128
200	0.035	1.128
2760	0.003	1.128

the baseline to experimental measurements for drawing physics conclusions. Hence in the Tables 4.1, 4.2, 4.3 and 4.4 we provide values of $\chi_x^{(3)}/\chi_x^{(2)}$ and $\chi_x^{(4)}/\chi_x^{(2)}$ for typical ongoing experimental acceptances. The values quoted in the tables are for static fireball and without including the resonance decay products. The $\chi_Q^{(3)}/\chi_Q^{(2)}$ and $\chi_Q^{(4)}/\chi_Q^{(2)}$ values are provided for two typical acceptances $|\eta| < 0.5$, $0.2 < p_T < 2.0$ GeV/c and $|\eta| < 0.35$, $0.3 < p_T < 1.0$ GeV/c (Table 4.1 and Table 4.2). The $\chi_S^{(3)}/\chi_S^{(2)}$ and $\chi_S^{(4)}/\chi_S^{(2)}$ are provided for a typical acceptance of $|\eta| < 0.5$, $0.2 < p_T < 2.0$ GeV/c (Table 4.3). The $\chi_B^{(3)}/\chi_B^{(2)}$ and $\chi_B^{(4)}/\chi_B^{(2)}$ are provided for a typical acceptance of $|\eta| < 0.5$, $0.4 < p_T < 0.8$ GeV/c (Table 4.4).

4.3 Summary

In summary, using a hadron resonance gas model we have studied the effect of limited experimental acceptance on observables like n^{th} order susceptibilities $\chi_x^{(n)}$, associated with conserved quantities like net-charge ($x = Q$), net-strangeness ($x = S$) and net-baryon number ($x = B$). The various order susceptibilities which can also be calculated

Table 4.4. Ratios of the moments for net-proton within $|\eta| < 0.5$, and $0.4 < p_T < 0.8$ GeV/c .

$\sqrt{s_{NN}}$ (GeV)	$\chi_p^{(3)}/\chi_p^{(2)}$	$\chi_p^{(4)}/\chi_p^{(2)}$
5	0.981	0.961
7.7	0.987	0.975
11.5	0.962	0.984
15	0.920	0.988
19.6	0.851	0.991
27	0.737	0.993
39	0.586	0.995
62.4	0.407	0.996
130	0.210	0.997
200	0.139	0.997
2760	0.010	0.997

in QCD based models are related to the moments (σ , S and κ) of the corresponding measured conserved number distributions. These observables have been widely used to understand the freeze-out conditions in heavy-ion collisions and various aspects of the phase structure of the QCD phase diagram. Present work demonstrates the importance of considering experimental acceptances of different kinds before measurements are compared to theoretical calculations, specifically in the use of HRG model as a baseline for such fluctuation based study. We observe finite kinematic acceptances in η and p_T have a strong effect on the $\chi_Q^{(n)}$ and $\chi_S^{(n)}$ values. These susceptibilities are also very sensitive to the accepted electric charge states and strangeness states in the experiment. However, the effect of flow is less than (2 - 4)% on the ratios of susceptibilities for net-baryon, net-charge and net-strangeness and the improvements can be done in implementation of the radial dependent transverse flow velocities. In addition, in this model we find that, the $\chi_Q^{(n)}$ and $\chi_S^{(n)}$ values depend on the experimental acceptance of the decay daughters from various resonances produced in high energy heavy-ion collisions. Within this model and the kinematic regions used in our study, we find that the dependence on acceptance and resonance decays are stronger for both net-charge and net-strangeness compared to that of net-baryons.

Chapter 5

Unfolding of event-by-event net-charge distributions in heavy-ion collision

It has been discussed earlier that higher moments of the event-by-event distribution of conserved quantities like net-charge, net-baryon number and net-strangeness in heavy-ion collisions have been found to be useful observable to characterize the system formed in the collisions [126]. Higher moments have been shown to be related to the correlation length [56] and susceptibilities [99, 100] of the system and hence can be used to look for signals of phase transition and critical point [55, 127, 131]. They have also been shown to be useful for studying the bulk QCD thermodynamics at high temperature [123]. Specifically, proposals have been made to extract the freeze-out properties of the system using higher moments of net-charge and net-baryon number distributions, in a way very similar to that done using the particle yields and ratios [122, 124, 129].

All the experimental measurements are susceptible to the effects such as the finite acceptance, finite efficiency of counting the number of particles produced in the collisions and other background effects [101]. It is almost impossible to know some of these quantities for each event so as to correct for the effects in an event-by-event distribution. Hence most of the experimentally measured event-by-event distributions are presented without these corrections [102–104, 126]. These corrections are carried out on an average level for reporting the yields of the produced particles (typically the first moment of the

multiplicity distributions) [101]. Comparison of uncorrected experimental event-by-event distributions to theoretical calculations needs to be done carefully. For example, using the corrected mean multiplicities to explain the uncorrected measured event-by-event distributions could lead to different conclusions [106, 128].

Judicious construction of event-by-event observables have been proposed to cancel out detector effects to first order [107–109, 112]. However, while making these constructs, one may sometimes lose the ability to compare them to the theoretically calculated quantities in order to extract meaningful physical insights. That introduces additional complexities which makes it difficult for a proper physical interpretation of the observable. As an example, the moments of the multiplicity distribution of conserved quantities can be shown to be proportional to correlation length (ξ) of the system. The variances ($\sigma^2 \equiv \langle (\Delta N)^2 \rangle$; $\Delta N = N - M$; M is the mean) of these distributions are related to ξ as $\sigma^2 \sim \xi^2$, skewness ($S = \langle (\Delta N)^3 \rangle / \sigma^3$) goes as $\xi^{4.5}$ and kurtosis ($\kappa = [\langle (\Delta N)^4 \rangle / \sigma^4] - 3$) goes as ξ^7 [56]. Their products such as $\kappa\sigma^2$ are related to the ratio of fourth order ($\chi^{(4)}$) to second order ($\chi^{(2)}$) susceptibilities [99, 100]. Where $\chi^{(2)} = \frac{\langle (\Delta N)^2 \rangle}{VT}$, V is the volume, and ΔN could be the net-baryon number or net-charge number. In order to cancel out the acceptance and efficiency effects to first order for these observables, constructs such as normalized factorial moments (defined later) can be made. The factorial moments of a particular order however become complicated function of lower order moments. Thereby making their interpretation difficult in terms of physical observables such as ξ or χ calculated in a standard theory.

Here we give a simple example to illustrate our point of view. Let N represent the produced multiplicity and n being the actually measured multiplicity in an experiment. We parametrize the detector response in the experiment by a binomial probability distribution function given by,

$$B(n : N, \epsilon) = \frac{N!}{n!(N-n)!} \epsilon^n (1-\epsilon)^{N-n}, \quad (5.1)$$

where ϵ is the particle counting efficiency.

We further consider that the produced multiplicity follows probability distribution function $P(N)$, and for measured distribution is $P(n)$. Then the mean of measured multiplicity distribution $\langle n \rangle$ can be related to the mean of the actually produced multiplicity distribution as,

$$\begin{aligned}\langle n \rangle &= \int n P(n) dn = \int n dn \int B(n | N) P(N) dN \\ &= \int P(N) dN \int B(n | N) n dn = \epsilon \int P(N) N dN = \epsilon \langle N \rangle.\end{aligned}\quad (5.2)$$

Similarly it can be shown that,

$$\langle n^2 \rangle = \epsilon(1 - \epsilon)\langle N \rangle + \epsilon^2\langle N^2 \rangle. \quad (5.3)$$

Now let us suppose that we can correct event-by-event particle counting efficiency, then the variance of the resultant measured distribution can be shown to be,

$$\sigma^2(n/\epsilon) = \frac{1 - \epsilon}{\epsilon}\langle N \rangle + \sigma^2(N) \quad (5.4)$$

We find that the variance of n/ϵ is not equal to the variance of N even though the mean of n/ϵ is equal to the mean of N . Similar derivations and conclusions can be done for higher order moments.

Alternatively, one can construct second order factorial moments such as

$$\frac{\langle n(n-1) \rangle}{\langle n \rangle^2} = \frac{\epsilon^2 \langle N(N-1) \rangle}{\epsilon^2 \langle N \rangle^2} = \frac{\langle N(N-1) \rangle}{\langle N \rangle^2}, \quad (5.5)$$

and the fourth order factorial moment as,

$$\frac{\langle n(n-1)(n-2)(n-3) \rangle}{\langle n \rangle^4} = \frac{\langle N(N-1)(N-2)(N-3) \rangle}{\langle N \rangle^4}. \quad (5.6)$$

These are found to be independent of efficiency effects. In these we also assume that ϵ does not vary event-by-event.

However, a closer look at these construct will reveal that:

$$\frac{\langle n(n-1) \rangle}{\langle n \rangle^2} = \frac{\sigma^2}{\langle n \rangle^2} - \frac{1}{\langle n \rangle} + 1 \quad (5.7)$$

and

$$\begin{aligned} \frac{\langle n(n-1)(n-2)(n-3) \rangle}{\langle n \rangle^4} = & 11 \frac{\sigma^2}{\langle n \rangle^4} + \frac{1}{\langle n \rangle^2} \\ & - 6S \frac{\sigma^3}{\langle n \rangle^4} - 18 \frac{\sigma^2}{\langle n \rangle^3} + \kappa \frac{\sigma^4}{\langle n \rangle^4} \\ & + 4S \frac{\sigma^3}{\langle n \rangle^3} - 3 \frac{\sigma^2}{\langle n \rangle^2} - 2 - \frac{6}{\langle n \rangle^3}. \end{aligned} \quad (5.8)$$

While trying to remove the detector effects we have arrived at constructs which loose the purity of moments or become involved functions of lower order moments. Thereby making it difficult to directly connect to physical observables such as susceptibilities or their ratios which can give important insight to the bulk properties of the system formed in heavy-ion collisions.

Keeping in view the importance of higher moments of multiplicity distributions to characterize the system formed in heavy-ion collisions, it is necessary to have a proper way to compare the measurements and theory calculations. At the same time ensure that experimental artifacts like acceptance and particle counting efficiency are removed. In this paper, we propose an approach based on unfolding of the measured (actually measured in experiments) multiplicity distribution to get back the true (actually produced in the collisions) distributions produced in the collisions. Such a method seems

to work only if the detector response can be satisfactorily modeled and the statistics is large enough [117].

This chapter is organized as follows. In the next section we discuss the event generators used in this study. In section 3.2 we discuss method of unfolding. In section 3.3 we present the results for the moments of the net-charge distribution as a function of collision centrality (defined in terms of the number of participating nucleons, N_{part}). A brief discussion of the limitations of the approach is also presented. Finally we summarize our study in the last section.

5.1 Event generators

In this study we have used two event generators HIJING [63] (version 1.37) and THERMINATOR [118] (version 2.0). They provide the possibility of different probability distribution for charged particle multiplicity, to study our proposal. While HIJING distributions are based on the physics due to QCD inspired models for multiple jet production, the THERMINATOR distributions are based on systems in thermodynamical equilibrium. The further details of the models can be found in Ref. [63] for HIJING and in Ref. [118] for THERMINATOR. For HIJING the events were generated with default settings and jet quenching on, while for THERMINATOR the default settings were used. We only focus on the net-charge distributions within a realistic acceptance of the current experiments at RHIC, that is pseudorapidity range between $-0.5 < \eta < 0.5$, transverse momentum range between $0.2 < p_T < 2.0 \text{ GeV}/c$ with full azimuthal coverage. The analysis is carried out for 19.6 GeV Au+Au collisions using the events from HIJING model and 200 GeV Au+Au collisions using the events from the THERMINATOR model as a function of collision centrality. About 5 million events are produced for each centrality studied in both the event generators. We have checked that the conclusions from each model at other energies are similar to that presented in this chapter. Such a combination of model and beam energy is an arbitrary choice done to reflect

a wide range of kinematics and physics of particle production. The average charge particle multiplicity counting efficiency is taken to be 65% following the efficiency as a function of p_T available for charged pions in Ref. [101].

5.2 Bayes method for unfolding of distributions

The Bayes unfolding algorithm of RooUnfold package is used in general to remove the effects of measurement resolutions, systematic biases and detection efficiency to determine the true distributions [119]. The RooUnfoldBayes algorithm based on Bayes theorem uses the method described by D'Agostini in Ref. [120].

The procedure of Bayes unfolding can be explained by the causes C and effects E . In our study, *causes* correspond to the true multiplicity values and *effects* to the measured multiplicity values which are affected by the inefficiencies. If one observes $n(E)$ events with effect E due to several independent causes ($C_i, i = 1, 2, \dots, n_C$) then the expected number of events assignable to each of the causes is given by:

$$\hat{n}(C_i) = n(E)P(C_i|E) \quad (5.9)$$

where

$$P(C_i|E) = \frac{P(E|C_i)P(C_i)}{\sum_{l=1}^{n_c} P(E|C_l)P(C_l)} \quad (5.10)$$

Now if we observe that the outcome of a measurement has several possible effects $E_j (j = 1, 2, 3, \dots, n_E)$ for a given cause C_i then the expected number of events to be assigned to each of the causes and only due to the observed events can be calculated to each effect by:

$$\hat{n}(C_i) = \sum_{j=1}^{n_E} n(E_j)P(C_i|E_j). \quad (5.11)$$

$P(C_i|E_j)$ is the probability that different causes C_i were responsible for the observed effect E_j and is calculated by Bayes theorem as:

$$P(C_i|E_j) = \frac{P(E_j|C_i)P_0(C_i)}{\sum_{l=1}^{n_c} P(E_j|C_l)P_0(C_l)} \quad (5.12)$$

where $P_0(C_i)$ are the initial probabilities. If we take into account the inefficiency then the best estimate of the true number of events is given by,

$$\hat{n}(C_i) = \frac{1}{\epsilon_i} \sum_{j=1}^{n_E} n(E_j)P(C_i|E_j) \quad \epsilon_i \neq 0 \quad (5.13)$$

where ϵ_i is the efficiency of detecting the cause C_i in any of the possible effects. If $\epsilon_i = 0$ then $\hat{n}(C_i)$ is set to zero, since the experiment is not sensitive to the cause C_i .

The above equation can be written in terms of unfolding or response matrix M_{ij} as:

$$\hat{n}(C_i) = \sum_{j=1}^{n_E} M_{ij} n(E_j) \quad (5.14)$$

The response matrix is constructed by repeated application of Bayes theorem and the regularization is achieved by stopping the iterations before reaching the "true" inverse. Further details of the procedure can be found in [120].

For the present study, 5M Au+Au collision events are produced for each centrality bin at $\sqrt{s_{NN}} = 19.6$ GeV and 200 GeV using HIJING and THERMINATOR event generators respectively. With these events, the *true* distribution of net-charge ($\Delta N = N^+ - N^-$) is constructed on an event-by-event basis. The positive (N^+) and negative (N^-) charge particles are selected for each event with transverse momentum range between $0.2 < p_T < 2.0$ GeV/c and pseudorapidity range between $-0.5 < \eta < 0.5$ with full azimuthal coverage.

The individual *true* N^+ and N^- are smeared with a Gaussian function with the mean value corresponding to the average efficiency of 65% as obtained from the parametrization of the p_T dependent efficiency for charged pions from STAR experiment [101]. The width of the Gaussian distribution is taken as 10% of the mean.

The smeared N^+ and N^- distributions will be called as *measured* distributions. The measured net-charge distribution is then constructed with these *measured* N^+ and N^- distributions.

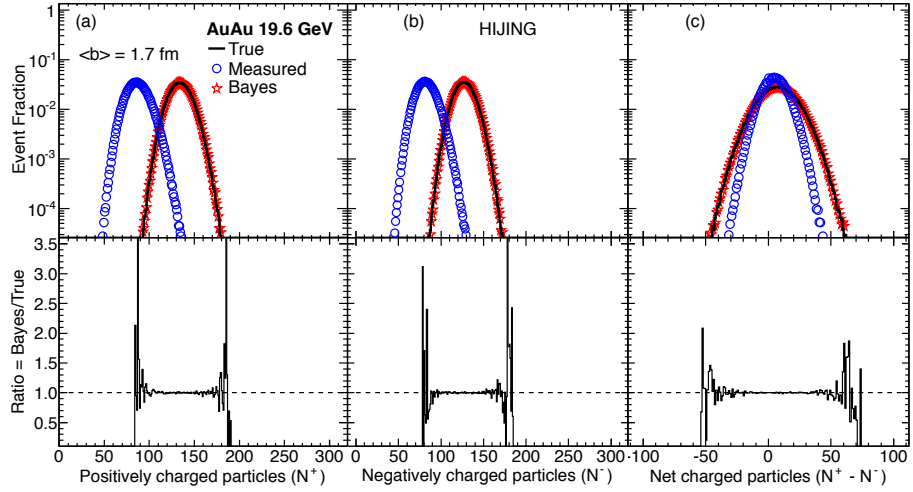


Figure 5.1. Top panel: Event-by-event distribution of positive, negative and net-charge (denoted as “True”, solid line) in Au+Au collisions for impact parameter $b = 1.7$ fm at $\sqrt{s_{NN}} = 19.6$ GeV from HIJING event generator. Also shown are the corresponding distributions after applying acceptance and efficiency effects as discussed in the text (denoted as “Measured”, open circles). The unfolded distributions are shown as red stars and denoted as “Bayes”. Bottom panel: Shows the ratio of the unfolded to the True distributions.

To construct the response matrix for each centrality, 2.5M events are used as *training true* distribution of net-charge and rest of the events are used as *training measured* (after smearing on an event-by-event basis) distribution. The events for *training true* and *training measured* are selected separately to construct the response matrix in order to avoid the effect of auto-correlation. It also uses the information of an event that is not measured out of true distributions and is counted towards the inefficiency while constructing the response matrix.

The measured distribution of net-charge from the remaining 2.5M events is unfolded with response matrix obtained from the training procedure using iterative Bayes theorem. The number of iterations is called the regularization parameter. The present

study uses the optimal value of 4 for the regularization. True, measured and unfolding are done for finer bins of each centrality and then combined to make 5% bin to eliminate the finite centrality bin-width effect. The moments of net-charge distributions are derived using cumulant method as described in [121] and are compared for true, measured and unfolded distributions.

5.3 Results and Discussions

Fig. 5.1 shows the true, measured and unfolded distributions for positive charge (panel a), negative charge (panel b) and net-charge (panel c) for most central events corresponding to an average impact parameter of 1.7 fm of Au+Au collisions from HIJING at $\sqrt{s_{NN}} = 19.6$ GeV on an event-by-event basis. The true distributions are shown as solid lines, measured distributions (subjected to particle counting efficiency) are shown as blue open circles and the unfolded distributions denoted as “Bayes” are shown as red star. For all the cases, the respective true distributions are reproduced from the measured distribution using the unfolding technique. The bottom panel of Fig.5.1 shows the ratio of unfolded to the true distributions corresponding to the same distributions as shown in the respective top panels of Fig.5.1.

The ratio is close to unity within the statistical errors, suggesting that the unfolding procedure is able to get back the true distribution from a measured distribution which is subjected to inefficiencies in particle counting. Similar conclusions are obtained for distributions for Au+Au collisions at $\sqrt{s_{NN}} = 200$ GeV from THERMINATOR.

The four moments M , σ , S and κ of the net-charge distributions in Au+Au collisions at $\sqrt{s_{NN}} = 19.6$ GeV from the constructed true, measured and unfolded distributions as a function of centrality (N_{part}) are shown in Fig. 5.2. The mean and standard deviation increases with N_{part} , while the skewness and kurtosis decreases with N_{part} . This is in accordance with the central limit theorem [126]. The mean and

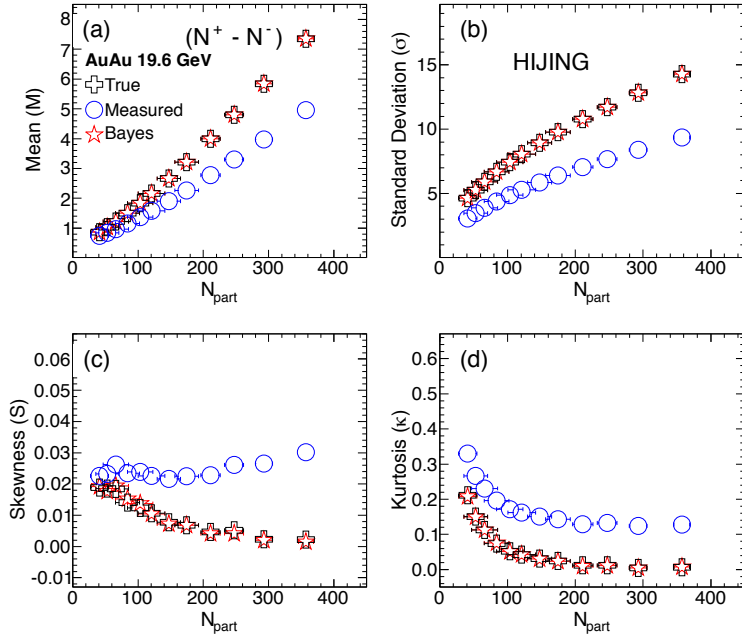


Figure 5.2. Mean, standard deviation, skewness and kurtosis of net-charge distribution in Au+Au collisions at $\sqrt{s_{\text{NN}}} = 19.6$ GeV from HIJING event generator. Results are shown for the True, measured and Bayes unfolded distributions as a function of N_{part} .

variance of the measured distribution are smaller compared to those of the true, as we have particle counting inefficiencies for the measured case. The unfolded moments are found to closely follow the corresponding values of their respective true distributions. This can be more clearly seen from the ratio plots in Fig. 5.3. The value of the ratio of unfolded to true distribution as a function of N_{part} is around unity for all the four moments studied. Thus the unfolding method followed in this work reproduces all the moments of true distribution from the measured distribution. Although not shown here, similar conclusions are obtained separately for the positive and negative charge particle multiplicity distributions.

The centrality dependence of ratio of moments (σ^2/M) and product of moments ($S\sigma$ and $\kappa\sigma^2$) are shown in Fig. 5.4. The importance of unfolding is clearly demonstrated by looking at the dependences of the ratio and product of moments on the N_{part} .

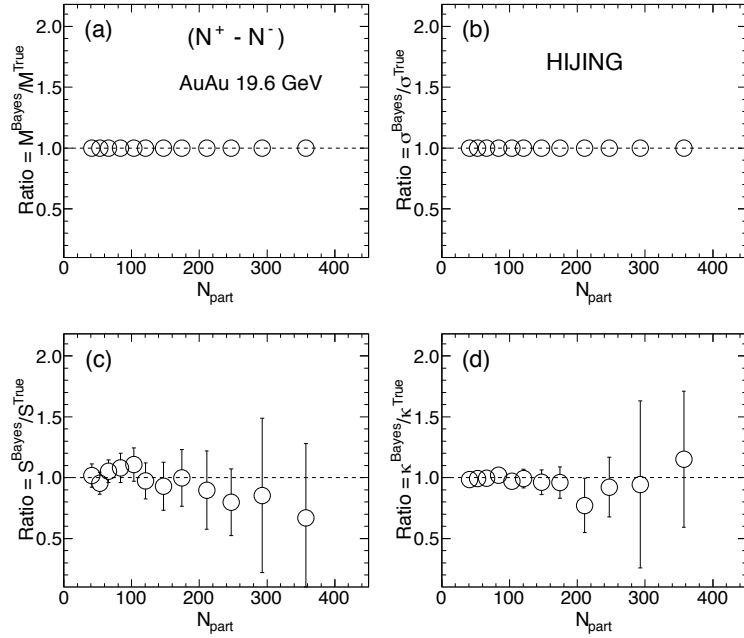


Figure 5.3. Ratio of the unfolded to the True net-charge distribution moments of Fig. 5.2 as a function of N_{part} .

While for the true distribution the product of moments decreases with N_{part} , those for measured actually has an opposite trend. Indicating any physics conclusions associated with variation of $S\sigma$ and $\kappa\sigma^2$ with N_{part} for net-charge distributions could be highly misleading. However, very nice agreement between true and unfolded distributions are observed. They are nicely consistent even for the product of higher moments ($S\sigma$ and $\kappa\sigma^2$) which are very sensitive to the shape of the distributions. Suggesting that the unfolded distributions are well reproduced as the true distributions by using Bayes unfolding algorithm.

In order to validate the applicability of unfolding algorithm for different physics processes, a thermal model based THERMINATOR event generator is also used. Fig. 5.5 shows the centrality dependence of various moments of net-charge distribution in Au+Au collisions at $\sqrt{s_{\text{NN}}} = 200$ GeV from the true, measured and unfolded distributions. The trends of the moments as a function of N_{part} is similar to that seen for

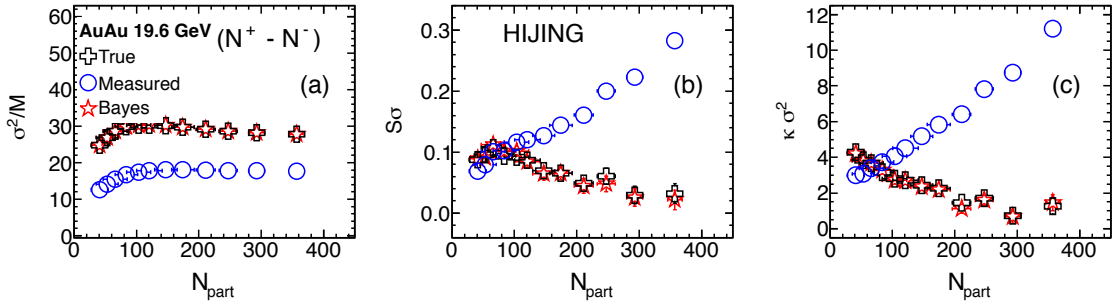


Figure 5.4. Ratio (panel a) and product of moments (panel (b) and (c)) of net-charge distributions in Au+Au collisions at $\sqrt{s_{\text{NN}}} = 19.6$ GeV from HIJING event generator. The results are for the True, measured and Bayes unfolded distributions as a function of N_{part} .

HIJING (Fig. 5.2), although the magnitude of the moments are different. All the four moments of the unfolded distributions are well reproduced as the true distributions.

Fig. 5.6 shows the σ^2/M , $S\sigma$ and $\kappa\sigma^2$ as a function of N_{part} of net-charge distributions from the true, measured and unfolded distributions. Here also, as was seen for the HIJING results (Fig. 5.4), the ratio and products of moments from unfolded distributions are reproduced as true distributions up to a good extent. This suggests that the method proposed, works equally well for parent distributions produced from very different particle production mechanisms as well as over a wide range of beam energies.

To study the effect of variation of efficiency on ratio and product of moments, the true distributions are smeared with a constant efficiency of 65% to obtain the measured distributions. Fig. 5.7 and Fig. 5.8 show the σ^2/M , $S\sigma$ and $\kappa\sigma^2$ as a function of N_{part} of net-charge distributions from the true, measured and unfolded distributions with constant efficiency in Au+Au collisions at $\sqrt{s_{\text{NN}}} = 19.6$ GeV and 200 GeV from HIJING and THERMINATOR event generators, respectively. Panel (a) of Fig. 5.7 and Fig. 5.8 shows similar effect as for event-by-event variation of efficiency (panel (a) of Fig. 5.4 and Fig. 5.6) on the σ^2/M of the measured distributions. The effect of constant efficiency on $S\sigma$ and $\kappa\sigma^2$ (panel (b) and (c) of Fig. 5.7 and Fig. 5.8) of measured distributions is

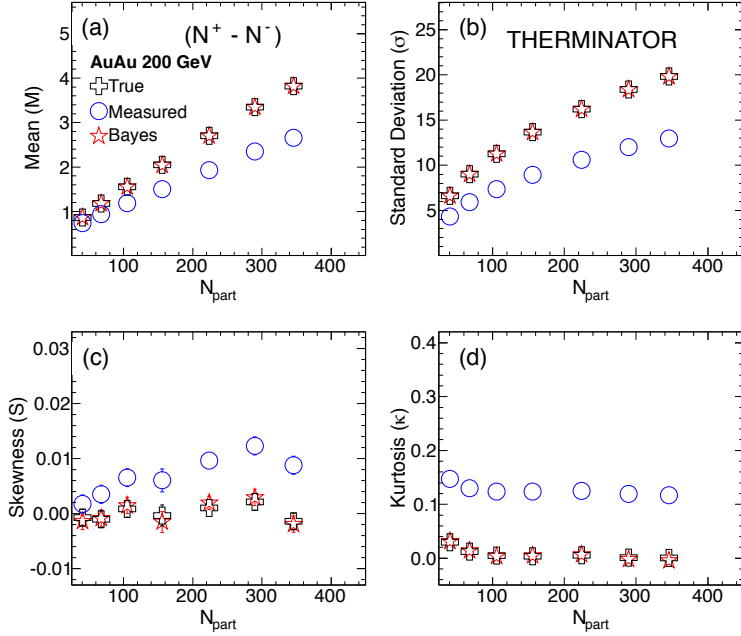


Figure 5.5. Mean, standard deviation, skewness and kurtosis of net-charge distribution in Au+Au collisions at $\sqrt{s_{\text{NN}}} = 200$ GeV from THERMINATOR event generator. Results are shown for the True, measured and Bayes unfolded distributions as a function of N_{part} .

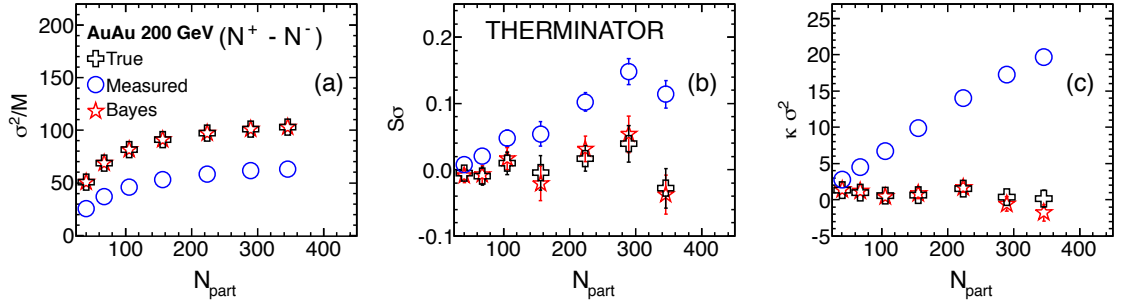


Figure 5.6. Product of moments of net-charge distributions in Au+Au collisions at $\sqrt{s_{\text{NN}}} = 200$ GeV from THERMINATOR event generator. The results are for the True, measured and Bayes unfolded distributions as a function of N_{part} .

small as compared to event-by-event varying efficiency.

In order to see the effect of energy dependence on our results we have carried out this study for net-charge distributions at midrapidity in 0-5% central Au+Au collisions

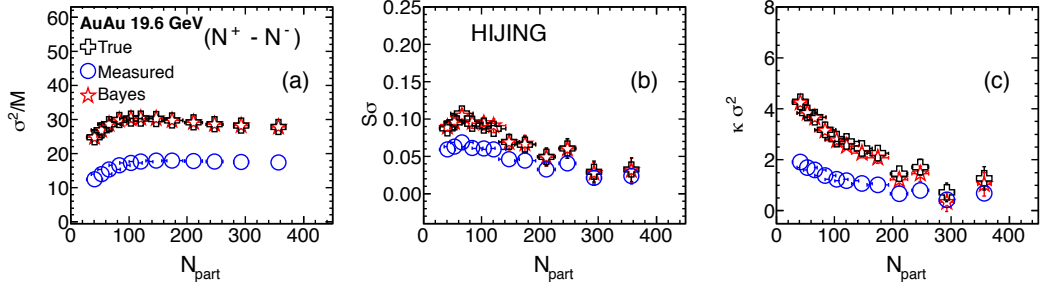


Figure 5.7. Product of moments of net-charge distributions in Au+Au collisions at $\sqrt{s_{\text{NN}}} = 19.6$ GeV from HIJING event generator with constant efficiency of 65%. The results are for the True, measured and Bayes unfolded distributions as a function of N_{part} .

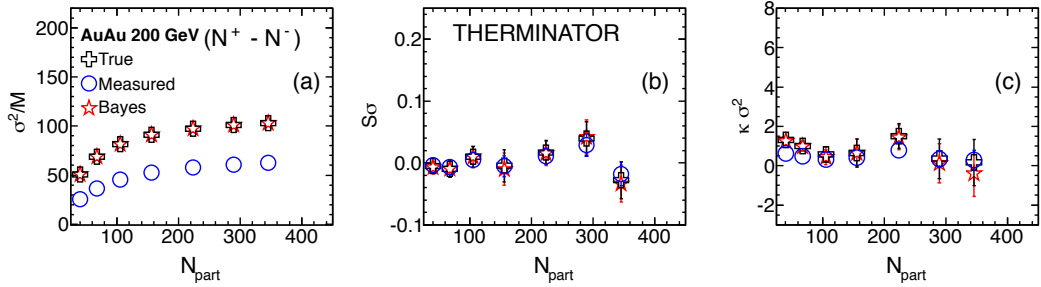


Figure 5.8. Product of moments of net-charge distributions in Au+Au collisions at $\sqrt{s_{\text{NN}}} = 200$ GeV from THERMINATOR event generator with constant efficiency of 65%. The results are for the True, measured and Bayes unfolded distributions as a function of N_{part} .

in HIJING model for $\sqrt{s_{\text{NN}}} = 19.6, 27, 39, 62.4, 130$ and 200 GeV. The efficiency varies event-by-event as per a Gaussian distribution with mean of 65% and width of 10% of the mean. Fig. 5.9 shows the Mean, standard deviation, skewness and kurtosis for the above system as a function of beam energy. The mean and variance of the measured distribution are smaller compared to those of the true, as we have seen in the centrality dependence study (Fig. 5.2 and Fig. 5.5). This is due to the particle counting inefficiencies for the measured case. The unfolded moments are found to closely follow the corresponding values of their respective true distributions. Fig. 5.10 shows the σ^2/M , $S\sigma$ and $\kappa\sigma^2$ as a function of $\sqrt{s_{\text{NN}}}$ of 0-5% Au+Au collisions net-

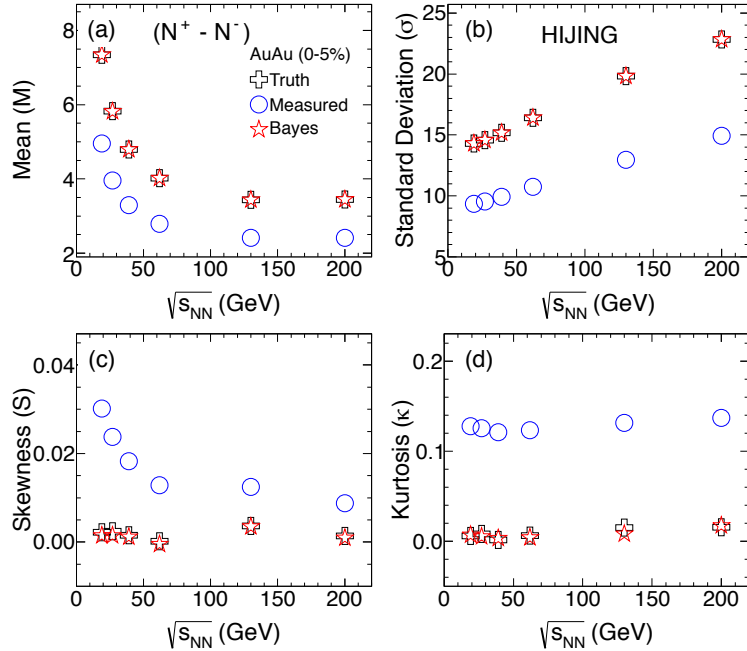


Figure 5.9. Mean, standard deviation, skewness and kurtosis of net-charge distribution in 0-5% Au+Au collisions as a function of $\sqrt{s_{NN}}$ from HJING event generator. Results are shown for the True, measured and Bayes unfolded distributions

charge distributions from the true, measured and unfolded distributions. Here also, as was seen for the centrality dependence results, the ratio and products of moments from unfolded distributions are reproduced as true distributions up to a good extent. This suggests that the method works for parent distributions produced over a wide range of beam energies.

Present study shows that it is important to correct for event-by-event detector related effects before proper conclusions can be obtained from higher moments studies in heavy-ion collisions. We have provided a method of obtaining the true distributions through an unfolding technique. Such a method keeps the observables same and hence has an advantage of being used to compare with theoretical calculations. Although this procedure can be easily adapted to experimentally measured distributions, it has two major drawbacks. Unlike the current case, where we have used an event generator for

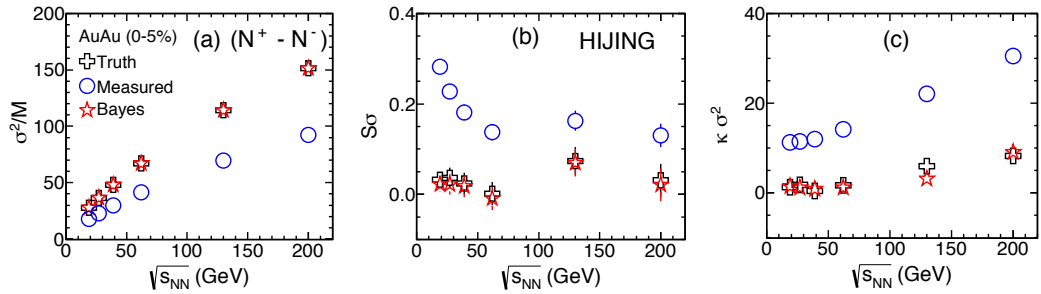


Figure 5.10. Product of moments of net-charge distribution in 0-5% Au+Au collisions as a function of $\sqrt{s_{NN}}$ from HIJING event generator. The results are for the True, measured and Bayes unfolded distributions.

the study and the true distribution is available for comparison, in a real experiment the true distribution is unknown. Hence it is very crucial that a realistic modeling of the detector response and particle production is available to obtain the response matrix for the unfolding calculations. In most cases, the modeling of the particle production and the detector response is highly event generator dependent and on how realistically the experimental conditions are simulated. The other disadvantage is, that the procedure works well for high event statistics as well as high average particle multiplicity per event. We have seen that large uncertainties enter into the unfolded distributions if we carry out this study with net-protons.

5.4 Summary

We have discussed a method to obtain the event-by-event true distributions of net-charge from the corresponding measured distributions which are subjected to detector effects like finite particle counting efficiencies. The approach used is based on the Bayes method for unfolding of distributions. We have used event generators HIJING and THERMINATOR to simulate the charged particle distributions produced in Au+Au collisions at $\sqrt{s_{NN}} = 19.6$ to 200 GeV respectively. The charge particle counting ef-

ficiency was varied by smearing the true distributions on event-by-event basis using a Gaussian function with mean 0.65 and width 0.065, to construct the measured distributions. We have shown that the unfolded distribution has similar mean, variance, skewness and kurtosis as the true distributions for all the collision centralities studied. The product of the moments σ^2/M , $S\sigma$ and $\kappa\sigma^2$ which show an opposite trends versus N_{part} for the measured distributions compared to the true distributions are faithfully unfolded back to agree with the true distributions. For cases where the efficiency of charged particle counting is constant for all events, the differences between the measured and true are small for the product $S\sigma$ and $\kappa\sigma^2$ compared to the ratio σ^2/M . The unfolding process is demonstrated to work for distributions obtained from widely differing physical mechanism for production of charge particle and over a wide range of beam energy and collision centrality. They also work for the cases where the charged particle counting efficiencies vary event-by-event as well as for the case where the efficiencies are constant.

This method has some limitations, in terms of need for a proper modeling of the detector response and works well for high multiplicity and high event statistics dataset. However the main advantage of this method is that we do not have to construct new observables which cancels out the detector effects. The new constructs are usually subjected to difficulties in physical interpretation and cannot be directly compared to standard theoretical calculations.

Chapter 6

Summary

In present thesis work, the performance studies carried with p+p data show good hadron rejection power of HBD and good separation between electrons coming from resonances or heavy quarks and neutral hadrons. Thus, there will be consequent improvements in di-electron S/B by using HBD and the final results will be exciting to see in near future.

Main focus of the RHIC beam energy scan program is to map the QCD phase diagram and to search for the location of critical point. In order to achieve these goals, the PHENIX experiment has collected data for Au+Au collisions at $\sqrt{s_{NN}} = 7.7, 19.6, 27, 39, 62.4$ and 200 GeV. PHENIX detector has unique advantages with uniform η vs p_T acceptance. This program covers the large range of baryon chemical potential (μ_B) in the QCD phase diagram. All these make the PHENIX experiment one of the unique detector system to search for the QCD critical point. Lattice QCD calculations have proposed that the higher order moments such as variance (σ^2), skewness (S) and kurtosis (κ), of the conserved charges (Q, B and S) are related to their respective higher order susceptibilities. At critical point, the higher order susceptibilities of the conserved charges are expected to diverge. Therefore, the higher order moments of conserved charge distribution as a function of beam energy may show non-monotonic behavior at the critical point. Various suitable moments products, such as $\frac{\sigma^2}{M}$, $S\sigma$ and $\kappa\sigma^2$ are constructed to cancel the volume in the susceptibilities of the conserved charges. In this thesis work the higher moments of net-charge distribution at RHIC energies are studied with PHENIX detector. In order to understand the effect of background physics like, jet production, jet-quenching, resonance production, baryon stopping and

thermal equilibrium etc., on the higher moments of the net-charge distribution, various models, like HIJING, UrQMD and Hadron Resonance Gas are studied. These model predictions set baseline for the analysis. For the estimation of higher moments of the net-charge distribution, extensive data clean up processes have been performed. Centrality bin width correction has been done to avoid centrality bin width effect. To avoid auto-correlation effect in the higher moments of the net-charge distribution, centrality definitions are selected carefully. Besides, the statistical error estimation for higher moments analysis is done using Delta theorem. The efficiency corrections for higher moments in real data are done by assuming that the detector efficiency is binomially distributed.

The mean and width of net-charge distributions increases with increase in centrality and also with the increase in beam energy. The skewness and kurtosis of the distributions decrease with increasing centrality. The products of moments are also studied to cancel the volume dependance in the higher moments of the net-charge distribution. The $\frac{\sigma^2}{M}$ shows slight increase from peripheral to central collisions, whereas $S\sigma$ and $\kappa\sigma^2$ show negligible centrality dependence within the statistical uncertainties.

The values of $\frac{\sigma^2}{M}$ are observed to increase with increasing beam energy. The values of $S\sigma$, which are close to zero for $\sqrt{s_{NN}} = 200$ GeV, increase with decreasing beam energy for all centralities. The energy dependence of $S\sigma$ shows systematically large deviations from that of HRG expectations below $\sqrt{s_{NN}} = 19.6$ GeV compared to those at higher energies. The values of $\kappa\sigma^2$ as a function of beam energy show almost no energy dependence for central collision within the statistical errors, excluding at $\sqrt{s_{NN}} = 19.6$ GeV and 27 GeV. The non-monotonic behavior with energy and higher values of $\kappa\sigma^2$ as compared to HRG predictions make these energies interesting to explore. Although, these two energies need to be explored with higher statistics of events and with more sophisticated efficiency corrections to conclude about the position of QCD critical point.

Further, a hadron resonance gas model has been explored to study the effect

of limited experimental acceptance on observables like n^{th} order susceptibilities $\chi_x^{(n)}$, associated with conserved quantities like net-charge ($x = Q$), net-strangeness ($x = S$) and net-baryon number ($x = B$). This work demonstrates the importance of considering experimental acceptances before the experimental data is compared with the theoretical calculations. In addition, in this model we find that, the $\chi_Q^{(n)}$ and $\chi_S^{(n)}$ values depend on the experimental acceptance of the decay daughters from various resonances, produced in high energy heavy-ion collisions. Within this model and the kinematic regions used in our study, we also find that the dependence on acceptance and resonance decays are stronger for both net-charge and net-strangeness compared to that of net-baryons.

We have also outlined the importance of event-by-event efficiency corrections to experimentally measured higher moments of net-charge distributions. In this work a method is discussed to obtain the event-by-event true distributions of net-charge from the corresponding measured distributions which are subjected to detector effects like finite particle counting efficiencies. The approach used is based on the Bayes method for unfolding of distributions. The product of the moments $\frac{\sigma^2}{M}$, $S\sigma$ and $\kappa\sigma^2$ which show an opposite trend versus N_{part} for the measured distributions compared to the true distributions are faithfully unfolded back to agree with the true distributions by this method.

Also the unfolding process is demonstrated to work for distributions obtained from widely differing physical mechanism for production of charge particle and over a wide range of beam energy and collision centrality. This method has some limitations, in terms of need for a proper modeling of the detector response and works well for high multiplicity and high event statistics dataset. However the main advantage of this method is that we do not have to construct new observables which cancels out the detector effects.

Bibliography

- [1] G. Dissertori, I. Knowles, and M. Schmelling, *Quantum Chromodynamics - High Energy Experiments and Theory*, Oxford University Press (2003).
- [2] D. J. Gross and F. Wilczek, *Phys. Rev. Lett.* **30**, 1343 (1973).
- [3] H. D. Politzer, *Phys. Rev. Lett.* **30**, 1346 (1973).
- [4] S. Bethke, *Nucl. Phys. Proc. Suppl.* **39BC**, 198 (1995).
- [5] S. Bethke, *Prog. Part. Nucl. Phys.* **58**, 351 (2007) [hep-ex/0606035].
- [6] C. P. Singh, *Phys. Rept.* **236**, 147 (1993).
- [7] C. P. Singh and S. Uddin, In **Calcutta 1993, Physics and astrophysics of quark-gluon plasma** 266-274
- [8] C. P. Singh, *Int. J. Mod. Phys. A* **7**, 7185 (1992).
- [9] H. Satz, *Nucl. Phys. A* **418**, 447C (1984).
- [10] The Frontiers of Nuclear Science, 2007 NSAC Long Range Plan.
- [11] J. D. Bjorken, *Phys. Rev. D* **27**, **140** (1983).
- [12] B. Mohanty, *Nucl. Phys. A* **830**, 899C (2009) [arXiv:0907.4476 [nucl-ex]].
- [13] D. Bailin, J. Cleymans and M. D. Scadron, *Phys. Rev. D* **31**, 164 (1985).
- [14] A. Kocic, *Phys. Rev. D* **33**, 1785 (1986).

- [15] V. F. Galina and K. S. Viswanathan, Phys. Rev. D **38**, 2000 (1988).
- [16] P. M. Damgaard, D. Hochberg and N. Kawamoto, Phys. Lett. B **158**, 239 (1985)
- [17] M. Asakawa and K. Yazaki, Nucl. Phys. A **504**, 668 (1989).
- [18] A. Barducci, R. Casalbuoni, S. De Curtid, R. Gatto and G. Pettini, Phys. Lett. B **231**, 463 (1989); Phys. Rev. D **41**, 1610 (1990).
- [19] J. M. Cornwall, R. Jackiw and E. Tomboulis, Phys. Rev. D **10**, 2428 (1974).
- [20] R. D. Pisarski and F. Wilczek, Phys. Rev. D **29**, 338 (1984).
- [21] J. Berges and K. Rajagopal, Nucl. Phys. B **538**, 215 (1999).
- [22] M. A. Halasz, A. D. Jackson, R. E. Shrock, M. A. Stephanov and J. J. M. Verbaarschot, Phys. Rev. D **58**, 096007 (1998).
- [23] N. G. Antoniou and A. S. Kapoyannis, Phys. Lett. B **563**, 165 (2003).
- [24] Y. Hatta and T. Ikeda, Phys. Rev. D **67**, 014028 (2003)
- [25] T. Hatsuda, M. Tachibana, N. Yamamoto, and G. Baym, Phys. Rev. Lett. **97**, 122001 (2006).
- [26] Z. Fodor and S. D. Katz, Phys. Lett. B **534**, 87 (2002); JHEP **0203**, 014 (2002).
- [27] Z. Fodor and S. D. Katz, JHEP **0404**, 050 (2004).
- [28] C. R. Alton et al., Phys. Rev. D **66**, 074507 (2002).
- [29] D. Smith and C. Schmidt, arXiv:1109.6729v1[hep-lat].
- [30] Y. D. Mercado, H. G. Evertz and C. Gattringer, Phys. Rev. Lett. **106**, 222001 (2011).
- [31] P. D. Powell and G. Baym, Phys. Rev. D **85**, 074003 (2012).

- [32] P. Bicudo, arXiv:1102.5531v1[hep-lat].
- [33] K. Fukushima, Phys. Lett. B **695**, 387 (2011).
- [34] F. R. Brown et al, Phys. Rev. Lett. **65**, 2491 (1990).
- [35] [http://en.m.wikipedia.org/wiki/Critical_point_\(thermodynamics\)](http://en.m.wikipedia.org/wiki/Critical_point_(thermodynamics))
- [36] S. Hands, Contemp. Phys. **42**, 209 (2001) [physics/0105022 [physics.ed-ph]].
- [37] K. Fukushima and T. Hatsuda, Rept. Prog. Phys. **74**, 014001 (2011) [arXiv:1005.4814 [hep-ph]].
- [38] Y. Aoki, G. Endrodi, Z. Fodor, S. D. Katz and K. K. Szabo, Nature **443**, 675 (2006) [hep-lat/0611014].
- [39] C. DeTar and U. M. Heller, Eur. Phys. J. A **41**, 405 (2009) [arXiv:0905.2949 [hep-lat]].
- [40] M. A. Stephanov, PoS LAT **2006**, 024 (2006) [hep-lat/0701002].
- [41] S. Ejiri, C. R. Allton, S. J. Hands, O. Kaczmarek, F. Karsch, E. Laermann and C. Schmidt, Prog. Theor. Phys. Suppl. **153**, 118 (2004) [hep-lat/0312006].
- [42] G. H. Corral, CERN Yellow Report CERN-2010-001, 393-416 [arXiv:1010.3164 [nucl-th]].
- [43] L. P. Csernai. “Introduction to relativistic heavy ion collisions”, J. Wiley and Sons, (1993)
- [44] M. G. Mustafa, S. Raniwala, T. Awes, B. Rai, R. S. Bhalerao, J. G. Contreras, R. V. Gavai and S. K. Ghosh *et al.*, Pramana **67**, 961 (2006) [hep-ph/0607117].
- [45] G. Peilert, H. Stoecker and W. Greiner, Rept. Prog. Phys. **57**, 533 (1994).
- [46] E. Iancu, arXiv:1205.0579 [hep-ph].

- [47] M. Gazdzicki and St. Mrowczynski, Z. Phys. C **54** (1992) 127.
- [48] G. L. Melkumov et al., (NA49 Collaboration), Nucl. Phys. B. **219-220** (2011), T. Anticic et al., (NA49 Collaboration), Phys. Rev. C **79** (2009) 044904.
- [49] C. Alt et al, (NA49 Collaboration), Phys. Rev. C **78** (2008) 034914.
- [50] T. Anticic et al., (NA49 Collaboration), arXiv:1208.5292 [nucl-ex].
- [51] B. I. Abelev et al., (STAR Collaboration), Phys. Rev. Lett. **103** (2009) 092301.
- [52] T. Anticic et al., (NA49 Collaboration), Phys. Rev. C **83** (2011) 061902.
- [53] S. Jeon and V. Koch, In *Hwa, R.C. (ed.) et al.: Quark gluon plasma* 430-490 [hep-ph/0304012].
- [54] M. A. Stephanov, K. Rajagopal and E. V. Shuryak, Phys. Rev. Lett. **81**, 4816 (1998) [hep-ph/9806219].
- [55] Y. Hatta and M. A. Stephanov, Phys. Rev. Lett. **91**, 102003 (2003) [Erratum-ibid. **91**, 129901 (2003)] [hep-ph/0302002].
- [56] M. A. Stephanov, Phys. Rev. Lett. **102**, 032301 (2009) [arXiv:0809.3450 [hep-ph]].
- [57] L. Adamczyk *et al.* [STAR Collaboration], Phys. Rev. Lett. **112**, no. 3, 032302 (2014) [arXiv:1309.5681 [nucl-ex]].
- [58] D. McDonald [STAR Collaboration], Nucl. Phys. A **904-905**, 907c (2013) [arXiv:1210.7023 [nucl-ex]].
- [59] L. Adamczyk *et al.* [STAR Collaboration], Phys. Rev. Lett. **113**, 092301 (2014) [arXiv:1402.1558 [nucl-ex]].
- [60] J. T. Mitchell [PHENIX Collaboration], Nucl. Phys. A **904-905**, 903c (2013) [arXiv:1211.6139 [nucl-ex]].

- [61] P. Garg, D. K. Mishra, P. K. Netrakanti, A. K. Mohanty and B. Mohanty, PoS CPOD **2013**, 041 (2013) [arXiv:1306.3029 [hep-ph]].
- [62] S. A. Bass, M. Belkacem, M. Bleicher, M. Brandstetter, L. Bravina, C. Ernst, L. Gerland and M. Hofmann *et al.*, Prog. Part. Nucl. Phys. **41**, 255 (1998) [Prog. Part. Nucl. Phys. **41**, 225 (1998)] [nucl-th/9803035].
- [63] M. Gyulassy and X. -N. Wang, Comput. Phys. Commun. **83**, 307 (1994) [nucl-th/9502021].
- [64] A. Franz, *et al.* Nucl. Instrum. Methods A **566**, 54 (2006).
- [65] K. H. Ackermann *et al.* Nucl. Instrum. Meth., A **499**, 624 (2003).
- [66] B. B. Back *et al.* Nucl. Instrum. Meth., A **499**, 603 (2003).
- [67] M. Adamczyk *et al.* Nucl. Instrum. Meth., A **499**, 437 (2003).
- [68] K. Adcox *et al.* Nucl. Instrum. Meth., A **499**, 469 (2003).
- [69] K. Adcox *et al.* Nucl. Instrum. Meth., A **499**, 489 (2003).
- [70] K. Ikematsu *et al.* Nucl. Instrum. Meth., A **411**, 238 (1998).
- [71] M. Allen *et al.* Nucl. Instrum. Meth., A **499**, 549 (2003).
- [72] Clemens Adler *et al.* Nucl. Instrum. Meth., A **470**, 488 (2001).
- [73] S. S. Adler *et al.* [PHENIX Collaboration], Phys. Rev. C **71**, 034908 (2005) [Erratum-ibid. C **71**, 049901 (2005)] [nucl-ex/0409015].
- [74] K. Adcox *et al.* Nucl. Instrum. Meth., A **499**, 489 (2003).
- [75] K. Adcox *et al.* Nucl. Instrum. Meth., A **499**, 489 (2003).
- [76] A. Oskarsson *et al.*, Nucl. Instrum. Meth., A **497/2-3**, 263 (2003).

- [77] P. Nilsson (for the PHENIX pad chamber group) Nucl. Instrum. Meth., A **661**, 665 (1999).
- [78] S. C. Johnson, In Proc. of Intl. Conf. on Computing in High Energy Physics (CHEP 98), Chicago IL, **32** 1998.
- [79] J. T. Mitchell *et al.*, Nucl. Instrum. Meth., A **482**, 491 (2002).
- [80] Y. Akiba *et al.*, Nucl. Instrum. Meth., A **453**, 279 (2000).
- [81] T. Sakaguchi *et al.*, Nucl. Instrum. Meth., A **453**, 382 (2000).
- [82] W. M. Yao *et.al.*, Review of particle physics. J. Phys., G **33** (2006).
- [83] Z. Fraenkel *et al.*, Nucl. Instrum. Meth. A **546** (2005) 466.
- [84] J. Wambach and R. Rapp, Nucl. Phys. A **638** (1998) 171.
- [85] A. Adare, *et al.*, Phys.Rev. C **81** (2010) 034911.
- [86] S. Turbide, R. Rapp and C. Gale, Phys. Rev. C **69** (2004) 014903.
- [87] F. Sauli, Nucl. Instrum. and Meth. A **386** (1997) 531.
- [88] P. Garg and B. K. Singh, Nucl. Phys. A **862-863**, 479 (2011).
- [89] S. S. Adler *et al.* [PHENIX Collaboration], Nucl. Instrum. Meth. A **499**, 593 (2003).
- [90] S. S. Adler *et al.* [PHENIX Collaboration], Nucl. Instrum. Meth. A **499**, 560 (2003).
- [91] A. Bzdak and V. Koch, Phys. Rev. C **86**, 044904 (2012) [arXiv:1206.4286 [nucl-th]].
- [92] M. M. Aggarwal *et al.* [STAR Collaboration], Phys. Rev. Lett. **105**, 022302 (2010) [arXiv:1004.4959 [nucl-ex]].

- [93] M. A. Stephanov, Phys. Rev. Lett. **107**, 052301 (2011) [arXiv:1104.1627 [hep-ph]].
- [94] M. Asakawa, S. Ejiri and M. Kitazawa, Phys. Rev. Lett. **103**, 262301 (2009) [arXiv:0904.2089 [nucl-th]].
- [95] S. Gupta, X. Luo, B. Mohanty, H. G. Ritter and N. Xu, Science **332**, 1525 (2011) [arXiv:1105.3934 [hep-ph]].
- [96] R. V. Gavai and S. Gupta, Phys. Lett. B **696**, 459 (2011) [arXiv:1001.3796 [hep-lat]].
- [97] F. Karsch and K. Redlich, Phys. Lett. B **695**, 136 (2011) [arXiv:1007.2581 [hep-ph]].
- [98] B. Friman, F. Karsch, K. Redlich and V. Skokov, Eur. Phys. J. C **71**, 1694 (2011) [arXiv:1103.3511 [hep-ph]].
- [99] A. Bazavov *et al.* [HotQCD Collaboration], Phys. Rev. D **86**, 034509 (2012) [arXiv:1203.0784 [hep-lat]].
- [100] M. Cheng, P. Hende, C. Jung, F. Karsch, O. Kaczmarek, E. Laermann, R. D. Mawhinney and C. Miao *et al.*, Phys. Rev. D **79**, 074505 (2009) [arXiv:0811.1006 [hep-lat]].
- [101] B. I. Abelev *et al.* [STAR Collaboration], Phys. Rev. C **79**, 034909 (2009) [arXiv:0808.2041 [nucl-ex]].
- [102] H. Appelshauser *et al.* [NA49 Collaboration], Phys. Lett. B **459** (1999) 679 [hep-ex/9904014].
- [103] M. M. Aggarwal *et al.* [WA98 Collaboration], Phys. Rev. C **65** (2002) 054912 [nucl-ex/0108029].
- [104] K. Adcox *et al.* [PHENIX Collaboration], Phys. Rev. Lett. **89** (2002) 082301 [nucl-ex/0203014].

- [105] P. Braun-Munzinger, B. Friman, F. Karsch, K. Redlich and V. Skokov, Phys. Rev. C **84**, 064911 (2011) [arXiv:1107.4267 [hep-ph]].
- [106] B. Mohanty, Talk given at CPOD2011, Wuhan, China. Presentation at CPOD 2011
- [107] S. Mrowczynski, Phys. Lett. B **465** (1999) 8 [nucl-th/9905021].
- [108] S. A. Voloshin, V. Koch and H. G. Ritter, Phys. Rev. C **60**, 024901 (1999) [nucl-th/9903060].
- [109] A. Bialas, Phys. Rev. C **75**, 024904 (2007) [hep-ph/0701074].
- [110] D. Bower and S. Gavin, Phys. Rev. C **64**, 051902 (2001) [nucl-th/0106010].
- [111] M. Bleicher, S. Jeon and V. Koch, Phys. Rev. C **62**, 061902 (2000) [hep-ph/0006201].
- [112] C. Pruneau, S. Gavin and S. Voloshin, Phys. Rev. C **66**, 044904 (2002) [nucl-ex/0204011].
- [113] O. E. Barndorff-Nielsen, D. G. Pollard, and N. Shephard, University of Oxford, Department of Economics, Discussion Paper Series **490** (2010).
- [114] T. C. Brooks *et al.* [MiniMax Collaboration], Phys. Rev. D **55**, 5667 (1997) [hep-ph/9609375].
- [115] M. Kirejczyk, Acta Phys. Polon. B **35**, 2425 (2004) [nucl-ex/0406029].
- [116] A. Kumar, P. K. Srivastava, B. K. Singh and C. P. Singh, Adv. High Energy Phys. **2013** (2013) [arXiv:1306.4185 [hep-ph]].
- [117] P. Garg, D. K. Mishra, P. K. Netrakanti, A. K. Mohanty and B. Mohanty, J. Phys. G **40**, 055103 (2013)

- [118] A. Kisiel, T. Taluc, W. Broniowski and W. Florkowski, *Comput. Phys. Commun.* **174**, 669 (2006) [nucl-th/0504047].
- [119] T. Adye, [arXiv:1105.1160 [physics.data-an]]. *RooUnfold* package
- [120] G. D' Agostini, *Nucl. Instrum. Meth. A* **362**, 487 (1995).
- [121] X. Luo, *J. Phys. G* **39**, 025008 (2012) [arXiv:1109.0593 [nucl-ex]].
- [122] F. Karsch and K. Redlich, *Phys. Lett. B* **695** (2011) 136.
- [123] S. Gupta, X. Luo, B. Mohanty, H. G. Ritter and N. Xu, *Science* **332** (2011) 1525.
- [124] R. V. Gavai and S. Gupta, *Phys. Lett. B* **696** (2011) 459.
- [125] A. Bazavov, H. T. Ding, P. Hegde, O. Kaczmarek, F. Karsch, E. Laermann, S. Mukherjee and P. Petreczky *et al.*, *Phys. Rev. Lett.* **109** (2012) 192302.
- [126] M. M. Aggarwal *et al.* [STAR Collaboration], *Phys. Rev. Lett.* **105** (2010) 022302.
- [127] M. A. Stephanov, *Phys. Rev. Lett.* **107** (2011) 052301.
- [128] P. Braun-Munzinger, B. Friman, F. Karsch, K. Redlich and V. Skokov, *Phys. Rev. C* **84** (2011) 064911.
- [129] B. Friman, F. Karsch, K. Redlich and V. Skokov, *Eur. Phys. J. C* **71** (2011) 1694.
- [130] C. B. Yang and X. Wang, *Phys. Rev. C* **84** (2011) 064908.
- [131] M. Asakawa, S. Ejiri and M. Kitazawa, *Phys. Rev. Lett.* **103** (2009) 262301.
- [132] P. Braun-Munzinger, K. Redlich and J. Stachel, In *Hwa, R.C. (ed.) et al.: Quark gluon plasma* 491-599 [nucl-th/0304013].
- [133] P. Garg, D. K. Mishra, P. K. Netrakanti, B. Mohanty, A. K. Mohanty, B. K. Singh and N. Xu, *Phys. Lett. B* **726**, 691 (2013)

- [134] V. P. Konchaovski, M. I. Gorenstein, E. L. Bratkovskaya and H. Stocker, Phys. Rev. C **74** (2006) 064911.
- [135] M. Hauer, Phys. Rev. C **77** (2008) 034909.
- [136] M. Hauer, G. Torrieri and S. Wheaton, Phys. Rev. C **80** (2009) 014907; M. Hauer, arXiv:1008.1990 and references there in.
- [137] J. Cleymans, H. Oeschler, K. Redlich and S. Wheaton, Phys. Rev. C **73** (2006) 034905 and references there in.
- [138] F. Becattini, M. Gazdzicki A. Keranen J. Manninen and R. Stock, Phys. Rev. C **69** (2004) 024905.
- [139] F. Becattini, J. Manninen and M. Gazdzicki, Phys. Rev. C **73** (2006) 044905.
- [140] J. Cleymans, J. Phys. G: Nucl. Part. Phys. **35** (2008) 044017.
- [141] F. Becattini, J. Cleymans and J. Strumpfer, PoS CPOD **07** (2007) 012.
- [142] P. V. Ruuskanen, Acta Physica Polonica B **18** (1987) 551.
- [143] B. I. Abelev et al., STAR Collaboration, Phys. Rev. C **79** (2009) 34909.

Publications

List of publications related to Thesis:

1. **Performance studies of the PHENIX Hadron Blind Detector at RHIC,**
P. Garg and B. K. Singh, Nucl. Phys. A 862-863, 479 (2011).
2. **Conserved number fluctuations in a hadron resonance gas model,**
P. Garg, et al., Phys. Lett. B 726, 691 (2013).
3. **Unfolding of event-by-event net-charge distributions in heavy-ion collision,**
P. Garg, et al., J. Phys. G 40, 055103 (2013).
4. **Moments of net-charge multiplicity distribution in Au+Au collisions measured by the PHENIX experiment at RHIC,**
P. Garg (for PHENIX collaboration), PoS (CPOD) 2013, 050 (2013).
5. **Unfolding of event-by-event net-charge distributions in heavy-ion collisions**
P. Garg, et al., PoS (CPOD) 2013, 041 (2013).

List of other publications

1. **Structural characterization of “as-deposited” cesium iodide films studied by X-ray diffraction and transmission electron microscopy techniques,**
Triloki, **P. Garg**, R. Rai and B. K. Singh,
Nucl. Instrum. Meth. A **736**, 128 (2014).
2. **VUV-induced radiation ageing processes in CsI photocathodes studied by microscopy and spectroscopy techniques,**
B. K. Singh, Triloki, **P. Garg**, A. Prakash, G. Di Santo, E. Nappi, M. A. Nitti and A. Valentini *et al.*,
Nucl. Instrum. Meth. A **610**, 350 (2009).
3. **Net-baryon number fluctuations with HRG model using Tsallis distribution,**
D. K. Mishra, **P. Garg**, P. K. Netrakanti and A. K. Mohanty,
arXiv:1310.3469 [nucl-th](under communication).

List of Publications as a part of PHENIX Collaboration:

1. **“sPHENIX: An Upgrade Concept from the PHENIX Collaboration”**
C. Aidala, N. N. Ajitanand, Y. Akiba, Y. Akiba, R. Akimoto, J. Alexander, K. Aoki and N. Apadula *et al.*.
arXiv:1207.6378 [nucl-ex]
2. **“Concept for an Electron Ion Collider (EIC) detector built around the BaBar solenoid”**
A. Adare *et al.* [PHENIX Collaboration].
arXiv:1402.1209 [nucl-ex]

3. “Nuclear matter effects on J/ψ production in asymmetric Cu+Au collisions at $\sqrt{s_{NN}} = 200$ GeV” C. Aidala *et al.* [PHENIX Collaboration].
arXiv:1404.1873 [nucl-ex]
4. “Comparison of the space-time extent of the emission source in d +Au and Au+Au collisions at $\sqrt{s_{NN}} = 200$ GeV”
A. Adare *et al.* [PHENIX Collaboration].
arXiv:1404.5291 [nucl-ex]
5. “Measurement of K_S^0 and K^{*0} in $p+p$, d +Au, and Cu+Cu collisions at $\sqrt{s_{NN}} = 200$ GeV”
A. Adare *et al.* [PHENIX Collaboration].
arXiv:1405.3628 [nucl-ex]
6. “Low-mass vector-meson production at forward rapidity in $p+p$ collisions at $\sqrt{s} = 200$ GeV”
A. Adare *et al.* [PHENIX Collaboration].
arXiv:1405.4260 [hep-ex]
7. “Cross Section and Transverse Single-Spin Asymmetry of η Mesons in $p^\uparrow + p$ Collisions at $\sqrt{s} = 200$ GeV at Forward Rapidity”
A. Adare *et al.* [PHENIX Collaboration].
arXiv:1406.3541 [hep-ex]
8. “Closing the Door for Dark Photons as the Explanation for the Muon g-2 Anomaly”
A. Adare *et al.* [PHENIX Collaboration].
arXiv:1409.0851 [nucl-ex]



Conserved number fluctuations in a hadron resonance gas model

P. Garg^a, D.K. Mishra^b, P.K. Netrakanti^b, B. Mohanty^{c,*}, A.K. Mohanty^b, B.K. Singh^a, N. Xu^{d,e}

^a Department of Physics, Banaras Hindu University, Varanasi 221005, India

^b Nuclear Physics Division, Bhabha Atomic Research Center, Mumbai 400085, India

^c School of Physical Sciences, National Institute of Science Education and Research, Bhubaneswar 751005, India

^d Nuclear Science Division, Lawrence Berkeley National Laboratory, Berkeley, CA 94720, USA

^e Key Laboratory of the Ministry of Education of China, Central China Normal University, Wuhan 430079, China



ARTICLE INFO

Article history:

Received 2 May 2013

Received in revised form 11 September 2013

Accepted 11 September 2013

Available online 18 September 2013

Editor: D.F. Geesaman

Keywords:

Hadron resonance gas

Susceptibilities

Higher moments

Fluctuations

Heavy-ion collisions

Critical point

ABSTRACT

Net-baryon, net-charge and net-strangeness number fluctuations in high energy heavy-ion collisions are discussed within the framework of a hadron resonance gas (HRG) model. Ratios of the conserved number susceptibilities calculated in HRG are being compared to the corresponding experimental measurements to extract information about the freeze-out condition and the phase structure of systems with strong interactions. We emphasize the importance of considering the actual experimental acceptances in terms of kinematics (pseudorapidity (η) and transverse momentum (p_T)), the detected charge state, effect of collective motion of particles in the system and the resonance decay contributions before comparisons are made to the theoretical calculations. In this work, based on HRG model, we report that the net-baryon number fluctuations are least affected by experimental acceptances compared to the net-charge and net-strangeness number fluctuations.

© 2013 Elsevier B.V. All rights reserved.

1. Introduction

Measurement of the moments of distribution for conserved quantities like net-baryon, net-charge and net-strangeness number for systems undergoing strong interactions as in high energy heavy-ion collisions, have recently provided rich physics insights [1–10]. The most crucial realization is that, the product of moments of the conserved number distributions are measurable experimentally and can be linked to susceptibilities (χ) computed in Quantum Chromodynamic (QCD) based calculations [1,5]. For example, $S\sigma = \chi^{(3)}/\chi^{(2)}$ and $\kappa\sigma^2 = \chi^{(4)}/\chi^{(2)}$, where σ is the standard deviation, S is the skewness, κ is the kurtosis of the measured conserved number distribution, $\chi^{(n)}$ are the n -th order theoretically calculated susceptibilities associated with these conserved numbers. Such a connection between theory and high energy heavy-ion collision experiment has led to furthering our understanding about the freeze-out conditions [2,4], details of the quark–hadron transition [1,8] and plays a crucial role for the search of possible QCD critical point in the QCD phase diagram [5]. In all such physics cases there is a need to establish a reference

point for the measurements. Computing these quantities within the framework of a hadron resonance gas (HRG) model [11] provides such a reference for both experimental data and QCD based calculations.

The experimental measurements have limitations, they are usually available for a fraction of the total kinematic phase space, due to the finite detector geometries and can detect only certain species of the produced particles. For example, measurements related to net-baryon number distribution is restricted by the kinematic range in p_T where their identification is possible. In addition, baryons like neutron are not commonly measured in most of the high energy heavy-ion collision experiments. While for the net-charge number distribution, the limitation is usually in kinematic range available in η and the details of how contribution from different charge states and resonances are dealt with in the measurements. The kinematic acceptance in a typical high energy heavy-ion collision experiment like STAR [12] and PHENIX [13] at the Relativistic Heavy-Ion Collider facility (RHIC) for net-charge multiplicity distributions are: $|\eta| < 0.5$, $0.2 < p_T < 2.0$ GeV/c and $|\eta| < 0.35$, $0.3 < p_T < 1.0$ GeV/c, respectively. While for net-baryon number and net-strangeness related studies carried out in the STAR experiment, within $|\eta| < 0.5$, is through the measurement of net-protons and net-kaons in the range of $0.4 < p_T < 0.8$ GeV/c and $0.2 < p_T < 2.0$ GeV/c, respectively [5,12].

* Corresponding author.

E-mail address: bedanga@rcf.rhic.bnl.gov (B. Mohanty).

The main goal of this Letter is to demonstrate using the HRG model (discussed in the next section), the effect of the above experimental limitations on the physics observables $\chi^{(3)}/\chi^{(2)}$ and $\chi^{(4)}/\chi^{(2)}$. Our model based study clearly shows that the value of the observables related to net-charge and net-strangeness strongly depends on the experimental kinematic and charge state acceptances. Where charge state could be electric charge ($Q = 1$ or higher for net-charge measurements and strangeness number ($S = 1$ or higher for net-strangeness measurements. In contrast, the net-baryon number studies are found to be minimally affected by these experimental limitations. In this work, we have not considered the initial baryon distribution due to the participant number fluctuations in the heavy-ion collisions on the results for net-baryon fluctuations [14]. Another important effect that could influence the values of the higher moments of the net-charge, net-strangeness and net-baryon number distributions in limited acceptance, are the conservation laws related to charge, strangeness and baryon number.

The Letter is organized as follows. In Section 2, we will discuss the HRG model used in this study. In Section 3, the results for the observable $\chi^{(3)}/\chi^{(2)}$ and $\chi^{(4)}/\chi^{(2)}$ are presented for different kinematic acceptances, charge states, effect of collective flow of particle in the system and the resonance decay contributions. We also provide a table listing the values of these observable for typical experimental conditions as encountered in STAR and PHENIX experiments at RHIC and ALICE experiment at the Large Hadron Collider (LHC) Facility. Finally in Section 4, we summarize our findings and mention about the implications of this work to the current experimental measurements in high energy heavy-ion collisions.

2. Hadron resonance gas model

In the HRG model, we include all the relevant degrees of freedom of the confined, strongly interacting matter and also implicitly take into account the interactions that result in resonance formation [3]. It is well known that the fireball created in heavy-ion collision does not remain static, rather expands both in longitudinal and transverse directions until freeze out occurs. However, to keep the model simple, we first consider a static homogeneous fireball and flow effects are included subsequently.

In heavy-ion collision, no fluctuation would be seen in measurements with full phase space coverage as B , Q and S are strictly conserved. However, since most of the experiments cover only limited phase space, the part of the fireball accessible to the measurements may resemble with the Grand Canonical Ensemble (GCE) where energy (momentum), charge and number are not conserved locally. In general, the magnitude of multiplicity fluctuations and correlations in limited phase space crucially depends on the choice of the statistical ensemble that imposes different conservation laws [15,16]. Since no extensive quantities like energy, momentum and charge are needed to be locally conserved in GCE, the particles following Maxwell–Boltzmann distribution are assumed to be uncorrelated and fluctuations are expected to follow Poisson statistics even in the limited phase space when quantum effects are ignored. In case of particles following Bose–Einstein or Fermi–Dirac distributions, within finite phase space, Poisson statistics is not expected to be obeyed and hence the deviations from Poisson limit can be studied.

In the ambit of GCE framework, the logarithm of the partition function (Z) in the HRG model is given as

$$\ln Z(T, V, \mu) = \sum_B \ln Z_i(T, V, \mu_i) + \sum_M \ln Z_i(T, V, \mu_i), \quad (1)$$

where

$$\ln Z_i(T, V, \mu_i) = \pm \frac{V g_i}{2\pi^2} \int d^3 p \ln \{1 \pm \exp[(\mu_i - E)/T]\}, \quad (2)$$

T is the temperature, V is the volume of the system, μ_i is the chemical potential, E is the energy and g_i is the degeneracy factor of the i -th particle. The total chemical potential $\mu_i = B_i \mu_B + Q_i \mu_Q + S_i \mu_S$, where B_i , Q_i and S_i are the baryon, electric charge and strangeness number of the i -th particle, with corresponding chemical potentials μ_B , μ_Q and μ_S , respectively. The ‘+’ and ‘-’ signs are for baryons and mesons, respectively. The thermodynamic pressure (P) can then be deduced for the limit of large volume as

$$\frac{P}{T^4} = \frac{1}{V T^3} \ln Z_i \\ = \pm \frac{g_i}{2\pi^2 T^3} \int d^3 p \ln \{1 \pm \exp[(\mu_i - E)/T]\}. \quad (3)$$

The n -th order generalized susceptibility for baryons can be expressed as [3]

$$\chi_{x,baryon}^{(n)} = \frac{X^n}{V T^3} \int d^3 p \sum_{k=0}^{\infty} (-1)^k (k+1)^{n-1} \\ \times \exp \left\{ \frac{-(k+1)E}{T} \right\} \exp \left\{ \frac{(k+1)\mu}{T} \right\}, \quad (4)$$

and for mesons,

$$\chi_{x,meson}^{(n)} = \frac{X^n}{V T^3} \int d^3 p \sum_{k=0}^{\infty} (k+1)^{n-1} \\ \times \exp \left\{ \frac{-(k+1)E}{T} \right\} \exp \left\{ \frac{(k+1)\mu}{T} \right\}. \quad (5)$$

The factor X represents either B , Q or S of the i -th particle depending on whether the computed χ_x represents baryon or electric charge or strangeness susceptibility.

For a particle of mass m in static fireball with p_T , η and ϕ (azimuthal angle), the volume element ($d^3 p$) and energy (E) can be written as $d^3 p = p_T m_T \cosh \eta d\eta d\eta d\phi$ and $E = m_T \cosh \eta$, where $m_T = \sqrt{p_T^2 + m^2}$, respectively. The experimental acceptances can be incorporated by considering the appropriate integration ranges in η , p_T , ϕ and charge states by considering the values of $|X|$. The total generalized susceptibilities will then be the sum of the contribution from baryons and mesons as $\chi_x^{(n)} = \sum \chi_{x,baryon}^{(n)} + \sum \chi_{x,meson}^{(n)}$.

In order to make the connection with the experiments, the beam energy dependence of μ and T parameters of the HRG model needs to be provided. These are extracted from a statistical thermal model description of measured particle yields in the experiment at various $\sqrt{s_{NN}}$ [17–19]. This is followed by the parameterization of μ_B and T as a function of $\sqrt{s_{NN}}$ [17]. The μ_B dependence of the temperature is given as $T(\mu_B) = a - b\mu_B^2 - c\mu_B^4$ with $a = 0.166 \pm 0.002$ GeV, $b = 0.139 \pm 0.016$ GeV $^{-1}$, and $c = 0.053 \pm 0.021$ GeV $^{-3}$. The $\sqrt{s_{NN}}$ dependence of μ_B is given as $\mu_B(\sqrt{s_{NN}}) = \frac{d}{1+e/\sqrt{s_{NN}}}$ with $d = (1.308 \pm 0.028)$ GeV and $e = (0.273 \pm 0.008)$ GeV $^{-1}$. Further the ratio of baryon to strangeness chemical potential is parameterized as $\frac{\mu_S}{\mu_B} \simeq 0.164 + 0.018\sqrt{s_{NN}}$. We have checked that the value of T and μ_B obtained using the yields extrapolated to 4π or from mid-rapidity measurements, have little impact on our study. However in order to study the rapidity (η) dependence, the μ_B parameterizations $\mu_B = 0.024 + 0.011\eta^2$ and $\mu_B = 0.237 + 0.011\eta^2$ at $\sqrt{s_{NN}} = 200$ GeV [20] and $\sqrt{s_{NN}} = 17.3$ GeV [21], respectively, are used in the calculations.

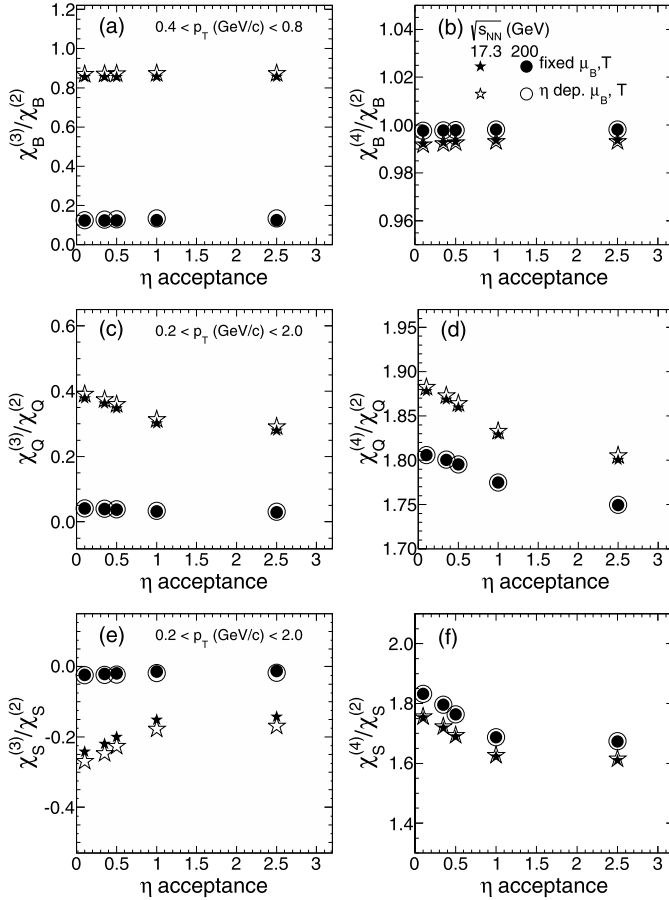


Fig. 1. The η acceptance dependence of $\chi_x^{(3)}/\chi_x^{(2)}$ and $\chi_x^{(4)}/\chi_x^{(2)}$ for two different beam energies. In panels (a) and (b) x = net-baryon B , (c) and (d) x = net-charge Q , and in (e) and (f) x = net-strangeness S . Also shown are the results with (labeled “dep.”) and without (labeled “fixed”) the η dependence of chemical freeze-out parameters μ_B and T .

3. Results

3.1. Kinematic acceptance in η and p_T

Fig. 1 shows the variation of $\chi_x^{(3)}/\chi_x^{(2)}$ and $\chi_x^{(4)}/\chi_x^{(2)}$ as a function of η acceptance for $\sqrt{s_{NN}} = 200$ GeV and $\sqrt{s_{NN}} = 17.3$ GeV. Where x stands for either net-baryon (B) (**Fig. 1(a)** and (**b**)), net-charge (Q) (**Fig. 1(c)** and (**d**)), or net-strangeness (S) (**Fig. 1(e)** and (**f**)). For each beam energy we show the effect of considering HRG parameters (μ, T) fixed to parameterization based on mid-rapidity data and also a parameterization based on the η dependent value of (μ, T). The difference between the two cases are small. For the subsequent studies we only present results for different $\sqrt{s_{NN}}$ using the parameterization of the chemical freeze-out parameters based on the measurement of particle yields at mid-rapidity. A clear dependence of $\chi_x^{(3)}/\chi_x^{(2)}$ and $\chi_x^{(4)}/\chi_x^{(2)}$ on η acceptance is observed for net-charge (**Fig. 1(c)** and (**d**)) and net-strangeness (**Fig. 1(e)** and (**f**)). The $\chi_B^{(3)}/\chi_B^{(2)}$ and $\chi_B^{(4)}/\chi_B^{(2)}$ values (**Fig. 1(a)** and (**b**)) are however found to be independent of η acceptance for the two beam energies studied. This underscores the need to carefully consider η acceptance effects when comparing HRG model results to experimental data, especially for net-charge and net-strangeness fluctuation measures.

Fig. 2 shows the variation of $\chi_x^{(3)}/\chi_x^{(2)}$ and $\chi_x^{(4)}/\chi_x^{(2)}$ as a function of $\sqrt{s_{NN}}$ for various p_T acceptances. The choice of these particular values of p_T acceptance ranges are motivated by exis-

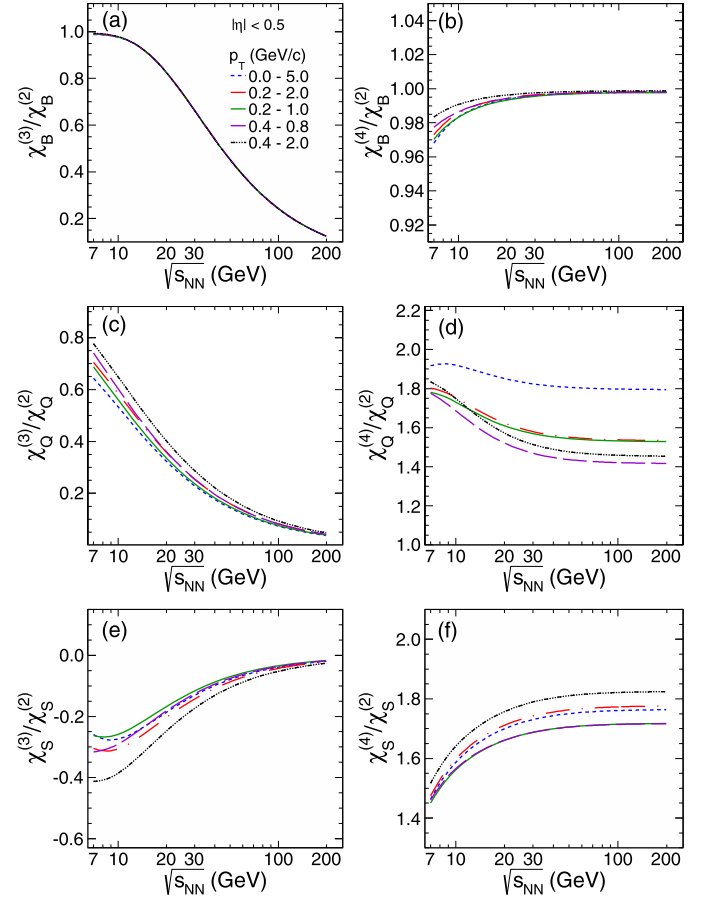


Fig. 2. (Color online.) The p_T acceptance dependence of $\chi_x^{(3)}/\chi_x^{(2)}$ and $\chi_x^{(4)}/\chi_x^{(2)}$ for different $\sqrt{s_{NN}}$. Where x stands for either net-baryon (B) (panels (a) and (b)), net-charge (Q) (panels (c) and (d)), and net-strangeness (S) (panels (e) and (f)).

tence of the corresponding experimental measurements [5,12,13]. It is observed that $\chi_x^{(3)}/\chi_x^{(2)}$ and $\chi_x^{(4)}/\chi_x^{(2)}$ have a clear p_T acceptance dependence at all beam energies for net-charge (**Fig. 2(c)** and (**d**)) and net-strangeness (**Fig. 2(e)** and (**f**)). However the p_T acceptance dependences for net-baryon (**Fig. 2(a)** and (**b**)) is substantially weaker. Hence the p_T acceptance study also emphasizes the need to consider the actual experimental acceptance for model comparisons in fluctuation measures. At the same time both the kinematic acceptance studies in η and p_T show net-baryon fluctuation measures are least affected.

3.2. Conserved charge states

Fig. 3 shows the variation of $\chi_x^{(3)}/\chi_x^{(2)}$ and $\chi_x^{(4)}/\chi_x^{(2)}$ as a function of $\sqrt{s_{NN}}$ for various types of baryons (**Fig. 3(a)** and (**b**)), values of electric charge states, $|Q| = 1$ and $|Q| > 1$ (**Fig. 3(c)** and (**d**)), and values of strangeness number, $|S| = 1$ and $|S| > 1$ (**Fig. 3(e)** and (**f**)). For each of the cases the observables are compared to the respective values with inclusion of all conserved charge states and baryons. We find a strong dependence of the $\chi_Q^{(3)}/\chi_Q^{(2)}$ and $\chi_Q^{(4)}/\chi_Q^{(2)}$ on whether we consider $|Q| = 1$ or $|Q| > 1$, both differing from the case of inclusion of all charge states. Same is the situation for net-strangeness. On the other hand, successive inclusion of different baryons, starting with protons seems to have some small effect on the $\chi_B^{(3)}/\chi_B^{(2)}$ and $\chi_B^{(4)}/\chi_B^{(2)}$ values only at the lower beam energies. The absence of baryons with $|B| > 1$ makes the net-baryon number fluctuations more advantageous and less

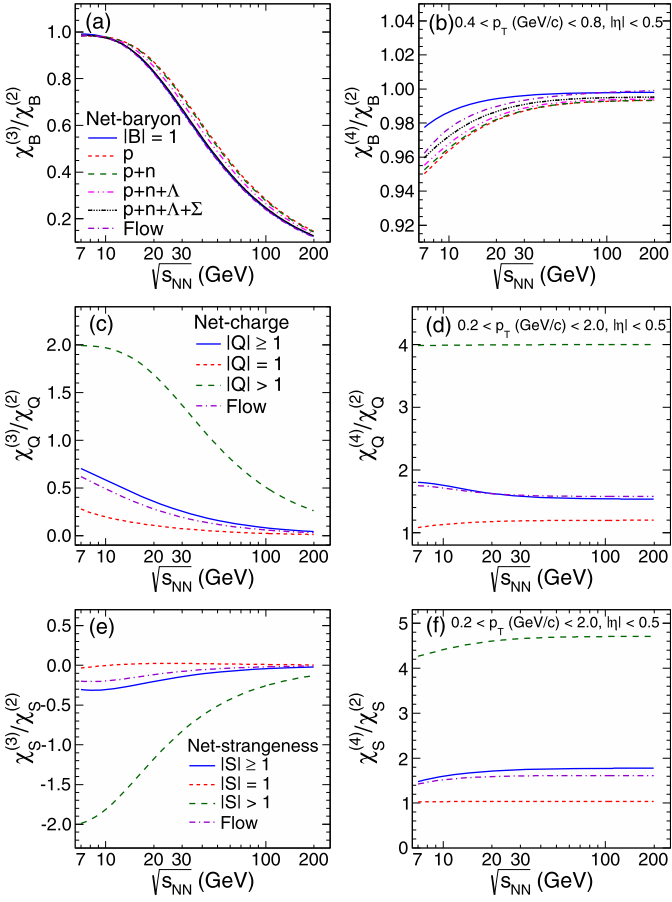


Fig. 3. (Color online.) The variation of $\chi_x^{(3)}/\chi_x^{(2)}$ and $\chi_x^{(4)}/\chi_x^{(2)}$ for net-baryon (B), net-charge (Q), and net-strangeness (S) as a function of collision energy ($\sqrt{s_{NN}}$). The results are shown for different baryons (panels (a) and (b)), electric charge states (panels (c) and (d)) and strangeness number (panels (e) and (f)) considered in the calculation.

prone to kinematic acceptances as compared to the net-charge or net-strangeness fluctuation measures.

3.3. Effect of flow

To study the effect of flow on the ratios of susceptibilities in the HRG model, we now consider an expanding fireball with four velocity,

$$u^\mu = \cosh y_T (\cosh y_0, \tanh y_T, 0, \sinh y_0), \quad (6)$$

where y_0 is the longitudinal and $y_T = \tanh^{-1}(\beta_r)$ is the transverse rapidity of the fireball flowing with radial flow velocity β_r . The four-momentum of the particle can be expressed as:

$$p^\mu = (m_T \cosh \eta, p_T \cos \phi, p_T \sin \phi, m_T \sinh \eta). \quad (7)$$

In the presence of flow, the logarithm of the partition function for i -th particle having four-momentum p^μ can be expressed as

$$\ln Z_i(T, V, \mu_i) = \pm \frac{g_i}{(2\pi)^3} \int d^3 p \frac{p^\mu d\sigma_\mu}{p^0} \times \ln \{1 \pm \exp[(\mu_i - p^\mu u_\mu)/T]\}, \quad (8)$$

where σ represents the space-time surface whose surface elements can be represented by four vector denoted by $d\sigma_\mu$ and p^0 is the energy of the particle. Assuming instantaneous freeze out (at time τ_f) in the radial direction r , $p^\mu d\sigma_\mu$ simplifies as [22]

$$p^\mu d\sigma_\mu = \tau_f r dr d\phi dy_0 m_T \cosh(\eta - y_0). \quad (9)$$

The limit of integration for r varies from 0 to R_f (freeze out radius), ϕ from 0 to 2π , y_0 from $-y_0^{\min}$ to y_0^{\max} ($= \ln(\sqrt{s_{NN}}/m_p)$, where m_p is mass of proton). The other variables p_T and η vary within the experimental acceptances. Note that we recover Eq. (2) for the case of static fireball ($y_T = y_0 = 0$) where $p^\mu u_\mu = E$ and the integral over $(p^\mu d\sigma_\mu)/p^0$ becomes proportional to $4\pi V$. Therefore, for a constant β_r , the flow effect on the susceptibilities can be incorporated by replacing $d^3 p$ integral in Eq. (4) and Eq. (5) with $p_T dp_T d\eta d\phi dy_0 m_T \cosh(\eta - y_0)$ and the energy E in the exponentials by the invariant $p^\mu u_\mu$ as defined above. Further, under the assumption that the flow velocity β_r is independent of radial position, the r integration turns out to be a constant which is proportional to the volume at freeze-out. For the simplicity of the calculations, we have used a constant β_r (same as β_s of Ref. [23]). Fig. 3 also shows the effect of flow (longitudinal + transverse) on the ratios of susceptibilities as a function of collision energy. It is noticed that the ratios of the susceptibilities like $\chi_x^{(4)}/\chi_x^{(2)}$ for net-baryon, net-charge and net-strangeness are affected by less than (2–4)% as compared to the corresponding static values represented by solid blue line.

3.4. Resonance decay

The generalized susceptibility of n -th order can be written as

$$\chi^n = \sum_p \chi_p^n + \sum_R \epsilon_R^n \chi_R^n, \quad (10)$$

where χ_p^n and χ_R^n are the contributions to the n -th order susceptibility due to primordial and resonance yields, respectively. The factor ϵ_R^n is an event averaged efficiency at which resonance R contributes to the generalized susceptibility. Note that $\epsilon_R^n = 1$ when all the decay particles are fully accepted and $\epsilon_R^n < 1$ due to finite detector and kinematic acceptances. Consider the example of the resonance Δ^{++} which decays into p and π^+ with branching ratio b . Using a toy Monte Carlo simulation, we generate Δ^{++} distribution with Poisson statistics and build the charge distributions both for Δ^{++} and the decay particles (proton and pion together) within the experimental acceptances. The Poisson distribution for Δ^{++} is a reasonable assumption as momentum distributions of resonance particles can be approximated by the classical Maxwell–Boltzmann function due to their large masses, although it is not true for their decay products. Therefore, we estimate the efficiency ϵ^n by taking the ratios of the n -th order cumulant of the charge distributions after and before decays. Similar procedures are adopted for other resonances to estimate the average efficiencies ϵ_R^n depending on the charge, strangeness and baryon number as appropriate.

The results of $\chi_x^{(3)}/\chi_x^{(2)}$ and $\chi_x^{(4)}/\chi_x^{(2)}$ with and without considering the effect of resonance daughter particle acceptances are shown in Fig. 4. In Fig. 4(a) and (b), three cases for $\chi_B^{(3)}/\chi_B^{(2)}$ and $\chi_B^{(4)}/\chi_B^{(2)}$ are shown within a realistic acceptance of $|\eta| < 0.5$ and $0.4 < p_T < 0.8$ GeV/c. The results for all baryons without any resonance decay (solid red curve), results for protons without any resonance decay contribution (dotted blue curve) and results for protons with resonance decay (dashed green curve). Similarly in Fig. 4(c) and (d) shows $\chi_Q^{(3)}/\chi_Q^{(2)}$ and $\chi_Q^{(4)}/\chi_Q^{(2)}$, respectively, for all charges without resonance decay (solid red curve), pions, kaons and protons without resonance decay (dotted blue curve) and pions, kaons and protons with resonance decay (dashed green curve). Fig. 4(e) and (f), are shown the results for all strangeness without resonance decay (solid red curve), kaons without resonance decay (dotted blue curve) and kaons with resonance decay (dashed green curve).

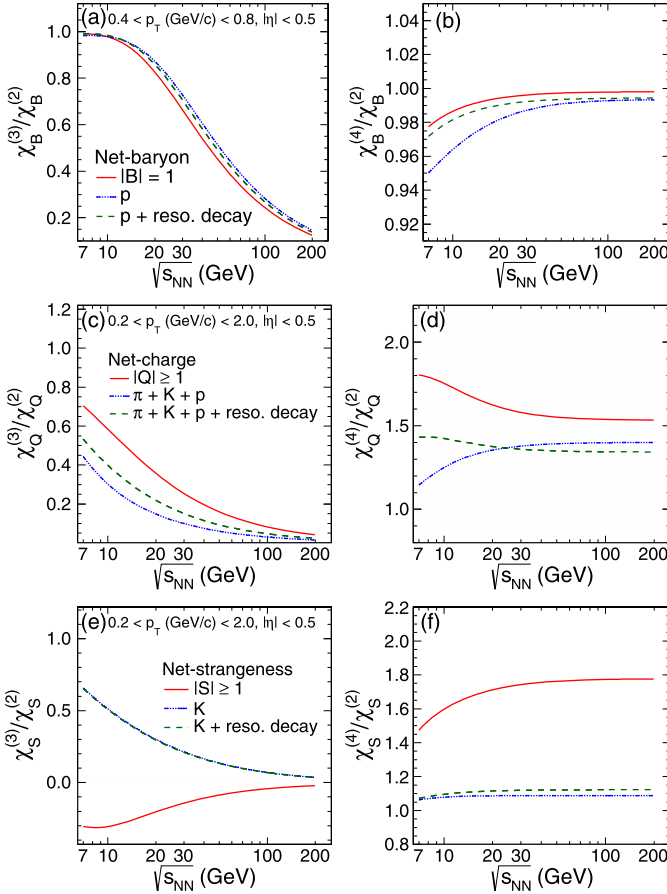


Fig. 4. (Color online.) The variation of $\chi_x^{(3)}/\chi_x^{(2)}$ and $\chi_x^{(4)}/\chi_x^{(2)}$ for net-baryon (B), net-charge (Q), and net-strangeness (S) with different beam energies ($\sqrt{s_{NN}}$) with and without resonance decay daughter particle acceptance effects.

It may be mentioned here that the efficiency ϵ_R^n is an event averaged quantity and will have fluctuations on an event by event basis. Although ϵ_R^n has inherent fluctuation, a rough estimate shows that its effect on the ratio of $\chi_Q^{(4)}/\chi_Q^{(2)}$ is $\sim 2\%$ which we have ignored in the present study. Therefore, the present estimate of the effect of resonance decays on the ratio of susceptibilities are approximate. Nevertheless, it brings out the importance of resonance decays which certainly affect all the ratios. With these assumption, the effects of resonance decay due to finite experimental acceptances are large for net-charge and net-strangeness as compared to net-baryons. The acceptance used in this study are modest and are close to the present experimental acceptances.

Through our work we have emphasized the need for considering experimental acceptances of various kinds in model, such as HRG, before they are considered to provide the baseline to experimental measurements for drawing physics conclusions. Hence in **Tables 1, 2, 3 and 4** we provide values of $\chi_x^{(3)}/\chi_x^{(2)}$ and $\chi_x^{(4)}/\chi_x^{(2)}$ for typical ongoing experimental acceptances. The values quoted in the tables are for static fireball and without including the resonance decay products. The $\chi_Q^{(3)}/\chi_Q^{(2)}$ and $\chi_Q^{(4)}/\chi_Q^{(2)}$ values are provided for two typical acceptances $|\eta| < 0.5$, $0.2 < p_T < 2.0$ GeV/c and $|\eta| < 0.35$, $0.3 < p_T < 1.0$ GeV/c (**Table 1** and **Table 2**). The $\chi_S^{(3)}/\chi_S^{(2)}$ and $\chi_S^{(4)}/\chi_S^{(2)}$ are provided for a typical acceptance of $|\eta| < 0.5$, $0.2 < p_T < 2.0$ GeV/c (**Table 3**). The $\chi_B^{(3)}/\chi_B^{(2)}$ and $\chi_B^{(4)}/\chi_B^{(2)}$ are provided for a typical acceptance of $|\eta| < 0.5$, $0.4 < p_T < 0.8$ GeV/c (**Table 4**).

Table 1

Ratios of the moments for net-charge within $|\eta| < 0.5$, and $0.2 < p_T < 2.0$ GeV/c.

$\sqrt{s_{NN}}$ (GeV)	$\chi_Q^{(3)}/\chi_Q^{(2)}$	$\chi_Q^{(4)}/\chi_Q^{(2)}$
5	0.526	1.413
7.7	0.414	1.430
11.5	0.321	1.407
15	0.265	1.390
19.6	0.215	1.375
27	0.165	1.361
39	0.119	1.352
62.4	0.077	1.346
130	0.038	1.343
200	0.025	1.342
2760	0.002	1.341

Table 2

Ratios of the moments for net-charge within $|\eta| < 0.35$, and $0.3 < p_T < 1.0$ GeV/c.

$\sqrt{s_{NN}}$ (GeV)	$\chi_Q^{(3)}/\chi_Q^{(2)}$	$\chi_Q^{(4)}/\chi_Q^{(2)}$
5	0.432	1.231
7.7	0.332	1.245
11.5	0.256	1.233
15	0.212	1.222
19.6	0.172	1.213
27	0.132	1.205
39	0.095	1.199
62.4	0.062	1.196
130	0.031	1.194
200	0.020	1.193
2760	0.001	1.193

Table 3

Ratios of the moments for net-kaon within $|\eta| < 0.5$, and $0.2 < p_T < 2.0$ GeV/c.

$\sqrt{s_{NN}}$ (GeV)	$\chi_K^{(3)}/\chi_K^{(2)}$	$\chi_K^{(4)}/\chi_K^{(2)}$
5	0.726	1.058
7.7	0.560	1.090
11.5	0.428	1.108
15	0.353	1.115
19.6	0.288	1.120
27	0.222	1.123
39	0.162	1.125
62.4	0.107	1.127
130	0.054	1.128
200	0.035	1.128
2760	0.003	1.128

Table 4

Ratios of the moments for net-proton within $|\eta| < 0.5$, and $0.4 < p_T < 0.8$ GeV/c.

$\sqrt{s_{NN}}$ (GeV)	$\chi_p^{(3)}/\chi_p^{(2)}$	$\chi_p^{(4)}/\chi_p^{(2)}$
5	0.981	0.961
7.7	0.987	0.975
11.5	0.962	0.984
15	0.920	0.988
19.6	0.851	0.991
27	0.737	0.993
39	0.586	0.995
62.4	0.407	0.996
130	0.210	0.997
200	0.139	0.997
2760	0.010	0.997

4. Summary

In summary, using a hadron resonance gas model we have studied the effect of limited experimental acceptance on observables like n -th order susceptibilities $\chi_x^{(n)}$, associated with conserved quantities like net-charge ($x = Q$), net-strangeness ($x = S$)

and net-baryon number ($x = B$). The various order susceptibilities which can also be calculated in QCD based models are related to the moments (σ , S and κ) of the corresponding measured conserved number distributions. These observables have been widely used to understand the freeze-out conditions in heavy-ion collisions and various aspects of the phase structure of the QCD phase diagram. Our study demonstrates the importance of considering experimental acceptances of different kinds before measurements are compared to theoretical calculations, specifically in the use of HRG model as a baseline for such fluctuation based study. We observe finite kinematic acceptances in η and p_T have a strong effect on the $\chi_Q^{(n)}$ and $\chi_S^{(n)}$ values. These susceptibilities are also very sensitive to the accepted electric charge states and strangeness states in the experiment. However, the effect of flow is less than (2–4)% on the ratios of susceptibilities for net-baryon, net-charge and net-strangeness and the improvements can be done in implementation of the radial dependent transverse flow velocities. In addition, we find in this model that, the $\chi_Q^{(n)}$ and $\chi_S^{(n)}$ values depends on the experimental acceptance of the decay daughters from various resonances produced in high energy heavy-ion collisions. Within this model and the kinematic regions used in our study, we find that the dependence on acceptance and resonance decays are stronger for both net-charge and net-strangeness compared to that of net-baryons.

Acknowledgements

We thank Sourendu Gupta for useful discussions related to this Letter. B.M. is supported by the DST SwarnaJayanti project fellow-

ship. P.G. acknowledges the financial support from CSIR, New Delhi, India.

References

- [1] S. Gupta, X. Luo, B. Mohanty, H.G. Ritter, N. Xu, *Science* 332 (2011) 1525.
- [2] R.V. Gavai, S. Gupta, *Phys. Lett. B* 696 (2011) 459.
- [3] F. Karsch, K. Redlich, *Phys. Lett. B* 695 (2011) 136.
- [4] A. Bazavov, H.T. Ding, P. Hegde, O. Kaczmarek, F. Karsch, E. Laermann, S. Mukherjee, P. Petreczky, et al., *Phys. Rev. Lett.* 109 (2012) 192302.
- [5] M.M. Aggarwal, et al., STAR Collaboration, *Phys. Rev. Lett.* 105 (2010) 022302.
- [6] M.A. Stephanov, *Phys. Rev. Lett.* 107 (2011) 052301.
- [7] P. Braun-Munzinger, B. Friman, F. Karsch, K. Redlich, V. Skokov, *Phys. Rev. C* 84 (2011) 064911.
- [8] B. Friman, F. Karsch, K. Redlich, V. Skokov, *Eur. Phys. J. C* 71 (2011) 1694.
- [9] C.B. Yang, X. Wang, *Phys. Rev. C* 84 (2011) 064908.
- [10] M. Asakawa, S. Ejiri, M. Kitazawa, *Phys. Rev. Lett.* 103 (2009) 262301.
- [11] P. Braun-Munzinger, K. Redlich, J. Stachel, in: R.C. Hwa, et al. (Eds.), *Quark Gluon Plasma*, pp. 491–599, arXiv:nucl-th/0304013.
- [12] D. McDonald, STAR Collaboration, arXiv:1210.7023 [nucl-ex].
- [13] J.T. Mitchell, PHENIX Collaboration, arXiv:1211.6139 [nucl-ex].
- [14] V.P. Konchakovski, M.I. Gorenstein, E.L. Bratkovskaya, H. Stocker, *Phys. Rev. C* 74 (2006) 064911.
- [15] M. Hauer, G. Torrieri, S. Wheaton, *Phys. Rev. C* 80 (2009) 014907; M. Hauer, arXiv:1008.1990, and references therein.
- [16] M. Hauer, *Phys. Rev. C* 77 (2008) 034909.
- [17] J. Cleymans, H. Oeschler, K. Redlich, S. Wheaton, *Phys. Rev. C* 73 (2006) 034905, and references therein.
- [18] F. Becattini, M. Gazdzicki, A. Keranen, J. Manninen, R. Stock, *Phys. Rev. C* 69 (2004) 024905.
- [19] F. Becattini, J. Manninen, M. Gazdzicki, *Phys. Rev. C* 73 (2006) 044905.
- [20] J. Cleymans, *J. Phys. G, Nucl. Part. Phys.* 35 (2008) 044017.
- [21] F. Becattini, J. Cleymans, J. Strumpfer, PoS CPOD 07 (2007) 012.
- [22] P.V. Ruuskanen, *Acta Phys. Pol. B* 18 (1987) 551.
- [23] B.I. Abelev, et al., STAR Collaboration, *Phys. Rev. C* 79 (2009) 34909.

Unfolding of event-by-event net-charge distributions in heavy-ion collision

**P Garg¹, D K Mishra², P K Netrakanti², A K Mohanty²
and B Mohanty^{3,4}**

¹ Department of Physics, Banaras Hindu University, Varanasi 221005, India

² Nuclear Physics Division, Bhabha Atomic Research Center, Mumbai 400085, India

³ School of Physical Sciences, National Institute of Science Education and Research, Bhubaneswar 751005, India

E-mail: bedanga@niser.ac.in

Received 9 November 2012

Published 21 March 2013

Online at stacks.iop.org/JPhysG/40/055103

Abstract

We discuss a method to obtain the true event-by-event net-charge multiplicity distributions from a corresponding measured distribution which is subjected to detector effects such as finite particle counting efficiency. The approach is based on the Bayes method for the unfolding of distributions. We are able to faithfully unfold back the measured distributions to match their corresponding true distributions obtained for a widely varying underlying particle production mechanism, beam energy and collision centrality. Particularly the mean, variance, skewness, kurtosis and their products and ratios of net-charge distributions from the event generators are shown to be successfully unfolded from the measured distributions constructed to mimic a real experimental distribution. We demonstrate the necessity to account for detector effects before associating the higher moments of net-charge distributions with physical quantities or phenomena. The advantage of this approach is that one need not construct new observables to cancel out detector effects which lose their ability to be connected to physical quantities calculable in standard theories.

(Some figures may appear in colour only in the online journal)

1. Introduction

Higher moments of the event-by-event distribution of conserved quantities such as net-charge, net-baryon number and net-strangeness in heavy-ion collisions have been found to be useful observables to characterize the system formed in the collisions [1]. Higher moments have been shown to be related to the correlation length [2] and susceptibilities [3, 4] of the system and hence can be used to look for signals of phase transition and critical point [5–7]. They have also been shown to be useful for studying the bulk QCD thermodynamics at high temperature [8].

⁴ Author to whom any correspondence should be addressed.

Specifically, proposals have been made to extract the freeze-out properties of the system using higher moments of net-charge and net-baryon number distributions, in a way very similar to that done using the particle yields and ratios [9–11].

Any experimental measurement is susceptible to effects such as finite acceptance, finite efficiency of counting the number of particles produced in the collisions and other background effects [12]. It is almost impossible to know some of these quantities for each event so as to correct for the effects in an event-by-event distribution. Hence most of the experimentally measured event-by-event distributions are presented without these corrections [1, 13–15]. These corrections are carried out on an average level for reporting the yields of the produced particles (typically the first moment of the multiplicity distributions) [12]. Comparison of uncorrected experimental event-by-event distributions to theoretical calculations needs to be done carefully. For example, using the corrected mean multiplicities to explain the uncorrected measured event-by-event distributions could lead to different conclusions [16, 17].

Judicious construction of event-by-event observables has been proposed to cancel out detector effects to first order [18–21]. However, while making these constructs, one may sometimes lose the ability to compare them to the theoretically calculated quantities in order to extract meaningful physical insights. That introduces additional complexities which makes a proper physical interpretation of the observable difficult. As an example, the moments of the multiplicity distribution of conserved quantities can be shown to be proportional to correlation length (ξ) of the system. The variances ($\sigma^2 \equiv \langle (\Delta N)^2 \rangle$; $\Delta N = N - M$; M is the mean) of these distributions are related to ξ as $\sigma^2 \sim \xi^2$, skewness ($S = \langle (\Delta N)^3 \rangle / \sigma^3$) goes as $\xi^{4.5}$ and kurtosis ($\kappa = [\langle (\Delta N)^4 \rangle / \sigma^4] - 3$) goes as ξ^7 [2]. Their products such as $\kappa \sigma^2$ are related to the ratio of fourth order ($\chi^{(4)}$) to second order ($\chi^{(2)}$) susceptibilities [3, 4]. Where $\chi^{(2)} = \frac{\langle (\Delta N)^2 \rangle}{V T}$, V is the volume, and ΔN could be the net-baryon number or net-charge number. In order to cancel out the acceptance and efficiency effects to first order for these observables, constructs such as normalized factorial moments (defined later) can be made. The factorial moments of a particular order, however, become the complicated function of lower order moments, thereby making their interpretation difficult in terms of physical observables such as ξ or χ calculated in a standard theory.

Here we give a simple calculation to illustrate our point of view. Let N represent the produced multiplicity and n be the actually measured multiplicity in an experiment. We parametrize the detector response in the experiment by a binomial probability distribution function given by

$$B(n : N, \epsilon) = \frac{N!}{n!(N-n)!} \epsilon^n (1-\epsilon)^{N-n}, \quad (1)$$

where ϵ is the particle counting efficiency.

We further consider that the produced multiplicity follows probability distribution function $P(N)$, and that for measured distribution is $P(n)$. Then the mean of measured multiplicity distribution $\langle n \rangle$ can be related to the mean of the actually produced multiplicity distribution as

$$\begin{aligned} \langle n \rangle &= \int n P(n) dn = \int n dn \int B(n | N) P(N) dN \\ &= \int P(N) dN \int B(n | N) n dn = \epsilon \int P(N) N dN = \epsilon \langle N \rangle. \end{aligned} \quad (2)$$

Similarly it can be shown that

$$\langle n^2 \rangle = \epsilon(1-\epsilon)\langle N \rangle + \epsilon^2 \langle N^2 \rangle. \quad (3)$$

Now let us suppose that we can correct the event-by-event particle counting efficiency; the variance of the resultant measured distribution can be shown to be

$$\sigma^2(n/\epsilon) = \frac{1-\epsilon}{\epsilon} \langle N \rangle + \sigma^2(N). \quad (4)$$

We find that the variance of n/ϵ is not equal to the variance of N even though the mean of n/ϵ is equal to the mean of N . Similar derivations and conclusions can be done for higher order moments.

Alternatively, one can construct second order factorial moments such as

$$\frac{\langle n(n-1) \rangle}{\langle n \rangle^2} = \frac{\epsilon^2 \langle N(N-1) \rangle}{\epsilon^2 \langle N \rangle^2} = \frac{\langle N(N-1) \rangle}{\langle N \rangle^2}, \quad (5)$$

and the fourth order factorial moment as

$$\frac{\langle n(n-1)(n-2)(n-3) \rangle}{\langle n \rangle^4} = \frac{\langle N(N-1)(N-2)(N-3) \rangle}{\langle N \rangle^4}. \quad (6)$$

These are found to be independent of efficiency effects. In these we also assume that ϵ does not vary event-by-event.

However, a closer look at these constructs will reveal that

$$\frac{\langle n(n-1) \rangle}{\langle n \rangle^2} = \frac{\sigma^2}{\langle n \rangle^2} - \frac{1}{\langle n \rangle} + 1 \quad (7)$$

and

$$\begin{aligned} \frac{\langle n(n-1)(n-2)(n-3) \rangle}{\langle n \rangle^4} = & 11 \frac{\sigma^2}{\langle n \rangle^4} + \frac{1}{\langle n \rangle^2} - 6S \frac{\sigma^3}{\langle n \rangle^4} - 18 \frac{\sigma^2}{\langle n \rangle^3} + \kappa \frac{\sigma^4}{\langle n \rangle^4} \\ & + 4S \frac{\sigma^3}{\langle n \rangle^3} - 3 \frac{\sigma^2}{\langle n \rangle^2} - 2 - \frac{6}{\langle n \rangle^3}. \end{aligned} \quad (8)$$

While trying to remove the detector effects we have arrived at constructs which lose the purity of moments or become involved functions of lower order moments, thereby making it difficult to directly connect to physical observables such as susceptibilities or their ratios, which can give important insights as to the bulk properties of the system formed in heavy-ion collisions.

Keeping in mind the importance of higher moments of multiplicity distributions to characterize the system formed in heavy-ion collisions, it is necessary to have a proper way of comparing the measurements and theory calculations, while at the same time ensuring that experimental artifacts like acceptance and particle counting efficiency are removed. In this paper, we propose an approach based on unfolding of the measured (actually measured in experiments) multiplicity distribution to get back the true (actually produced in the collisions) distributions produced in the collisions. Such a method seems to work only if the detector response can be satisfactorily modeled and the statistics is large enough.

This paper is organized as follows. In the next section we discuss the event generators used in this study. In section 3 we discuss the method of unfolding. In section 4 we present the results for the moments of the net-charge distribution as a function of collision centrality (defined in terms of the number of participating nucleons, N_{part}). A brief discussion of the limitations of the approach is also presented. Finally we summarize our study in section 5.

2. Event generators

In this study we have used two event generators, HIJING [22] (version 1.37) and THERMINATOR [23] (version 2.0). They provide the possibility of different probability distribution for charged particle multiplicity in order to study our proposal. While HIJING distributions are based on the physics due to QCD inspired models for multiple jet production,

the THERMINATOR distributions are based on systems in thermodynamical equilibrium. Further details of the models can be found in [22] for HIJING and in [23] for THERMINATOR. For HIJING the events were generated with default settings and jet quenching on, while for THERMINATOR the default settings were used. We only focus on the net-charge distributions within a realistic acceptance of the current experiments at RHIC, that is a pseudorapidity range between $-0.5 < \eta < 0.5$ and a transverse momentum range between $0.2 < p_T < 2.0$ GeV/c with full azimuthal coverage. The analysis is carried out for 19.6 GeV Au+Au collisions using the events from the HIJING model and 200 GeV Au+Au collisions using the events from the THERMINATOR model as a function of collision centrality. About five million events are produced for each centrality studied in both the event generators. We have checked that the conclusions from each model at other energies are similar to that presented in this paper. Such a combination of model and beam energy is an arbitrary choice made to reflect a wide range of kinematics and physics of particle production. The average charged particle multiplicity counting efficiency is taken to be 65% following the efficiency as a function of p_T available for charged pions in [12].

3. Bayes method for the unfolding of distributions

The Bayes unfolding algorithm of the RooUnfold package is generally used to remove the effects of measurement resolutions, systematic biases and detection efficiency to determine the true distributions [24]. The RooUnfoldBayes algorithm based on the Bayes theorem uses the method described by D'Agostini in [25].

The procedure of Bayes unfolding can be explained by causes C and effects E . In our study, *causes* correspond to the true multiplicity values and *effects* to the measured multiplicity values which are affected by the inefficiencies. If one observes $n(E)$ events with effect E due to several independent causes ($C_i, i = 1, 2, \dots, n_C$) then the expected number of events assignable to each of the causes is given by:

$$\hat{n}(C_i) = n(E)P(C_i|E) \quad (9)$$

where

$$P(C_i|E) = \frac{P(E|C_i)P(C_i)}{\sum_{l=1}^{n_C} P(E|C_l)P(C_l)} \quad (10)$$

Now if we observe that the outcome of a measurement has several possible effects $E_j (j = 1, 2, 3, \dots, n_E)$ for a given cause C_i then the expected number of events to be assigned to each of the causes and due only to the observed events can be calculated to each effect by:

$$\hat{n}(C_i) = \sum_{j=1}^{n_E} n(E_j)P(C_i|E_j). \quad (11)$$

$P(C_i|E_j)$ is the probability that different causes C_i were responsible for the observed effect E_j and is calculated by the Bayes theorem as:

$$P(C_i|E_j) = \frac{P(E_j|C_i)P_0(C_i)}{\sum_{l=1}^{n_C} P(E_j|C_l)P_0(C_l)} \quad (12)$$

where $P_0(C_i)$ are the initial probabilities. If we take into account the inefficiency then the best estimate of the true number of events is given by

$$\hat{n}(C_i) = \frac{1}{\epsilon_i} \sum_{j=1}^{n_E} n(E_j)P(C_i|E_j) \quad \epsilon_i \neq 0 \quad (13)$$

where ϵ_i is the efficiency of detecting the cause C_i in any of the possible effects. If $\epsilon_i = 0$ then $\hat{n}(C_i)$ is set to zero, since the experiment is not sensitive to the cause C_i .

The above equation can be written in terms of unfolding or response matrix M_{ij} as

$$\hat{n}(C_i) = \sum_{j=1}^{n_E} M_{ij} n(E_j) \quad (14)$$

The response matrix is constructed by repeated application of the Bayes theorem and the regularization is achieved by stopping the iterations before reaching the ‘true’ inverse. Further details of the procedure can be found in [25].

For the present study, 5M Au+Au collision events are produced for each centrality bin at $\sqrt{s_{NN}} = 19.6$ GeV and 200 GeV using HIJING and THERMINATOR event generators respectively. With these events, the *true* distribution of net-charge ($\Delta N = N^+ - N^-$) is constructed on an event-by-event basis. The positive (N^+) and negative (N^-) charged particles are selected for each event with a transverse momentum range between $0.2 < p_T < 2.0$ GeV/c and a pseudorapidity range between $-0.5 < \eta < 0.5$ with full azimuthal coverage.

The individual *true* N^+ and N^- are smeared with a Gaussian function with the mean value corresponding to the average efficiency of 65% as obtained from the parametrization of the p_T dependent efficiency for charged pions from the STAR experiment [12]. The width of the Gaussian distribution is taken as 10% of the mean. The smeared N^+ and N^- distributions will be called *measured* distributions. The measured net-charge distribution is then constructed with these *measured* N^+ and N^- distributions.

To construct the response matrix for each centrality, 2.5 M events are used as *training true* distributions of net-charge and rest of the events are used as *training measured* (after smearing on an event-by-event basis) distributions. The events for *training true* and *training measured* are selected separately to construct the response matrix, in order to avoid the effect of auto-correlation. It also uses the information of an event that is not measured out of true distributions and is counted toward the inefficiency while constructing the response matrix.

The measured distribution of net-charge from the remaining 2.5 M events is unfolded with the response matrix obtained from the training procedure using the iterative Bayes theorem. The number of iterations is called the regularization parameter. This study uses the optimal value of 4 for the regularization. True, measured and unfolding are done for finer bins of each centrality and then combined to make 5% bin to eliminate the finite centrality bin-width effect. The moments of net-charge distributions are derived using a cumulant method as described in [26] and are compared for true, measured and unfolded distributions.

4. Results and discussions

Figure 1 shows the true, measured and unfolded distributions for positive charge (panel (a)), negative charge (panel (b)) and net-charge (panel (c)) for most central events corresponding to an average impact parameter of 1.7 fm of Au+Au collisions from HIJING at $\sqrt{s_{NN}} = 19.6$ GeV on an event-by-event basis. The true distributions are shown as solid lines, measured distributions (subjected to particle counting efficiency) are shown as blue open circles and the unfolded distributions denoted as ‘Bayes’ are shown as red stars. For all the cases, the respective true distributions are reproduced from the measured distribution using the unfolding technique. The bottom panel of figure 1 shows the ratio of unfolded to true distributions corresponding to the same distributions as shown in the respective top panels of figure 1.

The ratio is close to unity within the statistical errors, suggesting that the unfolding procedure is able to get back the true distribution from a measured distribution which is subjected to inefficiencies in particle counting. Similar conclusions are obtained for distributions for Au+Au collisions at $\sqrt{s_{NN}} = 200$ GeV from THERMINATOR, and hence are not shown in this paper. From now on we will only concentrate on the net-charge distributions.

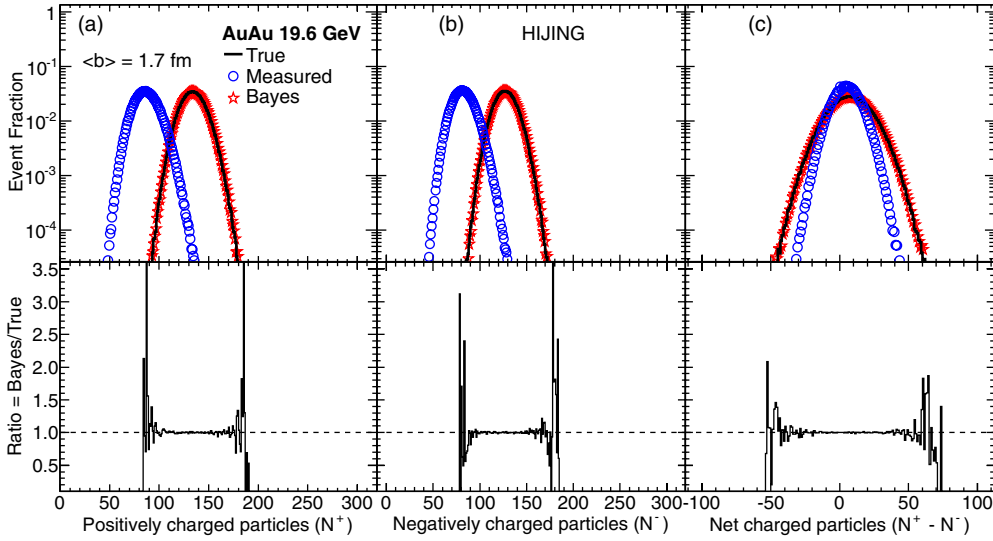


Figure 1. Top panel. Event-by-event distributions of positive, negative and net-charge (denoted as ‘true’; solid line) in Au+Au collisions for impact parameter $b = 1.7$ fm at $\sqrt{s_{\text{NN}}} = 19.6$ GeV from the HIJING event generator. Also shown are the corresponding distributions after applying acceptance and efficiency effects as discussed in the text (denoted as ‘measured’; open circles). The unfolded distributions are shown as red stars and denoted as ‘Bayes’. Bottom panel. The ratio of the unfolded to the true distributions.

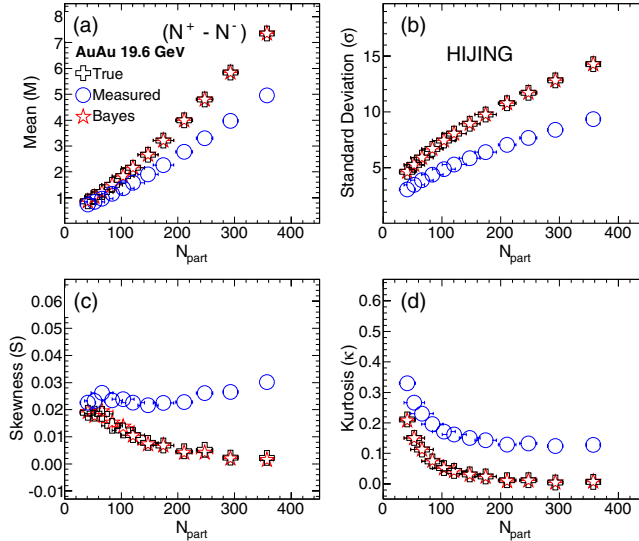


Figure 2. Mean, standard deviation, skewness and kurtosis of net-charge distribution in Au+Au collisions at $\sqrt{s_{\text{NN}}} = 19.6$ GeV from the HIJING event generator. Results are shown for the true, measured and Bayes unfolded distributions as a function of N_{part} .

The four moments M , σ , S and κ of the net-charge distributions in Au+Au collisions at $\sqrt{s_{\text{NN}}} = 19.6$ GeV from the constructed true, measured and unfolded distributions as a function of centrality (N_{part}) are shown in figure 2. The mean and standard deviation increases with N_{part} ,

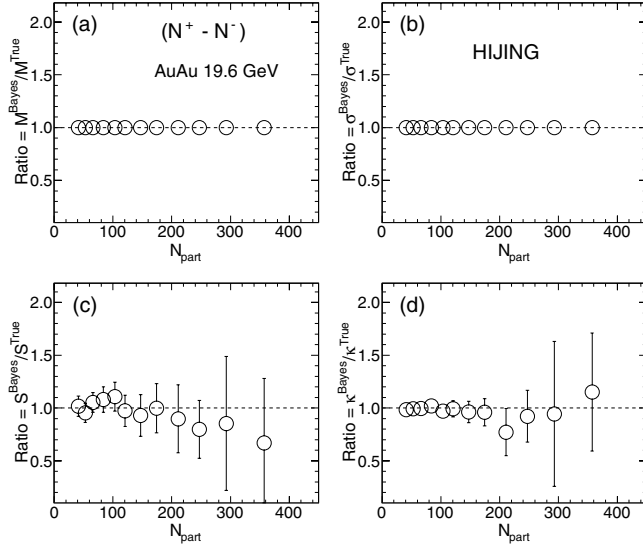


Figure 3. Ratio of the unfolded to the true net-charge distribution moments of figure 2 as a function of N_{part} .

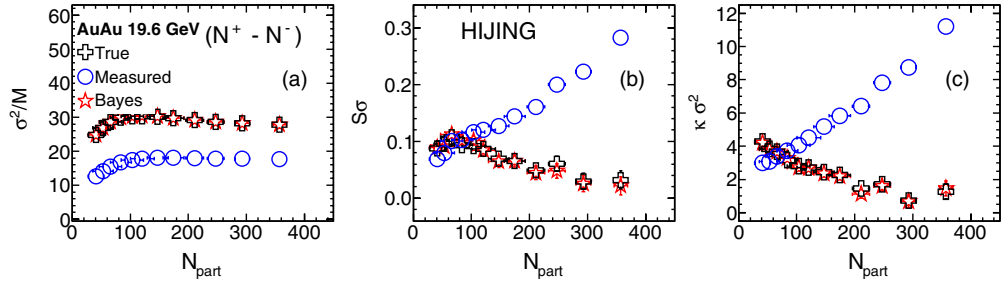


Figure 4. Ratio (panel (a)) and product of moments (panels (b) and (c)) of net-charge distributions in Au+Au collisions at $\sqrt{s_{\text{NN}}} = 19.6$ GeV from the HIJING event generator. The results are for the true, measured and Bayes unfolded distributions as a function of N_{part} .

while the skewness and kurtosis decreases with N_{part} . This is in accordance with the central limit theorem [1]. The mean and variance of the measured distributions are smaller compared to those of the true distributions, as we have particle counting inefficiencies for the measured case. The unfolded moments are found to closely follow the corresponding values of their respective true distributions. This can be more clearly seen from the ratio plots in figure 3. The value of the ratio of unfolded to true distributions as a function of N_{part} is around unity for all the four moments studied. Thus the unfolding method followed in this paper reproduces all the moments of the true distribution from the measured distribution. Although not shown here, similar conclusions are obtained separately for the positive and negative charged particle multiplicity distributions.

The centrality dependence of ratio of moments (σ^2/M) and product of moments ($S\sigma$ and $K\sigma^2$) are shown in figure 4. The importance of unfolding is clearly demonstrated by looking at the dependences of the ratio and product of moments on the N_{part} . While for the true distribution the product of moments decreases with N_{part} , those for the measured distribution actually have an opposite trend. Indicating any physics conclusions associated with the variation of $S\sigma$ and

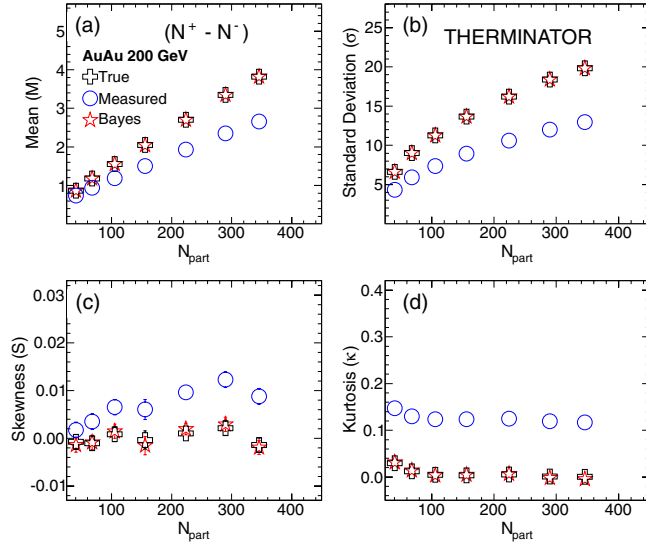


Figure 5. Mean, standard deviation, skewness and kurtosis of net-charge distribution in Au+Au collisions at $\sqrt{s_{NN}} = 200$ GeV from the THERMINATOR event generator. Results are shown for the true, measured and Bayes unfolded distributions as a function of N_{part} .

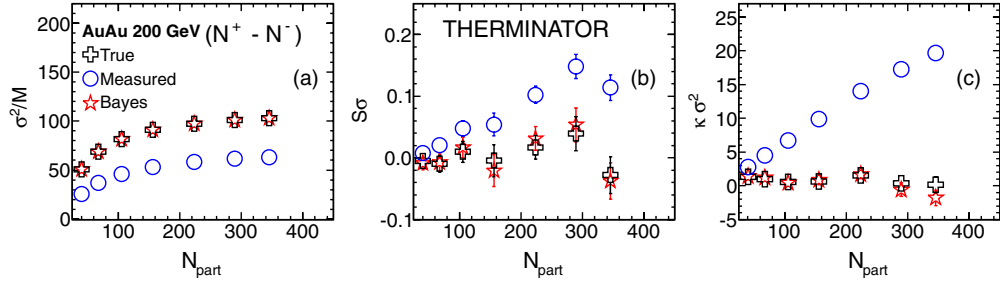


Figure 6. Product of moments of net-charge distributions in Au+Au collisions at $\sqrt{s_{NN}} = 200$ GeV from the THERMINATOR event generator. The results are for the true, measured and Bayes unfolded distributions as a function of N_{part} .

$\kappa\sigma^2$ with N_{part} for net-charge distributions could be highly misleading. However, very good agreement between true and unfolded distributions is observed. They are nicely consistent even for the product of higher moments ($S\sigma$ and $\kappa\sigma^2$) which are very sensitive to the shape of the distributions, suggesting that the unfolded distributions are well reproduced as the true distributions by using the Bayes unfolding algorithm.

In order to validate the applicability of the unfolding algorithm for different physics processes, a thermal model-based THERMINATOR event generator is also used. Figure 5 shows the centrality dependence of various moments of net-charge distribution in Au+Au collisions at $\sqrt{s_{NN}} = 200$ GeV from the true, measured and unfolded distributions. The trends of the moments as a function of N_{part} is similar to that seen for HIJING (figure 2), although the magnitude of the moments is different. All the four moments of the unfolded distributions are well reproduced as the true distributions.

Figure 6 shows the σ^2/M , $S\sigma$ and $\kappa\sigma^2$ as a function of N_{part} of net-charge distributions from the true, measured and unfolded distributions. Here also, as was seen for the HIJING

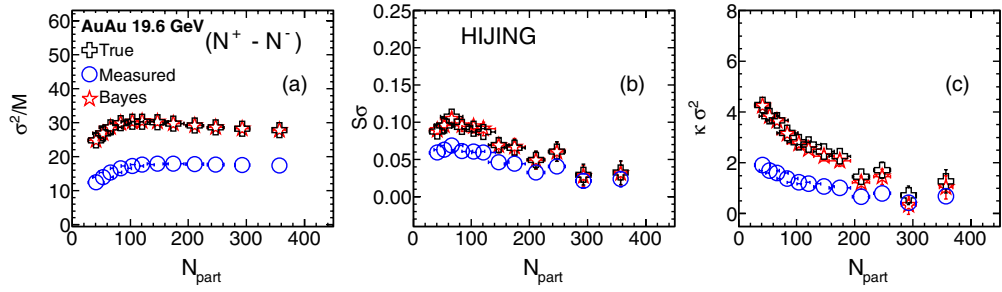


Figure 7. Product of moments of net-charge distributions in Au+Au collisions at $\sqrt{s_{\text{NN}}} = 19.6$ GeV from the HIJING event generator with constant efficiency of 65%. The results are for the true, measured and Bayes unfolded distributions as a function of N_{part} .

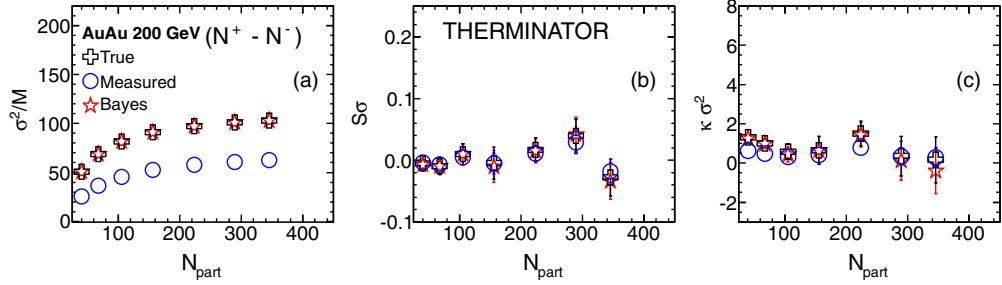


Figure 8. Product of moments of net-charge distributions in Au+Au collisions at $\sqrt{s_{\text{NN}}} = 200$ GeV from the THERMINATOR event generator with constant efficiency of 65%. The results are for the true, measured and Bayes unfolded distributions as a function of N_{part} .

results (figure 4), the ratio and products of moments from unfolded distributions are reproduced as true distributions to a good extent. This suggests that the method proposed in this paper works equally well for parent distributions produced from very different particle production mechanisms as well as over a wide range of beam energies.

To study the effect of variation of efficiency on the ratio and product of moments, the true distributions are smeared with a constant efficiency of 65% to obtain the measured distributions. Figures 7 and 8 show the σ^2/M , $S\sigma$ and $\kappa\sigma^2$ as a function of N_{part} of net-charge distributions from the true, measured and unfolded distributions with constant efficiency in Au+Au collisions at $\sqrt{s_{\text{NN}}} = 19.6$ GeV and 200 GeV from the HIJING and THERMINATOR event generators, respectively. Panel (a) of figures 7 and 8 shows a similar effect as for event-by-event variation of efficiency (panel (a) of figures 4 and 6) on the σ^2/M of the measured distributions. The effect of constant efficiency on $S\sigma$ and $\kappa\sigma^2$ (panels (b) and (c) of figures 7 and 8) of measured distributions is small as compared to event-by-event varying efficiency.

In order to see the effect of energy dependence on our results we have carried out this study for net-charge distributions at midrapidity in 0–5% central Au+Au collisions in the HIJING model for $\sqrt{s_{\text{NN}}} = 19.6, 27, 39, 62.4, 130$ and 200 GeV. The efficiency varies event-by-event as per a Gaussian distribution with a mean of 65% and width of 10% of the mean. Figure 9 shows the mean, standard deviation, skewness and kurtosis for the above system as a function of beam energy. The mean and variance of the measured distributions are smaller compared to those of the true distributions, as we have seen for the centrality dependence study (figures 2 and 5). This is due to the particle counting inefficiencies for the measured case. The unfolded moments are found to closely follow the corresponding values of their respective true

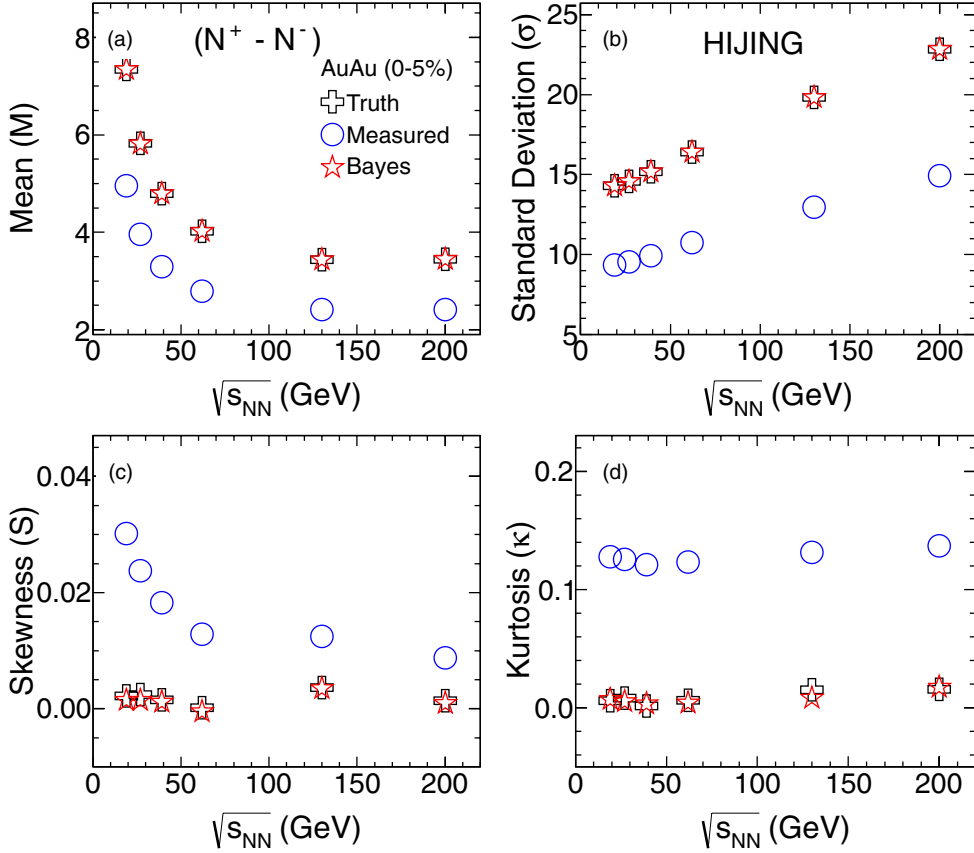


Figure 9. Mean, standard deviation, skewness and kurtosis of net-charge distribution in 0–5% Au+Au collisions as a function of $\sqrt{s_{NN}}$ from the HIJING event generator. Results are shown for the true, measured and Bayes unfolded distributions.

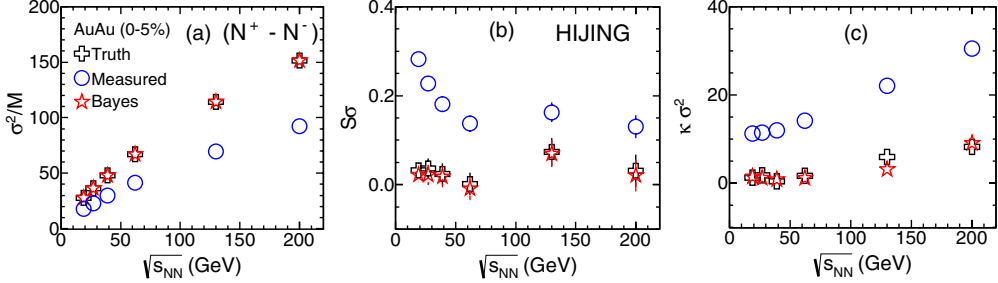


Figure 10. Product of moments of net-charge distribution in 0–5% Au+Au collisions as a function of $\sqrt{s_{NN}}$ from the HIJING event generator. The results are for the true, measured and Bayes unfolded distributions.

distributions. Figure 10 shows the σ^2/M , $S\sigma$ and $\kappa\sigma^2$ as a function of $\sqrt{s_{NN}}$ of 0–5% Au+Au collisions net-charge distributions from the true, measured and unfolded distributions. Here also, as was seen for the centrality dependence results, the ratio and products of moments from unfolded distributions are reproduced as true distributions to a good extent. This suggests that

the method proposed in this paper works for parent distributions produced over a wide range of beam energies.

Our study shows that it is important to correct for event-by-event detector related effects before proper conclusions can be obtained from higher moment studies in heavy-ion collisions. We have provided a method of obtaining the true distributions through an unfolding technique. Such a method keeps the observables the same and hence has the advantage of being used to make comparisons with standard theory calculations. Although this procedure can be easily adapted to experimentally measured distributions, it has two important drawbacks. Unlike the current case, where we have used an event generator for the study and the true distribution is available for comparison, in a real experiment the true distribution is unknown. Hence it is crucial that a realistic modeling of the detector response and particle production is available to obtain the response matrix for the unfolding calculations. In most cases, the modeling of the particle production and the detector response is highly dependent on the event generator and on how realistically the experimental conditions are simulated. The other disadvantage is that the procedure only works well for high event statistics as well as high average particle multiplicity per event. We have seen that large uncertainties enter into the unfolded distributions if we carry out this study with net-protons.

5. Summary

In summary, we have discussed a method to obtain the event-by-event true distributions of net-charge from the corresponding measured distributions which are subjected to detector effects such as finite particle counting efficiencies. The approach used is based on the Bayes method for the unfolding of distributions. We have used event generators HIJING and THERMINATOR to simulate the charged particle distributions produced in Au+Au collisions at $\sqrt{s_{\text{NN}}} = 19.6$ to 200 GeV, respectively. The charged particle counting efficiency was varied by smearing the true distributions, on an event-by-event basis using a Gaussian function with mean 0.65 and width 0.065, to construct the measured distributions. We have shown that the unfolded distribution has similar mean, variance, skewness and kurtosis as the true distributions for all the collision centralities studied. The products of the moments σ^2/M , $S\sigma$ and $\kappa\sigma^2$ which show opposite trends versus N_{part} for the measured distributions compared to the true distributions are faithfully unfolded back to agree with the true distributions. For cases where the efficiency of charged particle counting is constant for all events, the differences between the measured and the true are small for the product $S\sigma$ and $\kappa\sigma^2$ compared to the ratio σ^2/M . The unfolding process is demonstrated to work for distributions obtained from widely differing physical mechanisms for the production of charged particles and over a wide range of beam energies and collision centrality. They also work for the cases where the charged particle counting efficiencies vary event-by-event as well as for the case where the efficiencies are constant.

This method has some limitations, in terms of the need for a proper modeling of the detector response and works well for high multiplicity and for high event statistics datasets. However, the main advantage of this method is that we do not have to construct new observables which cancels out the detector effects, as the new constructs are usually subjected to difficulties in physical interpretation and cannot be directly compared to standard theoretical calculations.

Acknowledgments

Financial assistance from the Department of Atomic Energy, Government of India is gratefully acknowledged. BM is supported by the DST SwarnaJayanti project fellowship.

PG acknowledges financial support from CSIR, New Delhi, India. This work is carried out using the NPD-BARC cluster facility at HBNI.

References

- [1] Aggarwal M M *et al* (STAR Collaboration) 2010 *Phys. Rev. Lett.* **105** 022302 (arXiv:1004.4959 [nucl-ex])
- [2] Stephanov M A 2009 *Phys. Rev. Lett.* **102** 032301 (arXiv:0809.3450 [hep-ph])
- [3] Bazavov A *et al* (HotQCD Collaboration) 2012 *Phys. Rev. D* **86** 034509 (arXiv:1203.0784 [hep-lat])
- [4] Cheng M *et al* 2009 *Phys. Rev. D* **79** 074505 (arXiv:0811.1006 [hep-lat])
- [5] Stephanov M A 2011 *Phys. Rev. Lett.* **107** 052301 (arXiv:1104.1627 [hep-ph])
- [6] Asakawa M, Ejiri S and Kitazawa M 2009 *Phys. Rev. Lett.* **103** 262301 (arXiv:0904.2089 [nucl-th])
- [7] Hatta Y and Stephanov M A 2003 *Phys. Rev. Lett.* **91** 102003 (arXiv:hep-ph/0302002)
Hatta Y and Stephanov M A 2003 *Phys. Rev. Lett.* **91** 129901 (erratum)
- [8] Gupta S, Luo X, Mohanty B, Ritter H G and Xu N 2011 *Science* **332** 1525 (arXiv:1105.3934 [hep-ph])
- [9] Gavai R V and Gupta S 2011 *Phys. Lett. B* **696** 459 (arXiv:1001.3796 [hep-lat])
- [10] Karsch F and Redlich K 2011 *Phys. Lett. B* **695** 136 (arXiv:1007.2581 [hep-ph])
- [11] Friman B, Karsch F, Redlich K and Skokov V 2011 *Eur. Phys. J. C* **71** 1694 (arXiv:1103.3511 [hep-ph])
- [12] Abelev B I *et al* (STAR Collaboration) 2009 *Phys. Rev. C* **79** 034909 (arXiv:0808.2041 [nucl-ex])
- [13] Appelshauser H *et al* (NA49 Collaboration) 1999 *Phys. Lett. B* **459** 679 (arXiv:hep-ex/9904014)
- [14] Aggarwal M M *et al* (WA98 Collaboration) 2002 *Phys. Rev. C* **65** 054912 (arXiv:nucl-ex/0108029)
- [15] Adcox K *et al* (PHENIX Collaboration) 2002 *Phys. Rev. Lett.* **89** 082301 (arXiv:nucl-ex/0203014)
- [16] Braun-Munzinger P, Friman B, Karsch F, Redlich K and Skokov V 2011 *Phys. Rev. C* **84** 064911
(arXiv:1107.4267 [hep-ph])
- [17] Mohanty B 2011 Talk given at *Int. Workshop on Critical Point and Onset of Deconfinement (Wuhan, China)*
- [18] Mrowczynski S 1999 *Phys. Lett. B* **465** 8 (arXiv:nucl-th/9905021)
- [19] Voloshin S A, Koch V and Ritter H G 1999 *Phys. Rev. C* **60** 024901 (arXiv:nucl-th/9903060)
- [20] Bialas A 2007 *Phys. Rev. C* **75** 024904 (arXiv:hep-ph/0701074)
- [21] Pruneau C, Gavin S and Voloshin S 2002 *Phys. Rev. C* **66** 044904 (arXiv:nucl-ex/0204011)
- [22] Gyulassy M and Wang X-N 1994 *Comput. Phys. Commun.* **83** 307 (arXiv:nucl-th/9502021)
- [23] Kisiel A, Taluc T, Broniowski W and Florkowski W 2006 *Comput. Phys. Commun.* **174** 669
(arXiv:nucl-th/0504047)
- [24] Adye T 2011 RooUnfold package arXiv:1105.1160 [physics.data-an]
- [25] D'Agostini G 1995 *Nucl. Instrum. Methods A* **362** 487
- [26] Luo X 2012 *J. Phys. G: Nucl. Part. Phys.* **39** 025008 (arXiv:1109.0593 [nucl-ex])



ELSEVIER

Available online at www.sciencedirect.com



ScienceDirect

Nuclear Physics A 862–863 (2011) 479–482

NUCLEAR
PHYSICS A

www.elsevier.com/locate/nuclphysa

Performance studies of the PHENIX Hadron Blind Detector at RHIC

P. Garg and B. K. Singh
(For PHENIX Collaboration)

Department of Physics, Banaras Hindu University, Varanasi-221005, India

Abstract

Electron pairs or di-leptons in general are unique probes to study the hot and dense matter formed in relativistic heavy ion collisions at RHIC. Particularly, low mass di-leptons are sensitive to chiral symmetry restoration effects and to thermal radiation emitted by the plasma via virtual photons, providing a direct measurement of the quark gluon plasma temperature. But the experimental challenge is the huge combinatorial background created by e^+e^- pairs from copiously produced π^0 Dalitz decay and γ conversions. In order to reduce this background, a Hadron Blind Detector was proposed in PHENIX for electron identification in high-density hadron environment. In the present paper some of the performance studies of the HBD carried with data from 2009 Run are discussed.

Keywords: Quark Gluon Plasma, Low mass Dileptons, Hadron Blind Detector

1. Introduction

Hadron Blind Detector (HBD) was developed and installed as an upgrade of the PHENIX experiment at the Relativistic Heavy Ion Collider (RHIC) experiment for the measurement of electron pairs, particularly in the low mass region ($m \leq 1 \text{ GeV}/c^2$ including the light vector mesons ρ , ω and ϕ)[1]. Dileptons are valuable probes for the hot and dense matter formed in ultra-relativistic heavy-ion collisions. They play a crucial role in the quest for the QCD phase transition from hadron gas (HG) to the quark gluon plasma (QGP) expected to be formed in these collisions. They can provide evidence of chiral symmetry restoration and deconfinement phase transition[2].

Dileptons offer also the possibility to identify the thermal radiation emitted from the QGP via $q\bar{q}$ annihilation. Such a radiation is regarded as a very strong signal of deconfinement. There is no convincing evidence for thermal radiation from the QGP at lower energies, either in the dilepton or in the real photon channels. Theoretical calculations have singled out the dilepton intermediate mass range ($m = 1 - 3 \text{ GeV}/c^2$) as the most appropriate window for the observation of QGP thermal radiation[4].

The measurement of dileptons in heavy ion collisions is a challenging task because of the huge combinatorial background in the low mass region. Electron pairs measured in PHENIX from the 2004 Run showed very low signal-to-background ratio $S/B \sim 1/200$ in the low mass region with large statistical and systematic uncertainties (Fig.1). Moreover, the limited azimuthal angular acceptance in the central arms and the strong magnetic field beginning radially at $R=0$, makes the identification and rejection of electron-positron pairs from Dalitz decays and photon conversions very difficult. Therefore, the improved S/B is needed for further studies of low mass dilepton spectra. The main sources of combinatorial background are coming from $\pi^0 \rightarrow \gamma e^+e^-$ and $\pi^0 \rightarrow \gamma\gamma \rightarrow \gamma e^+e^-$, and we exploited the fact that these channels have small opening angle so by using the opening angle we must be able to distinguish single hits from double hits in HBD.

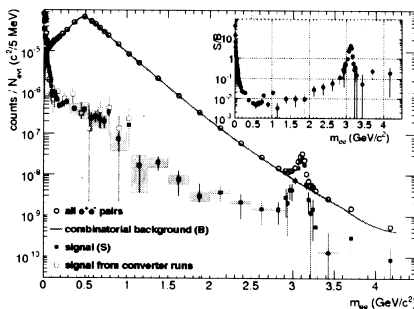


Figure 1: Background(B) and Signal(S) with statistical(bar) and systematic(boxes) uncertainties. The inset shows S/B ratio[3].

2. Hadron Blind Detector and Performance Studies

2.1. Detector concept

The main task of HBD was to recognize and reject γ -conversions and π^0 Dalitz decay pairs using the fact of their small opening angle. In order to conserve the opening angle of the decay pairs, HBD was placed in the magnetic field free region as is shown in figure 2(b). HBD consists of a Cherenkov radiator operated with pure CF_4 in a proximity focus configuration directly coupled to a triple-GEM detector element with a CsI photocathode on the top GEM[5] and a pad readout.

The choice of CF_4 both as radiator and detector gas in a windowless geometry results in a very large bandwidth (from ~ 6 eV given by the threshold of the CsI to ~ 11.5 eV given by the CF_4 cut-off) and consequently in a large figure of merit N_0 and a large number of photo electrons N_{pe} . One of the important advantage of using GEMs is that it allows the use of a reflective photocathode which is totally screened from photons produced in the avalanche process. HBD contains two arms in east and west side of PHENIX co-ordinate system and its acceptance in pseudorapidity is $|\eta| \leq 0.45$ and in azimuthal angle ($\Delta\Phi$) is 135° .

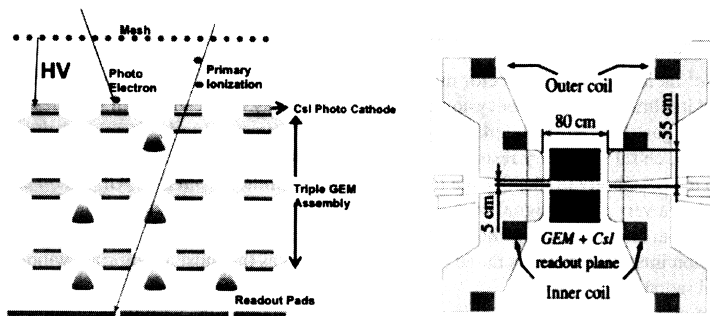


Figure 2: Schematic of (a) HBD working principle and (b) position of HBD in PHENIX.

2.2. Performance

HBD position resolution is estimated by the matching of the Central Arm tracks to the HBD. The matching distributions (difference between projection point and the closest cluster in HBD) of electron tracks in Φ and Z were

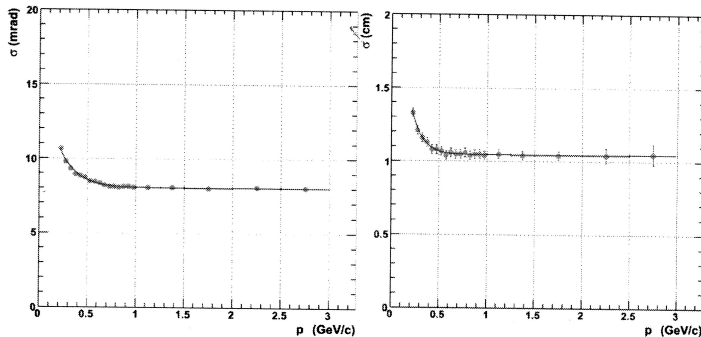


Figure 3: The variation of matching resolution of the electron tracks in Z and Φ with respect to momentum.

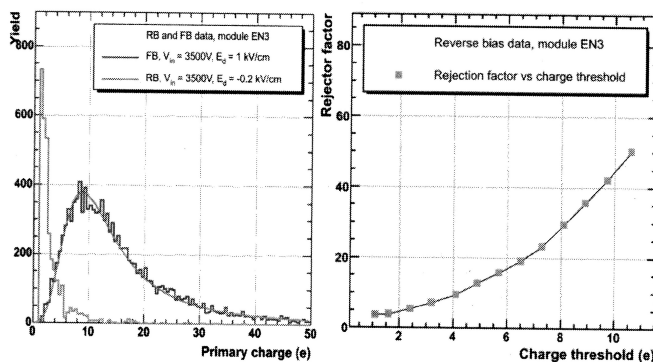


Figure 4: (a) Hadron charge spectra in reverse(red) and forward bias(blue) (b) Hadron Rejection Factor as a function of charge threshold.

determined for different track momentum bins. In Fig. 3, the momentum dependence of the sigma of ΔZ and $\Delta\Phi$ is shown and the asymptotic resolution in Z and Φ are obtained ~ 1.05 cm and 8 mrad respectively.

In Fig. 4(a), a drop in pulse height of hadrons in RB mode of HBD is demonstrated. Hadron rejection factor (ratio of the number of hadron tracks identified in central arm detectors to the number of corresponding matched hits in the HBD) as a function of threshold charge in reverse bias mode of HBD for a single module is shown in Fig. 4(b). Also a very good separation between single electrons and hadrons in RB has been observed as single electron response peaked at ~ 20 photoelectrons whereas electrons from hadrons are peaked at ~ 40 due to single and double hits in HBD respectively. Single electron efficiency for the full HBD extracted from di-electrons in the J/Ψ mass region is obtained approximately as 90%.

3. Conclusion

Hadron Blind Detector performed well in PHENIX during RHIC Runs in 2009 ($p+p$) and 2010 (Au+Au). The performance studies carried with $p+p$ data, the hadron rejection power achieved, good separation between electrons coming from resonances or heavy quarks and neutral hadrons are consequent improvement in the di-electron S/B. The studies of Au+Au data set are in progress.

4. Acknowledgements

Authors acknowledge the financial support from Department of Science and Technology (DST), Government of India, New Delhi.

References

- [1] Z. Fraenkel et al., Nucl. Instr. Meth. A 546 (2005) 466.
- [2] J. Wambach and R. Rapp, Nucl. Phys. A 638 (1998) 171.
- [3] A. Adare, et al., Phys. Rev. C 81 (2010) 034911.
- [4] S. Turbide, R. Rapp and C. Gale, Phys. Rev. C 69 (2004) 014903.
- [5] F. Sauli, Nucl. Instr. and Meth. A 386 (1997) 531.

Moments of net-charge multiplicity distribution in Au+Au collisions measured by the PHENIX experiment at RHIC

P. Garg * (for PHENIX collaboration)

Department of Physics, Banaras Hindu University, Varanasi-221005, India

E-mail: prakhar@rcf.rhic.bnl.gov

Beam Energy Scan (BES) program at RHIC is important to search for the existence of the critical point in the QCD phase diagram. Lattice QCD have shown that the predictions of the susceptibility of the medium formed in heavy-ion collisions can be sensitive to the various moments (mean (μ) = $\langle x \rangle$, variance (σ^2) = $\langle (x - \mu)^2 \rangle$, skewness (S) = $\frac{\langle (x - \mu)^3 \rangle}{\sigma^3}$ and kurtosis (κ) = $\frac{\langle (x - \mu)^4 \rangle}{\sigma^4} - 3$) of conserved quantities like net-baryon number (ΔB), net-electric charge (ΔQ) and net-strangeness (ΔS). Any non-monotonic behavior of the higher moments would confirm the existence of the QCD critical point. The recent results of the higher moments of net-charge multiplicity distributions for Au+Au collisions at \sqrt{s}_{NN} varying from 7.7 GeV to 200 GeV from the PHENIX experiment at RHIC are presented. The energy and centrality dependence of the higher moments and their products ($S\sigma$ and $\kappa\sigma^2$) are shown for the net-charge multiplicity distributions. Furthermore, the results are compared with the values obtained from the heavy-ion collision models, where there is no QCD phase transition and critical point.

8th International Workshop on Critical Point and Onset of Deconfinement
March 11 - 15, 2013
Napa, California, USA

*Speaker.

1. Introduction

The phenomenology of Quantum Chromodynamics (QCD) at finite temperature and baryon number density is one of the least explored regimes of the theory [1]. QCD predicts a phase transition from hadron gas (HG) phase to quark gluon plasma (QGP) phase at high temperature and/or baryon density. The exact nature of the phase transition is still not established, however, various QCD based model indicate that at large μ_B and lower T the transition from hadronic phase to the Quark Gluon-Plasma (QGP) phase is of first order. On the other hand, lattice QCD calculations with physical quark masses suggests that the phase transition at high T and lower μ_B could be a simple cross over from QGP to hadron phase. It further suggest that the first order phase transition line should end somewhere at finite μ_B and T and that point will be a critical point of second order[1].

It has been proposed that a critical point is a genuine thermodynamic singularity at which susceptibilities diverge and the order parameter fluctuates on long wavelengths [2]. But all the signatures share the common property that they are non-monotonic as a function of an experimentally varied parameter such as collision energy [3]. Typically, most of the fluctuation measures are related to quadratic variances of event-by-event observables, such as particle multiplicities, net charge, baryon number, particle ratios or mean transverse momentum in the event. However, higher non-Gaussian moments of the fluctuations are much more sensitive to the proximity of the critical point than the commonly employed measures based on quadratic moments[3]. Further, It has been suggested by lattice QCD calculations that the first three cumulants of net electric charge fluctuations are well suited for a determination of freeze-out parameters in a heavy ion collision [4].

Recently, Beam Energy Scan (BES) program at relativistic heavy ion collider (RHIC) has been started to search the location of critical point. It has been suggested that the medium created in heavy ion collision experiments at different center of mass energy ($\sqrt{s_{NN}}$) follow different trajectories on the temperature (T) and baryon chemical potential (μ_B) plane during their time evolution [1]. This will enable us to locate the critical point in T- μ_B plane by experimentally measuring the fluctuations in higher moments of net charge, net baryon etc. with respect to $\sqrt{s_{NN}}$. In the present work, fluctuations of the net charge and it's higher moments are obtained from the net charge distributions measured by PHENIX experiment at RHIC.

2. Analysis details

In the present work, 200 GeV Au+Au data of RUN07 and 62.4 GeV, 39 GeV and 7.7 GeV data of RHIC RUN10 taken by PHENIX experiment is used. The event-by-event net-charge distribution is measured for Au+Au collisions occurring within ± 30 cm along the z position of the interaction point. The charged particles are measured between the transverse momentum (p_T) range $0.3 \text{ GeV}/c < p_T < 1.0 \text{ GeV}/c$ and pseudorapidity (η) range at $|\eta| < 0.35$ region. The standard PHENIX track quality cuts are used for this analysis. To avoid the auto-correlation effect in the higher moments analysis, the centrality selection has been done by using tracks in a different pseudo rapidity range. The finite centrality bin width effect has been corrected by using a centrality

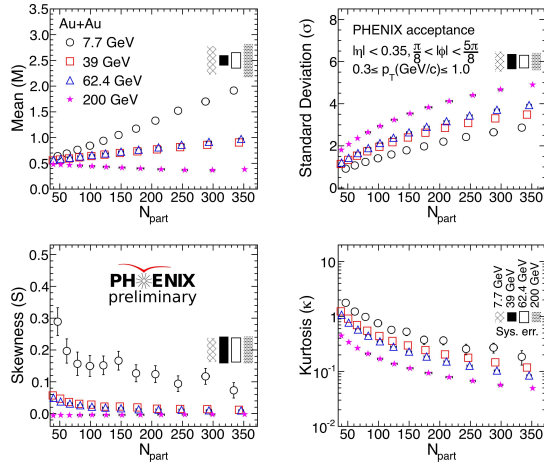


Figure 1: (Color online) Mean, Standard Deviation (σ), Skewness and Kurtosis obtained from net-charge distributions for Au+Au collision at $\sqrt{s_{NN}} = 200$ GeV, 62.4 GeV, 39 GeV and 7.7 GeV for most-central to most-peripheral events are shown.

bin width correction. Delta theorem is used for the statistical error estimation of higher moments [5].

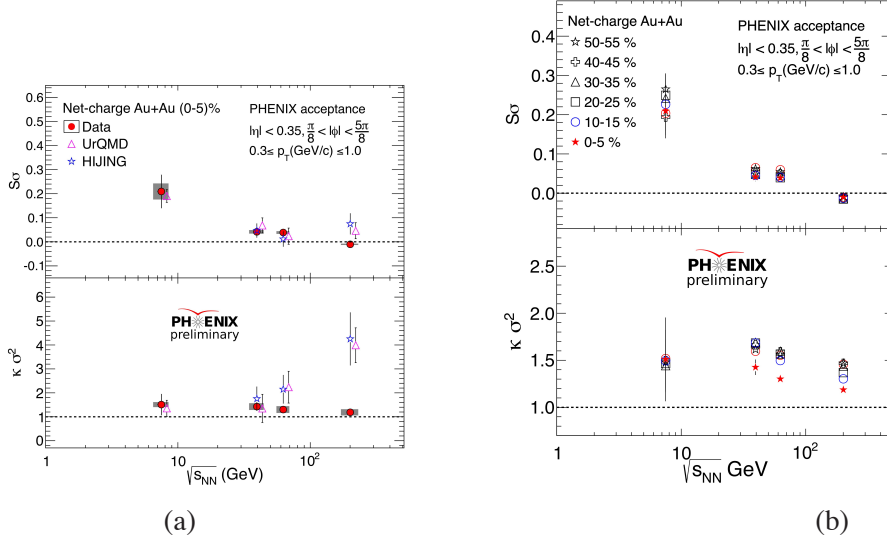


Figure 2: (Color online) The skewness multiplied by the standard deviation and the kurtosis multiplied by the variance from net charge distributions for Au+Au collisions as a function of $\sqrt{s_{NN}}$. (a) The circles represent the data for most central collision events. The grey error bars represent the systematic errors. (b) $S\sigma$ and $\kappa\sigma^2$ for different centralities as a function of $\sqrt{s_{NN}}$.

3. Results

Mean, Standard Deviation, Skewness and Kurtosis, calculated from event-by-event net-charge multiplicity distributions for Au+Au collisions at $\sqrt{s_{NN}} = 7.7$ GeV, 39 GeV, 62.4 GeV and 200 GeV are shown in Fig. 1 as a function of number of participants (N_{part}). Mean and Standard deviation increases with N_{part} while Skewness and Kurtosis decreases with N_{part} , although for 200 GeV, mean is almost constant within the systematic errors. Also the Mean, Skewness, and Kurtosis increases with decreasing $\sqrt{s_{NN}}$ while the trend is opposite in case of Standard Deviation as is evident from Fig. 1.

The skewness and kurtosis, calculated from the net-charge distributions, are expressed in terms that can be associated with the quark number susceptibilities, $\chi : S\sigma \approx \chi(3)/\chi(2)$ and $\kappa\sigma^2 \approx \chi(4)/\chi(2)$ [6]. Theoretically, if we take the ratio of the susceptibilities, the volume effect is canceled out. The energy dependence of $S\sigma$ and $\kappa\sigma^2$ of net-charge distributions are shown in Fig. 2. The statistical and systematic uncertainties are shown along with the data points. The experimental values are compared with the model calculations from UrQMD and HIJING within the PHENIX acceptance.

The HIJING and URQMD results match the data points except at highest energies, which may be due to the contribution of resonance production. $S\sigma$ and $\kappa\sigma^2$ are shown for different centralities as a function of $\sqrt{s_{NN}}$ as shown in Fig. 2 (b).

4. Summary

The higher moments of the net-charge multiplicity distributions have been measured for Au+Au collisions at $\sqrt{s_{NN}} = 7.7$ to 200 GeV. The values of $S\sigma$ decreases with $\sqrt{s_{NN}}$ while $\kappa\sigma^2$ remains constant within uncertainties for all centralities. There is no significant deviation from the simulation results as observed in the data at these four collision energies. It will be interesting to study at lower energies like 19.6 GeV and 27 GeV which are still under investigation.

5. Acknowledgement

PG acknowledges the financial support from CSIR, New Delhi, India.

References

- [1] M. A. Stephanov, Prog. Theor. Phys. Suppl. **153**, 139 (2004) [Int. J. Mod. Phys. A **20**, 4387 (2005)] [hep-ph/0402115].
- [2] M. A. Stephanov, K. Rajagopal and E. V. Shuryak, Phys. Rev. D **60**, 114028 (1999) [hep-ph/9903292].
- [3] M. A. Stephanov, Phys. Rev. Lett. **102**, 032301 (2009) [arXiv:0809.3450 [hep-ph]].
- [4] A. Bazavov, H. T. Ding, P. Hegde, O. Kaczmarek, F. Karsch, E. Laermann, S. Mukherjee and P. Petreczky *et al.*, Phys. Rev. Lett. **109**, 192302 (2012) [arXiv:1208.1220 [hep-lat]].
- [5] X. Luo, J. Phys. G: Nucl. Part. Phys. **39**, 025008 (2012)
- [6] F. Karsch and K. Redlich, Phys. Lett. B **695**, 136 (2011) [arXiv:1007.2581 [hep-ph]].